Investigations of Redox-active Dithiafulvenyl-substituted Polycyclic Aromatic Hydrocarbon Systems: DFT and TD-DFT Studies

by

© Ramin Eradeh

A thesis submitted to the School of Graduate Studies in partial fulfilment of

the requirements for the degree of

Ph.D.

Department of Chemistry

Memorial University of Newfoundland

November 2023

St. John's Newfoundland

Abstract

This PhD thesis demonstrates the design, implementation, and applications of the redox-active 1,4-dithiafulvene and its arene-substituted derivatives. The research is mainly based on computational modeling and simulations, employing techniques such as density functional theory (DFT), time-dependent density functional theory (TD-DFT), molecular dynamics (MD), and other quantum mechanical methods. These investigations include a broad range of fundamental properties, including attractive and repulsive non-covalent interactions between redox-active 1,4-dithiafulvenes and their reaction mechanisms associated with such interactions. Additionally, the UV-vis and fluorescence behaviors of a modified self-condensed pyrene-4,5-dione product has been studied through a combined approach of experimental and theoretical analyses. The results of this thesis disclose the fundamental mechanisms and intermolecular interactions that underpin the behaviors of the above mentioned compounds.

Experimentally, 1,4-dithiafulvene (DTF) derivatives have been found to reduce Au (III) species in organic media to yield gold nanoparticles (AuNPs). This reaction provides a promising method for the synthesis of AuNPs, however, theoretical investigations into the surface thermodynamic properties of AuNPs, interactions between DTF and Au clusters, and solvent effects were lacking. In the first project of this thesis, systematic computational studies were carried out to gain in-depth understanding of the bind mechanisms of DTF radical cations and AuNP surface. DFT analysis indicated that sulfur and oxygen atoms in the DTF moiety serve as primary binding sites, while TD-DFT calculations predicted electronic transition bands agreeing with the experimental UV-Vis absorption spectra of AuNP/DTF complexes. The results in this work provide valuable guidance for controlled AuNP synthesis and functionality engineering.

In the second project, the oxidative dimerization mechanism for a phenyl-substituted 1,4-dithiafulvene (Ph-DTF) was examined by DFT calculations. Detailed thermodynamic and kinetic properties of the various possible reaction pathways were obtained. The effects of electron-withdrawing and electron-donating substitutions as well as organic solvents on the dimerization reactivity was also studied. The computational results showed that these effects play critical roles in the dimerization mechanism, which deepen the understanding of the dimerization mechanism for various arene-substituted DTF molecules.

The third project of this thesis focuses on a series of arene-substituted dithiafulvene (Ar-DTF) compounds, investigating their molecular structures and electronic properties. A correlation emerges between the π-system size and radical cation stability upon oxidation, driven by increased π-delocalization. Exceptions to this trend emphasize the role of molecular geometry. Charge transfer phenomena highlight efficient electron-hole distribution with larger π-systems, offering design principles for tailoring electronic properties.

In the fourth and last study, a π-conjugated compound obtained from a self-condensation reaction of pyrene-4,5-dione was characterized. Its excimeric emissions were investigated in various organic solvents to show significant solvatochromic effects. Host-guest complexes with cyclodextrins illustrate potential applications in chemical sensing and optoelectronics. X-ray crystallography, TD-DFT, and conformer calculations deepen the understanding of its molecular structure and excimer formation.

Overall, this thesis presents a multi-dimensional perspective on DTF and its π-conjugated derivatives, elucidating their behavior and potential applications. The insights gained from these studies pave a way for future research endeavors, inspiring the development of innovative materials and technologies across diverse scientific and technological domains.

Acknowledgements

First and foremost, I am deeply grateful to my supervisor, Prof. Yuming Zhao, whose unwavering guidance, insightful feedback, and continuous support have been instrumental throughout this journey. His mentorship has been a cornerstone of my academic and personal growth. I am always indebted to him for everything he has taught me during my PhD program.

I extend my heartfelt appreciation to my supervisory committee members, Profs. Sunil Pansare, Heloise Therien-Aubin, and Christopher Rowley. Their expertise, feedback, and constructive discussions have greatly enriched the quality of this work.

I'd like to express my sincere appreciation to Prof. Christopher Flinn for his invaluable guidance in computational chemistry, serving as a consultant in computational methods, and meticulously proofreading my thesis. His expertise and meticulous attention to detail have enhanced the rigor of this research.

I extend my gratitude to Prof. Graham Bodwell who taught me the course of Organic Synthesis, and also to Prof. Huck Grover for teaching me the course of Heterocyclic Chemistry. Their dedication, support, and perceptive teachings have been pivotal to my academic growth.

I am privileged to have worked alongside Dr. Jian-Bin Lin, a distinguished crystallographer. His expertise and guidance in crystallography have been invaluable in enhancing the quality of this research.

I dedicate this thesis to the cherished memory of my father and my beloved brothers, Mehrab and Hossein. Their unwavering belief in me fueled my journey.

Though they're no longer here, their spirits remain my guiding lights. Their legacies are interwoven throughout this work, a testament to their lasting impact.

I extend my heartfelt appreciation to my mother for her constant support and love. To my dear siblings, Vahideh, Reza, Farideh, and Sasan. Their encouragement, unwavering support, and belief in me have been the foundation of my journey.

My heartfelt appreciation goes to my love, my life, beautiful Mona, for her unyielding support, encouragement, and insightful discussions. Her presence has brought joy to every step of this journey. Without her, this journey would never be possible.

I extend my gratitude to my exceptional colleagues: Farshid Shahrokhi, Zahra Ahmadian Tabasi, Monther Zeird, Maryam Faghih Abdollahi, Fatemeh Salami, Azin Afzali, Cheng Wang, Matthew Johnson, and Christopher Qiu. Their camaraderie and collaboration have enriched my research experience.

To my friends in St. John's, their friendship and companionship have been a source of joy and solace. Their support made this journey more vibrant and memorable.

I am grateful to Debbie Hickey, Mary Flinn, and other faculty members and staff of the Chemistry Department of Memorial University for fostering a welcoming and nurturing environment for students.

I sincerely acknowledge the support of Memorial University of Newfoundland, NSERC, and Compute Canada for funding this research, enabling me to pursue my academic aspirations.

Lastly, to everyone who played a role, big or small, in my academic and personal journey, their contributions are cherished and appreciated beyond words. Thank you.

Contents

List of Figures

List of Schemes

List of Tables

List of Abbreviations and Symbols

A	electron acceptor
Å	Angstrom unit (a unit of length, equal to 10^{-10} meters)
ACN	acetonitrile
AIEE	aggregation-induced emission enhancement
AIMD	ab initio molecular dynamics
aq	aqueous
Ar-DTF	arene substituted 1,4-dithiafulvene
AS	aromatic system
Au_n	n-atom gold cluster
Au_n/DTF	complex of n-atom gold cluster with 1,4-dithiafulvene
AuNPs	gold nanoparticles
Au SAMs	self-assembled gold monolayers

B3LYP	Becke's three-parameter hybrid functional combined with LYP correlation
B97	Becke's hybrid functional
BCP	bond critical point
BHJ	bulk heterojunction
C_{60}	[60]fullerene
c_x	fractional number in hybrid functionals
ca.	circa
calcd	calculated
CAM-B3LYP	coupled-cluster approximation method with B3LYP exchange
CD	cyclodextrin
CDCA	chenodeoxycholic acid
$CHCl_3$	chloroform
−CHO	aldehyde
cm	centimeter(s)
−CN	nitrile
−COMe	acetyl
−COOH	carboxylic acid

CP-AFM	colloidal probe atomic force microscopy
CREST	conformer-rotamer ensemble sampling tool
CT	charge-transfer
CV	cyclic voltammetry
CX	complex
d	doublet
D	Debye
D	electron donor
D/A	donor/acceptor
DC	dication
DCM	dichloromethane
D-DFT	dispersion-corrected density functional theory
DFT	density functional theory
DMF	*N*,*N*-dimethylformamide
DMSO	dimethylsulfoxide
DP-TTFV	diphenyl tetrathiafulvalene vinylogue
DSSC	dye-sensitized solar cell

DTF	1,4-dithiafulvene
E	total energy of the molecular system
E_{ox}^{1}	first oxidation potential
E_{ox}^{2}	second oxidation potential
E_c	correlation energy
E_{D-DFT}	energy in dispersion-corrected DFT
E_{xc}^{hyb}	hybrid exchange-correlation energy
E_{xc}	exchange-correlation energy
E_x^{HF}	Hartree-Fock exchange energy
E_x^{LSDA}	local spin density approximation exchange energy
E_c^{LSDA}	local spin density approximation correlation energy
E_c^{LYP}	Lee, Yang, and Parr's GGA correlation energy
$E_x^{B97,SR}$	short-range B97 exchange energy
E_c^{B97}	B97 correlation energy
$E_x^{HF,LR}$	long-range HF exchange energy
$E_x^{HF,SR}$	short-range HF exchange energy
$E_x^{DFT,SR}$	short-range DFT exchange energy

E_c^{DFT}	DFT correlation energy
E_{KS-DFT}	Kohn-Sham energy
$E_{O/R}$	oxidation potential
$E^{\circ}_{O/R}$	standard oxidation potential
EDG	electron-donating group
Et	ethyl
EtOAc	ethyl ethanoate (ethyl acetate)
eV	electron volt
EWG	electron-withdrawing group
exTTFs	π-extended tetrathiafulvalene derivatives
F	Faraday constant
FMOs	frontier molecular orbitals
g	gram(s)
G_{Au}	Gibbs energy of the Au_n cluster
$G_{complex}$	Gibbs energy of the Au_n/DTF complex
G_{DTF}	Gibbs energy of 1,4-dithiafulvene
GGA	generalized gradient approximation

h	hour(s)
h	Planck's constant
$\hat{H}$	total Hamiltonian operator
HF	Hartree-Fock
HOMO	highest occupied molecular orbital
ICT	intramolecular charge transfer
IGM	independent gradient model
IR	infrared
IRC	intrinsic reaction coordinate
ISC	intersystem crossing
ISE	isomerization stabilization energy
ITO	indium tin oxide
J	Joule(s)
J	coupling constant
$\hat{J}_j$	Coulomb's operator
k	C-C$_{AS}$ bond length
kcal mol^{-1}	kilocalories per mole

l	C_{DTF}-C bond length
LDA	local density approximation
LSDA	local spin density approximation
LUMO	lowest unoccupied molecular orbital
LYP	Lee, Yang, and Parr's correlation functional
m	multiplet
M	molar
M	number of nuclei in the system
M*	excited molecule
m_e	mass of an electron
M_A	mass of the nucleus of atom A
MALDI-TOF	matrix-assisted laser desorption/ionization-time of flight
MCBJ	mechanically controlled break-junction
Me	methyl
mg	milligram(s)
min	minute(s)
mL	milliliter(s)

mmol	millimole(s)
mM	milimolar
mol	mole(s)
m.p.	melting point
MS	mass spectrometry
MV	mixed-valence
mV	millivolt(s)
mW	milliwatt(s)
MW	microwave
m/z	mass-to-charge ratio
N	number of electrons in the system
N	neutral state
$-NH_2$	amine
NICS	nucleus independent chemical shift
NLO	nonlinear optical
nm	nanometer(s)
NMR	nuclear magnetic resonance

$-NO_2$	nitro
OFETs	organic field effect transistors
OLEDs	organic light emitting devices
$-OMe$	methoxy
OPEs	oligo(phenylene ethynylene)s
OPVs	organic photovoltaics
ORTEP	Oak Ridge thermal ellipsoid plot
PAH	polycyclic aromatic hydrocarbon
PBE0	Perdew-Burke-Ernzerhof hybrid functional
PCM	polarizable continuum model
Ph-DTF	phenyl 1,4-dithiafulvene or 1,4-dithiolene, 5-phenylmethylene
phenyl-DTFs	benzylidenedithioles
ppm	parts per million
PRB	plasmon resonance band
PV	photovoltaic
PVSCs	perovskite solar cells
PW91	Perdew-Wang 1991 functional

QTAIM	quantum theory of atoms in molecules
r_{iA}	distance between nucleus A and electron i
r_{ij}	distance between electrons i and j
R_{AB}	distance between nuclei A and B
RC	radical cation state
S_0	electronic ground state
S_1	electronic first excited state
SAMs	self-assembled monolayers
SCF	self-consistent field
SHE	standard hydrogen electrode
SOMO	singly occupied molecular orbital
SPR	surface plasmon resonance
STM-BJ	scanning tunneling microscopy break-junction
SWCNTs	single-walled carbon nanotubes
$\hat{T}$	kinetic energy operator
TD-DFT	time-dependent density functional theory
TFA	trifluoroacetic acid

THF	tetrahydrofuran
TLC	thin-layer chromatography
TPA	triphenylamine
TS	transition state
TTF	tetrathiafulvalene
TTFAQ	anthraquinone-type π-extended tetrathiafulvalene
TTFV	tetrathiafulvenyl vinylogue
UV	ultraviolet
UV-Vis	ultraviolet-visible
V	volt(s)
$\hat{V}_{ext}(t)$	external potential operator
$\hat{V}_{e-e}$	electron-electron repulsion operator
vdW	van der Waals
Vis	visible
v/v	volume-to-volume ratio
VWN	Vosko, Wilk, and Nusair
XRD	X-ray diffraction

Z_A	charge of the nucleus of atom A
α	torsion angle
β	central bond angle (C_{DTF}-C-C_{AS} bond angle)
δ	chemical shift
$\mathit{\Delta} G^{\circ}$	Gibbs free energy change at standard conditions
$\mathit{\Delta} G_{binding}$	binding Gibbs free energy
∇_i^2	Laplacian operator for electron i
$\nabla\rho$	gradient of the electron density
ϵ_i	orbital energy
ε_0	permittivity of free space
ε_{xc}	exchange-correlation energy density
η	power conversion efficiency
λ_{ex}	excitation wavelength
λ_{max}	maximum absorption wavelength
ρ	electron density
$\upsilon_{ext}(r,t)$	time-dependent external potential
υ_{xc}	exchange-correlation potential functional

$\varPhi$	quantum yield
$\varPsi$	total wave function
$\psi_i(r,t)$	time-dependent Kohn-Sham wavefunction

Chapter 1

Introduction

1.1 Introduction to tetrathiafulvalene (TTF) and its derivatives

Sulfur-containing π-conjugated heterocyclic compounds have been utilized in diverse chemical applications such as synthetic materials, biological and medicinal chemistry.[1–3] A fascinating example of these compounds is tetrathiafulvalene (TTF), which has been well recognized as the most investigated molecular system in the literature of organic materials chemistry.[4–10] TTF consists of two non-aromatic 1,4-dithiole rings, which can be either sequentially or simultaneously transformed into aromatic dithiolium rings under oxidative conditions. Scheme 1.1 shows reactions where TTF loses one electron at $E_{ox}^{1} = +0.34$ V (vs Ag/AgCl) to generate a radical cation intermediate through a single-electron transfer process, and then undergoes another single-electron transfer at $E_{ox}^{2} = +0.78$ V (vs Ag/AgCl) to form a dication product.[11]

In the early 1970s, Fred Wudl and co-workers reported the first use of TTF

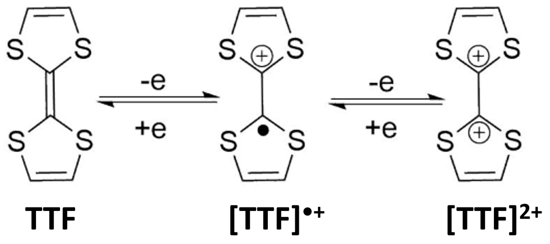

Scheme 1.1: Stepwise single-electron transfer reactions of TTF.

as an active component in making organic semiconductors.[12] This discovery soon sparked the pursuit of organic semiconductors, organic conductors, and organic superconductors. Extensive and in-depth investigations on TTF-based materials in the following years aided in the swift advancement of contemporary organic electronics and optoelectronics.[13]

TTF is redox-active and electron-rich. When interacting with various electron acceptors, TTF can form charge-transfer (CT) complexes with them, acting as an excellent electron donor. Certain TTF-based CT complexes were found to exhibit metallic and semiconducting properties.[6,14,15] The exceptional aromaticity-stabilized cationic states of TTF, which are the consequence of one and two electron oxidation, are responsible for its superior electron-donating ability (Scheme 1.1). Additionally, the oxidation of TTF results in substantial molecular structural changes. For instance, the geometry of a neutral TTF is nearly planar with a slight degree of twist. TTF dication (TTF^{2+}), in contrast, has two dithiolium moieties perpendicular to each other, so that the disfavored internal charge repulsion between the two dithiolium rings is minimized. Such a dramatic shape adjustment helps to stabilize the TTF dication.[16]

1.1.1 π-Extended TTFs

For the creation of novel π-extended TTF derivatives (exTTFs), functionalization of TTF by attaching various functional groups is a very effective method. Due to the π-extension in their molecular structures, several exTTFs have been shown to exhibit good electron-donating properties and diverse electrochemical redox activity. Because their increased π-conjugation has a stabilizing effect on the cationic states of most exTTFs, the oxidation potentials of exTTFs are typically lower than those of the unsubstituted TTF. Additionally, the structural characteristics of exTTFs differ significantly from those of TTF in the neutral and oxidized states. We will have this aspect discussed in detail in Chapter 5.

In order to fabricate nanoscale molecular devices with sensitive responses to environmental stimuli at the molecular and supramolecular levels, exTTFs have been frequently incorporated as redox-active π-building blocks.[15,17] The class of rotaxane and catenane-based molecular machines created by Fraser Stoddart and co-workers represents one of the most prominent application of exTTFs.[18] For his remarkable contributions to the field of molecular machines, Stoddart shared the Nobel Prize in Chemistry with two other renownd chemists, Jean-Pierre Sauvage and Bernard L. Feringa in 2016.[19–23]

The special features and applicability of exTTFs have inspired materials chemists to develop useful organic electronic materials and molecular devices.[24–26] Two different methods can be used to create exTTF derivatives: (i) attaching π-conjugated units to the dithiole rings (such as the dibenzo-TTF shown in Figure 1.1); and (ii) inserting π-spacers between the two dithiole rings (such as anthraquinone-type

π-extended tetrathiafulvalene (TTFAQ) and tetrathiafulvalene vinylogue (TTFV). These exTTFs have significant applications in the disciplines of nanotechnology and materials science, owing to their versatile redox-activities.[11,15,27,28]

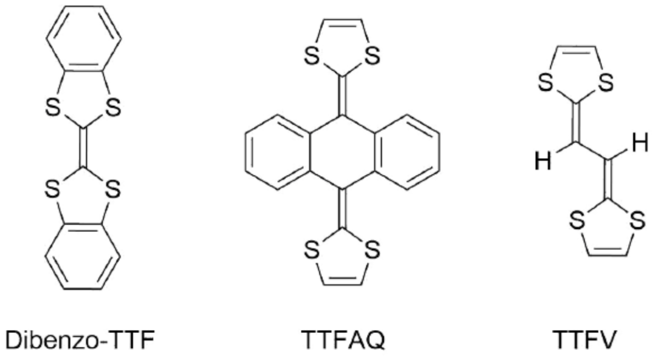

Figure 1.1: Selected examples of exTTFs.

1.2 Introduction to 1,4-dithiafulvene (DTF)

1,4-Dithiafulvene (DTF), an important organic electron-donating functional group, is the half structure of TTF. To create certain exTTFs, DTF can be used as the starting material. Functionalized DTFs can be made by applying insertion and/or annulation reactions on DTF, and π-extended DTF derivatives can be used as organic semiconducting materials and effective π-electron donors.

1.2.1 Electron-donating properties of DTF

Under oxidative conditions, the electron-rich heterocyclic DTF can readily release one of its π-electrons. The thermochemical and structural characteristics of the unsubstituted DTF, 2-methylene-1,3-dithiole, have been computationally examined in the literature.[29,30] Nucleus independent chemical shift (NICS) and isomerization stabilization energy (ISE) calculations suggested that unsubstituted DTF should act as a reliable organic π-electron donor.[31] Nevertheless, unsubstituted DTF has limited stability and thus is not easy to prepare.

To improve the stability and enhance desirable electronic characteristics, substituted DTFs have been developed. These compounds usually contain other functional groups which are in π-conjugation with the DTF moiety. It is interesting to note that π-extended DTF derivatives can lead to improvement in synthetic accessibility, stability, redox activities, and electronic characteristics, which pave the way for many novel applications in organic electronics.

1.2.2 Chemical and redox reactivities of DTFs

As an electron-rich heterocycle, DTF can readily release an electron upon oxidation to generate a radical cation. In 1958, Kirmse and Horner[32] described the oxidative dimerization of DTF. In their work, DTF became oxidized, yielding a reddish-violet salt. In 1974, Mayer and Krober explored the oxidation of a number of diaryl-substituted DTFs (Scheme 1.2) and proposed the structures of the oxidized products based on elemental and UV–Vis absorption measurements.[33] They also suggested a mechanism as shown in Scheme 1.2 to account for the oxidative dimerization of DTF.

While the presence of the vinyl proton is necessary for the elimination step to produce a stable dication product, known as a tetrathiafulvalene vinylogue (TTFV) in its neutralized form, the introduction of an aryl group to the DTF vinyl position makes the production of the radical cation intermediate easier.

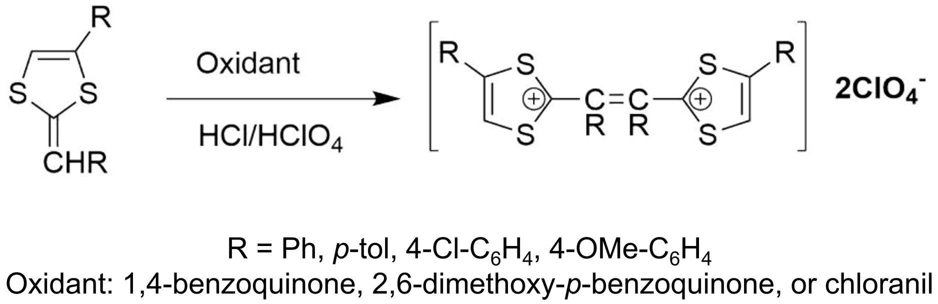

Scheme 1.2: Oxidative dimerization of DTFs.

To promote the DTF dimerization process, a variety of oxidants can be used, including $(BrC_6H_4)_3SbCl_6$,[34,35] I_2,[36,37] Br_2,[38,39] and $AgBF_4$.[40–42] In addition, various TTFV compounds can be produced by DTF dimerization reactions induced by electrochemical methods.[39,43–45] Utilizing cyclic voltammetric (CV) measurements, Hapiot et al. in 1996 conducted a detailed investigation on the DTF oxidative dimerization mechanism.[46] According to their reported mechanism, a fast single-electron transfer initially produces a DTF radical cation, which is followed by the formation of a dicationic dimer (Scheme 1.3). Next, the two vinylidene hydrogens are eliminated, and this double deprotonation step produces a TTFV product. TTFV has an oxidation potential lower than that of DTF. So, it is quickly oxidized into the TTFV dication.

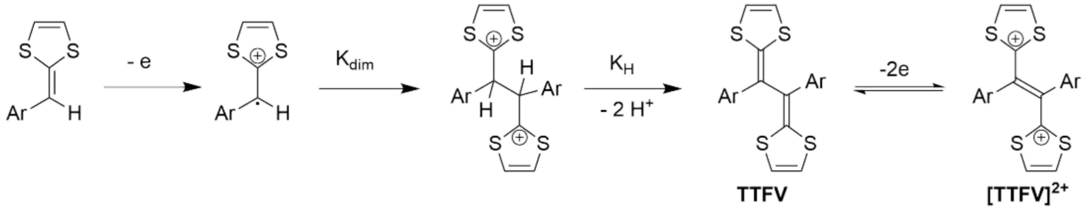

Scheme 1.3: Mechanism for DTF oxidative dimerization.

In the literature, some other DTF reactivities were also mentioned. Scheme 1.4

provides a summary of DTF involved reactions.[47] In most of these reactions, the DTF vinylidene proton is replaced by various electrophilic groups (i.e., substitution reactions). According to Hartzler,[48] resonance effects made benzylidenedithioles (i.e., phenyl-DTFs) into quasi-aromatic systems. As a result, there are several substitution processes that the exo-ring C=C bond can go through, such as bromination,[49] diazotization, nitrosylation,[50] and formylation with oxalyl chloride.[51]

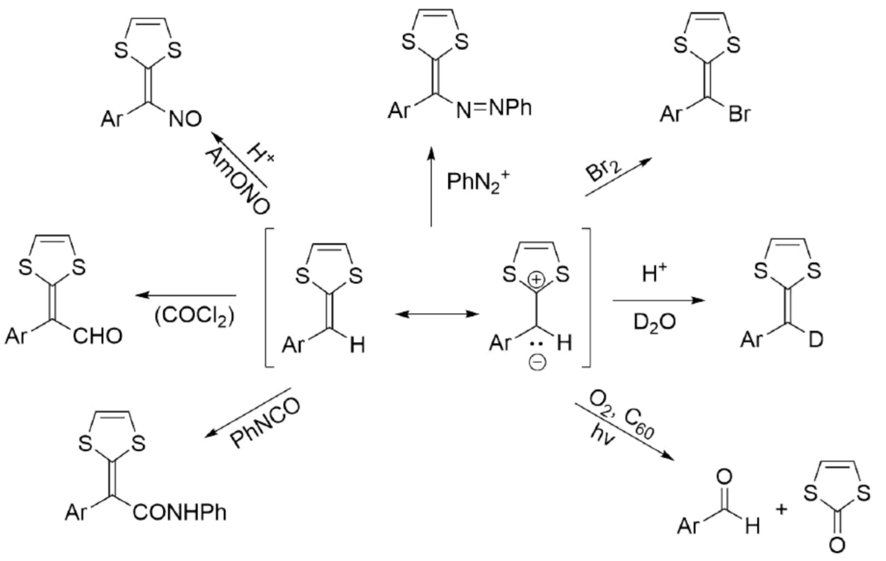

Scheme 1.4: Substitution reactions of DTF with various electrophiles.

Recently in our group, strong acids was used to protonate DTF, which then underwent a hydrogen/deuterium exchange when quenched with D_2O.[52] Additionally, the activated C=C bond of DTFs allows cycloaddition reactions to occur.[53] Moreover, a photo-oxidative cleavage event involving DTF is possible in the presence of air and C_{60} fullerene.[34,54] Once singlet oxygen is formed as a result of the photo-excitation of C_{60}, it combines with the C=C bond to cleave DTF into an aldehyde and a 1,3-

dithiol-2-one product. Recent research by the Zhao group has revealed other unique reactivities of DTFs. When phenyl-DTF derivatives contain an *ortho*-substituent (such as CH_3 or Br), for instance, the iodione assisted oxidative coupling process results in a bis-spiro-tricyclic structure (refer to Scheme 1.5).

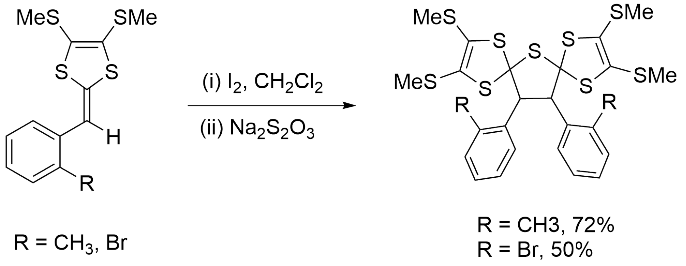

Scheme 1.5: Oxidative dimerization of phenyl-DTFs with *ortho*-substituents.

The *ortho*-substituted group in the DTF (Scheme 1.5) prevents the deprotonation step from occurring. As a result, during the workup, $Na_2S_2O_3$ interacts with the protonated dication intermediate to produce the bis-spiro-tricyclic final product. Sometimes, the π-extended aryl groups that are connected to DTF can stabilize the intermediate radical cation owing to strong resonance effects and hence decrease the reactivity of oxidative dimerization. The substitution reactions of 1-naphthyl or 9-anthryl-substituted DTFs with 1,3,4-thiadiazole-2-thiols are another intriguing DTF reaction. Scheme 1.6 shows that iodine oxidizes DTF, and then the resulting radical cation reacts with 1,3,4-thiadiazole-2-thiols to give thiadiazolyl-substituted products in good yields.[55]

An intramolecular alkyne-dithiolium cycloaddition reaction was recently reported by the Zhao group. Through iodine assisted DTF oxidative coupling, a bis-DTF was first created as a precursor for oxidative polymerization. However, the main

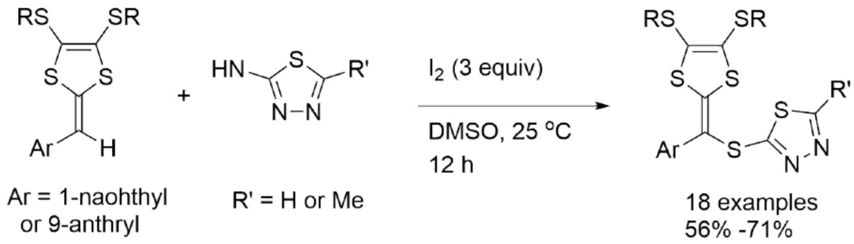

Scheme 1.6: Iodine-mediated oxidative vinylic C(sp^2)-H sulfenylation.

product of this reaction was bis(indenothiophene).[56] When TFA, a strong acid, was used to treat the dialkyne diDTF (Scheme 1.7), a cycloaddition product was observed. Based on these experimental findings, the protonation of the vinylic carbon of the aforementioned diDTF was identified as a crucial step in this cycloaddition reaction. According to density functional theory (DFT) studies, the mechanism of this reaction was established as follows. First, a dithiolium cation is formed through protonation, and this intermediate reacts with the *ortho*-alkynyl group to produce an intramolecular cycloaddition product (Scheme 1.7).[57]

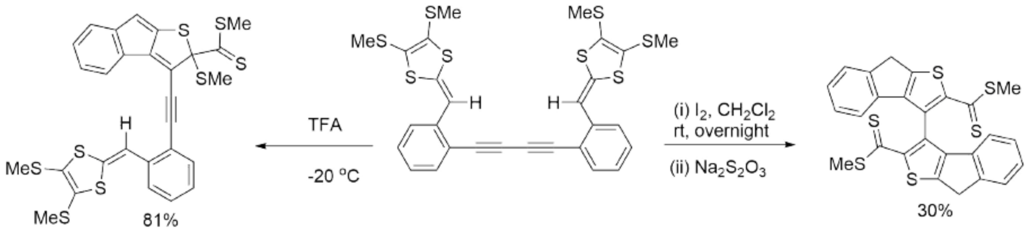

Scheme 1.7: Intramolecular alkynyl-dithiolium cycloaddition reactions.

1.3 Applications of DTF and TTFV

1.3.1 Organic solar cells

The optoelectronic performance of π-conjugated systems can be improved by attaching DTF as a donor group. For instance, in 2008, Leriche and colleagues created six different DTF-functionalized triphenylamines (TPAs) (Figure 1.2), and investigated the potential application of these substances as active components in photovoltaic (PV) and organic field-effect transistor (OFET) devices.[58]

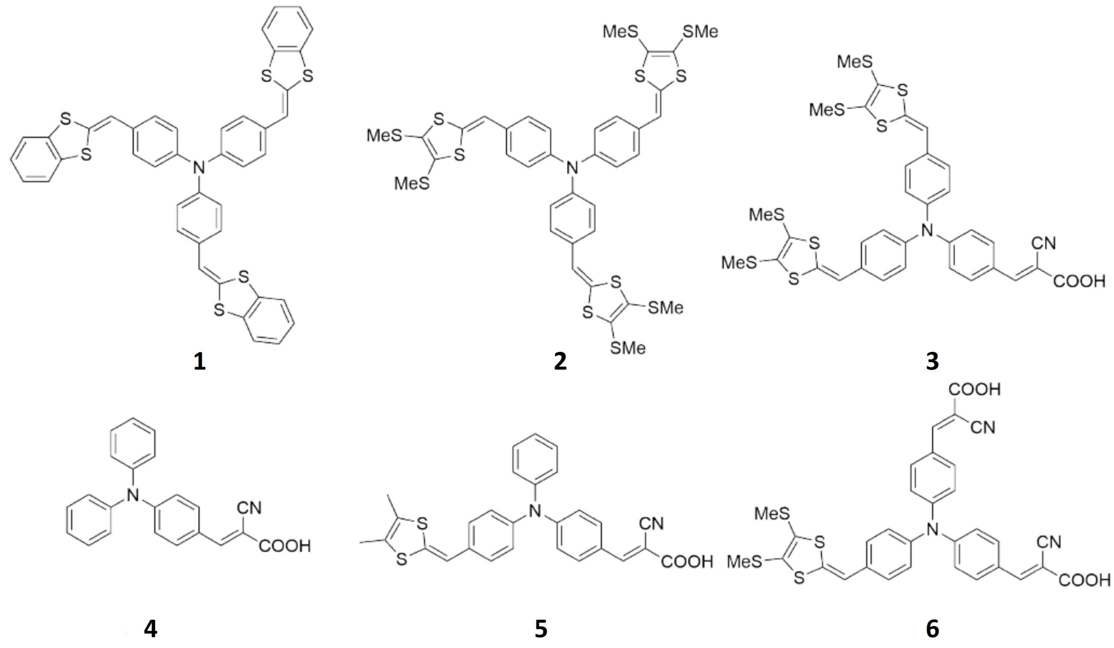

Figure 1.2: Examples of DTF-functionalized triphenylamines for solar cell devices.

Compound **1** shows a better hole mobility than the other compounds due to its greater π-stacking efficiency in the solid state. This compound can also be used with C_{60} fullerene to generate a bilayer bulk heterojunction (BHJ) solar cell. The solar cell achieved a reasonable power conversion efficiency, but the device's stability was poor. In 2012, Yang and colleagues[59] produced a class of DTF(Donor)-π-A(Acceptor)-type metal-free organic sensitizers for the fabrication of dye-sensitized solar cells (DSSCs) (Figure 1.3).

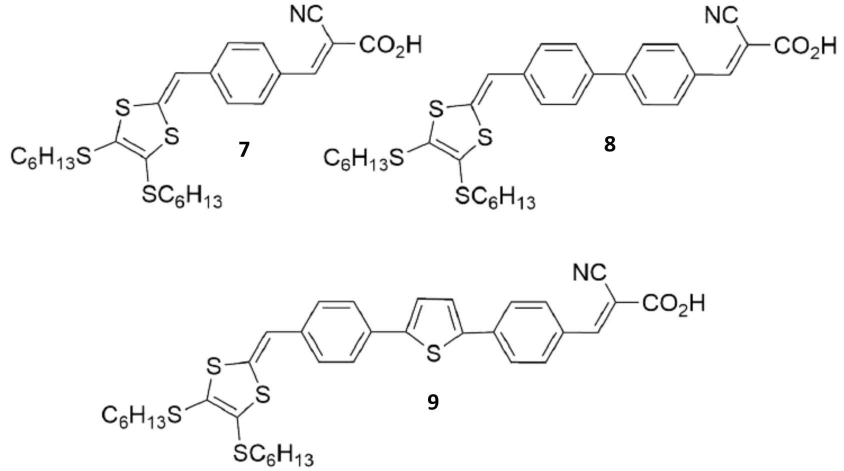

Figure 1.3: High-efficiency dye-sensitized solar cells using a DTF-unit as a donor.

With longer π-bridges, the performance of devices based on DTF sensitizers increases. The maximum power conversion efficiency (η), 8.29%, was achieved by using compound **9**. It is reasonable to predict a bright future for the development of high-performance organic DSSCs based on DTF-functionalized dye molecules when comparing these compounds to metal-based sensitizers. For example, the power conversion efficiency (η) for Ru-based N719 is 8.76%. Recently, DTF-functionalized devices were reported as effective dye-sensitized solar cells by Guo and colleagues.[60] They synthesized two V-shaped dye compounds (Figure 1.4) and co-adsorbed them with chenodeoxycholic acid (CDCA) on TiO_2. Using these compounds, they prepared a solar cell with a high value of η (9.04%). A similar DTF/(2-cyanoacetic acid)-

functionalization method was used to prepare a star-shaped triphenylamine derivative for high performance DSSC.[60]

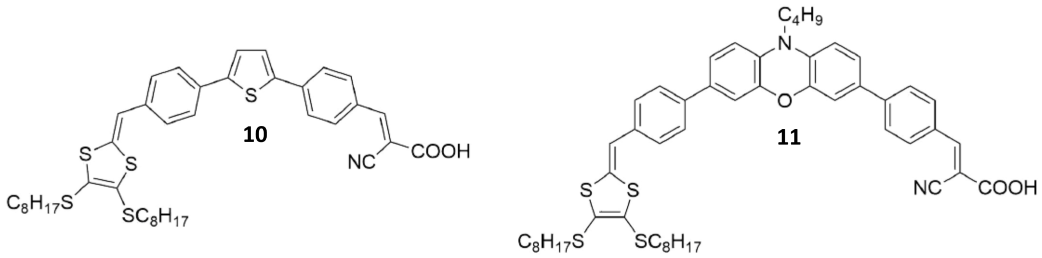

Figure 1.4: V-shaped DTF-functionalized dyes for high-performance DSSCs.

Wu and colleagues[61] developed spiro[fluorene-9,9'-xanthene] compounds with dithiafulvenyl functionalization (Figure 1.5). The use of two of these compounds as dopant-free hole-transporting components in perovskite solar cells (PVSCs) was examined. Due to the advantageous S–S contact in the solid state, the DTF group produced high hole mobility and strong air stability. The hole mobility of the upper compound in Figure 1.5 was found to be about five times larger than that of the lower compound. According to their research, the DTF-functionalized positions on the spiro[fluorene-9,9'-xanthene] structure can significantly affect the device performance.

1.3.2 Molecular wires

It is possible to generate molecular wires from linear π-conjugated oligomers and polymers for a variety of applications, including nanoscale electrical and optoelectronic devices.[62–66] Since 2006, Nielsen and co-workers have developed a variety of DTF-functionalized oligo(phenylene ethynylene)s (OPEs) (Figure 1.6).[67–71]

The molecular conductance of these OPE wires was investigated in order

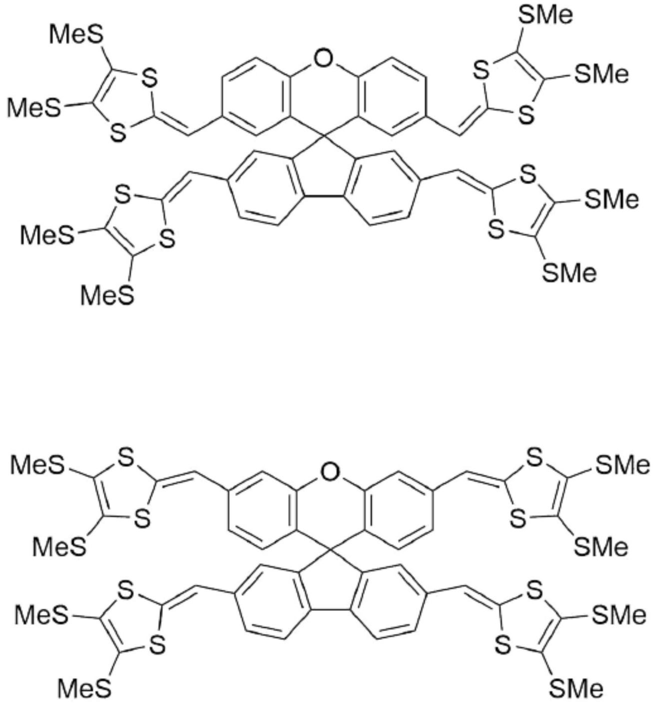

Figure 1.5: Hole-transporting application of DTF-functionalized spiro[fluorene-9,9'-xanthene]s in PVSCs.

to understand their molecular wire behavior and associated structure-property relationships. Self-assembled monolayers (SAMs), mechanically controlled break-junction (MCBJ) experiments on single molecules, and scanning tunneling microscopy break-junction (STM-BJ) experiments on single molecules were carried out.[72,73] According to CP-AFM analysis, the molecular conductance of these OPE wires increases when more DTF groups are orthogonally positioned along the wires. On the other hand, single-molecule studies using the STM-BJ and MCBJ techniques revealed that DTF groups cause the junction formation probability to decrease and exhibit insignificant impacts on single-molecule conductance. Interfacial features are among the other factors that play important roles. Nevertheless, measuring molecular

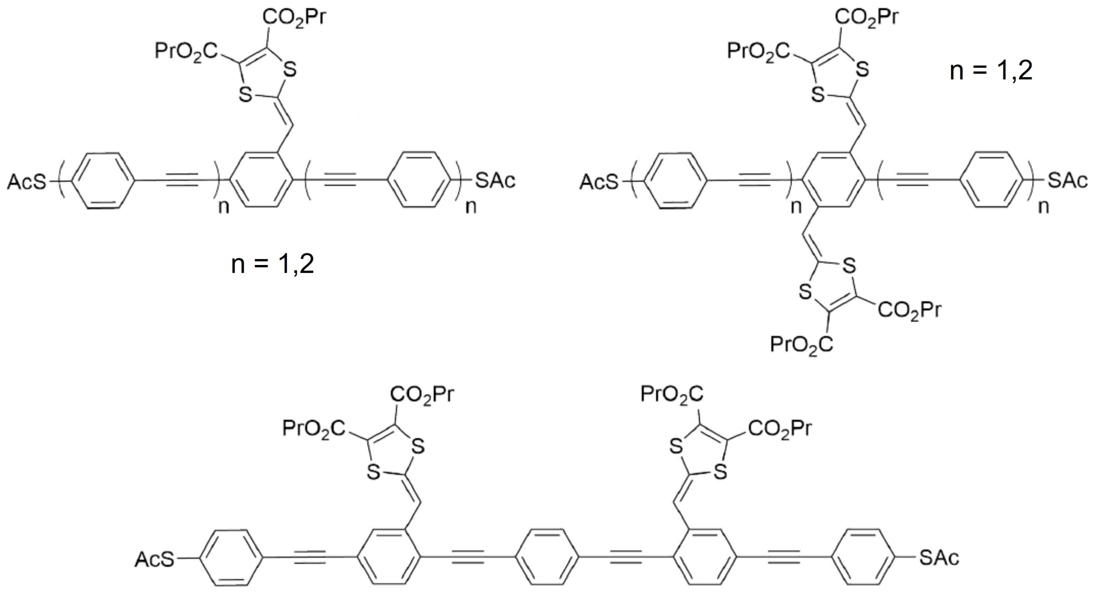

Figure 1.6: DTF-functionalized OPEs as molecular wires.

conductance is a difficult and challenging process.

A collection of linear and cross-conjugated D-A substituted OPE wires were recently studied by Lissau et al.[74] In this work, the molecular characteristics of two DTF-functionalized OPEs were investigated and compared (Figure 1.7).

By using the MCBJ method with gold contacts to measure conductance, both compounds showed noticeably widened conductance peaks. Due to distinct resonance effects, the upper compound in Figure 1.7 exhibits linear conjugation whereas the other compound exhibits cross-conjugation, resulting in the apparent differences in their observed conductance histograms.[74]

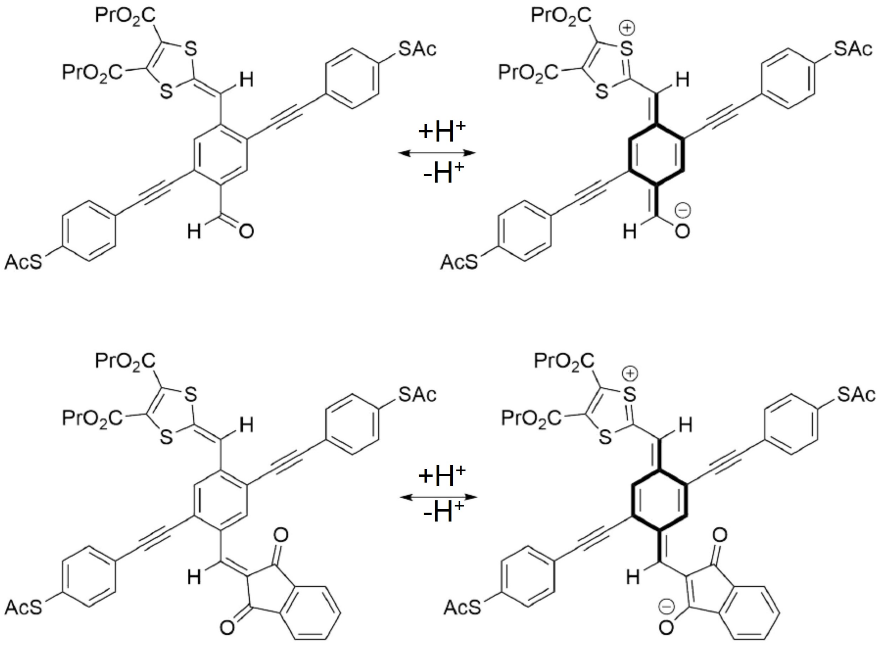

Figure 1.7: Cruciform-shaped D-A substituted OPE molecular wires.

1.3.3 DTF building blocks for redox-active sensors

As previously described, the oxidative coupling of DTF results in C–C bond formation. With multi-DTF-substituted systems as precursors, this reactivity can be used to synthesize polymers, oligomers, and even macrocycles. Hascoat et al.[45] reported in 1997 that the oxidative coupling of bis(DTF) compounds led to the formation of macrocyclic products (Scheme 1.8).

Through the oxidative coupling of a bis(DTF)-pyrene, Khadem and colleagues reported the synthesis of a TTFV-pyrene macrocycle in 2016.[75] The two phases of the synthesis are shown in Scheme 1.9. The monomer DTF-pyrene underwent iodine oxidation in the first stage. The process was stopped after 45 minutes, in which a combination of monomer and dimer remained. The mixture was mechanically ground

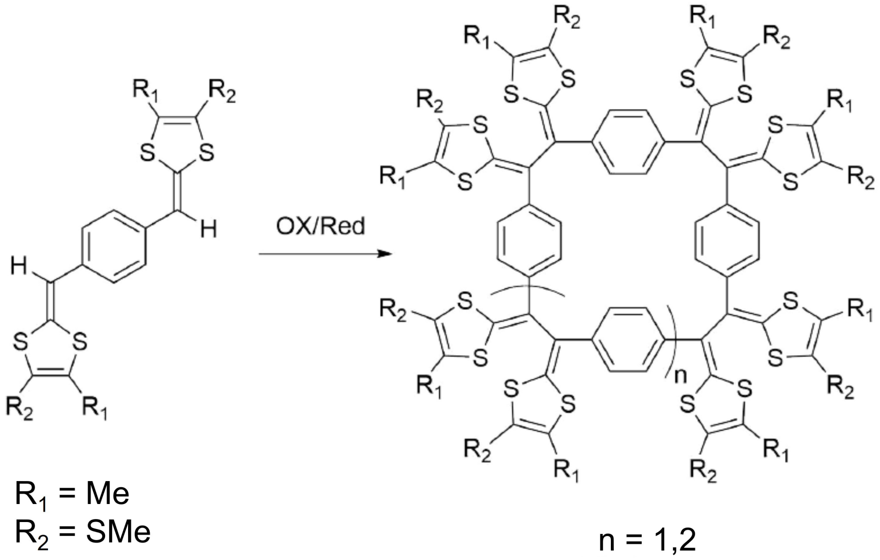

Scheme 1.8: Preparation of TTFV macrocycles under oxidative conditions.

with iodine to produce the macrocyclic compound in 37% yield. The reaction time is crucial in the synthesis of this macrocycle.

Further investigations demonstrated that the macrocycle in Scheme 1.9 may serve as a supramolecular host for nitrobenzenes. According to a molecular modeling study, the electron-rich DTF groups in the aformentioned macrocycle serve as binding sites for electron-deficient aromatic compounds. Being motivated by this observation, Khadem et al. decided to pursue this idea further. They developed and synthesized a class of multivalent DTF-functionalized polyarene building blocks (Figure 1.8) for the development of redox-active polymer thin film sensors with high sensitivity for nitrobenzene explosives.[76]

After multi-cycle cyclic voltammetric scans, the octa-DTF compound in Figure 1.8 generated a microporous cross-linked polymer thin film on the surface of a glassy carbon working electrode. Tetra-DTF, however, failed to create a durable

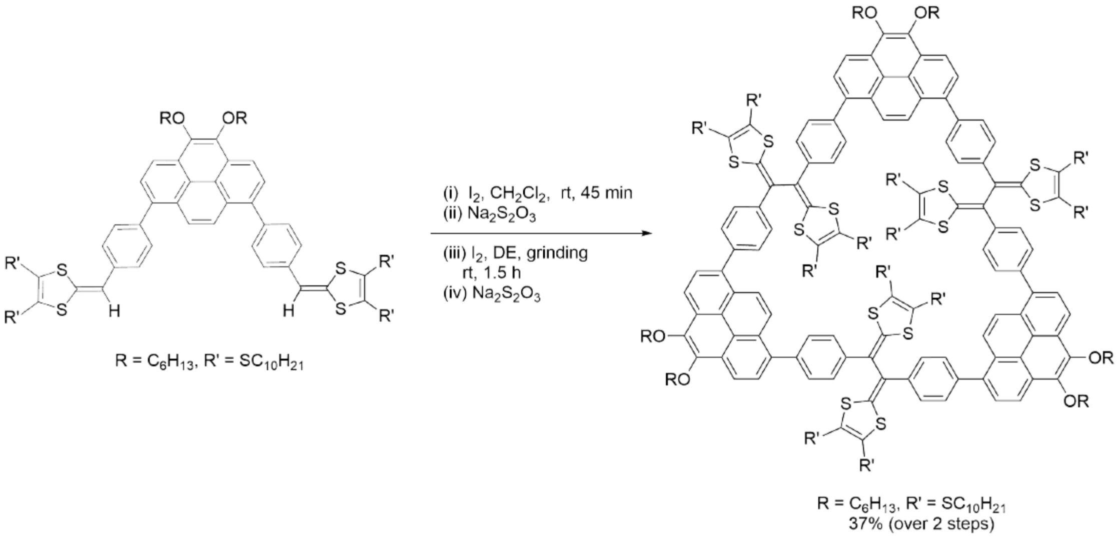

Scheme 1.9: Preparation of a pyrene-TTFV macrocycle.

polymer thin film. The DTF-polymer-coated working electrode showed sensitive electrochemical responsiveness to nitrobenzene at concentrations below mM. The reusability of these thin film sensors was restricted by its poor durability and stability. The Zhao group came up with a double-layer technique to increase the stability of the cross-linked polymer thin films (Scheme 1.10). In their study, the double-layer approach has produced an effective and selective electrochemical sensor for three nitrobenzenes. Their double-layer method is crucial in trapping dimerized DTFs (TTFV) on the cyclic voltammetry working electrode, ensuring that its performance is stable and long-lasting.[77]

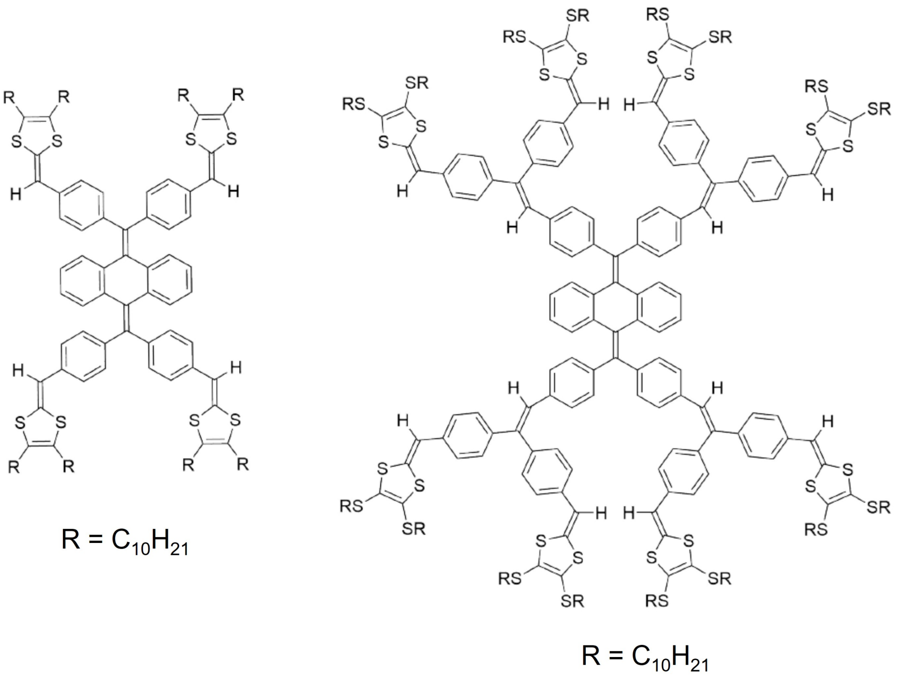

Figure 1.8: Multivalent DTF building blocks applicable for redox-active polymers.

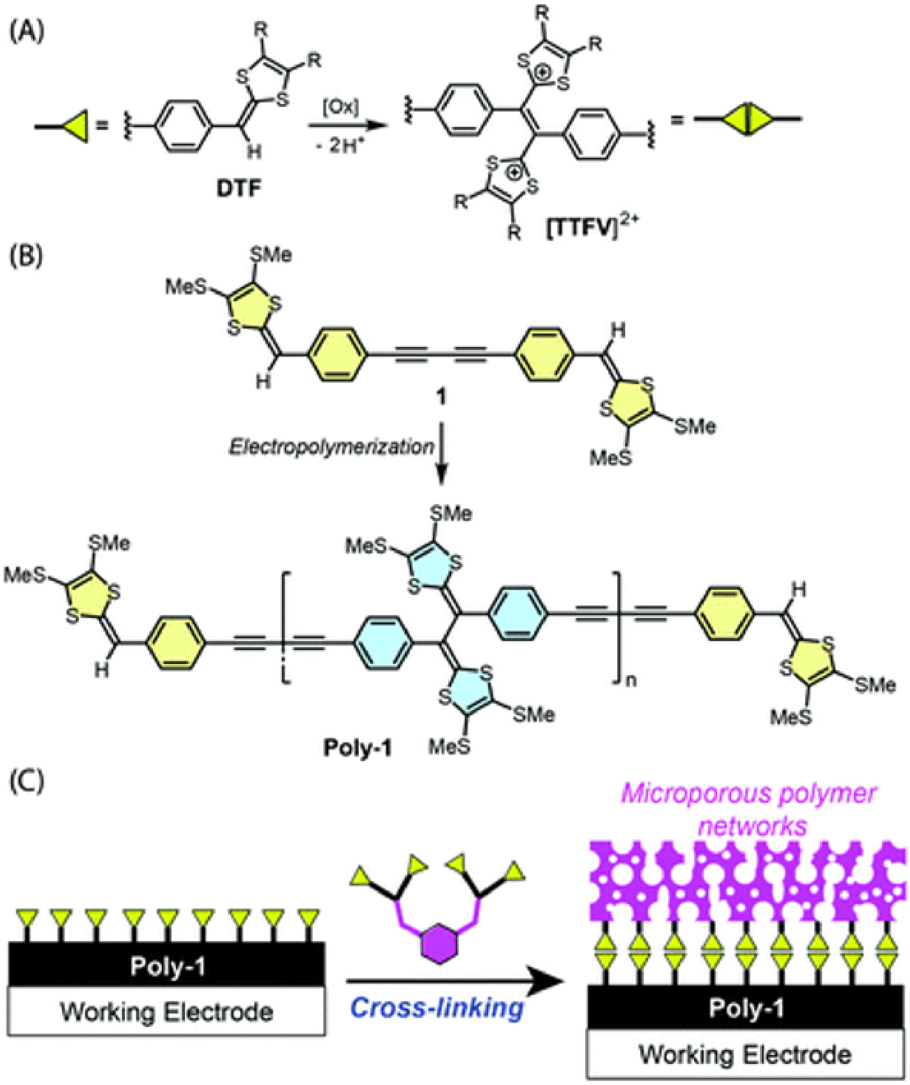

Scheme 1.10: DTF dimerization to form a stable double-layer TTFV. Scheme adapted by permission from F. Shahrokhi and Y. Zhao, *New J. Chem.*, **2019**, 43, 5277-5281.

In addition, Shahrokhi et al. have designed and synthesized six different *ortho*, *meta*, and *para*-substituted dithiafulvenyl-functionalized tetraphenylpyrene compounds with unique electronic and electrochemical redox properties as shown by cyclic voltammetry analysis (Scheme 1.11). According to their experimental findings, the *para*-substituted compound and the pyrene core can assemble redox-active supramolecular structures in electrochemical environments. In addition, These compounds exhibited acid sensitivity; in particular, the vinylic proton of the DTF group could efficiently exchange protons with deuterium under acidic conditions.[52]

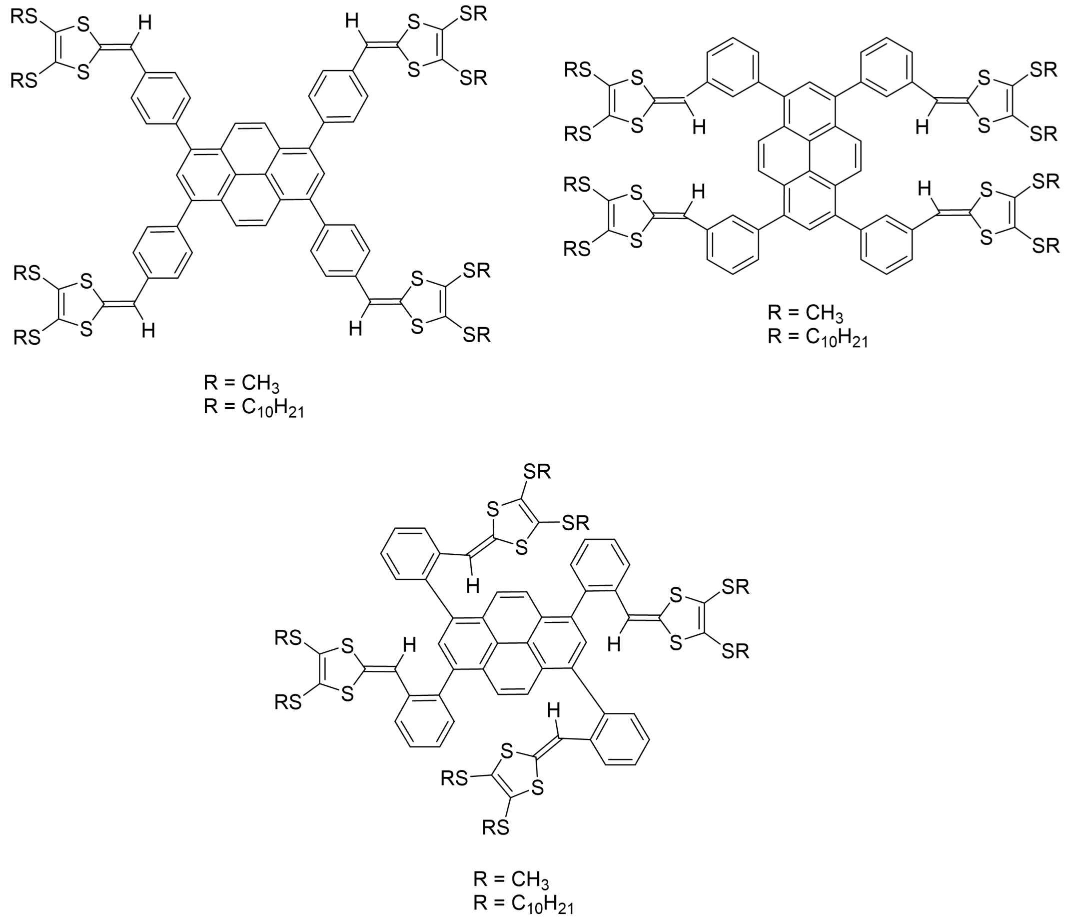

Scheme 1.11: Redox active DTF-functionalized tetraphenylpyrene susceptible to acids.

1.3.4 DTF-based functional organic chromophores

The use of DTF as a useful electron-donating (D) group in the synthesis of functional organic chromophores has long been studied. In the design strategies, DTF and electron-acceptors (A) are frequently combined through π-conjugated linkers. A number of push-pull DTF-π-A systems were previously developed as nonlinear optical (NLO) chromophores.[78–80] New varieties of organic chromophores based on DTF have been developed and studied recently. A DTF-TPA-dicarbazole (Scheme 1.12) was developed by Deng et al.[81] as a starting material for electrochemical polymerization. The electrochemical polymerization of the compound in Scheme 1.12 resulted in the formation of a polymer film on an indium tin oxide (ITO) surface. At different voltages, the film displayed color variations. The transitions from pale yellow to green to blue-grey were reversible. The evidence for the product polymer being the active colored species was insufficient since no characterization approach could confirm the suggested structure of the material.

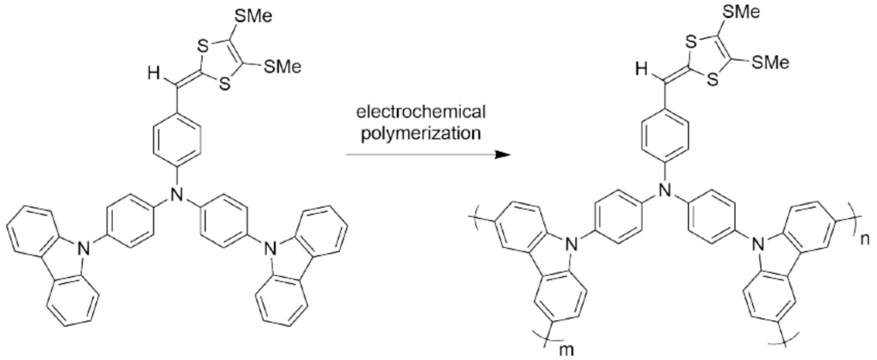

Scheme 1.12: Preparation of an electrochromic polymer via electrochemical polymerization.

Recently, Guo and co-workers[82] created a bis(DTF)-substituted π-oligomer (Figure 1.9). Surprisingly, for this compound, they observed unusual aggregation-induced enhanced emission (AIEE) behavior. The compound's fluorescence quantum yield increases from 8% in THF to 13% in the solid thin-film state. In π-conjugated systems, DTF functionalization often causes quenched fluorescence. An excimer mechanism was proposed to explain the observed AIEE behavior. In this system, DTF is a potent electron donor that can boost intramolecular charge transfer (ICT) and cause the production of an excimer. The fluorescence peak of this compound was observed to shift to a longer wavelength and higher intensity when the excimer was formed.

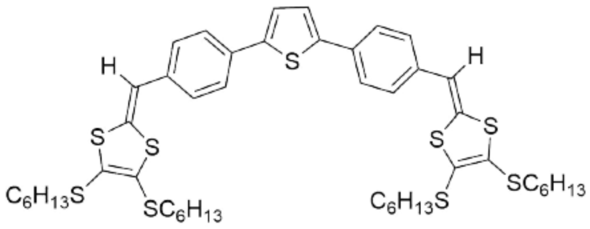

Figure 1.9: DTF-substituted organic chromophore that shows AIEE behavior.

There are other applications for DTF and TTFV-functionalized organic materials, for example, as selective dispersants for single-walled carbon nanotubes (SWCNTs) to separate them from other by-products in the solution phase.[83–92] DTF and TTFV-funtionalized molecules can also act as reducing agents to trigger the conversion of gold salts into gold nanoparticles (AuNPs) in the solution phase. Moreover, they can form a protective layer to stabilize the AuNPs. Details of these studies will be discussed in Chapter 3.

1.4 Objectives and organization of this thesis

This PhD thesis work includes four research projects. Three of these projects (Chapters 3–5) deal with DFT and time-Dependent DFT analyses as well as ab initio molecular dynamics simulations (AIMD) of redox-active π-conjugated molecules and their supramolecular assemblies previously prepared by our group or reported in the literature. These modeling studies have provided in-depth understanding of these molecular systems and benefit future exploration of their application as functional organic optoelectronic materials. The last research project encompasses experimental and computational studies of a new type of organic fluorophore featuring an extended π-conjugated polycyclic aromatic hydrocarbon framework resulting from a facile self-condensation reaction of pyrene-4,5-dione.

As the majority of the research projects in this thesis relies on computational calculations, Chapter 2 is dedicated to explaining the computational principles and methodologies utilized to accomplish these projects. A literature review and the history of the density functional theory, its emergence, corrections, estimations, and evolution have been provided in this chapter as well. Time-dependent density functional theory (TD-DFT) is also discussed in detail, which is a method used for modeling the electronic absorption properties in this thesis.

In the literature, considerable attention has been directed towards the examination of the ability of DTF derivatives to reduce Au (III) into gold nanoparticles.[93–96] Moreover, some discussions have postulated that these compounds may also serve as efficient stabilizing or capping agents for the resultant gold nanoparticles.[97,98] However, what remains obviously absent within this discourse is a comprehensive elucidation of the mechanism underlying the ability of DTFs to stabilize the reduced gold nanoparticles. One notable contribution to this matter comes from Granados and coworkers,[99] who have proposed a mechanistic framework for the aforementioned interaction. Nevertheless, it is noteworthy that their proposal lacks evidence to verify its reliability. Consequently, a gap persists, wherein the precise mode of action by which DTFs stabilize gold nanoparticles remains elusive. In Chapter 3, we endeavor to bridge this gap in understanding by explaining upon the intricate mechanism responsible for the stabilizing effect exerted by DTFs upon gold nanoparticles. Through a systematic analysis, we aim to shed light on the interactions that underlie this phenomenon through modeling the interactions of DTFs with various gold clusters, which are believed to play a vital role in the early stage of the formation of ligand-stabilized gold nanoparticles.

Chapter 4 utilizes various modeling methods, including DFT, TD-DFT, and AIMD, to study the oxidative dimerization mechanism of 1,4-dithiolene-5-phenylmethylene. Although the mechanism proposed previously in the literature generally describes the redox reactivity of various DTF-containing molecules,[46] some mechanistic details are still missing and warrant further investigation. A key point worth reflecting upon is how the two Ph-DTF molecules are associated under oxidative conditions. According to the general mechanism in the literature, two Ph-DTF radical cations approach each other to initiate the dimerization reaction. If this is the case, the dimerization must overcome a certain energy barrier(s) imposed by significant cation–cation repulsion. In the meantime, the association of two Ph-DTF species could be facilitated by $\pi--\pi$ stacking, orbital interactions, and solvation effects. Whether these factors are sufficient to offset the negative impact of electrostatics on the dimerization mechanism has not yet been quantitatively examined prior to this study. Moreover, the radical cation of an organic π–system is known to attractively interact with a neutral π–counterpart, yielding a mixed-valenced (MV) dimer. For example, TTF radical cations have been reported to form MV dimers with neutral TTFs through weak interactions.[100–102] Considering that TTF and DTF are π–analogues to each other, the formation of MV dimers of Ph-DTF is likely to occur as well. In Chapter 4, the radical cation of a Ph-DTF is proposed to interact with a neutral Ph-DFT molecule through face–to–face stacking to form a MV π–dimer. In this π–dimer, the cation and radical characters are equally distributed on the two Ph-DFT segments. Orbital interactions would further induce the formation of a C-–C bond between the two vinylic carbons, converting the π–dimer into a MV σ–dimer. Theoretically, all of the aforementioned Ph-DTF dimers are possibly involved in the oxidative dimerization processes. An in-depth understanding of their properties and roles in the reaction mechanism is therefore fundamentally important. However, it is very challenging to experimentally detect and examine these reactive and short–lived species. Computational modeling has to be resorted to gain a deeper insight into these species. With this objective in mind, we carried out density functional theory (DFT) calculations in this work to comprehensively examine various Ph-DTF dimers at different oxidation states. To line up with experimental conditions commonly applied to Ph-DTF dimerization, the effects of two organic solvents (CH_2Cl_2, and CH_3CN) were calculated and the solution-phase properties were compared with those in the gas phase. Detailed molecular structural, energetic, and electronic properties are discussed in their corresponding sections.

Chapter 5 of this thesis aims to explore the influence of arene moiety expansion on the geometrical, electrochemical, and optical properties of dithiafulvenyl-functionalized polycyclic aromatic hydrocarbons (Ar–DTFs) in neutral and radical cation oxidation states. To achieve this objective, DFT and TD-DFT calculations have been applied. The geometrical, electrochemical, and optical properties of these compounds were investigated using computational methodologies. Additionally, charge and spin density population analyses have been conducted using different calculation methods. The electronic energies of frontier molecular orbitals and their changes upon oxidation were systematically discussed in this chapter.

In Chapter 6, a combination of time-dependent density functional theory (TD-DFT) studies and the experimental characterizations of an organic fluorophore obtained from the self-condensation reaction of pyrene-4,5-dione are reported. The UV–Vis absorption and fluorescence spectroscopic studies of the π-conjugated organic fluorophore product were experimentally measured. The spectroscopic data were further simulated and analyzed through TD-DFT calculations. The joint computational and theoretical studies provide a deep understanding of the electronic and photophysical properties of this organic fluorophore.

The results of this thesis are summarized in the last chapter. In addition, future research directions which may lead to potential applications and significant scientific discoveries are forecast based on the results described in the previous chapters of this thesis.

Chapter 2

Theoretical Approach

The fundamental molecular properties and reactivities that have been examined in this thesis work cannot be readily investigated by experimental methods and techniques. Instead, we heavily rely on various state-of-the-art computational modeling approaches to gain deeper insight into these aspects. Therefore, in this chapter, we will first introduce the theoretical approaches that we employed to examine the electronic and geometric properties of various molecules and their intermolecular interactions. The main discussions of this chapter are focused on density functional theory (DFT), whose primary goal is to solve the well-known time-independent Schrödinger equation. In addition, dispersion corrected and time-dependent versions of DFT (DFT-D and TD-DFT, respectively) will be discussed.

2.1 The Schrödinger equation

The electronic structure of matter can be predicted by a wave equation introduced by Schrödinger in 1926.[103] For any given system, including M nuclei and N electrons, this equation is expressed as,

$$\hat{H}\mathit{\Psi} = E\mathit{\Psi} \tag{2.1}$$

where $\hat{H}$ is an operator representing the total Hamiltonian, Ψ is the total wave function, and E is the total energy of the molecular system. The Hamiltonian operator consists of both the kinetic and potential energies of a many-electron system and it is described as follows,

$$\begin{aligned}\hat{H} = &-\frac{h}{4\pi m_e}\sum_{i}^{N}\nabla_i^2 - \frac{h}{4\pi}\sum_{A}^{M}\frac{1}{M_A}\nabla_A^2 - \frac{e^2}{4\pi\varepsilon_0}\sum_{i}^{N}\sum_{A}^{M}\frac{Z_A}{r_{iA}} \\ &+ \frac{e^2}{4\pi\varepsilon_0}\sum_{i}^{N}\sum_{j}^{N}\frac{1}{r_{ij}} + \frac{e^2}{4\pi\varepsilon_0}\sum_{A}^{M}\sum_{B}^{M}\frac{Z_A Z_B}{R_{AB}}\end{aligned} \tag{2.2}$$

where m_e represents the mass of an electron, M_A is the mass of the nucleus of atom A, ∇_i^2 is the Laplacian of electron i, Z_A is the charge of the nucleus of atom A, r_{iA} is the distance between nucleus A and electron i, r_{ij} is the distance between electrons i and j, R_{AB} is the distance between nuclei A and B, ε_0 is the permittivity of free space, and h is the Planck's constant.

As the Hamiltonian consists of all energy sources of a multi-body system, equation 2.2 can be rewritten as follows,

$$\hat{H} = \hat{T}_e + \hat{T}_n + \hat{V}_{n-e} + \hat{V}_{e-e} + \hat{V}_{n-n} \tag{2.3}$$

where $\hat{T}_e$ and $\hat{T}_n$ signify the electronic and nuclear kinetic energies, respectively, $\hat{V}_{n-e}$ represents the potential energy due to nucleus–electron attraction. In addition,

$\hat{V}_{e-e}$ and $\hat{V}_{n-n}$ represent the potential energies of electron–electron and nucleus–nucleus repulsion, respectively.

For a system with $(3N + 3M)$ degrees of freedom, approximations are required to solve the Schrödinger equation. The first approximation, which is very useful for simplifying the equation, is the Born-Oppenheimer approximation.[104] This approximation is based on the motion of the nuclei versus electrons. As the electrons move faster than the nuclei, one can assume that the nuclei are stationary relative to the electrons. According to this assumption, the second and last terms of Equation 2.3 are zero and constant, respectively, resulting in the following electronic Schrödinger equation.

$$\hat{H}^{elec}\Psi^{elec} = E^{elec}\Psi^{elec} \tag{2.4}$$

Based on the Born-Oppenheimer approximation, $\hat{H}^{elec}$ is expressed as follows.

$$\hat{H}^{elec} = -\frac{h}{4\pi m_e}\sum_{i}^{N}\nabla_i^2 - \frac{e^2}{4\pi\varepsilon_0}\sum_{i}^{N}\sum_{A}^{M}\frac{Z_A}{r_{iA}} + \frac{e^2}{4\pi\varepsilon_0}\sum_{i}^{N}\sum_{j}^{N}\frac{1}{r_{ij}} \tag{2.5}$$

The approximation made by Born and Oppenheimer reduces the complexity of solving the multi-body Schrödinger equation. However, Equation 2.4 is still not solvable for many-electron systems, and further approximations are hence needed.

2.2 Hartree–Fock method

The second approximation for solving the Schrödinger equation is known as the Hartree-Fock (HF) method.[105,106] In this approach, one can assume that each electron is independent of the other electrons and is only affected by their average field. In the

HF method, the individual electrons are represented by spin orbitals ψ_i. Spin orbitals are one-electron orbitals with either a -$\frac{1}{2}$ or +$\frac{1}{2}$ spin state that can only interact with the average field of the other electrons in the system. For fermions, the total (multi-electron) wave function must be anti-symmetric upon interchange of electron coordinates to comply with the Pauli exclusion principle. In the HF approximation, the total wave function is often written in the form of a single determinant called the Slater determinant,

$$\Psi = \frac{1}{\sqrt{n!}} \begin{vmatrix} \psi_1(1) & \psi_2(1)... & \psi_n(1) \\ \psi_1(2) & \psi_2(2)... & \psi_n(2) \\ ... & ... & ... \\ \psi_1(n) & \psi_2(n)... & \psi_n(n) \end{vmatrix} \tag{2.6}$$

where $\frac{1}{\sqrt{n!}}$ is the normalization factor for an n-electron determinant.

In order to solve the Slater determinant, spin orbitals must be determined. Lenard and Jones[107] proposed the linear combination of atomic orbitals (LCAO) approximation. In this approximation, the molecular orbitals (ψ_i) are treated as linear combinations of atomic orbitals (ϕ_i),

$$\psi_i = \sum_{i}^{N} c_i \phi_i \tag{2.7}$$

where c_i is the coefficient of each atomic orbital, ϕ_i, involved in the combination.

When applying both the HF and LCAO approximations to the electronic Schrödinger equation based on the Born-Oppenheimer approximation, the HF operator becomes as follows,

$$\hat{f}\psi_i = \epsilon_i\psi_i \tag{2.8}$$

where ϵ_i is the orbital energy and $\hat{f}$ is the HF operator described as follows,

$$\hat{f} = \hat{h} + \sum_j^N (2\hat{J}_j - \hat{K}_j) \tag{2.9}$$

where $\hat{h}$ is the sum of the kinetic and nucleus–electron potential energies of a single electron, and $\sum_j^N (2\hat{J}_j - \hat{K}_j)$ is the electron–electron repulsion energy of a single electron due to its interaction with all other electrons. Indeed, $\hat{J}_j$ and $\hat{K}_j$ are representing the Coulomb and exchange operators, respectively. By having all of these parameters in hand, one can solve Equation 2.8 using the self-consistent field (SCF) method iteratively.[108]

2.3 Moving beyond HF method

The main problem with using the HF approximation is that it does not give accurate results with respect to the calculation of many observables. This is due to the fact that it excludes electron correlation in its general formulation. Accordingly, the energy difference between the exact and HF energies is called the electron correlation energy ($E_{corr} = E_{exact} - E_{HF}$). Correlation energy arises from the fact that the interaction between electrons with different spins is not included in the HF approximation. The most popular approaches (referred to as post HF methods) that include correlation energy are configuration interactions (CI),[109] Moller-Plesset perturbation theory (MP),[110] and coupled-cluster theory (CC)[111,112]. The problem with these methods, however, is that they are extremely computationally intensive especially when evaluating relatively large molecular systems. Therefore, there is a critical demand for efficient and less expensive methods that can describe the both intermolecular and intramolecular properties accurately.

2.4 Density functional theory

Density functional theory (DFT) is an alternative first-principle approach for solving the Schrödiner equation with electron correlations taken into account. It uses electron density ρ(x, y, z) as the main variable rather than electron wave functions. When the Born–Oppenheimer approximation is utilized, the DFT electronic energy is expressed as

$$E_{elec}[\rho(r)] = T_e[\rho(r)] + V_{n-e}[\rho(r)] + V_{e-e}[\rho(r)] + Q_{e-e}[\rho(r)] \tag{2.10}$$

where $T_e[\rho(r)]$ represents the kinetic energy of the electrons, $V_{n-e}[\rho(r)]$ is the nucleus–electron attraction energy, $V_{e-e}[\rho(r)]$ is the electron–electron repulsion energy, and $Q_{e-e}[\rho(r)]$ is the non-classical electron–electron repulsion energy. It should be noted that the last term indicates a correction to self-repulsion included in the classical $V_{e-e}[\rho(r)]$. However, the two middle terms in Equation 2.10 are already known and can be described as follows,

$$V_{n-e}[\rho(r)] = \sum_{A}^{M} \int \frac{Z_A}{|r - r_A|} \rho(r) dr \tag{2.11}$$

$$V_{e-e}[\rho(r)] = \frac{1}{2} \int \int \frac{\rho(r_1)\rho(r_2)}{r_{12}} dr_1 dr_2 \tag{2.12}$$

In the case of $T_e[\rho(r)]$ and $Q_{e-e}[\rho(r)]$, the exact mathematical expressions are not known and approximations must be used in order to obtain them. A simple approximation of $T_e[\rho(r)]$ was proposed by Thomas and Fermi, which is exact in the case of a uniform electron gas.[113,114] The Thomas-Fermi method, however, failed in various ways (e.g., it cannot reproduce chemical bonds), and as a result, it had been abandoned until the mid-1960s. Indeed, the formalism of DFT has been established based on the Thomas-Fermi method.[115,116]

2.4.1 Hohenberg-Kohn theorem

Hohenberg and Kohn published two basic theorems of DFT in 1964.[117] The first theorem (later called the existence theorem) states that all the ground-state electron properties of a given system are determined by the ground-state electron density function $\rho_0(x, y, z)$ as determined by an external potential (v). In addition, it indicates that the ground-state energy of a molecule is a functional of $\rho_0(x, y, z)$. Therefore,

$$E_0 = E_0[\rho_0] \tag{2.13}$$

It is noteworthy that the exact energy functional for the ground state is unknown.

The second theorem, with the energy variational principle taken into consideration, states that any trial electron density function (ρ_t) will give an energy higher than or equal to the exact ground state energy calculated with ρ_0,

$$E_v[\rho_t] \geq E_0[\rho_0] \tag{2.14}$$

where E_v is the electronic energy of the system.

2.4.2 Kohn–Sham formalism

A practical approach to obtain the electronic properties of a molecular system was proposed by Kohn and Sham in 1965,[118] who used both the Hohenberg and Kohn theorems. To deal with the problem of not having accurate kinetic energy functionals, Kohn and Sham assumed that kinetic energy describes a hypothetical system of non-interacting electrons with the same density as the original set of interacting electrons. An approximated value of the kinetic energy of the non-interacting electrons can be calculated by a single Slater determinant of the Kohn–Sham orbitals (ψ_i^{KS}), and this value can be calculated as follows,

$$T_s[\psi_i^{KS}] = -\frac{1}{2}\sum_i^N \int \psi_i^{KS}(r)\nabla^2\psi_i^{KS}(r)dr \tag{2.15}$$

In addition, based on the Kohn–Sham (KS) orbitals, the electron density can be defined as follows,

$$\rho(r_1) = \sum_i^N \left|\psi_i^{KS}(r_1)\right|^2 \tag{2.16}$$

In order to obtain the Kohn–Sham orbitals, and thus the Kohn–Sham equation, the variational principle requires the energy to be a minimum with respect to ψ_i^{KS},

$$\hat{h}^{KS}\psi_i^{KS} = \epsilon_i\psi_i^{KS} \tag{2.17}$$

where $\hat{h}^{KS}$ is the Kohn-Sham operator and it is defined as,

$$\hat{h}^{KS} = \hat{h} + \sum_{j}^{N} 2\hat{J}_j + \upsilon_{xc} \tag{2.18}$$

where $\hat{h}$ corresponds to the energy of a single electron, including both the kinetic and nucleus–electron potential energies, $\hat{J}_j$ is the Coulomb's operator, and υ_{xc} represents the exchange–correlation potential functional. The only difference between the Kohn–Sham operator in Equation 2.18 and the HF operator in Equation 2.9 is that υ_{xc} is used to replace the HF exchange operator. The exchange–correlation potential functional can be obtained as the first derivative of the exchange–correlation energy functional with respect to the electron density,

$$\upsilon_{xc} = \frac{\delta E_{xc}}{\delta \rho} \tag{2.19}$$

Similarly to the HF equations, Kohn–Sham equations can also be solved using the iterative method of SCF.

Due to the fact that the kinetic energy of a non-interacting system ($T_s[\psi_i^{KS}]$ in Equation 2.15) is not equal to $T_e[\rho(r)]$, a difference between both terms will be added to the non-classical electronic repulsion energy $Q_{e-e}[\rho(r)]$ in order to define the exchange–correlation functional ($E_{xc}[\rho]$) as follows,

$$E_{xc}[\rho(r)] = T_e[\rho(r)] - T_s[\psi_i^{KS}] + Q_{e-e}[\rho(r)] \tag{2.20}$$

As a result, applying the Kohn–Sham DFT approach, equation 2.10 for the electronic energy of an N-electron system can be rewritten as,

$$\begin{aligned} E_{elec} = &-\frac{1}{2}\sum_{i}^{N}\int \psi_i^{KS}(r)\nabla^2\psi_i^{KS}(r)dr + \sum_{A}^{M}\int \frac{Z_A}{|r-r_A|}\rho(r)dr \\ &+\frac{1}{2}\int\int\frac{\rho(r_1)\rho(r_2)}{r_{12}}dr_1dr_2 + E_{xc}[\rho] \end{aligned} \tag{2.21}$$

The exchange–correlation functional is the only term that is unknown in Equation 2.21 and therefore, approximations should be made in order to solve it. There have been many accurate methods of approximating $E_{xc}[\rho]$.[116] This has led to an increase in our understanding of the electronic and structural properties of a huge number of compounds in several fields. This thesis is devoted to investigating the intermolecular and intramolecular interactions, either attractive or repulsive, between different types of molecules and supramolecular structures using dispersion-corrected DFT and time-dependent DFT. Since these approaches are built on the foundation of the conventional DFT approximations, in the following section we summarize the DFT functionals that were available prior to the development of the dispersion correction and TD-DFT.

2.5 Classification of exchange–correlation functionals

2.5.1 LDA functionals

Most of the advanced exchange–correlation functionals are based on the local density approximation (LDA). In fact, the LDA uses the local density of a uniform electron gas in E_{xc}. The local exchange–correlation energy functional in this model is usually expressed as follows,

$$E_{xc}[\rho(r)] = \int \rho(r)\varepsilon_{xc}[\rho(r)]dr \tag{2.22}$$

where $\varepsilon_{xc}[\rho(r)]$ represents the energy density of a uniform electron gas, and it is often shown as a sum of the exchange and correlation energies,

$$\varepsilon_{xc} = \varepsilon_x + \varepsilon_c \tag{2.23}$$

The exact form of the LDA exchange functional term for this model is given as,

$$E_x^{LDA}[\rho(r)] = -\frac{3}{4}(\frac{3}{\pi})^{\frac{1}{3}} \int [\rho(r)]^{\frac{4}{3}} dr \tag{2.24}$$

Vosko, Wilk, and Nusair (VWN) in 1980 proposed a correlation functional.[119] When an open-shell system is considered, the electronic density is replaced by the spin electronic densities (ρ_α and ρ_β), and this method is often called the local spin density approximation (LSDA). In reality, however, due to the inhomogeneous density distributions in most real-life systems, such functionals lead to inaccurate estimates of the molecular properties of these systems.[116].

The calculation of exchange and correlation energies is usually done separately in many DFT approximations. In addition, different exchange-correlation functionals are categorized according to their formulations.

2.5.2 GGA functionals

The second exchange–correlation approximation after LDA is the generalized gradient approximation (GGA) that is based on both the local electron density (ρ) as well as the gradient of the electron density ($\nabla\rho$). The gradient of the electron density is used to account for the density inhomogeneity. Therefore, we can have the functional expressed as follows.

$$E_{xc}^{GGA}[\rho(r)] = \int \rho(r)\varepsilon_{xc}[\rho(r), \nabla\rho(r)]dr \tag{2.25}$$

Generalized GGA functionals including the LDA functional have the following form,

$$\varepsilon_{xc}^{GGA}[\rho(r)] = \varepsilon_{xc}^{LDA}[\rho(r)] + \mathit{\Delta}\varepsilon_{xc}[\frac{\nabla\rho(r)}{\rho^{\frac{4}{3}}(r)}] \tag{2.26}$$

There are many GGA exchange and correlation functionals. The most common GGA exchange functionals include PBE,[120] B,[121] and PW91.[122] In addition, some of the most widespread GGA correlation functionals are LYP,[123] PBE,[120] and PW91.[122] It is noteworthy that they can be combined to make more powerful GGA exchange-correlation functionals. Such functionals will obtain more information of the system than the LDA ones. However, they are not always accurate. Therefore, to improve the accuracy of DFT, additional factors must be considered in the exchange–correlation functional.

2.5.3 Hybrid functionals

Currently, the most popular DFT functionals are the hybrid functionals. Basically, hybrid functionals combine the GGA functionals with a fraction of the HF exchange term to improve the accuracy of the results. Therefore, we can have,

$$E_{xc} = c_x E_x^{HF} + E_{xc}^{DFT} \tag{2.27}$$

where c_x is a fractional number. The only difference between the hybrid functionals is the percentage of the HF exchange energy applied in the functional. This section will introduce some of the most successful hybrid functionals that have demonstrated significant accuracy for many molecular systems.

2.5.3.1 B3LYP

B3LYP[123–125] is the first hybrid functional and the most widely used method in all DFT calculations. It applies Becke's three parameters (see below) in the combination of some exchange and correlation functionals. Indeed, it connects the HF exchange integral and LSDA exchange functional to the Lee, Yang, and Parr's (LYP) GGA correlation functional and the LSDA correlation functional, and finally adds the GGA part of the Becke's (B) exchange functional as follows,

$$E_{xc}^{B3LYP} = (1-a)E_x^{LSDA} + aE_x^{HF} + b\Delta E_x^{B} + (1-c)E_c^{LSDA} + cE_c^{LYP} \tag{2.28}$$

where a, b, and c are the three parameters (i.e. the "3" in "B3LYP" represents the number of parameters in the method.).

2.5.3.2 PBE0

Perdew, Burke, and Ernzerhof introduced the other important hybrid functional known as PBE0.[126,127] Using the PBE GGA exchange–correlation function as a reference, it mixes the PBE GGA exchange function with the HF exchange integral as follows,

$$E_{xc}^{PBE0} = E_{xc}^{PBE} + \frac{1}{4}(E_x^{HF} - E_x^{PBE}) \tag{2.29}$$

With the simplicity of the hybrid PBE0 functional and the lack of parameters in the functional formation, it has been a widely applicable method in quantum chemistry.

2.5.3.3 B97

The B97 functional[128] was developed by Becke in 1997. Becke proposed to expand the GGA exchange–correlation functional by including the local spin density and its first derivative, as well as a small fraction of the HF exchange as follows,

$$E_{xc}^{B97} = E_x^{B97} + E_c^{B97} + c_x E_x^{HF} \tag{2.30}$$

The resulting B97 exchange–correlation functional has led to the development of a new generation of many accurate functionals such as ωB97x, which will be discussed later.

2.5.3.4 M06 and M06-2X

Another popular type of hybrid functional is the one proposed by Truhlar's group at the University of Minnesota in 2006, known as M06 and M06-2X (M stands for Minnesota and 06 is the year of publication).[129] Indeed, six strategies have been introduced in order to design a hybrid density functional. In recent years, these strategies have been widely applied to design many new effective functionals. These strategies include: (1) local density approximation (LDA), (2) density gradient expansion, (3) constraint satisfaction, (4) modeling the exchange-correlation hole, (5) empirical fits, and (6) mixing Hartree-Fock and approximate DFT exchange.[130] M06-2X is a compelling method that has been demonstrated to be highly effective in the DFT studies of a broad range of compounds, including organic and organometallic systems. It is also compatible with various basis sets for the study of dispersion and non-covalent interactions as well as time-dependent DFT. That is why it has been increasingly employed in the majority of DFT studies since the last decade.[131–136]

The general exchange–correlation energy calculation format in M06 and M06-2X is shown as follows,

$$E_{xc}^{hyb} = \frac{X}{100}E_x^{HF} + (1 - \frac{X}{100})E_x^{DFT} + E_c^{DFT} \tag{2.31}$$

where the E_c is,

$$E_c = E_c^{\alpha\beta} + E_c^{\alpha\alpha} + E_c^{\beta\beta} \tag{2.32}$$

where α and β show different electron spins.

The only difference between M06 and M06-2X is the amount of nonlocal exchange

(X), which is double in the latter (i.e., 2X).[129] In this thesis, most of the studies have been done using M06-2X as the default functional.

2.6 Corrections beyond ground state conventional DFT

It has been more than twenty years since the scope of DFT analysis went beyond the traditional job of merely optimizing ground-state geometries. Thanks to the efforts of computational physicists and chemists worldwide, DFT has now been developed as the most accurate and fastest QM method for electronic structure calculations of various molecular systems. The conventional functionals have neglected some important intra- and intermolecular interactions, such as long–range electron–electron exchange and dispersion interactions. Indeed, these interactions are significant in determining the properties of noncovalently bonded systems. To accommodate these particular physical properties, various types of correction methods have been developed.

2.6.1 Long–range correction

Long–range corrections have been introduced to conventional exchange functionals to address the lack of explicit consideration of the electron–electron interactions at large distances (i.e., $r \rightarrow \infty$). In order to formulate the long–range correction, the electron–electron interactions can be split into two parts, namely, the short and the long interactions described as follows,

$$\frac{1}{r} = \frac{1-g(r)}{r} + \frac{g(r)}{r} \tag{2.33}$$

where $g(r)$ is the error function. As shown in Equation 2.33, the first term shows the short–range operator, while the second term represents the long–range operator. The basic idea of this approach is to apply a DFT exchange functional for the short–range (SR) term and a 100% HF exchange functional for the long–range (LR) interactions. As a result, the following form of the long–range corrected functional is established.

$$E_{xc} = E_x^{HF,LR} + E_x^{DFT,SR} + E_c^{DFT} \tag{2.34}$$

2.6.1.1 ωB97x

Adding the long-range correction to the B97 hybrid functional, ωB97x[137] is one of the most popular long–range corrected functionals. It includes 100% long–range HF exchange, a small fraction of short–range HF exchange, short–range B97 exchange functional, and B97 correlation functional as follows,

$$E_{xc}^{\omega B97x} = E_x^{HF,LR} + c_x E_x^{HF,SR} + E_x^{B97,SR} + E_c^{B97} \tag{2.35}$$

2.6.2 Dispersion correction

DFT correlation functionals neglect the dispersion interactions (i.e., van der Waals type interactions), although they contribute significantly to the correlation energies, especially in non-covalently bonded systems. A dispersion interaction occurs when there is an instantaneous dipole moment in the electron distribution of two adjacent atoms or molecules, leading to an attractive interaction. As a classical expression, the London-dispersion interaction is governed by the well-known relationship given below,

$$E_{disp} \propto \frac{c_6}{R^6} \tag{2.36}$$

where c_6 is the dispersion coefficient and R^6 is the distance between two molecular or atomic fragments. According to Equation 2.36, the dispersion energy depends on the sixth power of the distance between the two fragments, indicating that it is naturally a non-local feature. The conventional correlation DFT functionals do not include such a long–range regime of the dispersion energy since DFT calculations contain only short–range contributions to electron correlations. As a result, conventional DFT calculations always fail to describe the long–range dispersion interactions. Dispersion corrections have been incorporated in many ways so far. Among them, the so-called dispersion-corrected DFT method is the most promising one, which will be briefly discussed in the next section.

2.7 Dispersion–corrected DFT approach

In the DFT dispersion-corrected approach (known as DFT-D), the empirical dispersion term is added to the derived Kohn-Sham energy using the KS-DFT method (E_{KS-DFT}). Therefore, the total energy is given by

$$E_{DFT-D} = E_{KS-DFT} + E_{disp} \tag{2.37}$$

The dispersion correction will be computed separately once the conventional DFT computation is completed. Since the dispersion interaction has a negligible effect on the electron densities, the correction can be calculated separately. Therefore, DFT-D has become a favored technique for large molecular systems since it entails negligible extra computational costs. This approach was adopted by Grimme, who developed two versions of corrections (DFT-D2[138] and DFT-D3[139]) that refined his original version, DFT-D1. The DFT-D2 and DFT-D3 are compatible with any DFT functional. Grimme's dispersion correction was first successfully implemented in the B97-D functional, in which DFT-D2 has been applied. Dispersion corrections were also reported to show better performance than uncorrected functionals (such as B3LYP and PBE0).[139]

Similarly, the Grimme dispersion corrections can also be applied to long–range hybrid functionals. As an example, the ωB97x-D and ωB97x-D3 are long–range hybrid functionals that utilize the DFT-D2 and -D3 corrections, respectively. The following subsections focus on the comparison between both corrections.

2.7.1 Comparison between DFT-D2 and DFT-D3

The DFT-D2 correction is applicable to elements up to xenon. The DFT-D3 correction, on the other hand, can be used to study the first 94 elements in the periodic table due to the fact that there is more flexibility in the formulation of DFT-D3, which is dependent on the coordination sphere of each atom within a molecule. One cannot see this flexibility in the DFT-D2 formulation. In the DFT-D3 model, the dispersion coefficients (C_n^{AB}, n can be 6 or 8, AB shows that the interaction between atoms A and B is considered) are system dependent, whereas in the DFT-D2 model the dispersion coefficients (C_6^{AB}) are fixed for each element. This makes DFT-D3 more accurate and more flexible than DFT-D2.

The other difference involves the number of parameters in the dispersion corrections that can be adjusted. For each DFT functional, DFT-D2 requires one fit parameter (s_6, called global scaling parameter), whereas DFT-D3 requires two fit parameters ($s_{r,6}$ and s_8). Using a least-squares fit, 130 noncovalent interaction energies are applied to determine the parameters.[140] In the DFT-D2 correction, global scaling parameters (s_6) are fitted empirically for each DFT method to account for the different behaviors of DFT functionals in the short–range and medium–range regimes. For instance, they are found to be 1.05 for B3LYP and 1.25 for B97-D functionals.[138] On the other hand, s_6 are kept at unity in the DFT-D3 correction whereas s_8 are empirically adjusted for each DFT method.

From the comparison between DFT-D2 and DFT-D3, it is evident that DFT-D3 is a better choice for dispersion corrected calculations. It has been shown that the DFT-D2 and DFT-D3 corrections have been extensively benchmarked when combined with DFT functionals and that both have led to improvements such as increased accuracy in computational studies where non-covalently bonded molecular systems are investigated.[141]

2.8 Time-dependent DFT

The DFT methods discussed above are limited to calculations of the properties of electronic ground states. In order to calculate the properties of molecules involved in either excited states or time-dependent external fields, time-dependent density-functional theory (TD-DFT) can be utilized as a powerful method for excited-state calculations. TD-DFT is based on the time-dependent Schrödinger equation for the many-electron wave function $\Psi(t)$. It is given by,

$$i\frac{\partial \Psi(t)}{\partial t} = \hat{H}(t)\Psi(t) \tag{2.38}$$

$$\hat{H}(t) = \hat{T} + \hat{V}_{e-e} + \hat{V}_{ext}(t) \tag{2.39}$$

where $\hat{T}$ is the kinetic energy, $\hat{V}_{e-e}$ represents the electron–electron repulsion, and $\hat{V}_{ext}(t)$ is the external potential that includes the nuclear attraction and any other fields applied to the system. The central theorem of TD-DFT was established by Runde and Gross,[142] who proposed that there is a one-to-one correspondence between the time-dependent external potential, $\upsilon_{ext}(r,t)$, and the time-dependent electron density, $\rho(r,t)$. In fact, TD-DFT can be seen as an extension of Hohenberg–Kohn's theorem to all time-dependent systems by demonstrating that starting from an initial state $\Psi(0)$, all observable properties of many-electron systems can be extracted from the time-dependent electron density. The electron density of many-electron systems interacting with one another can therefore be calculated as the electron density of the non-interacting system using the time-dependent Kohn-Sham (KS) equation,

$$i\frac{\partial \psi_i(r,t)}{\partial t} = \left(-\frac{\nabla^2}{2} + \upsilon_{KS}[\rho](r,t)\right)\psi_i(r,t) \tag{2.40}$$

Time-dependent Kohn-Sham potentials also include the exchange–correlation energy, which is unknown and hence has to be approximated. The most popular application of TD-DFT is the calculation of excited states as well as both absorption and emission spectra using the B3LYP, CAM-B3LYP, and other functionals.[143] It is also possible to use the dispersion–corrected DFT functionals in the TD-DFT calculations. The application of TD-DFT will be seen in the later chapters of this thesis, where the electronic absorption and emission properties of certain molecular and supramolecular systems are examined.

Chapter 3

Interactions of Dithiafulvene Derivatives with Gold Clusters

3.1 Introduction

The application of gold nanoparticles (AuNPs) and self-assembled gold monolayers (Au SAMs) in the context of nanoscience and nanotechnology has been increasingly studied due to their unique physicochemical properties, including relatively large surface area, small size, high reactivity towards living cells, and stability over a high-temperature range.[144] AuNPs are the most stable metal nanoparticles, while Au SAMs on various substrates allow their surface properties to be flexibly modified. AuNPs and Au SAMs display many interesting features that have attracted broad attention, for example, particle size-regulated electrical, magnetic, and optical properties (quantum size effect) and relevant applications in catalysis and biology.

According to the laws of quantum mechanics, metal nanoparticles with diameters on the nanometer scale (between the size of nanoscale molecules and that of bulk metal) would exhibit unique quantized electronic structures and properties.[145] The attributes of metal nanoparticles are neither like the bulk metal nor like those of individual metal atoms. Rather, they are substantially influenced by factors such as particle size, interparticle spacing, the nature of the covering organic shell, and the form of the nanoparticles.[146] Tunneling occurs between adjacent particles by the few "last metallic electrons". This effect can be seen using impedance measurements that discriminate between intra- and inter-particle processes. When the size of the particle is in the same order as the de Broglie wavelength of the valence electrons (i.e., 5 to 20 nm diameter range), the electronic properties of the particle will behave like zero-dimensional quantum dots (or quantum boxes). Freely moving electrons are imprisoned in these metal cages and exhibit the plasma resonance's distinctive collective oscillation frequency, creating the so-called plasmon resonance band (PRB), which usually gives rise to absorption in the visible region of the spectrum. In contrast to bulk metals, metallic nanoparticles exhibit a gap between the valence band and the conduction band. If the metal particle is small enough (e.g., ∼20 nm), size-dependent quantum effects take place. The size-induced metal–insulator transition was first reported in 1988.[147] The effects result in the formation of standing electron waves with distinct energy levels. If the electrostatic energy, $E_{el} = e^2/2C$, is higher than the thermal energy, $E_T = kT$, single-electron transitions between a tip and a nanoparticle can lead to the detection of so-called Coulomb blockades. As particles get smaller, the capacitance C decreases. Because nanoparticles are small enough ($C \approx 10^{-18}F$), single-electron transitions can only be seen at a given temperature if C is extremely small. When the energy level spacing surpasses the thermal energy, significant fluctuations in electrical and optical characteristics are seen, and this flexibility is very useful for the applications in transistors, switches, electrometers, oscillators, biosensors, and catalysis.[148–154]

AuNPs are also known as gold colloids. Compared to other metallic nanoparticles, AuNPs stand out as the most extensively investigated nanomaterials in modern nanoscience and nanotechnology. Applications of AuNPs so far have been found in the disciplines of materials science, nanotechnology, catalysis, optical sensing, diagnostics, and therapeutics.[155] As early as the fifth or fourth century, Egyptians, Greeks, and Romans already started using AuNPs as colored pigments for ornamental reasons in structures, pottery, and glassware. One renowned example is the Lycurgus Cup, which was produced by Romans around the fourth century (see Figure 3.1).[156] The most distinctive quality of this cup is how its color changes; it appears to be red when light passes through it, but turns green when light is reflected off it. This peculiar characteristic has prompted scientists to conduct chemical investigations, which revealed that the cup contains trace amounts of silver nanoparticles (approximately 300 parts per million) and gold nanoparticles (about 40 parts per million).[156]

Gold had been used to cure tumours, diarrhoea, epilepsy, sexual diseases, and heart and venal disorders during the Middle Ages.[157] AuNPs are highly adjustable nanomaterials for a range of applications thanks to recent advances in their synthesis with controlled morphologies and sizes. Additionally, it is simple to execute surface modifications on AuNPs during their production, which provides access to nanogolds with a variety of forms, structures, and functions; for instance, gold nanospheres,[158] nanorods,[159] nanoshells,[160] and nanocages,[161]. In general, the dimensions of gold-based nano-objects vary from 1 to 100 nm.[162]

.

Figure 3.1: Photographic images of the Lycurgus Cup by courtesy of the British Museum. Adapted with permission from Wagner et al., *Nature*, **2000**, *407*, 691–692

Since the ancient times, AuNPs have been recognised for their distinct red color, which is the result of the photophysical responses of metal nanoparticles to radiation, known as surface plasmon resonance (SPR). SPR does not occur in non-metallic particles. In theory, the free electrons on a gold metal are collectively vibrating in the conduction band produced by the oscillating electromagnetic field of the light when an AuNP is exposed to light.[162] A dipole oscillates in the direction of the electric field as a result of electron oscillation around the surface of the particle, which causes charge separation with regard to the ionic lattice. SPR or the maximum extent of oscillation is a frequency where there is high absorption and scattering of the incoming light. UV–Vis absorption analysis can be used to quantify the SPR phenomena. Depending on the size of the detected AuNPs, the SPR for AuNPs often produces an absorption band in the visible range about 520 nm. Figure 3.2 shows how the SPR bands change from spherical to rod-like when AuNP forms change.[163] It is well known that the electric field density on the Au surface is significantly influenced by the size, shape, surface area, and aggregation condition of AuNPs. As seen for the variously sized gold nanospheres, the optical characteristics of AuNPs significantly alter as their diameter increases. In addition to size, the optical characteristics of a nanoparticle are significantly altered when an anisotropy is added, such as the formation of nanorods.

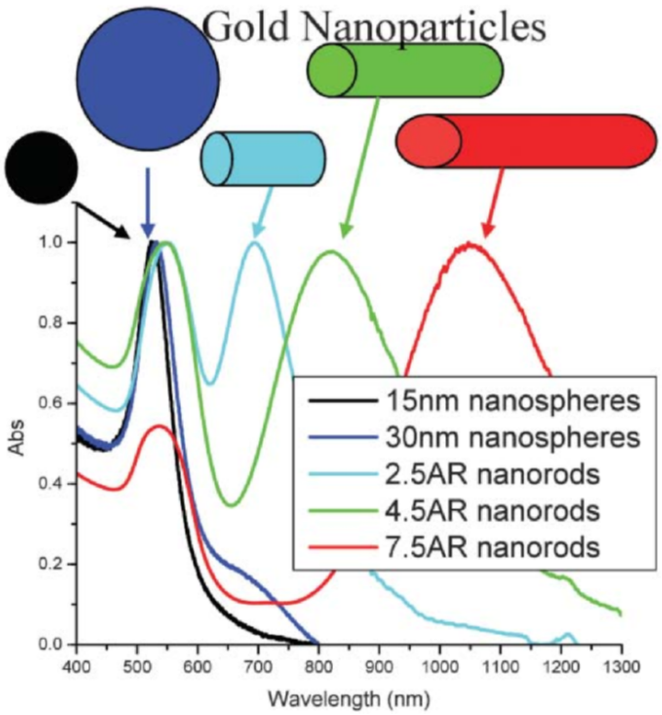

Figure 3.2: UV–Vis absorption behavior of nanogolds in various sizes and shapes. Adapted with permission from Eustis et al., *Chem. Soc. Rev.*, **2006**, *35*, 209–217.

As already indicated, AuNPs exhibit a significant SPR band in the visible part of the spectrum, often between 500 and 600 nm. The maximum absorption wavelength rises along with the particle diameter (see Figure 3.3). As a result, to assess the size of AuNPs, UV–Vis analysis is more frequently employed than time-consuming electron microscopic techniques (such as SEM and TEM). Additionally, the aggregation state of AuNPs in solution can result in striking color changes (such as from red to blue or purple) that are linked to a broader SPR band and a drop in absorption intensity. The formation of AuNPs under various chemical circumstances may be observed and characterized based on these distinctive spectroscopic properties.

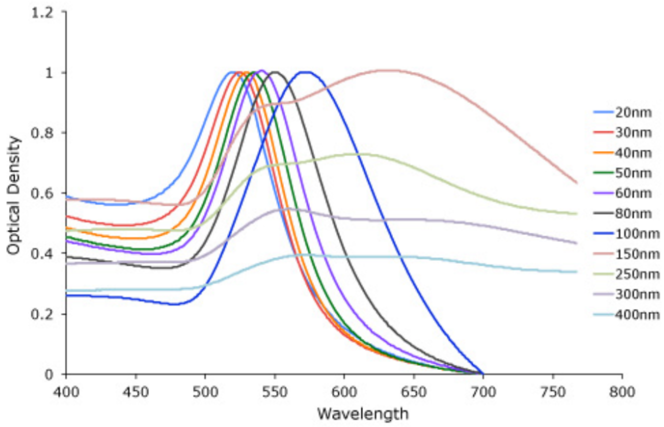

Figure 3.3: SPR absorption bands of AuNPs showing dependence on their size and aggregation state. Adapted from *Introduction to Gold Nanoparticle Characterization* at www.cytodiagnostics.com with permission.

3.1.1 Synthesis of AuNPs

Several synthetic approaches for producing AuNPs with control over size, shape, solubility, stability, and functionality have been established. Most of the synthetic procedures use capping reagents such as surfactants or polymers to prevent the resulting AuNPs from aggregating and precipitating out of the solution. Faraday described the observation of a deep red color during the reduction of an aqueous solution of chloroaurate ($AuCl_4^-$) with phosphorus in carbon disulfide.[164] Turkevich's subsequent work established a common technique for the preparation of AuNPs by citrate reduction of $HAuCl_4$ in water.[165] In this method, citric acid serves as both a reductant and a stabilizing agent, and the AuNPs formed are typically with a diameter of about 20 nm. To date, the most widely used method for AuNP synthesis is the technique developed by Brust and Schiffrin in 1994. In the field of AuNPs chemistry, this method (known as the Brust–Schiffrin method) has made a profound influence on fundamental research and technological applications.[95]

3.1.1.1 The Brust–Schiffrin method

The Brust–Schiffrin method[95] is unique in that it uses a biphasic synthetic procedure to generate AuNPs and further preserve the AuNPs with a thiol as the capping agent. The Brust–Schiffrin method is particularly beneficial for generating small AuNPs with controllable dispersity. Figure 3.4 depicts the detailed steps involved in this method. To begin, the ion $AuCl_4^-$ transfers from an aqueous phase to toluene with the aid of a phase-transfer reagent, tetraoctylammonium bromide (TOAB). In the organic phase, the $AuCl_4^-$ ion is reduced to Au(I) by dodecanethiol. When $NaBH_4$ is added, Au(I) is further reduced to Au(0). Experimentally, the occurrence of such reduction reactions can be confirmed by the observation that the color of the solution changes from orange to a dark brown color. The sizes of AuNPs formed in the organic phase are usually in the range of 1.5 to 5.0 nm. The surface of the AuNPs are anchored with thiol ligands, which prevent the aggregation of the resultant AuNPs by forming a robust self-assembled layer on the particle surface. As such, the thiol-functionalized AuNPs can be readily dispersed in various organic solvents without aggregation or decomposition. Furthermore, the Burst–Schifrin approach can flexibly control the particle size by adjusting the preparation conditions, such as the type of thiol, Au/thiol ratio, temperature, pH, and reduction rate.[96]

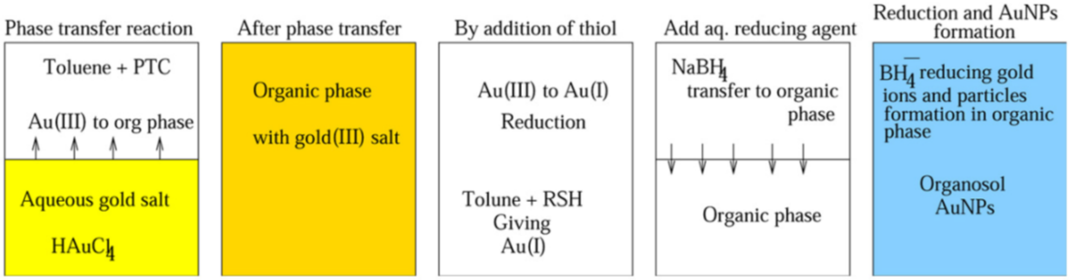

Figure 3.4: Schematic illustration of the Brust–Schiffrin biphasic synthesis of AuNPs. Figure adapted with permission from Perala et al., *Langmuir*, **2013**, *29*, 9863–9873.

Numerous mechanistic investigations have been carried out to shed light on the intricate reduction processes entailed in the two-phase system of the Brust–Schiffrin technique.[166] It has been known that TOAB, as a phase transfer catalyst, first facilitates the transfer of chloroauric acid ($HAuCl_4$) to the organic phase (toluene) through the following steps,[95]

$$H^+AuCl_4^-(aq) + (R_8)_4N^+Br^-(org) \longrightarrow (R_8)_4N^+AuCl_4^-(org) + HBr(aq)$$

$$(R_8)_4N^+AuCl_4^- + 3RSH \longrightarrow AuSR + RSSR + (R_8)_4N^+ + 4Cl^- + 3H^+$$

The next step is to reduce Au^{3+} to Au^+ using alkanethiol (RSH), as illustrated in the above reactions.[95,167,168] At this stage, the organic phase consists of TOAB, dialkyl disulfide (RSSR), and Au^+ in the form of -$(AuSR)_n$-polymer. In addition,

$AuCl_4^-$ may be complexed with the tetraoctylammonium (TOA) ion or an excess of RSH. The following reactions are predicted to occur during the reduction of Au^{3+} and Au^+ to Au^0 by sodium borohydride.[167,168]

$$(AuSR)_n + NaBH_4 + RSH + RSSR \longrightarrow Au_x(SR)_y$$

$$(R_8)_4N^+AuCl_4^- + NaBH_4 + RSH + RSSR \longrightarrow Au_x(SR)_y$$

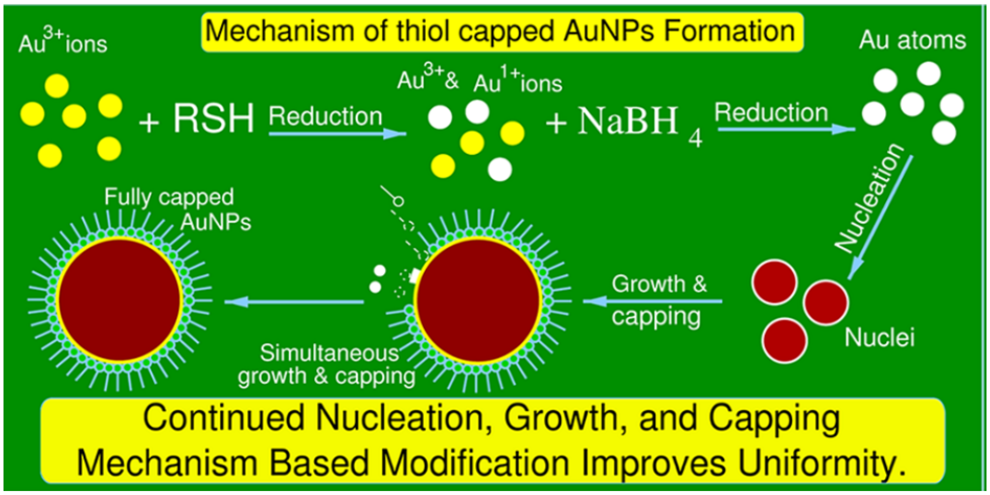

Figure 3.5: The mechanism of thiol-capped AuNP production using the Brust–Schiffrin technique. Figure adapted with permission from Perala et al., *Langmuir*, **2013**, *29*, 9863–9873.

Despite the fact that multiple studies have been reported in the present literature, the mechanism of AuNP production and size regulation remains unclear. The nucleation of Au(0) seeds and their development into AuNPs, for example, take place through very complex processes, while a population balance model indicates that particle formation in the Brust–Schiffrin synthesis is correlated with conditions such as continuous particle nucleation, growth, and capping agents.

3.1.2 Redox interactions of Au(III) with carboxylated dithiafulvenes and tetrathiafulvalene analogues

A typical method for making AuNPs involves the reduction of Au(III) species like $HAuCl_4$ with a reducing agent, such as citrate,[93,94,169–171] $NaBH_4$,[172,173] and block copolymers.[171,174–176] After reduction, appropriate ligands are added to stabilize the resultant AuNPs and exert control over their shape and functionality. As aforementioned, the popular Brust-Schiffrin two-phase method[95,96,177] has made it possible to synthesize stable, monodispersed, and flexible functionalized AuNPs.

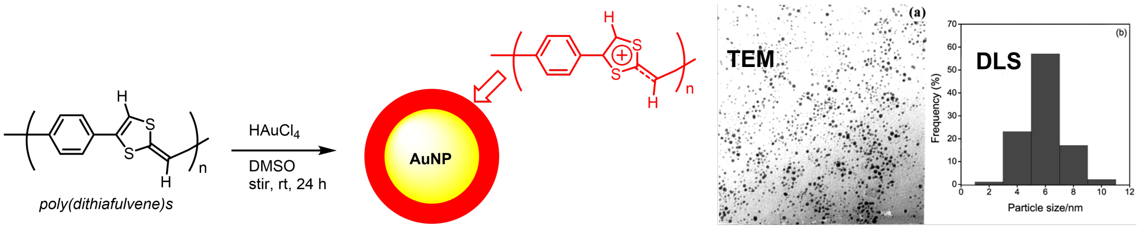

Scheme 3.1: The use of poly(dithiafulvene)s as reductants for AuNP formation. TEM and DLS figures are adapted with permission from Chujo et al., *Chem. Commun.* **2001**, 613–614.

There have been some studies in the literature on the direct reduction of $HAuCl_4$ into AuNPs in organic media using π-conjugated electron donors as reductants. In the early 2000s, Chujo and co-workers[97,98] reported the use of π-conjugated polymers that contain electron-rich dithiafulvene (DTF) units to transform $HAuCl_4$ into narrowly distributed AuNPs. Their method took advantage of the reductive properties of DTF groups as well as the protective effects of the oxidized polymers on AuNPs (Scheme

3.1).[178] Later, the groups of Chujo[179] (Scheme 3.2) and Granados[99] (Scheme 3.3) developed methods of using small DTF-based compounds to reduce $HAuCl_4$ in organic solvents such as acetonitrile.

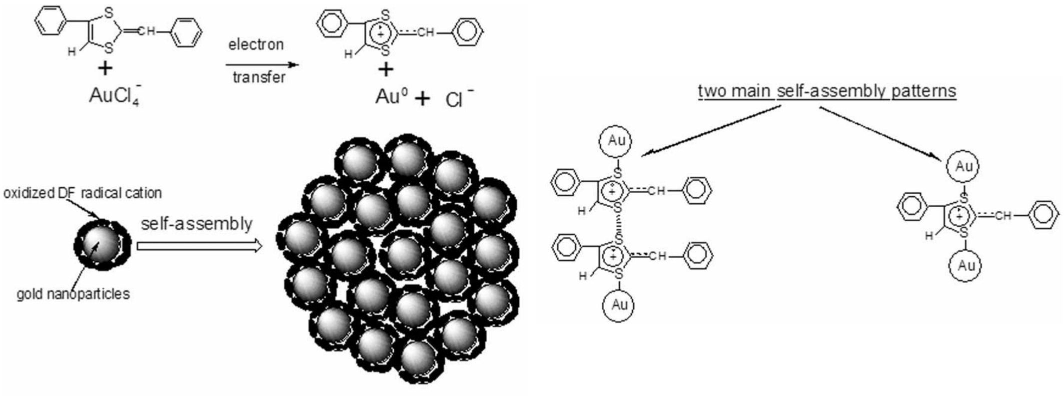

Scheme 3.2: Mechanism for the reduction of Au(III) ions to AuNPs with a redox-active DTF compound. Figure adapted with permission from *J. Macromol. Sci. Part A: Pure Appl. Chem.* **2006**, *43*, 1801–1805.

Electron transfer from DTF to Au(III) is a key step in the formation of AuNPs. Once formed, the surface of AuNPs is bound to oxidized DTFs via S–Au interactions, providing stability to the AuNPs (Schemes 3.2 and 3.3). The proposed model of oxidized DTF–Au interactions can reasonably explain the experimental outcomes; however, concrete evidence for the occurrence of such events has not yet been sufficiently established by vigorous experimental and theoretical analyses. The oxidative dimerization process of DTFs, as demonstrated in Chapter 4 of this thesis, and their impact on AuNP formation and stabilization was completely neglected in the theoretical rationalizations made in the early studies on DTF-induced AuNPs.

The Zhao group and others have actively studied DTF oxidative dimerization re-

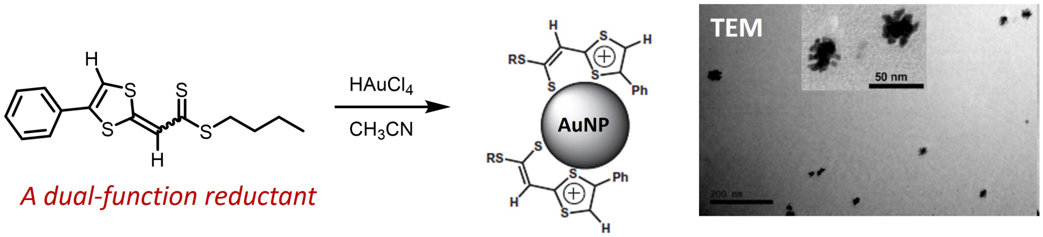

Proposed reduction mechanism

Au(III) + DTF $\longrightarrow$ DTF_{ox}-Au(I) Complex formation

3 DTF_{ox}-Au(I) $\longrightarrow$ 3 DTF_{ox} + 2 Au(0) + Au(III) Disproportionation

Au(0) $\longrightarrow$ AuNP@DTF_{ox} AuNP growth and Stabilization

Scheme 3.3: Reduction of Au(III) to AuNPs using DTF based compounds as the reductants and stabilizers as well as a proposed reduction mechanism. TEM image adapted with permission from Granados et al., *Tetrahedron Lett.* **2015**, *56*, 4871–4876.

actions during recent years as efficient synthetic methods for preparing π-conjugated polymers,[87,89,180] redox-active ligands,[42,181] macrocycles,[75,182] chemosensors,[182–185], and other useful molecular devices.[37,186] Earlier in our group, four different carboxylated DTFs and TTFVs (Scheme 3.4) were designed and synthesized.[181]

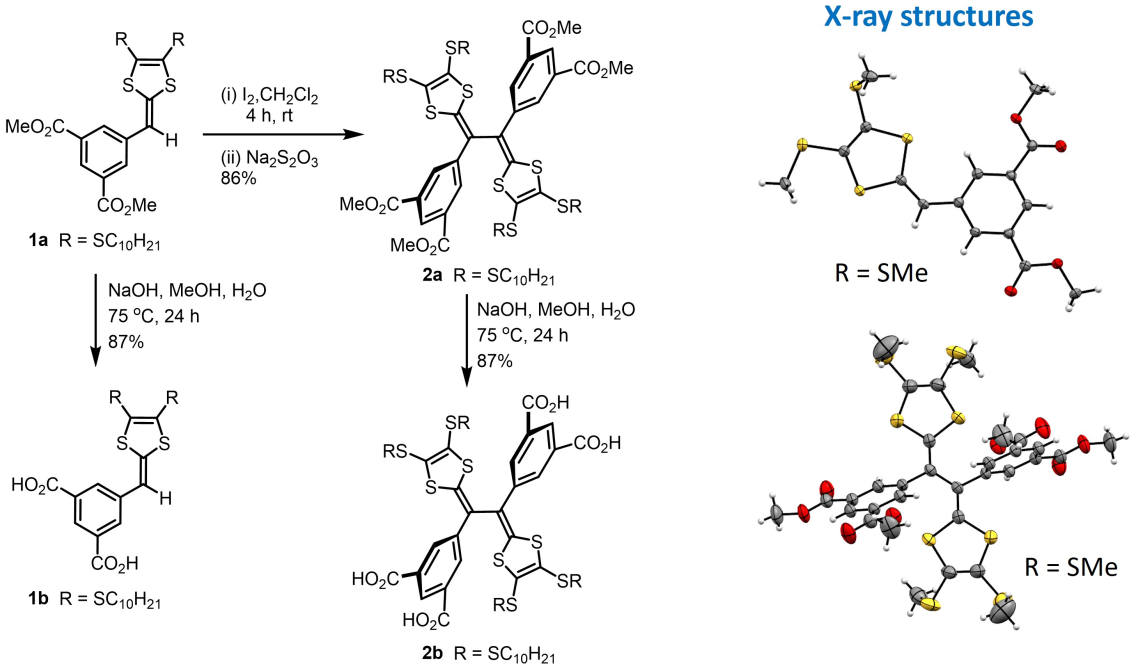

Scheme 3.4: Design and synthesis of carboxylated DTFs and TTFVs and related x-ray structural analyses.

In another study, these compounds were reacted with $HAuCl_4$ in order to examine the S–Au interactions involved in the reaction as well as to explore the applicability of these reactions in the synthesis of AuNPs (Schemes 3.5 and 3.6).[187] The main reason for having carboxyl and DTF combined together was to attain improved solubility in certain polar organic solvents, where the reduction of Au(III) to Au(0) could take place effectively. Additionally, it was predicted that the ability of carboxyl groups to induce hydrogen bonds and to interact with Au particle surfaces would deliver beneficial effects on stabilizing the reduced Au(0) species in the form of AuNPs. In this chapter, the detailed roles of the DTF and carboxyl groups have been investigated by DFT computational analyses.

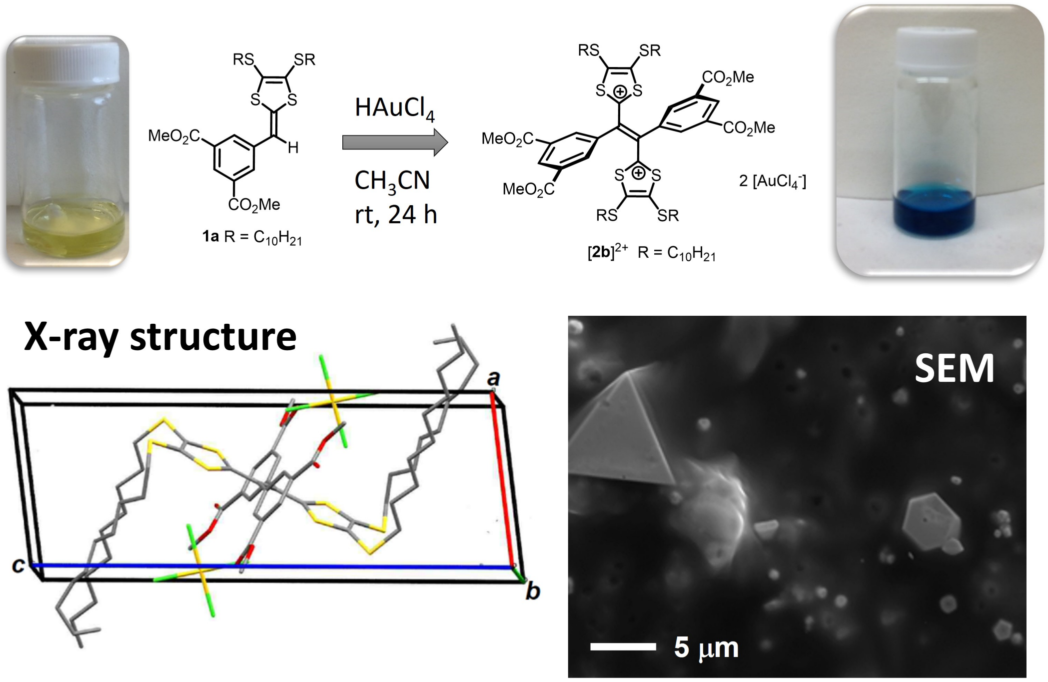

Scheme 3.5: Top: the reaction of a carboxylated DTF with $HAuCl_4$ in CH_3CN. Photoimages show a solution of carboxylated DTF before and after the addition of $HAuCl_4$. Bottom: the X-ray structure of the resulting TTFV dication, and the SEM image of the gold particles formed.

The interactions of carboxylated DTFs and TTFVs with $HAuCl_4$ were investigated in a range of polar organic solvents. It was found that the *meta*-dicarboxyl-substituted-DTF behaves differently from the other π-donors. Its reaction with $HAuCl_4$ produced highly stable AuNPs in DMSO and DMF.

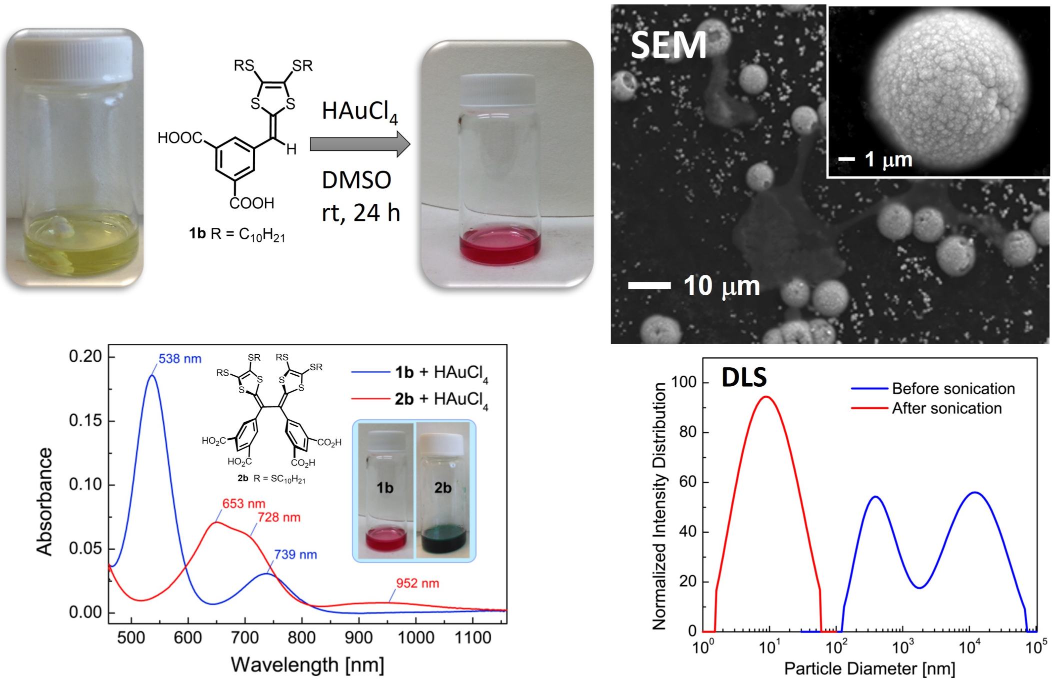

Scheme 3.6: Reduction of $HAuCl_4$ with carboxylated DTFs and TTFVs monitored by UV–Vis, SEM, and DLS analyses.

Based on the experimental results of these studies, we subsequently carried out the investigations on the mechanisms for these reactions. In particular, we have been interested in understanding the detailed steps and molecular interactions occurring during these reactions. To achieve this goal, computational studies have been carried out in this thesis work to model the interactions of Au_n ($n = 3, 4, ..., 10$) clusters with oxidized DTF species (radical cations). The main objective of this study is to find clear answers to the following questions. (1) Why does carboxylated DTF perform better than carboxylated TTFV in reducing Au(III) into AuNPs? (2) Is COOH an effective ligand to bind with Au(0)? (3) Can the oxidized species (e.g., the DTF radical cation) act as an effective capping agent to stabilize AuNPs? (4) If so, how strong are the DTF/AuNP interactions? The following sections discuss the results of our computational modelling studies based on DFT and TD-DFT calculations.

3.2 Methodologies

3.2.1 Computational modelling and visualization methods

DFT calculations have been conducted using the Gaussian 16 software package.[188] The geometries of all calculated compounds, including carboxylated DTF molecules, the gold clusters, and the complexes of Au–DTF, were first optimized by the semi-empirical PM6 method[189] to find suitable initial geometries that are close to true global minima. Then DFT geometry optimization was conducted on these structures using the hybrid functional, M06-2X,[129,190] in conjunction with the Karlsruhe basis set, def2-SVP.[191,192] Following the optimization step, each structure was subjected to vibrational analysis at the same level of theory to verify that it is a true global energy minimum (i.e., no imaginary frequencies). Analysis of atomic charge populations was calculated using the atomic dipole moment corrected Hirshfeld population method proposed by Lu and Chen.[193,194] Solvent effects were analyzed using the continuum solvation model based on the charge density (SMD) developed by Truhlar et al.[195] In addition, visualization of molecular structures and molecular orbitals was carried out via the CYLview[196] and GaussView 6[197] software packages, respectively. Topological analysis of electron density and its visualization were performed using the Multiwfn program[198] and the VMD software package.[199] The energies of excitation and calculated excited-state properties as well as calculations of UV–Vis absorption spectra were determined using the time-dependent density functional theory (TD-

DFT)[142] approach at the M06-2X/def2-SVP level. We considered only singlet to singlet transitions in the TD-DFT calculations in order to save computational costs and maintain sufficient accuracy. Simulated UV–Vis absorption spectra were generated by GaussSum[200] and plotted using the OriginPro 8 software package.[201] The analyses using the independent gradient model (IGM) and quantum theory of atoms in molecules (QTAIM) methods were performed with the Multiwfn program, while the VMD software package was used to visualize the outcomes. All energies are Gibbs free energies calculated via the Shermo program,[202] a general code for calculating molecular thermodynamic properties. All the DFT calculations have been done at the temperature of 298.15 K and the pressure of 1.00 Atm.

3.2.2 Procedures for obtaining the most stable structure for each Au_n/DTF complex

In order to perform a thorough investigation of the covalent and non-covalent interactions between Au clusters and DTF compounds, the geometries of a carboxylated DTF (in the form of a radical cation) and various Au clusters were first optimized separately using DFT calculations. Moreover, the geometry optimization was first carried out in the gas phase, and then the optimized structures were used as the inputs for calculations in solvents. The initial structure of each Au cluster was adapted from the literature.[203] For each Au cluster (Au_n), the DTF molecule was placed around it at different positions for optimization in the gas phase. Next, we utilized the gas-phase optimized geometries as the inputs for geometry optimization calculations in different solvents, including tetrahydrofuran (THF), acetonitrile (ACN), *N*,*N*-dimethylformamide (DMF), and dimethylsulfoxide (DMSO). For smaller clusters, such as Au_3 to Au_5, seven distinct initial structures were designed. However, with an increase in the number of Au atoms within the clusters, certain initial structures began to overlap, leading to a decrease in the number of initial-guess geometries for Au_6 to Au_{10}. Moreover, a few of these initial-guess geometries encountered error 9999, indicating their inadequacy as suitable starting points (due to their failure to approach any local or global minima in the potential energy surface of their corresponding system). Consequently in some cases, this resulted in a reduction in the overall number of initial structures.

3.3 Results and discussion

The acronyms and structures of the systems computationally investigated in this work are first described in Scheme 3.7. For simplicity, we use DTF to refer the radical cation of a *meta*-dicarboxylated phenyldithiafulvene. In a previous study by the Zhao group, it was found that AuNPs were generated by mixing this compound in its neutral state with $HAuCl_4$ in polar organic solvents. The experimental results suggest that redox reactions occur between DTF and $HAuCl_4$, leading to the formation of an Au(0) atom and the radical cation of DTF as products at the early stage of the reactions. As to the subsequent fates of the Au(0) and the DTF radical cation, we hypothesized that the Au(0) atoms would aggregate into Au clusters, while DTF as a ligand bonds to the Au clusters to provide stablizing effects. To gain insight into the detailed interacting modes between Au clusters and a DTF radical cation, we chose to model systems where DTF is bonded to Au clusters containing varied number of gold atoms (hereafter referred to as Au$_n$) in which the subscript n indicates the number of Au atoms. The complex of a Au cluster with a DTF radical cation is denoted as Au$_n$/DTF in the following discussion. For each Au$_n$/DTF, there exists several stable structures according to DFT optimization calculations. In our work, we have modelled Au$_n$/DTF complexes, in which the number of gold atoms (n) ranges from 3 to 10. For each Au$_n$/DTF complex, the geometric and energetic properties of DFT optimized stable structures were examined and compared. Our analysis gave particular attention to the lowest-energy structure so as to find out the correlations between various DTF–Au interacting modes and the stabilizing effects they provide to the Au$_n$/DTF complex.

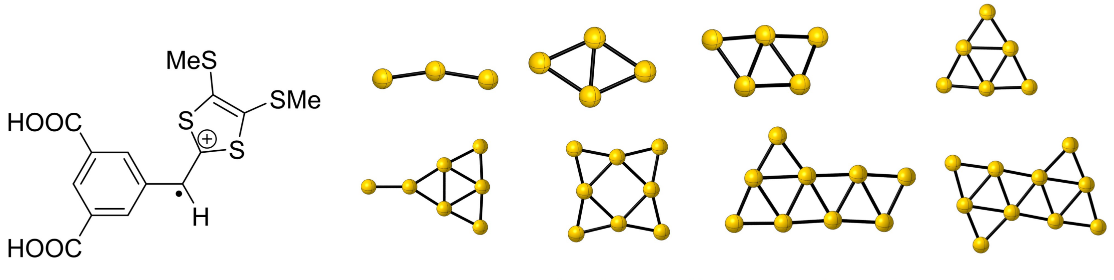

DTF

Au clusters (Au$_n$), n = 3, 4, …, 10

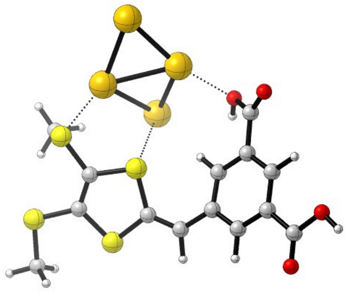

Au$_4$/DTF: Complex containing Au$_4$ cluster bound to the DTF moiety

Scheme 3.7: Schematic illustration of the DTF ligand (radical cation), Au$_n$ clusters, and an example of Au$_n$/DTF complexes (n = 4).

3.3.1 Au_3/DTF

Four stable structures of Au_3/DTF were found in the gas phase by DFT calculations, and they are illustrated in Figure 3.6. Among them, the most stable one is structure #1, which shows three distinct attractive intermolecular contacts between the Au_3 cluster and the DTF moiety, as opposed to the other three structures, for which only two significant intermolecular interactions exist. Table 3.1 lists the relative Gibbs free energies of these structures. It can be seen that structure #1 is more stable than the others by more than 10 kcal mol^{-1}. Structurally, #1 features two Au–S bonds and one Au–O bond. It is noteworthy that one of the Au–S bonds (3.29 Å) is notably longer than the average bond of this type. This bond is formed between one of the dithiole S atoms and Au. As this S atom is involved in the rigid dithiolium ring, its ability to interact with Au is somewhat attenuated due to geometric constraints. One of the methyl thiol ether S atoms of DTF, on the other hand, forms a relatively stronger bond with the same Au atom, showing a Au–S distance of 2.47 Å.

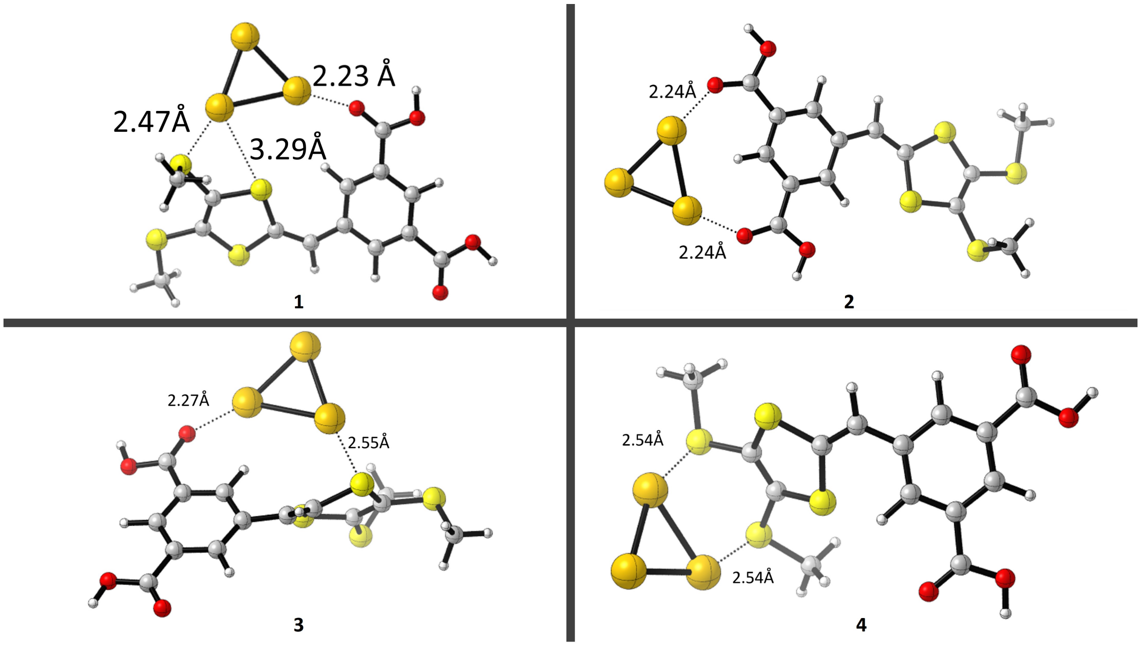

Figure 3.6: Optimized geometries of Au$_3$/DTF complexes in the gas phase.

The second most stable structure of Au$_3$/DTF is #3, which is assembled mainly through a Au–S bond and a Au–O bond between DTF and Au$_3$. The Au–S bond is formed between a dithiole S atom and Au, the bond distance of which is in line with a typical Au–S interaction. One of the carboxyl oxygen atoms forms a Au–O bond with another Au atom. Overall, structure #3 exhibits a bidentate binding mode. Compared with structure #1, it is less stable by 11.276 kcal mol^{-1} in the gas phase due to the lack of a Au–S interaction. However, in comparison with structure #2, which is the third most stable structure, structure #3 is slightly more stable in the gas phase by ca. 1.2 kcal mol^{-1}. Structure #3 also shows a bidentate binding mode. There are two interactions between Au and DTF in this structure, which are both Au–O bonds.

Table 3.1: Relative Gibbs free energies (in kcal mol^{-1}) of four optimized Au_3/DTF complexes

structure	**Gas**	**THF**	**ACN**	**DMF**	**DMSO**
1	0.000	0.000	0.000	0.000	0.000
2	12.492	9.927	10.110	9.487	9.336
3	11.276	8.188	8.388	7.461	7.232
4	14.230	6.840	6.961	6.063	5.795

When these structures are in organic solvents, the number of the attractive interactions in each remains the same as the gas-phase structure. However, as the polarity of the solvent increases, the bond distances of the attractive contacts between DTF and Au are increased. For example, the Au–S bond length between the Au_3 cluster and one of the SMe sulfur atoms is slightly increased from 2.50 Å in THF to 2.51 Å in DMSO. This trend can be rationalized by the following argument. The DTF moiety and Au_3 cluster possess different charge distributions and hence show electrostatic attractions. The large dielectric constant of a polar solvent, in theory, reduces electrostatic forces and hence makes the DTF moiety stay further from the Au cluster than in the complex in the gas phase. This argument is supported by charge transfer analysis, which is discussed in detail in a later subsection of this chapter.

3.3.2 Au_4/DTF

For the Au_4/DTF system, four stable structures have been identified by DFT calculations (see Figure 3.7). Among them, the most stable structure is #1. As in the case of Au_3/DTF, the most stable structure of Au_4/DTF shows the greatest number of intermolecular contacts. There are two Au–S bonds in this structure. One is greater than the average length and the other one is significantly shorter (3.23 and 2.50 Å, respectively). On the other side of the assembly, a Au–O bond is formed with a bond distance of 2.26 Å.

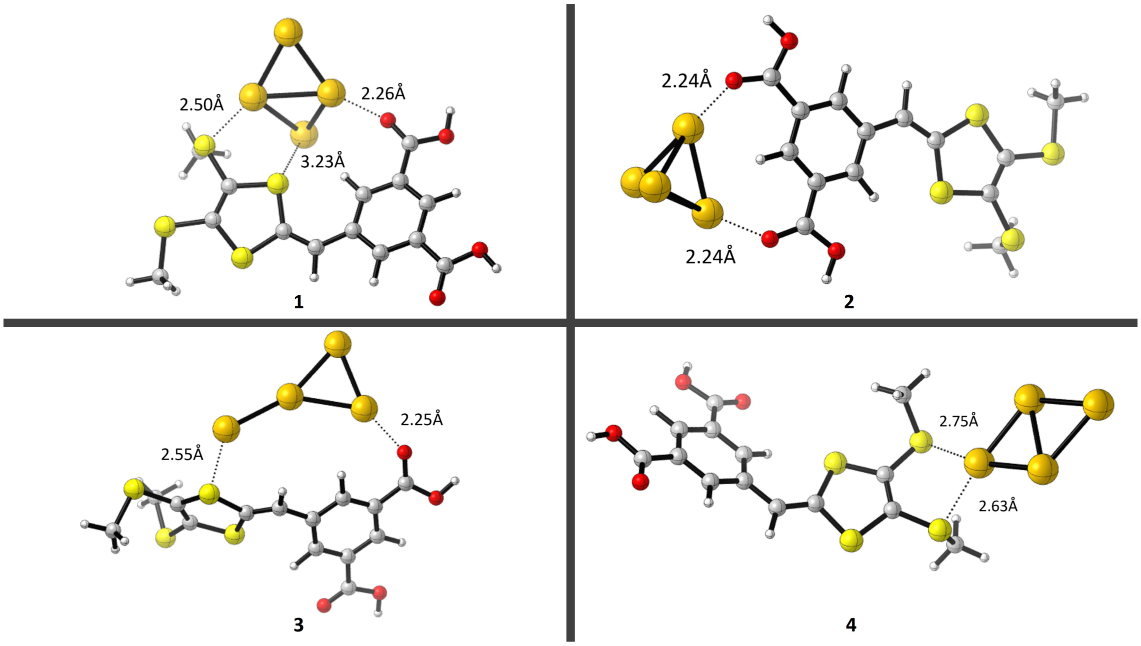

Figure 3.7: Optimized geometries of Au_4/DTF complexes in the gas phase.

The relative Gibbs free energies of these complexes are compiled in Table 3.2. As can be seen, the second most stable structure of Au_4/DTF is #3, which shows a Au–S bond and a Au–O bond. It is also worth noting that the Au_4 cluster in #3 takes on a nearly planar arrangement, which is very different from the gold cluster geometry of #1. Structure #2 is the third most stable assembly, which shows two Au–O bonds between two carboxyl groups and two Au atoms. The Au_4 cluster of #2 assumes a shape of a tetrahedron. Structure #4 actually is the least stable one among the optimized Au_4/DTF assemblies. The DTF–Au contacts in this structure

Table 3.2: Relative Gibbs free energies (in kcal mol^{-1}) of four optimized Au_4/DTF complexes.

structure	**Gas**	**THF**	**ACN**	**DMF**	**DMSO**
1	0.000	0.000	0.000	0.000	0.000
2	14.240	12.696	11.698	12.130	11.711
3	10.897		10.699		9.698
4	18.760		8.386		

afford a chelation mode, in which two SMe sulfur atoms interact with the same Au atom. The Gibbes free energy of this assembly is higher than the most stable one by 18.760 kcal mol^{-1} in the gas phase.

With solvent effects taken into account, all of the Au_4/DTF assemblies show a trend of geometric changes similar to the Au_3/DTF. The bond lengths of DTF–Au contacts become greater with increasing solvent polarity. For example, the lengths of two Au–S bonds and one Au–O bond in structure # 1 are 2.54, 3.38, and 2.35 Å in THF, while in DMSO, which is more polar, they are 2.55, 3.42, and 2.38 Å, respectively. Furthermore, the number of attractive interactions existing in structure # 1 (Figure 3.7) is increased to four in the solution phase. Also, the gold cluster is slightly further away from DTF when the system is in a solution phase.

3.3.3 Au_5/DTF

Figures 3.8 and 3.9 show the optimized structures of the Au_5/DTF assemblies. In Table 3.3, their relative energies calculated in the gas phase as well as in different solvents are listed. Similar to the trends observed in the previous Au_n/DTF complexes, the binding modes contain Au–S and Au–O contacts in all these structures.

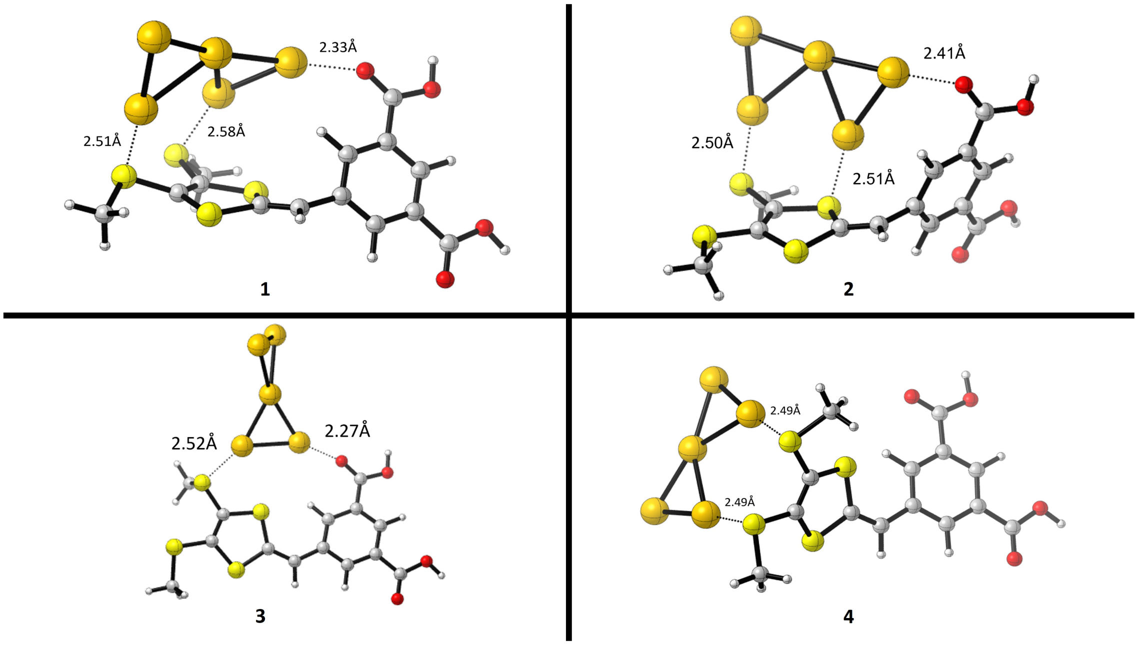

Figure 3.8: Optimized geometries of Au_5/DTF complexes in the gas phase (structures 1 to 4).

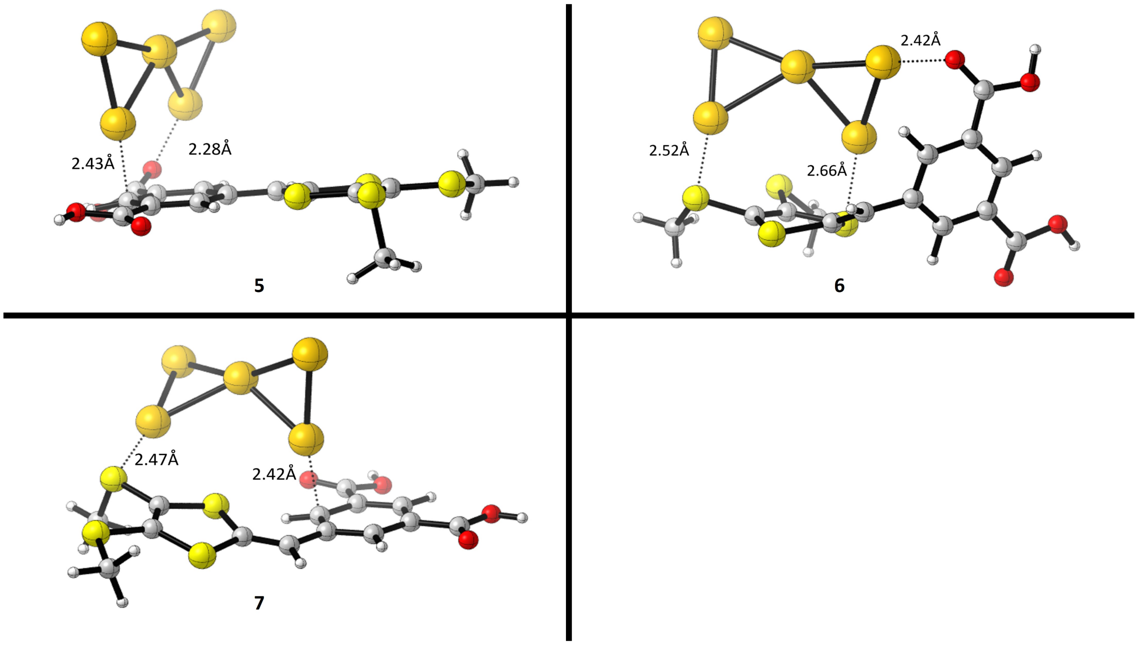

Figure 3.9: Optimized geometries of Au_5/DTF complexes in the gas phase (structures 5 to 7).

In structure # 1 which is the most stable one, the bond lengths include 2.51 and 2.58 Å for the two Au–S bonds and 2.33 Å for the only Au–O bond (Figure 3.8).

Table 3.3: Relative Gibbs free energies (in kcal mol^{-1}) of optimized Au_5/DTF complexes.

structure	**Gas**	**THF**	**ACN**	**DMF**	**DMSO**
1	0.000	0.000	0.000	0.000	0.000
2	0.295	0.639	0.037		
3	11.265	9.116	8.906	9.261	8.718
4	6.934	1.061	0.632	0.536	0.659
5	20.225	14.377	13.717		
6	3.470	2.807	2.847	2.947	2.873
7	6.181	2.850	1.618	0.881	0.912

Taking the solvent effects into consideration, the Au_5/DTF assemblies show insignificant changes in the bond lengths and geometry of the most stable structure, except that the Au–O bond length increases with increasing solvent polarity; from 2.33 Å in the gas phase to 2.44 Å in THF and 2.46 Å in DMSO.

3.3.4 Au_6/DTF

For the assemblies of Au_6/DTF, some new but weak non-covalent interactions emerge. Figure 3.10 shows that other than the two Au–S and Au–O bonds, there exist two Au–C bonds with bond distances more than 3 Å. The nature of these Au–C bonds and their contribution to the stability of the complex have been assessed through the approach of Quantum Theory of Atoms in Molecules (QTAIM) and will be discussed in a later section of this chapter. Among the optimized geometries, structure # 3 shows the greatest stability which makes sense since it forms more intermolecular

Table 3.4: Relative Gibbs free energies (in kcal mol^{-1}) of four optimized Au$_6$/DTF complexes.

structure	**Gas**	**THF**	**ACN**	**DMF**	**DMSO**
1	1.877		0.075	1.549	1.155
2	2.838	1.342	4.849	5.920	6.632
3	0.000	0.000	0.000	0.000	0.000
4	7.511	2.129	4.861	5.438	6.841

contacts than the others (see Table 3.4).

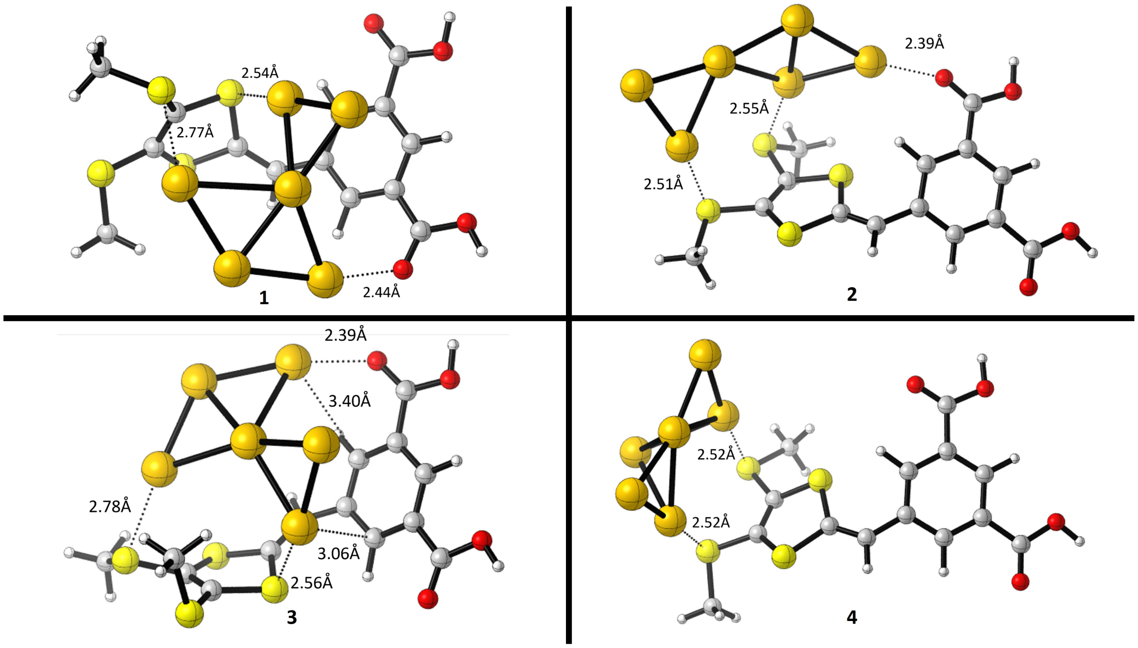

Figure 3.10: Optimized geometries of Au$_6$/DTF complexes in the gas phase.

For Au$_6$/DTF complexes, solvent effects are different from those for the previous complexes. As the Au cluster becomes larger, solvents with different polarities significantly alter the geometry and stability of the complexes. The interacting atoms

Table 3.5: Relative Gibbs free energies (in kcal mol^{-1}) of five optimized Au$_7$/DTF complexes.

structure	**Gas**	**THF**	**ACN**	**DMF**	**DMSO**
1	9.870		10.468	9.756	10.500
2	0.876	36.117	3.588	3.955	4.056
3	3.450	0.942	7.868	7.807	8.092
4	4.765		4.157	4.610	
5	0.000	0.000	0.000	0.000	0.000

between the two moieties (Au$_6$ cluster and DTF) in the gas phase are different from those in polar solvents. However, the most stable Au$_6$/DTF complex in a polar solvent still shows the highest number of interactions in comparison with the other structures.

3.3.5 Au$_7$/DTF

The most stable structure of Au$_7$/DTF has three gold atoms interacting with five different atoms of DTF (see Table 3.5 and Figure 3.11). In this structure, the Au–C interaction has a bond distance of 3.21 Å in the gas phase and 3.34 Å in DMSO.

Regarding solvent effects, it has been found that as the Au cluster grows larger, the geometry of the DTF moiety and its selective interactions with the gold cluster change significantly upon solvation.

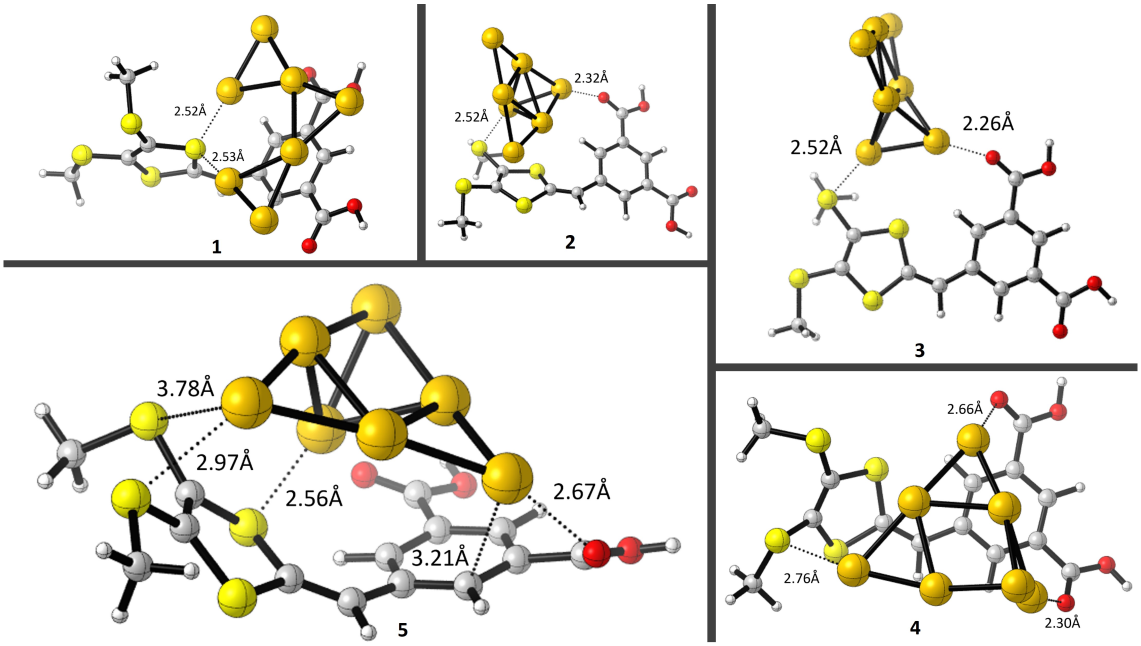

Figure 3.11: Optimized geometries of Au_7/DTF complexes in the gas phase.

3.3.6 Au_8/DTF

Figure 3.12 shows that in the most stable structure of Au_8/DTF (structure #4), there are six different interactions, including four Au–S bonds, one Au–O bond, and one Au–C bond. Solvent effects make these bond lengths somewhat elongated, while the shape of the Au_8 cluster is also slightly changed in the solution phase. Table 3.6 summarizes the relative Gibbs free energies calculated for different Au_8/DTF structures.

Table 3.6: Relative Gibbs free energies (in kcal mol^{-1}) of five different Au_8/DTF complexes.

structure	**Gas**	**THF**	**ACN**	**DMF**	**DMSO**
1	7.800		1.989	0.561	1.069
2	2.528	4.389	7.804	6.807	6.887
3	0.330		1.557	0.833	0.772
4	0.000	0.000	0.000	0.000	0.000
5	0.814			1.229	1.589

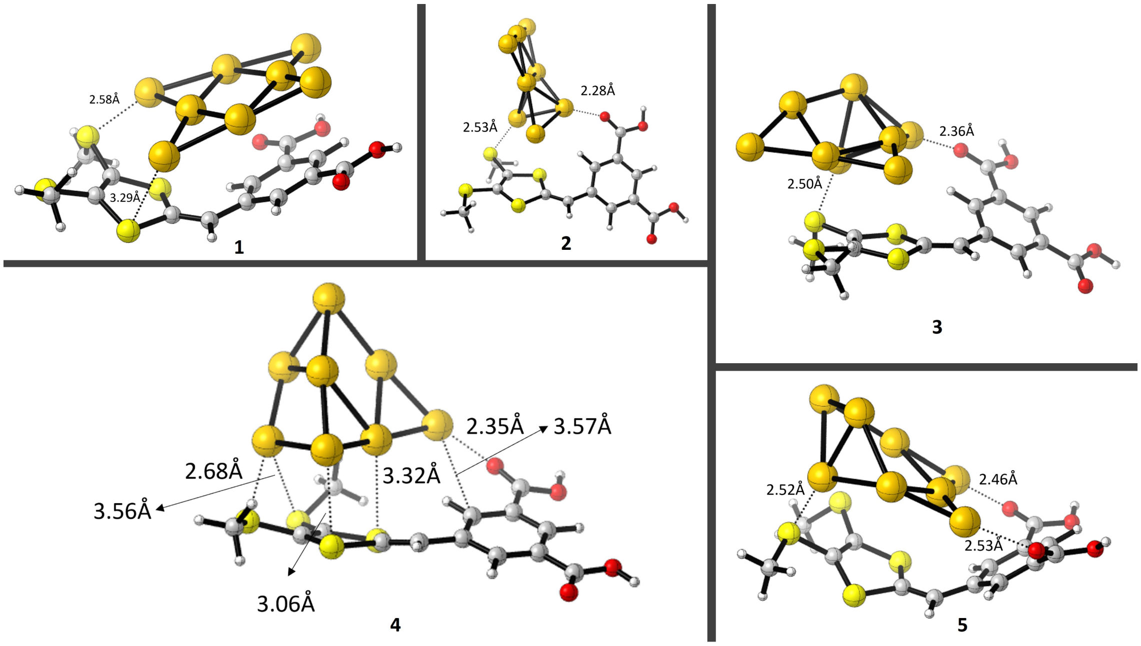

Figure 3.12: Optimized geometries of Au_8/DTF complexes in the gas phase.

3.3.7 Au_9/DTF

Figure 3.13 shows different optimized structures for Au_9/DTF. Their relative free energies are summarized in Table 3.7. It can be seen that among these structures, # 5 is the most stable. There are five different interactions between Au_9 and DTF in structure # 5. Two of these interactions are Au–C bonds with bond lengths of 3.21 and 2.98 Å, respectively. There is one Au–O bond with a length of 2.33 Å, and the other two are Au–S bonds with bond lengths of 2.60 and 2.80 Å, respectively. DFT calculations also disclosed that the lengths of these increase with increasing solvent polarity; for example, the Au–O distance is 2.64, 2.68, and 2.67 Å in ACN, DMF, and DMSO, respectively.

Table 3.7: Relative Gibbs free energies (in kcal mol^{-1}) of five different Au_9/DTF complexes.

structure	**Gas**	**THF**	**ACN**	**DMF**	**DMSO**
1	2.096			73.721	1.116
2	15.402	30.506			
3	4.689		1.624	1.618	
4	21.816		12.663	14.588	
5	0.000	0.000	0.000	0.000	0.000

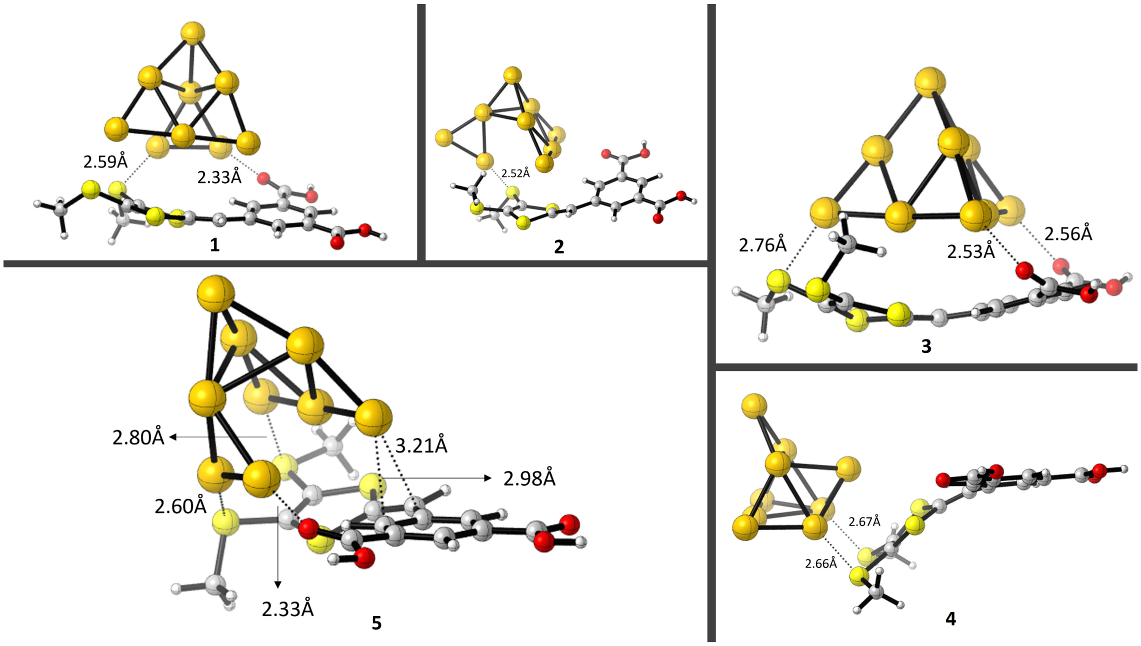

Figure 3.13: Optimized geometries of Au_9/DTF complexes in the gas phase.

3.3.8 Au_{10}/DTF

Figure 3.14 shows three optimized structures for Au_{10}/DTF. In addition, their relative Gibbs free energies are given in Table 3.8. Structure # 1 is the most stable due to the fact that there are 5 attractive interactions between Au_{10} and DTF in comparison with the other two, in which there are only three attractive interactions. In structure # 1, the intermolecular interactions include one Au–O bond (2.37 Å), one Au–C bond (2.86 Å), and three Au–S bonds (2.58, 3.46, and 2.77 Å, respectively). Solvent effects lead to expansion of the complex size; for example, the Au–O bond is increased to 2.60 Å in THF and 2.64 Å in DMSO. In addition, the Au–C bond is increased to 3.03 and 3.04 Å in THF and DMSO, respectively.

Table 3.8: Relative Gibbs free energies (in kcal mol^{-1}) of three different Au_{10}/DTF complexes.

structure	**Gas**	**THF**	**ACN**	**DMF**	**DMSO**
1	0.000	0.000	0.000	0.000	0.000
2	16.645		7.282	7.690	7.044
3	2.940	2.757			5.545

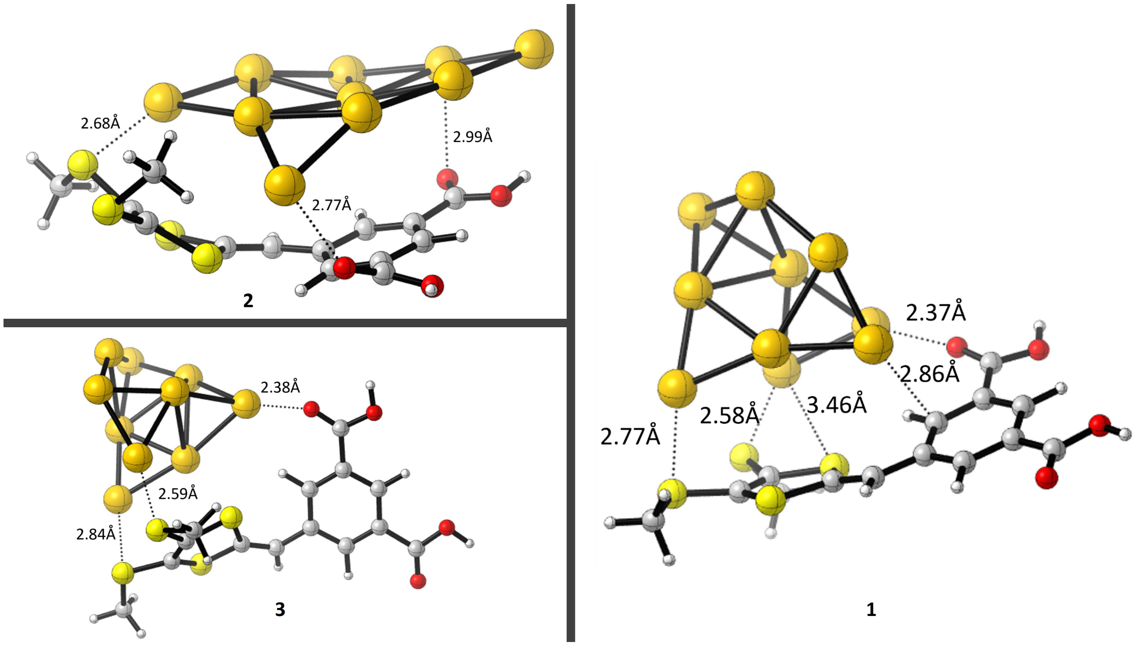

Figure 3.14: Optimized geometries of Au_{10}/DTF complexes in the gas phase.

In general, for the relatively small Au_n/DTF complexes (n = 3, 4, and 5), the solvent effects only lead to an increase in the bond length of the same two atoms. For larger Au_n/DTF complexes (n = 6, 7, 8, 9, 10), however, solvation results in a slight change in the geometry of the gold cluster in order to increase the stability of the whole complex. As such, in some cases the interactions take place between different pairs of atoms.

Moreover, the types of attractive interactions in the supramolecular assemblies are diverse. One type is the coordinate covalent (dative) bond between one or more gold atoms in the gold cluster, and oxygen and/or sulfur atoms in DTF. This bond type is the most abundant one amongst all Au_n/DTF complexes (see Figures 3.6–3.14). The second type is the intramolecular hydrogen bonding in the DTF moiety. Usually the H-bond donors are the S and O atoms in DTF (refer to QTAIM table of results in Figures 3.20 to 3.23). In addition, Au–C bonds are observed in some of the most stable complexes and their bond distances are longer than the average Au–C single bond (ca. 1.95 Å to 1.99 Å,[204] and ca. 1.92 Å to 2.24 Å[205]). Another observed non-covalent interaction that contributes to the stability of the structures is the Au–H bond which is again slightly longer than the average distance reported in the literature (ca. 2.60 Å to 2.87 Å,[206] and ca. 2.83 Å to 3.01 Å,[207] see structure #3 in Figure 3.10). It is noteworthy that the hyperconjugation interaction between the non-bonding electron pair of S and O atoms with the abundant free orbitals in Au has the largest contribution to the stability of the most stable structure in all complexes (see the most stable structures in Figures 3.6 to 3.14). The general trend observed from all of the most stable structures is that as the number of binding interactions increases, the stability of the complex increases. Regarding solvent effects, we can conclude that as the polarity of the solvent increases the distance between the DTF and Au_n increases. As a result, the total volume of the supramolecular assembly increases. In this section, we have also correlated the relative stability of a structure to the number of the attractive interactions. However, we will later discuss how Quantum Theory of Atoms in Molecule (QTAIM) can help us understand that the higher number of interactions does not necessarily determine the relative stability of a structure. Instead, the nature of the interactions is an important factor that should be taken into serious consideration.

3.3.9 Analysis of binding energies

With the optimized structures and energies of various Au_n/DTF complexes obtained, the binding Gibbs energies ($\mathit{\Delta} G_{binding}$) of the most stable structures for these systems were subsequently calculated. In our calculations, the $\mathit{\Delta} G_{binding}$ was calculated by the following equation,

$$\mathit{\Delta} G_{binding} = G_{complex} - G_{Au} - G_{DTF}$$

where $G_{complex}$, G_{Au}, and G_{DTF} are the Gibbs energies of Au_n/DTF complex, Au_n cluster, and DTF in their lowest-energy structures.

Figure 3.15 compares the binding energies of the most stable Au_n/DTF complexes, in which the size of the Au_n clusters vary from n = 3 to n = 10. As can be seen from this Figure, the binding energies show significant fluctuations between the complexes where the number of Au atoms are either odd or even. In general, the binding energies of complexes with odd numbers of gold atoms are much stronger than those containing even-number of gold atoms. The gold atom has a half-filled 6s orbital. It is therefore reasonable to anticipate that the complexation of a DTF radical cation with an odd-number gold cluster would form a closed-shell electron configuration to gain better stability. The binding of a DTF radical cation with a gold cluster containing an even number of gold atoms should lead to an open-shell system and hence is relatively less stable than a closed-shell system.

It can also be seen in Figure 3.15 that, for relatively small Au_n/DTF complexes (n = 3–6), the solvent exerts little effect on the binding energy; however, when the Au_n cluster grows larger (n = 7 and above), solvation contributes to stronger binding than in the gas phase. Among the Au_n/DTF complexes examined, the Au_9/DTF complex shows the greatest binding Gibbs free energy in the gas phase as well as in various solvents.

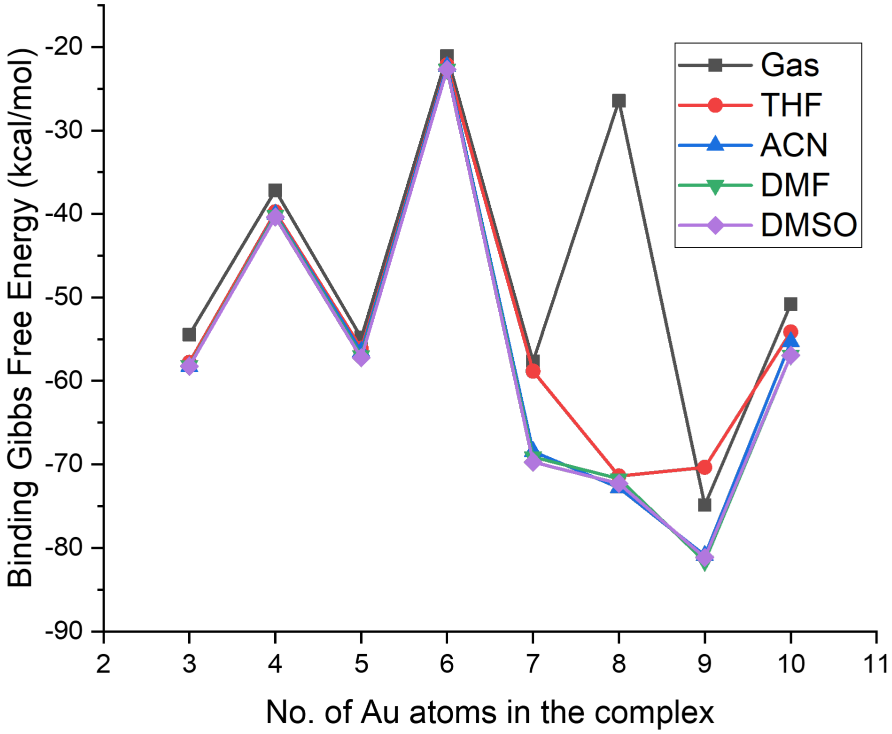

Figure 3.15: Binding Gibbs free energy of Au/DTF complexes in terms of the number of gold atoms.

3.3.10 Charge transfer analysis

As discussed above, the interactions of DTF with Au_n clusters result from various types of intermolecular forces, among which the transfer of charge from DTF to the

Au_n cluster was anticipated to play a significant role. To elucidate the charge transfer mechanism, it is imperative to consider the oxidation states of each constituent. According to previously published experimental results, gold is introduced into the system in the form of a salt, resulting in a non-zero oxidation state (e.g., Au(III) in $HAuCl_4$).[187] Conversely, the DTF moiety is present in its neutral state. However, during the electrochemical reaction, the gold undergoes reduction, resulting in the formation of gold nanoparticles that become stabilized by the oxidized DTF moiety (i.e. DTF radical cation). As a consequence, the gold attains a zero oxidation state while DTF exists in its radical cationic form. Subsequently, upon formation of the Au_n/DTF complex, the DTF moiety contributes one positive charge to the overall complex. Our computational analysis has quantified the extent of charge transfer from DTF to the AuNPs, as depicted in Figure 3.16. Considering that the total charge of the Au_n/DTF complex is unity, the magnitude of charge transfer ranges from 0.00 (indicating no transfer of charge from DTF to AuNP) to 1.00 (representing complete transfer of the positive charge from DTF to the AuNP cluster). Our charge analysis was done according to a modified Hirshfeld population method. In the gas phase, there is a decrease in the charge transfer to the Au_n cluster after the Au_4/DTF complex. However, by increasing the number of gold atoms available, the amount of charge transfer to the Au_n cluster increases so that there is a maximum charge transfer present in the Au_8/DTF complex. In solvents, on the other hand, we observed a two-fold behavior. The general trend in solvents is the same as in the gas phase. In the bigger Au_n/DTF complexes, however, there is a slight difference between polar and non-polar solvents. In THF, 0.76 and 0.75 of the positive charge is transferred onto the Au_n moiety in Au_7/DTF and Au_9/DTF, respectively, which demonstrate the maximum amount of charge transfer. In contrast, the Au_8/DTF complex shows the maximum amount of charge transferred to the Au_n moiety in all polar solvents, with 0.84 of the charge transferred. In addition, the stability graph based on the Gibbs free energy of all systems shows that the Au_8/DTF complex is the most stable among the complexes with doublet spin multiplicity and the second most stable complex in all the studied systems after the Au_9/DTF complex. According to these results, one can conclude that the more the positive charge present in the Au_n moiety, the more stable the system is (Figure 3.16). The rationalization of the observed phenomenon can be attributed to the inherent electropositivity exhibited by metals, which serves as a key factor influencing their reactivity, behavior, and tendency to form partially cations.

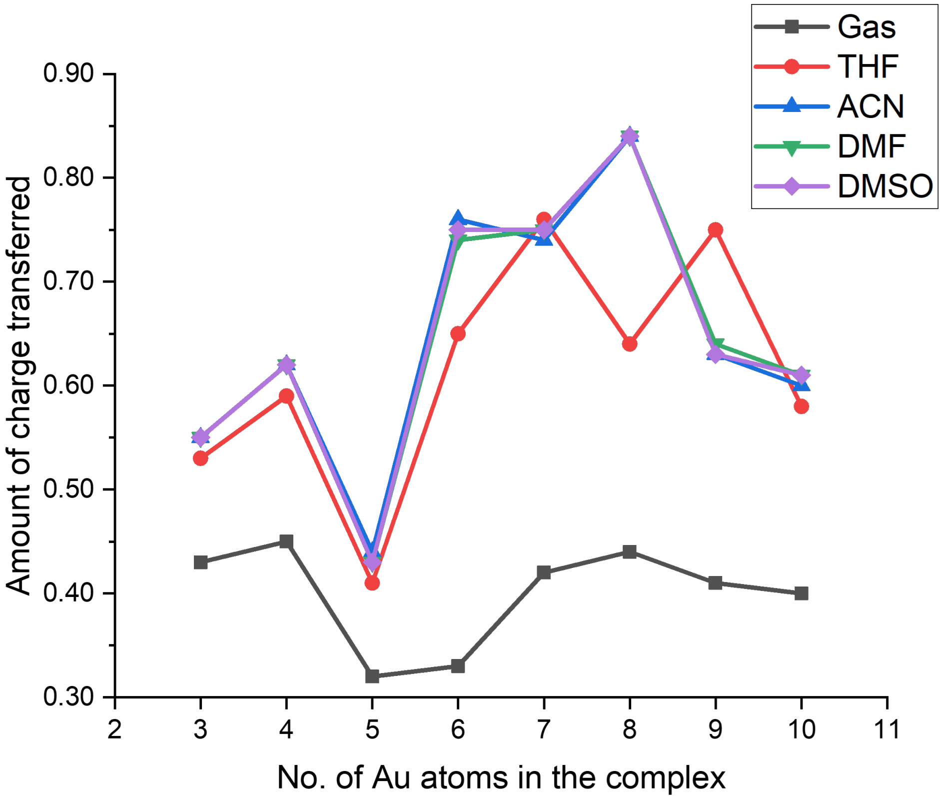

Figure 3.16: Amount of charge transferred from the DTF moiety to the Au_n cluster. 0.00 means all the positive charge is on the DTF, and 1.00 means all the positive charge is distributed on the Au_n cluster.

3.3.11 Non-covalent interaction analysis

3.3.11.1 Independent gradient model (IGM)

The Independent Gradient Model (IGM) is a new method for describing the nature of inter- or intra-molecular interactions based on analyzing the distribution of electron density.[208] It offers researchers a visual comprehension of the interactions occurring in chemical systems, similar to the well-established non-covalent interaction (NCI) method.[209] The electron density gradient is easily produced by summing the different gradient components that comprise the overall electron density gradient using absolute density values.[208] To visualize the results of IGM analysis, interaction isosurfaces are plotted to indicate the regions where significant non-covalent interactions occur. The isosurfaces are also colored by the RGB scheme, in which red color stands for strong repulsion, green color for van der Waals interactions, and blue color for strong attractive interactions.

Figures 3.17 and 3.18 show the results of IGM analysis on various Au_n/DTF systems. It has been shown that as the Au_n cluster grows, attractive interactions increase between the DTF and Au_n moieties (i.e., increasing blue-colored regions on the interaction isosurfaces). The nature of these interactions can be classified as chalcogen-like interactions with the difference that the chalcogen acceptor is empty orbitals in the valence layer of the neighboring gold atoms,[210] H-bonding, and van der Waals interactions.

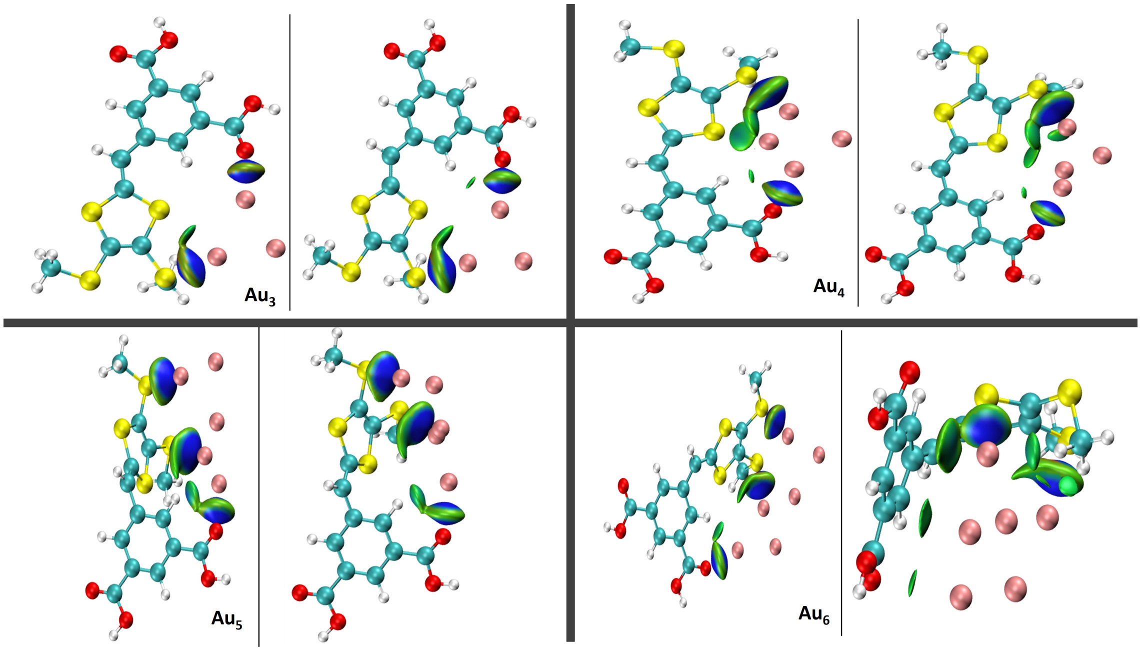

Figure 3.17: Independent gradient model of the Au$_3$/DTF to Au$_6$/DTF complexes. The picture on the left in each section is the IGM of the complex in the gas phase, and the one on the right is in DMSO (isosurface color coding in the range of -0.01 < $(\lambda_2) < 0.01$ au).

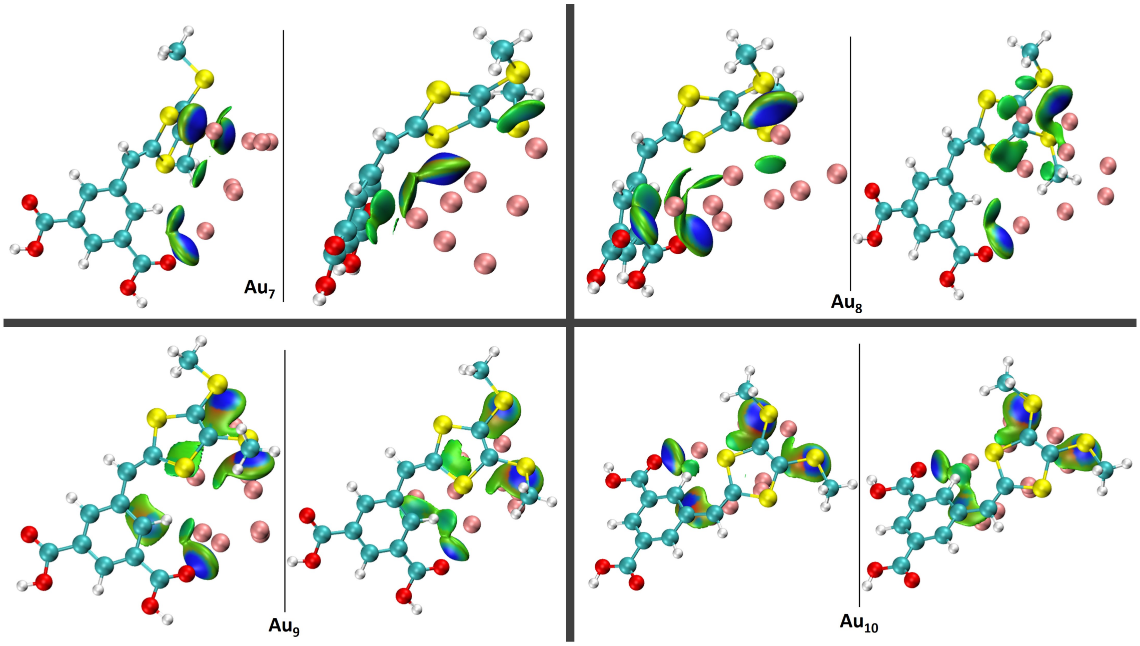

Figure 3.18: Independent gradient model of the Au_7/DTF to Au_{10}/DTF complexes. The picture on the left in each section is the IGM of the complex in gas, and the one on the right is in DMSO (isosurface color coding in the range of -0.01 < (λ_2) < 0.01 au).

3.3.11.2 QTAIM analysis

The Quantum Theory of Atoms in Molecules (QTAIM) is a powerful theoretical framework within the field of quantum chemistry that provides insights into the nature of chemical bonding and the electron density distribution in molecules. QTAIM was developed by Richard Bader in 1985,[211] building upon earlier works by others.[212] Bader's goal was to establish a rigorous mathematical description of chemical bonding based on the principles of quantum mechanics. At its core, QTAIM focuses on the analysis of the electron density, which can be partitioned into regions called "atoms in molecules", which are defined based on the topological properties of the electron density distribution. These atoms in molecules provide a localized description of the electronic structure, allowing for the characterization of individual atoms within a molecular system.[211] QTAIM employs the concepts of critical points, which are regions of space where the electron density and its associated properties exhibit significant changes. These critical points include the nucleus (where the electron density is greatest), bond critical points (indicating the presence of a chemical bond), and ring critical points (highlighting the presence of delocalized electron density within a ring).[211,213] By analyzing the topological features of the electron density and the associated critical points, QTAIM offers a detailed understanding of chemical bonding, intermolecular interactions, and the distribution of charge within molecules.[214,215]

The electron density (ED) distribution of a molecular system is generally recognized as the physical expression of the forces acting inside the molecular system.[211,213] The attractive forces of nuclei control the essential topological aspects of the ED of a multi-electronic system. The ED is a local maximum only at the site where a nucleus is located. With the use of local maxima displayed by the ED at the nuclei, it is possible to detect atomic shapes inside molecules. Figure 3.19 depicts the ED distribution, ED relief map, and molecular graph of benzene, which clearly illustrate the presence of local maxima at nuclear positions.[215]

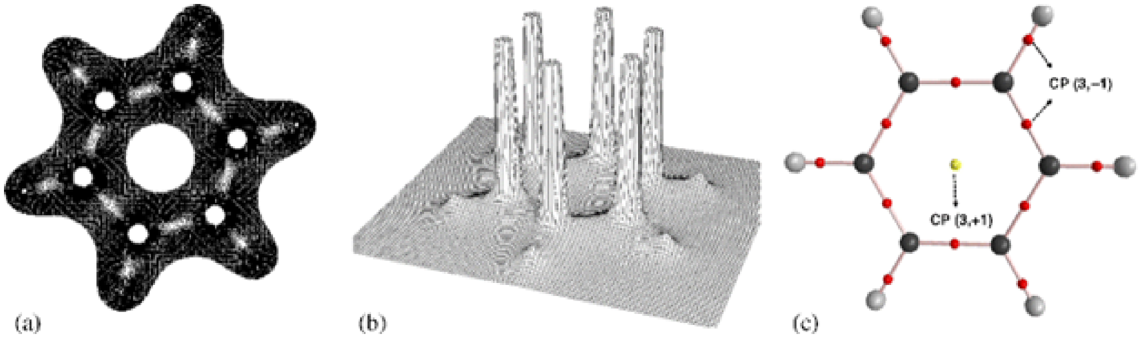

Figure 3.19: (a) Electron density contour map, (b) relief map, and (c) molecular graph of benzene. Adapted from *J. Chem. Sci.* **2016**, *128*, 1527–1536 with permission.

Figure 3.19 indicates that the ED has maxima, minima, and saddle points in space. These exceptional spots are known as critical points (CPs). The first derivatives of $\rho(\mathbf{r}_c)$ disappear at this point, i.e., $\nabla\rho(\mathbf{r}_c) = 0$, where $\nabla\rho(\mathbf{r}_c)$ is provided in Equation 3.1 and r_c is the CP.

$$\nabla\rho(\mathbf{r_c}) = \mathbf{i}\frac{\partial\rho}{\partial x} + \mathbf{j}\frac{\partial\rho}{\partial y} + \mathbf{k}\frac{\partial\rho}{\partial z} \tag{3.1}$$

At this stage, the sign of the second derivative of $\rho(\mathbf{r}_c)$ determines whether a maximum, minimum, or extremum exists. As a result, the second-order derivatives of ED must be determined. There are nine second-order derivatives for any set of coordinate axes. It is expressed as a real and symmetric matrix known as the Hessian of $\rho(\mathbf{r}_c)$. With the use of unitary transformation, it may be diagonalized to produce eigenvalues; λ_1, λ_2, and λ_3 which are the main axes of curvature since the magnitude of the three calculated second derivatives of $\rho(\mathbf{r}_c)$ are extremized with respect to any of these axes.

$$\nabla^2\rho(\mathbf{r_c}) = \frac{\partial^2\rho}{dx^2} + \frac{\partial^2\rho}{dy^2} + \frac{\partial^2\rho}{dz^2} \tag{3.2}$$

Generally, according to Bader's quantum theory of atoms in molecules (QTAIM), the classification and quantification of chemical bonds in isolated species and molecular crystals can be achieved by examining the characteristics of the bond critical points within the electron density, both theoretically and experimentally.[216] Atomic interactions can be broadly categorized into covalent, partially covalent, and weak interactions (e.g. van der Waals interactions).[217–228] The key disparity between the two extreme types of interactions, namely covalent and weak interactions, lies in the electron density features observed at the bond critical point. These features include the electron density magnitude (ρ), the sign of the Laplacian of electron density ($\nabla^2\rho$), and the energy density ($H_b(\mathrm{r}) = G_b(\mathrm{r}) + V_b(\mathrm{r})$), where $G_b(\mathrm{r})$ and $V_b(\mathrm{r})$ represent the kinetic and potential energy densities, respectively.[216,229] Based on the aforementioned quantities, each kind of interactions can be classified quantitatively,[226] so that covalent interactions are characterized by $\rho \geq 0.14$ au, $\nabla^2\rho < 0$, and $H_b(\mathrm{r}) < 0$, whereas weak interactions exhibit $\rho \leq 0.05$ au, $\nabla^2\rho > 0$, and $H_b(\mathrm{r}) > 0$. In addition, any interactions with $\nabla^2\rho > 0$ and $H_b(\mathrm{r}) < 0$ can be classified as an intermediate interaction.[216,226,229]

Moreover, the CPs are identified as (ω, σ), where ω denotes the CP's rank, and σ

denotes its signature. The total number of non-zero eigenvalues (non-zero curvatures of $\rho(\mathbf{r_c})$ at the CPs), determines the rank of a CP, while its signature is the algebraic sum of the signs of its eigenvalues with respect to x, y, and z (or the signs of the curvatures of $\rho(\mathbf{r_c})$ at the CPs).[230] The (ω, σ) of a CP can be one of four different possible values, including (3, -3), (3, -1), (3, +1), and (3, +3). All curvatures in the situation of (3, -3) are negative, and ρ has a local maximum at r_c. The two curvatures for (3, -1) are negative, and ρ is at its maximum at r_c in the plane delineated by their corresponding axes. Additionally, ρ is a minimum at a CP along the third axis, which is perpendicular to this plane. In the case of (3, +1) CP, there are two positive curvatures, and ρ on the plane delineated by their corresponding axes, is at its minimum at the CP. Moreover, ρ is a maximum at a CP along the third axis, which is perpendicular to this plane. The (3, +3) CP denotes that ρ at r_c is a local minimum, and all curvatures are positive.[211,213]

With the basic concepts of the AIM theory clarified, the outcomes of the QTAIM analysis performed on various Au_n/DTF complexes will be discussed. The QTAIM calculations show that as the Au_n cluster size increases, carbon atoms also contribute to the stability of the complex along with oxygen and sulfur atoms. What can be seen from our QTAIM analysis is that the factor that plays the most important role in the stability of the whole Au_n/DTF complex is the quality of the newly formed non-covalent interactions (see Figures 3.20 to 3.23).

According to the QTAIM results for $\mathrm{Au_3}$/DTF, only the $\mathrm{Au_1}$–$\mathrm{S_1}$ bond can be characterized as possessing partial covalent characteristics while the remaining bonds are identified as van der Waals interactions (Figure 3.20).

Bond type	d (Å)	ρ	$\nabla^2\rho$	$H_b(r)$	$G_b(r)$	$V_b(r)$
$Au_1…S_1$	2.514	0.066	0.179	-0.012	0.057	-0.069
$Au_1…S_2$	3.341	0.012	0.037	0.001	0.008	-0.008
$Au_2…O_1$	2.325	0.048	0.268	0.001	0.066	-0.064
$S_2…H_1$	2.508	0.015	0.048	0.001	0.011	-0.010

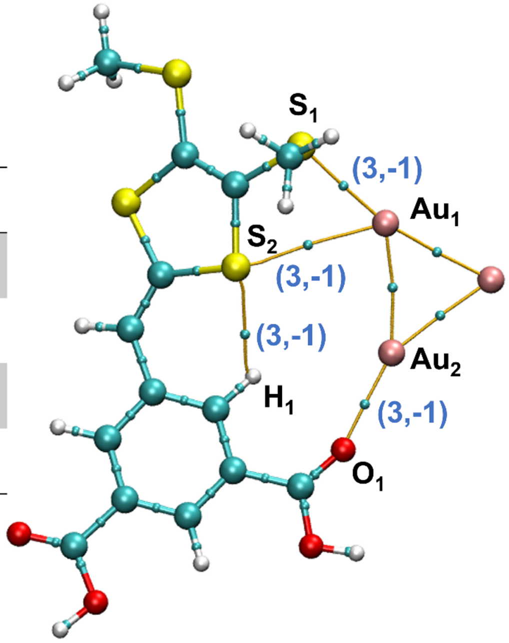

Figure 3.20: Bond nature description based on the QTAIM analysis of the Au_3/DTF complex (calculated in DMSO).

Similarly to the Au_3/DTF, the QTAIM results for Au_4/DTF showed that only one bond is in the partially covalent class (Au_1–S_1), and the rest are categorized as van der Waals interactions (Figure 3.21). In this case, however, the number of attractive interactions is more than that in the Au_3/DTF.

Bond type	*d* (Å)	ρ	$\nabla^2\rho$	$H_b(r)$	$G_b(r)$	$V_b(r)$
Au_1…S_1	2.547	0.062	0.170	-0.011	0.053	-0.063
Au_1…S_2	3.349	0.011	0.036	0.001	0.008	-0.007
Au_2…S_2	3.417	0.013	0.031	0.000	0.008	-0.007
Au_2…H_1	2.774	0.010	0.029	0.000	0.007	-0.006
Au_3…O_1	2.384	0.043	0.228	0.001	0.056	-0.055
S_2…H_2	2.453	0.016	0.049	0.001	0.011	-0.010

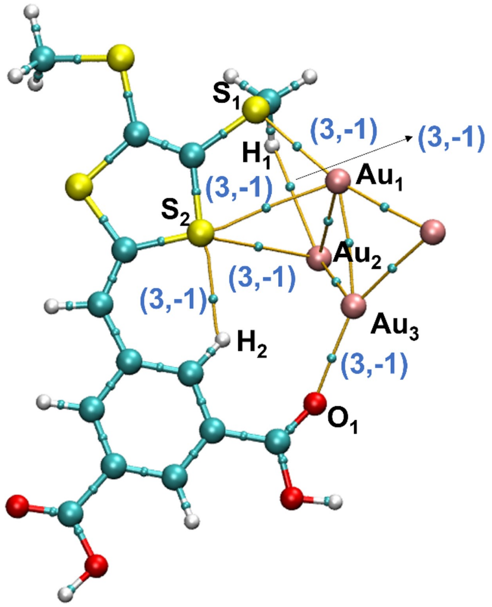

Figure 3.21: Bond nature description based on the QTAIM analysis of the Au_4/DTF complex (calculated in DMSO).

As previously discussed, the augmentation in the number of gold atoms within the complex corresponds to a proportional increase in the quantity of attractive interactions. Consequently, Figure 3.22 illustrates the presence of seven van der Waals interactions and two bonds (i.e. Au_4–S_3 and Au_5–S_4) characterized as partially covalent in the Au_9/DTF system.

Bond	*d* (Å)	ρ	$\nabla^2\rho$	$H_b(r)$	$G_b(r)$	$V_b(r)$	Bond Type
Au_1…C_1	3.182	0.011	0.037	0.001	0.008	-0.007	(3,-1)
Au_2…H_1	2.753	0.010	0.031	0.001	0.007	-0.006	(3,-1)
Au_2…O_1	2.674	0.025	0.107	0.001	0.026	-0.025	(3,-1)
Au_3…S_1	3.705	0.008	0.021	0.000	0.005	-0.005	(3,-1)
Au_3…S_2	3.774	0.007	0.018	0.000	0.004	-0.004	(3,-1)
Au_3…C_2	3.489	0.007	0.023	0.001	0.005	-0.004	(3,-1)
Au_4…S_3	2.672	0.048	0.136	-0.006	0.040	-0.046	(3,-1)
Au_5…S_4	2.901	0.031	0.086	-0.002	0.024	-0.026	(3,-1)
S_1…H_1	2.520	0.015	0.045	0.001	0.010	-0.010	(3,-1)

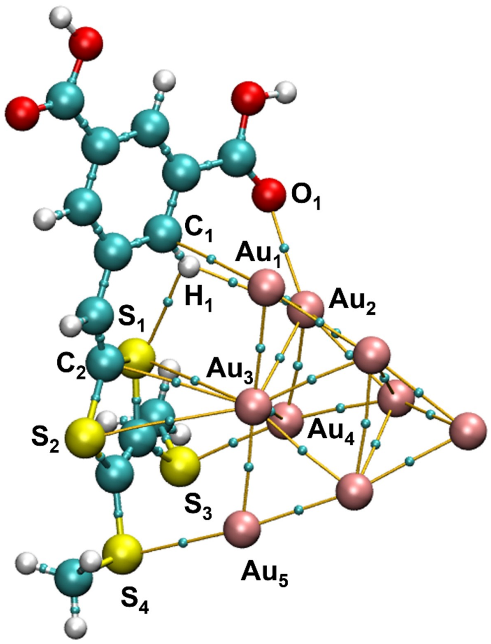

Figure 3.22: Bond nature description based on the QTAIM analysis of the Au_9/DTF complex (calculated in DMSO).

In case of Au_{10}/DTF, there are six van der Waals interactions and two bonds with partial covalent character, including Au_4–S_1 and Au_5–S_2 (Figure 3.23).

Bond	*d* (Å)	ρ	$\nabla^2\rho$	$H_b(r)$	$G_b(r)$	$V_b(r)$	Bond Type
$Au_1 \ldots C_1$	3.041	0.015	0.050	0.001	0.011	-0.010	(3,-1)
$Au_2 \ldots O_1$	2.637	0.026	0.117	0.001	0.028	-0.028	(3,-1)
$Au_2 \ldots H_1$	2.839	0.008	0.027	0.001	0.006	-0.005	(3,-1)
$Au_3 \ldots S_3$	3.866	0.006	0.016	0.000	0.003	-0.003	(3,-1)
$Au_3 \ldots S_4$	4.051	0.005	0.011	0.000	0.003	-0.002	(3,-1)
$Au_4 \ldots S_1$	2.677	0.047	0.135	-0.006	0.039	-0.045	(3,-1)
$Au_5 \ldots S_2$	2.833	0.035	0.099	-0.003	0.027	-0.030	(3,-1)
$S_3 \ldots H_1$	2.462	0.016	0.048	0.001	0.011	-0.011	(3,-1)

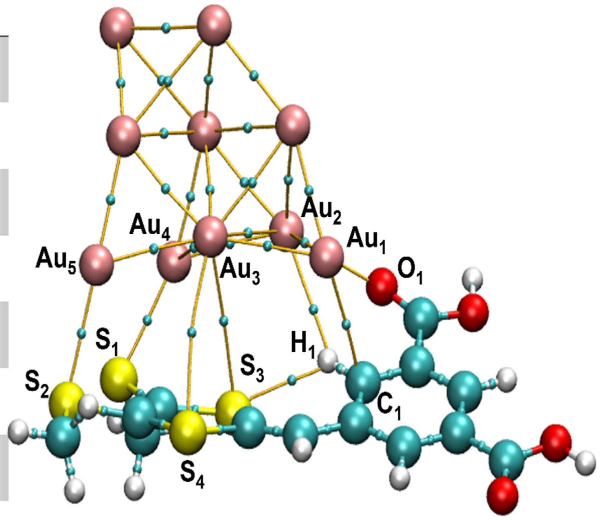

Figure 3.23: Bond nature description based on the QTAIM analysis of the Au_{10}/DTF complex (calculated in DMSO).

For QTAIM results of the remaining complexes, please refer to the Supporting Information of Chapter 3, provided in the Appendix.

3.3.12 Electronic transition properties of Au_n/DTF complexes

As mentioned in the introduction section, four different carboxylated DTFs and TTFVs have been previously synthesized and investigated as reducing agents for converting Au(III) into AuNPs in organic media. Among them, a carboxylated DTF (specifically referred to as DTF in this chapter) was found to produce AuNPs efficiently.[187] The previous sections of this chapter disclose the nature of Au_n/DTF interactions by DFT calculations, offering an in-depth understanding of the mechanisms for DTF-induced AuNP formation. Experimentally, the formation of AuNPs was examined by UV–Vis analysis. There are many spectral features in our experimental UV data which could not be clearly interpreted. To shed light on this, we have conducted TD-DFT calculations on various Au_n/DTF systems, focusing on understanding the physical origins of the electronic transitions involved in these supramolecular systems.

Figure 3.24 illustrates the experimental UV–Vis spectra of the mixture of AuNPs/DTF. The blue-colored absorption trace is due to AuNP/DTF (the product of the reaction of **1b** (DTF) and $\mathrm{HAuCl_4}$). In this spectrum, there are two significant electronic absorption peaks at 538 and 739 nm, the origins of which are to discussed here based on TD-DFT analysis.

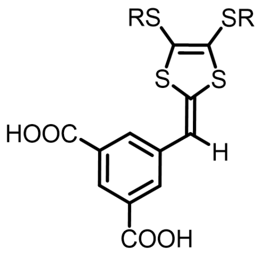

1b R = $C_{10}H_{21}$

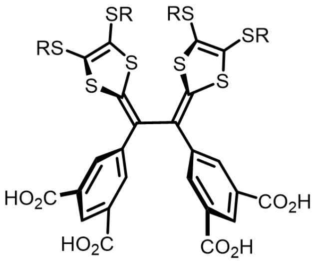

2b R = $SC_{10}H_{21}$

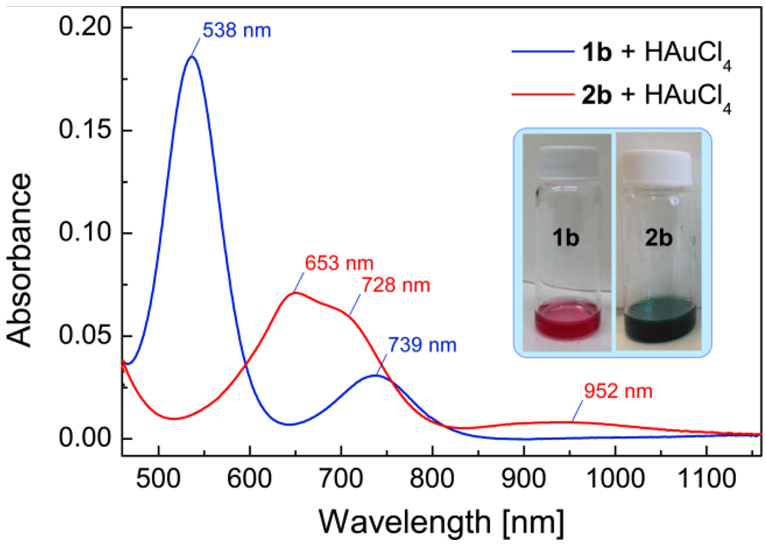

Figure 3.24: Experimental UV–Vis spectra of the DMSO solutions resulting from mixing $HAuCl_4$ with DTF and TTFV derivatives **1a** and **2b**, respectively. Inset: photographic images of the solutions.

Some basic information about the electronic arrangement of AuNPs, DTF moiety, and their resulting Au_n/DTF complexes are worth mentioning before we enter into detailed discussions of their TD-DFT calculated electronic transition properties. In the electronic structure of Au (atomic number = 79), there are 78 paired electrons and one unpaired electron in the 6s orbital. Therefore, if the n of an Au_n cluster is an odd number, the cluster will be open-shell, and if n is an even number, the cluster will be closed-shell. On the other hand, as the neutral DTF plays the role of a reducing agent in interacting with $HAuCl_4$, a radical cationic DTF will be formed after DTF releases an electron to reduce Au(III). Hence the DTF associated with a Au_n cluster should take an open-shell electron configuration. Accordingly, we can conclude that in an Au_n/DTF complex, if n is an odd number, the Au_n/DTF will be a closed-shell complex, and if n is even, then the supramolecular system (Au_n/DTF) will be open-shell.

Figure 3.25 shows the TD-DFT simulated absorption spectrum for the carboxylated DTF in the radical cation form, while Figures 3.26 and 3.27 show the TD-DFT results for the Au_3/DTF to Au_{10}/DTF in the gas phase and in four different solvents, including THF, acetonitrile (ACN), DMF and DMSO.

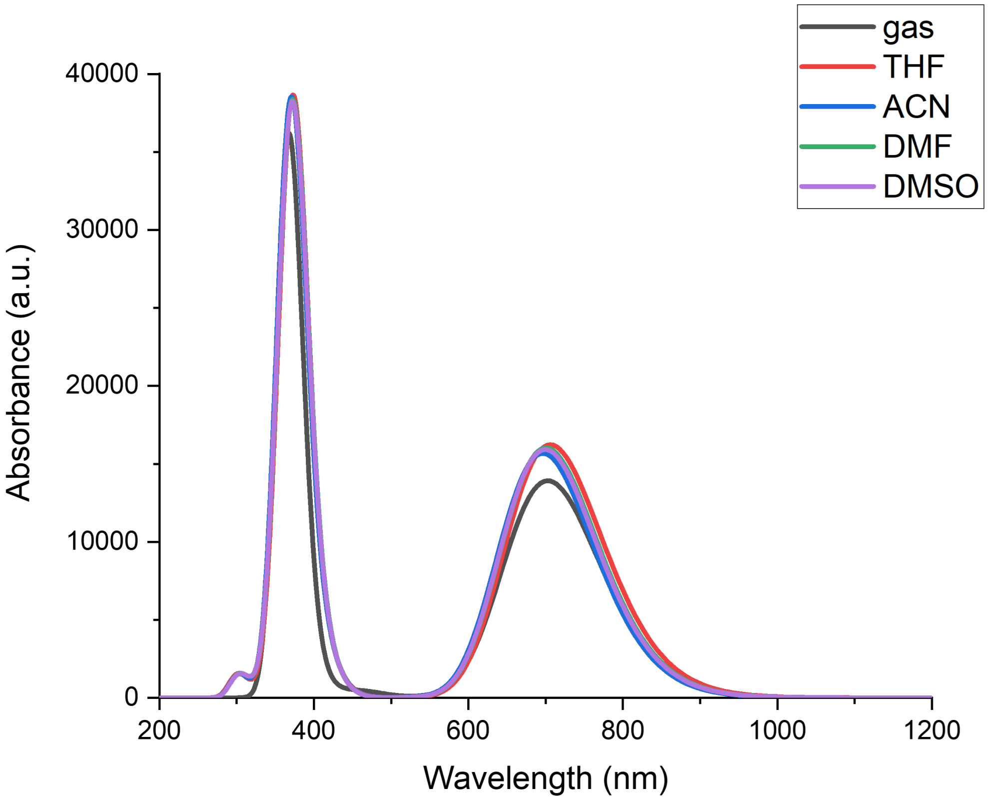

Figure 3.25: TD-DFT simulated UV–Vis absorption spectrum of carboxylated DTF radical cation.

When the n of Au_n/DTF is an odd number, the λ_{max} in the gas phase shifts toward shorter wavelengths as the size of the Au_n increases. λ_{max} shows a red-shift in solvents; for example, in Au_9/DTF in DMSO, an absorption occurs at 480 nm (Figure 3.26). For the open-shell complexes ($n = 4, 6, 8, 10$), a blue-shift in λ_{max} occurs in the gas phase upon increasing the size of the Au_n cluster and a red-shift in the solution phase; for instance, the λ_{max} in Au_{10}/DTF in DMSO is at 751 nm (Figure 3.27).

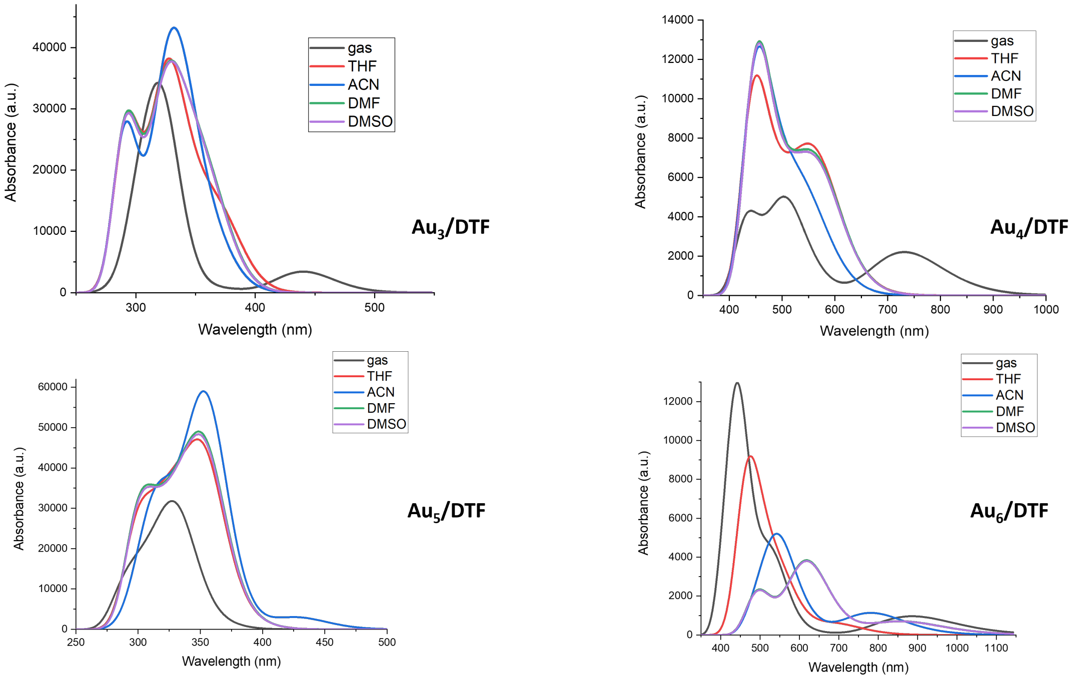

Figure 3.26: Simulated UV–Vis spectra of the Au_3/DTF to Au_6/DTF complexes.

According to the experimental results (Figure 3.24), the first peak at 538 nm can be attributed to the characteristic electronic transition of AuNPs. Based on our calculations in DMSO (the same solvent used in the experimental study), this peak is not related to the radical cationic DTF. Actually, the DTF radical cation is predicted to show an absorption peak at $\lambda_{max} = 699$ nm in DMSO, as a result of the SOMO to LUMO electronic transition (Figure 3.25). Therefore, the experimentally observed peak at 538 nm cannot be due to the DTF ligand. On the other hand, if n is odd in an Au_n/DTF complex, the Au_n/DTF will be a closed-shell system. As aforementioned, the simulated UV–Vis spectrum of Au_9/DTF (Figure 3.27) shows a λ_{max} at 480 nm, which is very close to the experimental result. Therefore, a question naturally arises; that is, which electronic transition is correlated to this peak? Is the electronic transition merely on the gold cluster, or is it an intermolecular charge transfer band?

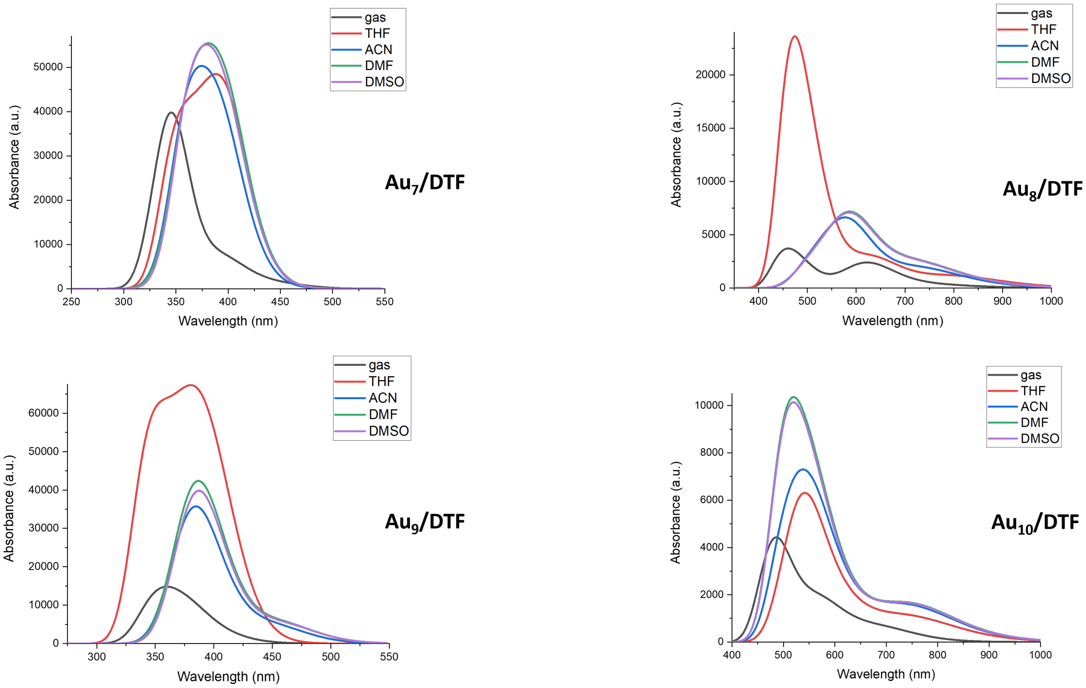

Figure 3.27: TD-DFT simulated UV–Vis absorption spectra of the Au$_7$/DTF to Au$_{10}$/DTF complexes.

Frontier molecular orbital (FMO) analysis has shed light on the nature of electronic transitions of interest. The maximum absorption wavelength in a closed-shell Au$_n$/DTF is majorly due to the HOMO to LUMO+1 transition, which occurs only on the gold cluster as HOMO, LUMO, and LUMO+1 are all distributed on the gold cluster with zero percent contribution made by the DTF moiety (Figure 3.28). According to our TD-DFT calculations, we can conclude that the peak at 538 nm in the experimental UV–Vis spectrum of the AuNP/DTF complex solution originates from the gold nanoparticles.

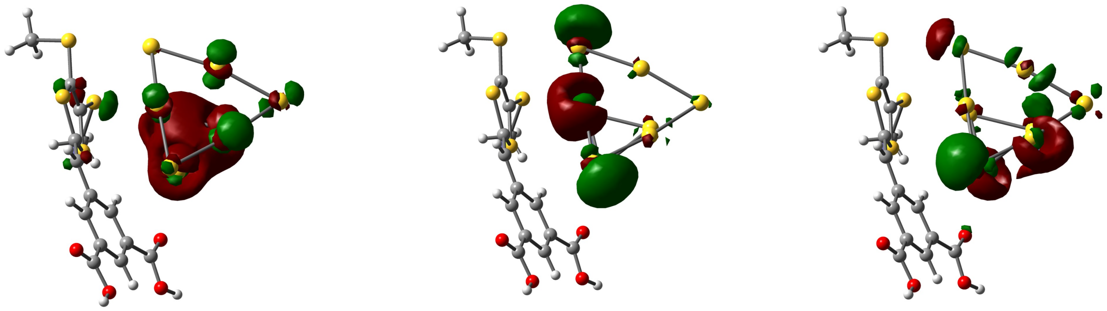

-5.861 ev
HOMO

-1.344 ev
LUMO

-1.315 ev
LUMO+1

Wavelength (nm)	Major contribs	Minor contribs
480	HOMO->L+1 (82%)	HOMO->LUMO (8%)
475	HOMO->LUMO (81%)	H-1->LUMO (3%), HOMO->L+1 (9%), HOMO->L+5 (2%)
436	HOMO->L+3 (82%)	HOMO->L+2 (5%), HOMO->L+5 (4%)

Figure 3.28: Frontier molecular orbitals of the Au_9/DTF complex in DMSO. The table shows the major and minor contributions of different electronic transitions to a specific absorption (L stands for LUMO and H denotes HOMO).

The following questions are, (i) what is the origin of the peak at 739 nm in the experimental UV–Vis spectrum (Figure 3.24)? ii) Why is its intensity much less than that of the peak at 538 nm? The simulated UV–Vis absorption spectrum of Au_{10}/DTF in DMSO shows a λ_{max} at 751 nm, which is fairly close to that of the experimental one (739 nm). Frontier molecular orbital analysis shows that the maximum absorption wavelength in an open-shell Au_n/DTF is majorly related to the SOMO to LUMO electronic transition, which occurs solely on the gold cluster as the HOMO, SOMO, and LUMO of the Au_n/DTF (if n is even) are all distributed only on the gold cluster (Figure 3.29). According to our TD-DFT studies, we can attribute the origin of the peak at 739 nm in the experimental UV–Vis spectrum to the AuNP/DTF complexes that take an open-shell configuration. The absorption peak at 538 nm, on the other hand, is due to the closed-shell AuNP/DTF systems in the solution. The closed-shell systems are more stable than the open-shell ones. It is therefore reasonable to propose that the closed-shell Au_n/DTF assemblies exist in a much greater abundance than the open-shell ones in the solution. As a result, the intensity of the peak due to the closed-shell systems (at 538 nm) was observed to be much stronger than that of the open-shell systems (at 739 nm).

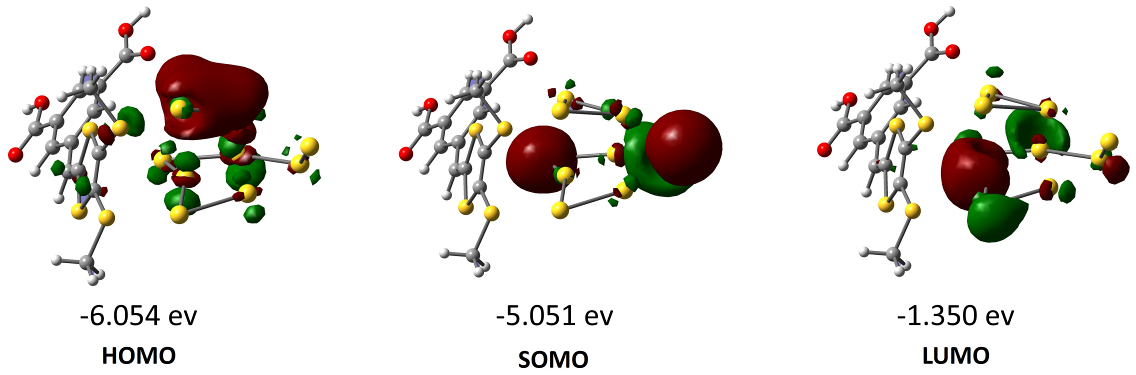

Wavelength (nm)	Major contribs	Minor contribs
801	HOMO->SOMO (87%)	SOMO->LUMO (3%)
751	SOMO->LUMO (78%)	SOMO->L+1 (7%)
662	H-1->SOMO (51%)	H-3->SOMO (20%)

Figure 3.29: Frontier molecular orbitals of the Au_{10}/DTF complex in DMSO. The table shows the major and minor contributions of different electronic transitions to UV–Vis absorption peaks.

3.4 Conclusions

The use of DTF derivatives to reduce Au(III) species has been experimentally demonstrated as a useful method for producing AuNPs in organic media. However, theoretical studies of the detailed mechanisms, especially the surface charge properties of the AuNPs, the nature of interactions between DTF and Au clusters, and solvent effects have not yet been conducted prior to the DFT studies in this chapter. Herein, we for the first time have carried out systematic investigations on the interactions of AuNPs with a representative DTF molecule. DTF can bind to the surface of AuNPs in the form of a radical cation rather than the neutral form. It has been found that the sulfur and oxygen atoms in the DTF moiety are the major active binding sites for interacting with the Au surface. Our TD-DFT calculations revealed that electronic transitions on the AuNP part dominate the UV–Vis absorption spectral patterns of AuNP/DTF complexes. We have also examined the effects of open-shell and closed-shell configurations on the UV–Vis absorption of Au_n/DTF complexes. Finally, it is worth remarking that solvents can critically influence the stability of DTF/AuNP assemblies and therefore deserve serious consideration in experimental practice. Overall, the DFT and TD-DFT studies described in this chapter offer useful guidance for further experimental exploration of AuNPs with controlled size and morphology as well as novel functionalities arising from the interactions of AuNPs and DTF ligands.

Chapter 4

Mechanistic Studies of the Oxidative Dimerization Reaction of Phenyl-substituted Dithiafulvene

4.1 Introduction

1,3-Dithiole can be readily oxidized to yield a 1,3-dithiolium cation that gains aromaticity and hence stability.[231–233] As a result, 1,3-dithiole exhibits excellent electron-donating ability and has been frequently used as a redox functional group in the development of organic electronic materials; for example, to yield the molecular structures of well-known organic donors, tetrathiafulvalene and its derivatives, which contain 1,3-dithiole groups connected through various π-conjugated bridges.[11,16,234–240] 1,4-Dithiafulvene (DTF) derivatives, particularly aryl-substituted dithiafulvenes (Ar-DTFs), have been studied as a class of redox-active molecular building blocks for diverse functional molecular materials and devices for more than twenty years.[59,241–243] Many Ar-DTF derivatives show facile oxidative dimerization (see Scheme 4.1).[17,34,44,46,237] In fact, the preparation of tetrathiafulvalene vinylogues (TTFVs), a different class of redox-active systems, is made simple and inexpensive by this type of atomically efficient C–C bond formation reaction. The superior electronic and redox-regulated conformational features of many TTFV-based molecular and supramolecular systems have led to applications in chemical sensors,[37,75,182] redox-active ligands,[42,181] functional nanomaterials,[85–87] molecular machinery,[186] and other molecular optoelectronic devices.

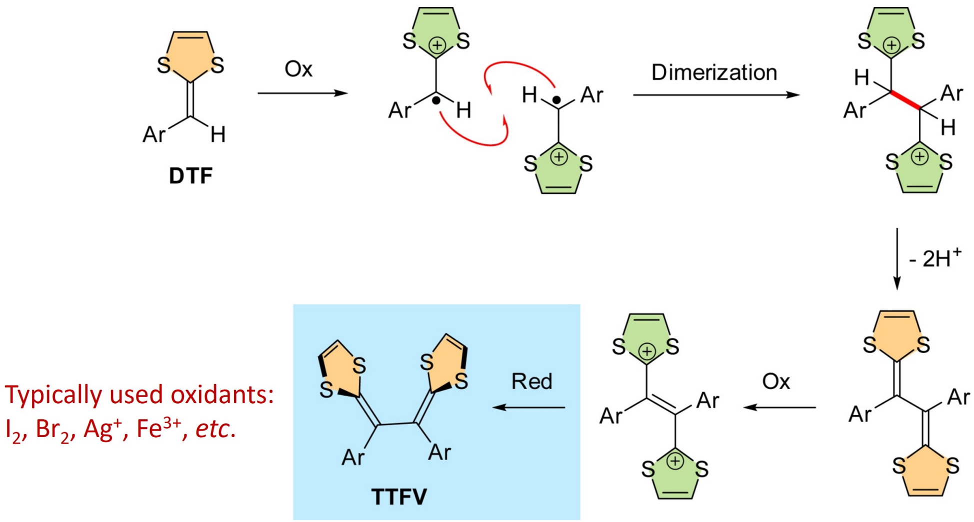

Typically used oxidants: I_2, Br_2, Ag^+, Fe^{3+}, *etc*.

Scheme 4.1: Suggested mechanism for the synthesis of TTFV and its derivatives via DTF dimerization.

The radical-cationic species ([**2**]$^{\bullet+}$ in Scheme 4.2) is produced when neutral tetrathiafulvene (**2**) first undergoes a one-electron oxidation.[244] Upon the second oxidation, a dication ([**2**]$^{2+}$) is produced. Due to the fact that both redox processes are entirely reversible and have unexpectedly low oxidation potentials (0.37 V and 0.74 V against Ag/AgCl in CH_3CN),[245] electrochemical switching is made possible.[246] The TTF system's stepwise aromatization can be used to explain the observed stability of the two oxidation states. TTF is composed of two pro-aromatic 1,3-dithiolylidene rings joined by a C=C double bond in its neutral state. One ring becomes an aromatic 6-π electron system after the initial oxidation, and is a mixed-valence resonance stabilized structure. A second aromatic 1,3-dithiolium cation with 6-π electrons is produced by the second oxidation and then, both cations are joined by a single C–C bond. A mixed-valence (MV) compound comprises two or more electroactive moieties that exist in more than one formal oxidation state.[18,247] Mixed valency often results in electronic coupling between the sites with different formal charges, leading to the rapid oscillation of charge between them, a process known as intervalence charge transfer (IVCT). Each oxidation state in TTF can be observed via UV-Vis spectroscopy (Figure 4.2). A pale yellow solution comes from the spectrum of **2**, which only exhibits mild absorption above 350 nm. The transition between the molecule's HOMO to LUMO is the lowest-energy band. However, an orange-brown solution results from the radical-cation's ($\mathbf{2}^{\bullet+}$) two prominent absorption bands ($\approx$ 450 and 800 nm). Originally, it was thought that the low-energy band of $\mathbf{2}^{\bullet+}$ between 600 and 1000 nm was a sign of a stable TTF dimer.[247] Later research revealed that this band is an inherent SOMO-1 to SOMO transition in the radical cation.[248] The dication ($\mathbf{2}^{2+}$), which has a prominent band around 700 nm, produces a deep-blue solution. It is quite simple to observe the electrochemical switching of TTF because of these significant color changes, which vary for derivatives of TTF that have various substituents.[246]

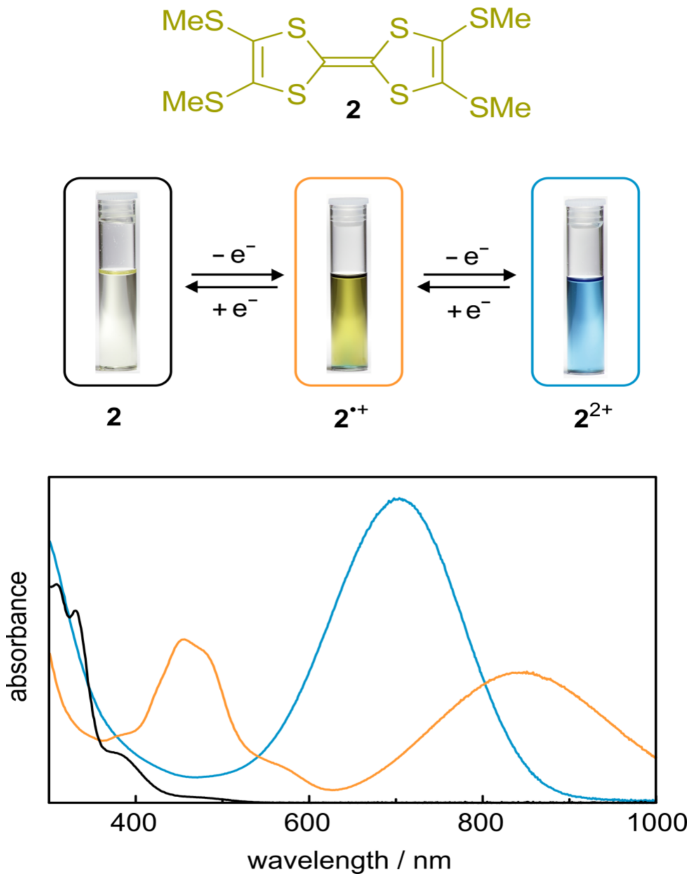

Scheme 4.2: UV-Vis spectrum of TTF demonstrating the presence of mixed-valence TTF compound in its three stable oxidation states (black line = **2**, orange line = $\mathbf{2}^{\bullet+}$, blue line = $\mathbf{2}^{2+}$). Picture adapted from *Beilstein J. Org. Chem.* **2018**, *14*, 2163–2185 with permission.

The presence of TTF in a mixed-valence oxidation state has motivated researchers to investigate more about its properties. Further studies have shown that mixed-valence TTF dimers, in which one monomer is a radical cation and the other is neutral, are inherently unstable, but they can still be characterized by using special methods, such as trapping the dimer in a molecular cage[249] (Figure 4.1) or a catenane (Figure 4.2).[18]

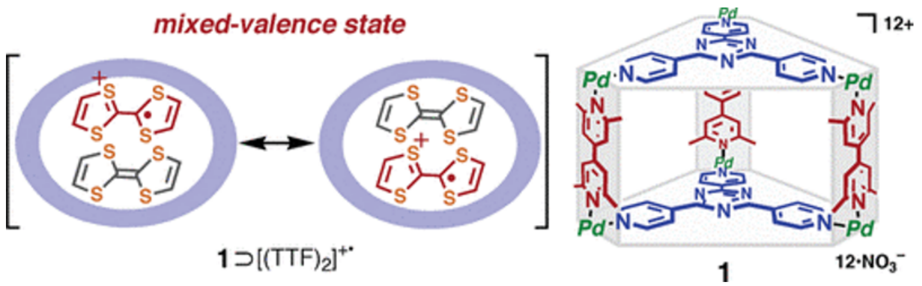

Figure 4.1: Trapping mixed-valence TTF dimers in molecular cages. Picture adapted from *J. Am. Chem. Soc.* **2005**, *127*, 13456–13457 with permission.

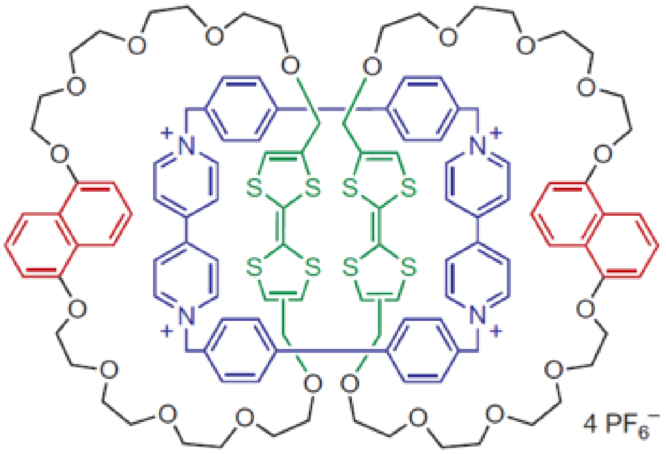

$\mathbf{2} \cdot 4PF_6$

Figure 4.2: Trapping mixed-valence TTF dimers in a catenane compound. Picture adapted from *Nat. Chem.* **2010**, *2*, 870–879 with permission.

The mixed-valency in TTF and its analogous compounds such as DTF led us to considering an important question regarding the DTF dimerization mechanism. Do two DTF monomers pass through a mixed-valence transition state to form a dimer or is the dimerization mechanism proposed by Hapiot *et al.* the predominant pathway? Does a stable mixed-valence intermediate exist as a separate stage in the DTF dimerization to afford TTFV? In this chapter, we have endeavored to answer these questions via DFT calculations and Atom Centered Density Matrix Propagation (ADMP) molecular dynamics simulations.

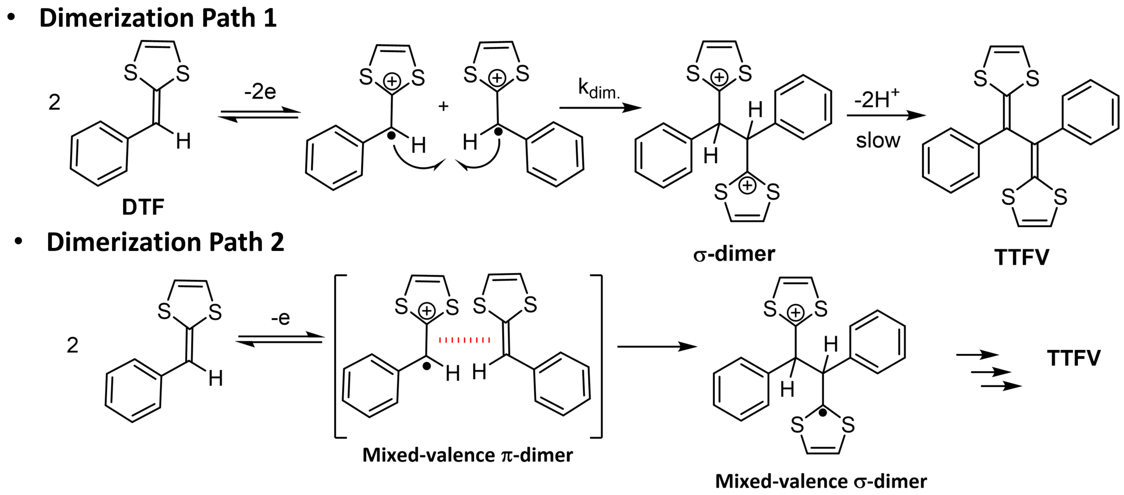

Figure 4.3: The mechanisms of DTF dimerization studied in this work.

4.2 Methodology

DFT calculations have been carried out using the Gaussian 16 software package.[188] The geometry of each compound, either as a monomer or a dimer, was optimized firstly via the semiempirical PM6 method[189] to find the best geometry around the global minimum and then using the University of Minnesota's hybrid functional (M06-2X)[129,190] with the Karlsruhe basis set of def2-SVP.[191,192] Following the optimization, each structure was subjected to vibrational analyses at the same level of theory to verify whether it is an energy minimum (no imaginary frequencies) or a transition state (one imaginary frequency). Solvent effects were analyzed using the continuum solvation model based on the charge density (SMD) developed by Truhlar et al.[195]

In addition, visualization of molecular structures and molecular orbitals was carried out via the CYLview[196] and the GaussView 6 software packages,[197] respectively. The Multiwfn program[198] was used for the topological analysis of electron density and visualizations were performed using VMD software package.[199] The energies of excitation and calculated excited-state properties were obtained through time-dependent density functional theory (TD-DFT)[142] using the Coulomb-attenuating method (CAM-B3LYP functional[250]) in conjunction with the 6-311++G(d,2p) basis set. In TD-DFT, only singlet to singlet transitions are calculated in order to save computational costs while maintaining the precision of the results. Simulated UV-Vis absorptions were generated by using the GaussSum[200] and OriginPro 8 software packages.[201] All the DFT calculations have been done at the temperature of 298.15 K and the pressure of 1.00 Atm.

4.3 Results and discussion

From the experimental point of view, diphenyl tetrathiafulvalene vinylogue (DP-TTFV) can be synthesized via a smooth oxidative dimerization reaction of phenyl dithiafulvene (Ph-DTF) monomers. Indeed, it has been widely considered that the two Ph-DTF monomers are first dimerized through oxidation before the dimerization happens.[76,77,89,251] In one mechanism investigated, TTFV is formed through the C–C bond formation of the two radical cations, and is called the dication (DC) pathway (Figure 4.3).

In this work, we have also investigated another dimerization mechanism which was inspired by the introduction of mixed-valence systems in the 1960s[252,253] along with the DC pathway. Accordingly, we proposed a second transition state-derived pathway for the Ph-DTF dimerization, in which the phenomenon occurs through the formation of a mixed-valence (MV) complex between a neutral and a radical cation of Ph-DTF monomer, which we designate as the mixed-valence (MV) pathway (Figure 4.3). Then, we evaluated which one is kinetically and thermodynamically favored. According to the mechanism proposed by Hapiot et al.[46] the oxidative dimerization of 1,4-dithiafulvene (DTF) consists of three steps: (1) electron transfer, which generates two radical cationic monomers. (2) The generated radical cations undergo a fast dimerization into a protonated dimer. (3) The protonated dication dimer deprotonates slowly to form tetrathiafulvalene vinylogues (TTFV, see dimerization path 1 in Figure 4.3). Indeed, our work has been focused on the second step of the mechanism proposed by Hapiot and co-workers. We considered this step as a sub-reaction and have investigated it in detail using transition state theory.

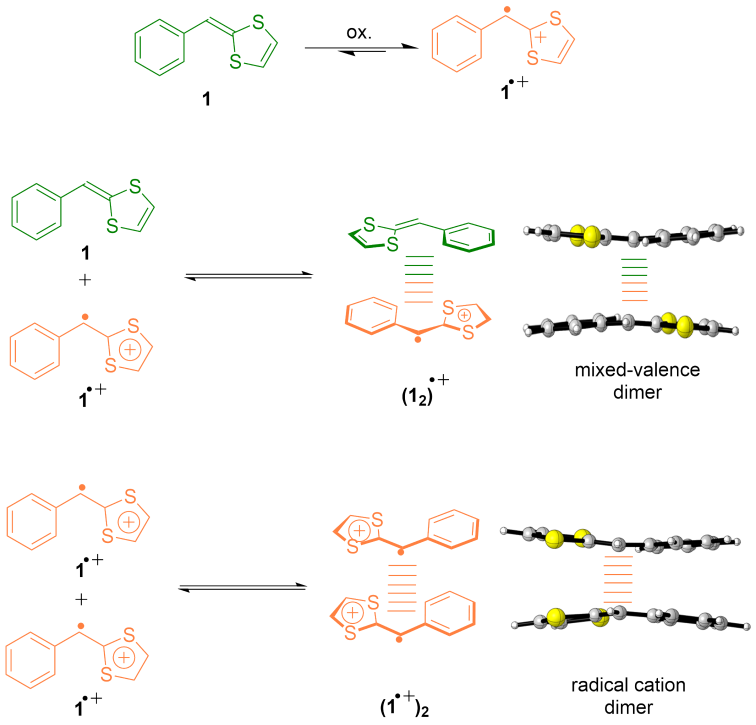

Scheme 4.3: Structure and conformations of the two complexations in vacuum, the mixed-valence dimer and the radical-cation dimer (Inspired by *Beilstein J. Org. Chem.* **2018**, *14*, 2163–2185.)

4.3.1 Mixed-valence (MV) pathway

As aforementioned, we considered two possible mechanisms for the dimerization step resulting in the protonated dimer. The first mechanism is the mixed-valence pathway in which one radical cation monomer gets close to a neutral monomer in order to make a mixed-valence complex.[246,254–259] On the other hand, the second mechanism is the direct dimerization of two radical cation monomers. While the two radical monomers are paramagnetic, their dimerized compound is diamagnetic due to radical pairing (i.e., singlet spin multiplicity). Following dimerization, the complex passes through a transition state to generate the protonated product (Scheme 4.3).

The MV pathway commences by stabilizing the two Ph-DTF units through complex formation (CX_{MV}) (see Figure 4.4). However, the stabilization energy decreases as the polarity of the medium increases so that in the gas phase the $\mathrm{CX}_{M}V$ is 8.03 kcal/mol more stable than the two separate monomers while this amount is decreased to 0.55 kcal/mol, and 0.37 kcal/mol in dichloromethane (DCM) and acetonitrile (ACN), respectively. The energy barrier for overcoming the transition state, on the other hand, is the least in the gas phase and the most in DCM (6.07 to 8.68 kcal/mol, respectively). Once the dimers pass their corresponding transition states, they form the protonated product, which in all cases, the energy levels of the products are more than that of the complex. It can be concluded that in spite of relative stabilization through complex formation especially in the gas phase, the MV pathway is endergonic, and indeed, ΔG is even more positive in solvents, demonstrating that the reaction is nonspontaneous both in the gas and the solution phases.

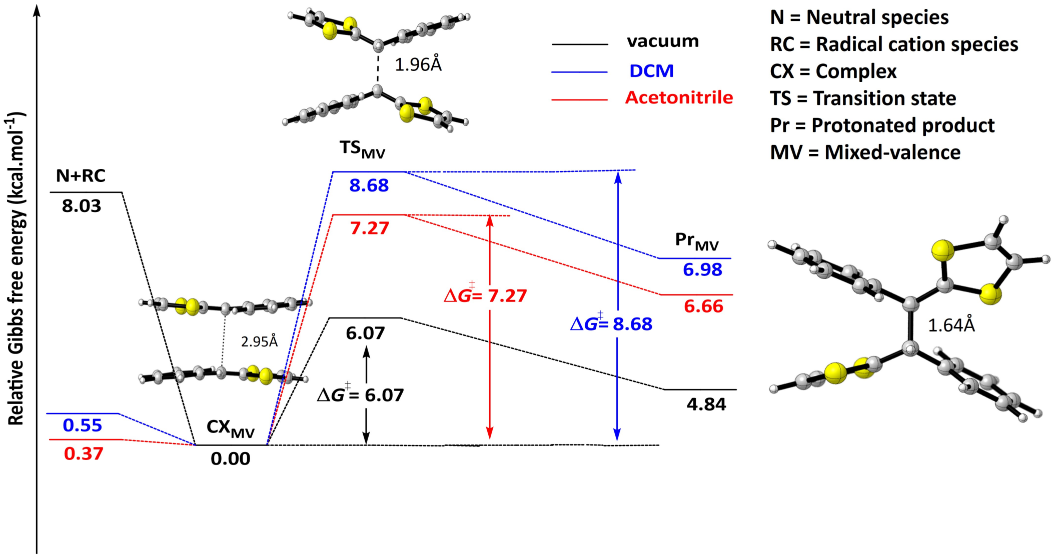

Figure 4.4: Potential energy surfaces for the MV dimer pathway.

To further examine the transition state, we have performed intrinsic reaction coordinate (IRC) calculations.[260–262] The IRC results proves that the dimerization through the MV pathway is endothermic (as the total energy is involved in this type of calculations) in both the gas phase and in solution (Figures 4.5 and 4.6).

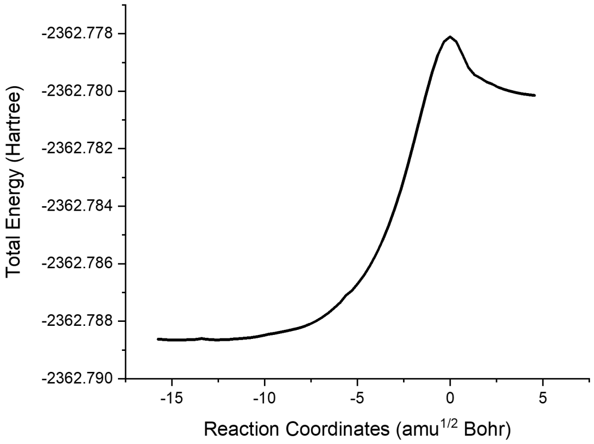

Figure 4.5: IRC trajectory of the MV dimer pathway in the gas phase.

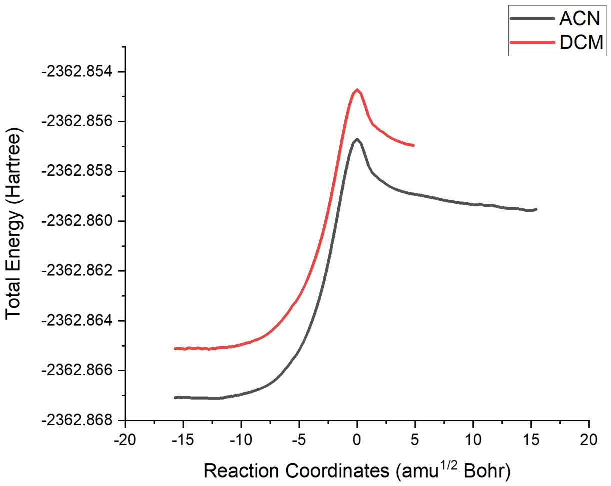

Figure 4.6: IRC trajectories of the MV dimer pathway in dichloromethane (DCM) and acetonitrile (ACN).

The Atom Centered Density Matrix Propagation molecular dynamics simulation (ADMP)[263–265] also shows that the two monomers in the MV pathway will separate from each other and don't have a tendency to make a dimer in the gas phase. In both solvents, however, they show oscillation between bond association and dissociation every *ca.* 80 fs (Figure 4.7). Therefore, our ADMP results also demonstrate that the MV pathway is not thermodynamically favored.

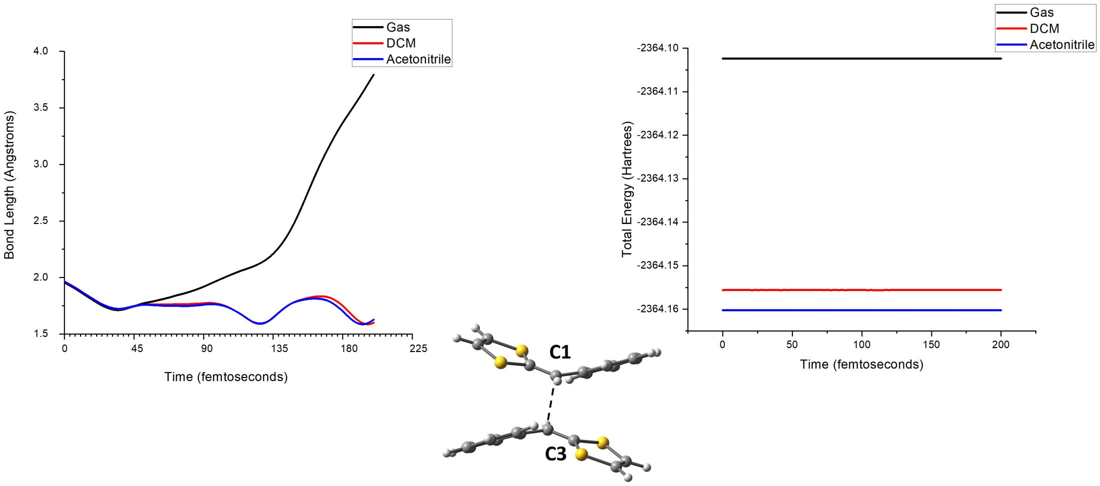

Figure 4.7: Time dependency of the C_1-C_3 bond length and total energy of the transition state of the mixed-valence π-dimer.

The molecular dynamics simulation of the product of the MV pathway also shows a fluctuation in the bond length of the two central carbons in the dimerized product, especially in the gas phase which again are in line with the previous results (Figure 4.8).

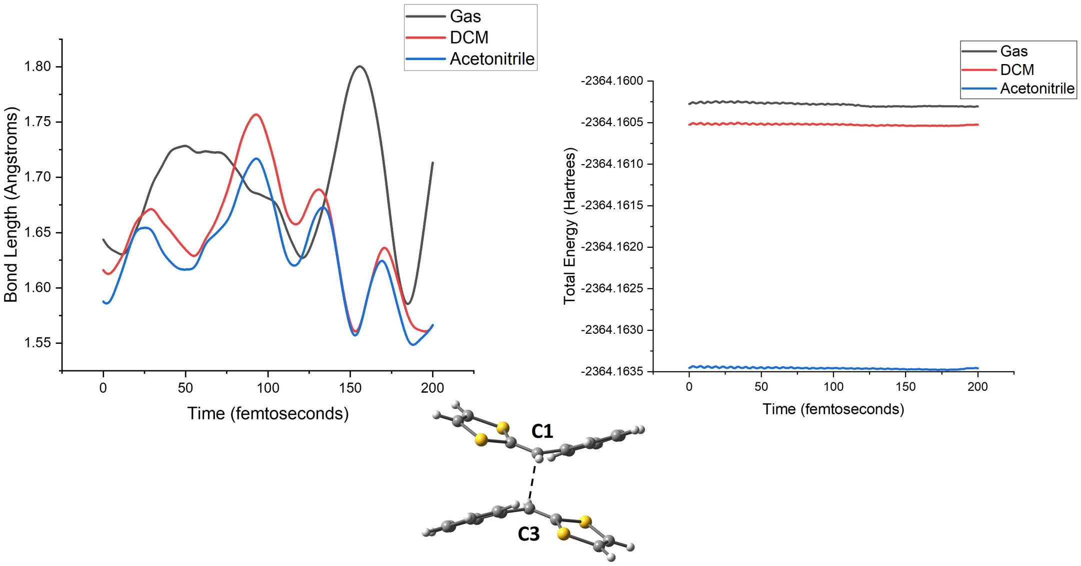

Figure 4.8: Time dependency of the C_1-C_3 bond length and total energy of the product of the mixed-valence π-dimer.

4.3.2 Dication (DC) pathway

The second mechanism deals with the combination of two radical cation monomers to form a dicationic dimer.[246] Our potential energy surface calculations proves that DC dimerization in the gas phase will not happen as the reaction is both thermodynamically and kinetically disfavored (refer to Figure 4.9). However, in the solution phase, the transition state energy barrier will decrease significantly, so that the reaction will be kinetically feasible both in dichloromethane and acetonitrile. Most importantly, the free energy levels of the protonated products in the both solvents are less than those of the reactants, making the DC pathway thermodynamically favored (Figure 4.9).

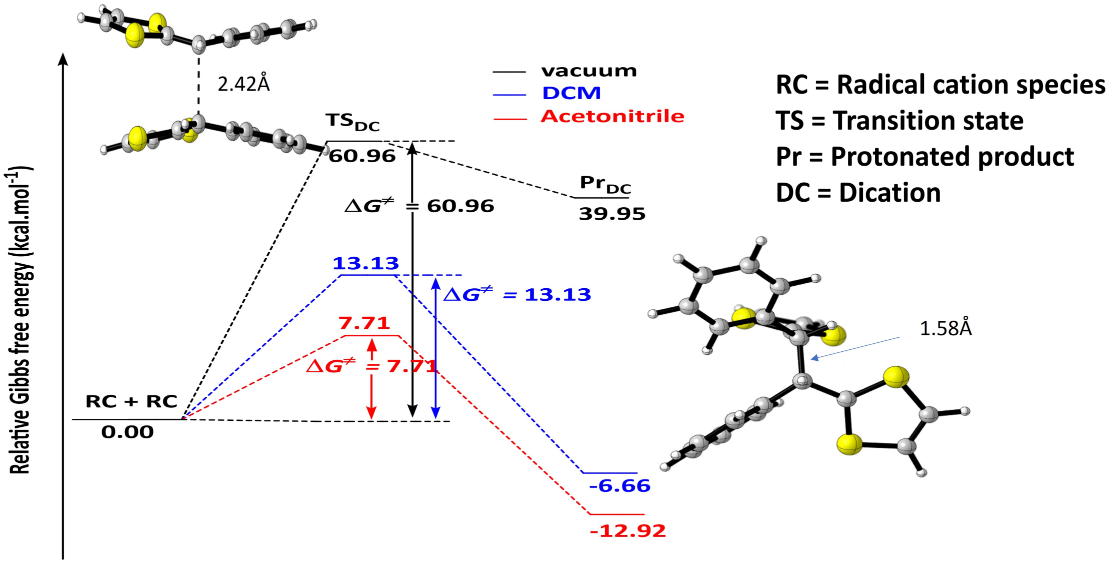

Figure 4.9: Potential energy surface of the DC dimer path.

The IRC results in the DC pathway are in line with the potential energy surface in both chosen solvents (Figure 4.11). The IRC profiles show the correlations between the total energy and intrinsic reaction coordinate of the DC dimer. These results indicate that the dimerization reaction in all media including the gas phase and in solution is exothermic (see Figures 4.10 and 4.11).

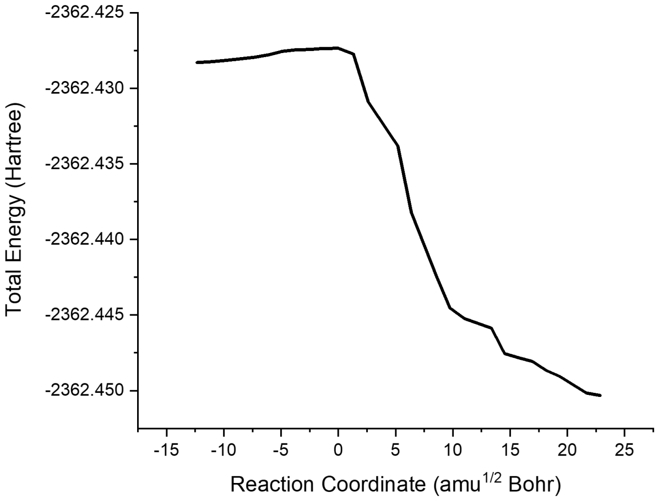

Figure 4.10: IRC trajectory calculated from the DC dimer transition state in the gas phase.

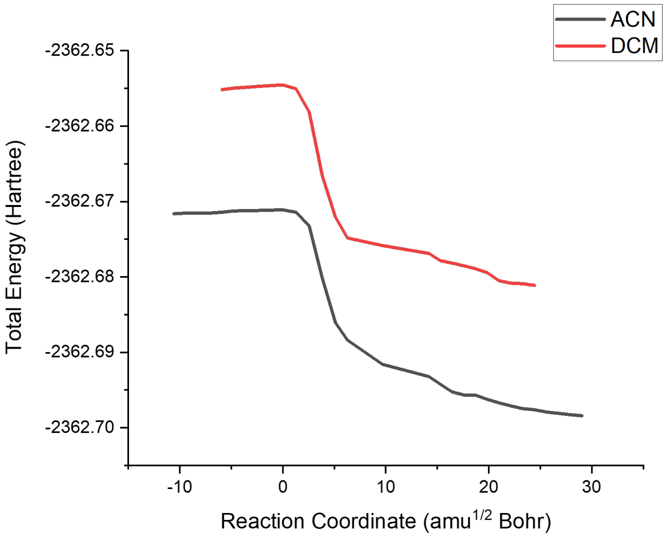

Figure 4.11: IRC trajectories calculated from the DC dimer transition states in dichloromethane (DCM) and acetonitrile (ACN).

We have considered both anti and syn constitutional isomers in the transition state studies as well as the IRC calculations. In both cases, the syn isomer is thermodynamically favored. However, we were not able to obtain a reasonable IRC for the anti isomer.

On the other hand, the ADMP calculations in the DC pathway for both syn and anti adducts led to different but interesting results. The ADMP simulations for the first 200 fs showed that the syn isomer is not favored kinetically as the two central carbons separate from each other as the time evolves (Figure 4.12).

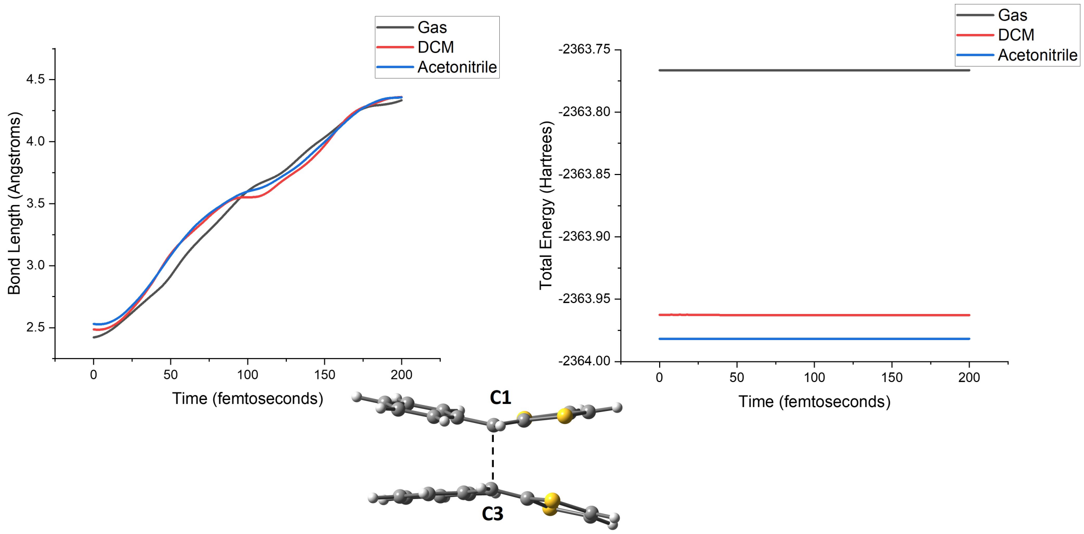

Figure 4.12: Time dependency of the C_1-C_3 bond length and total energy of the transition state of the syn isomer of the dication dimer.

However, the protonated product of the syn isomer shows a high degree of fluctuation in the bond distance between the two central carbon atoms so that at *ca.* 163 fs there is a minimum in this bond (1.51 Å), but exactly after 33 fs, this distance will rise to about 1.67 Å, which is longer than the average C–C single bond distance (Figure 4.13).

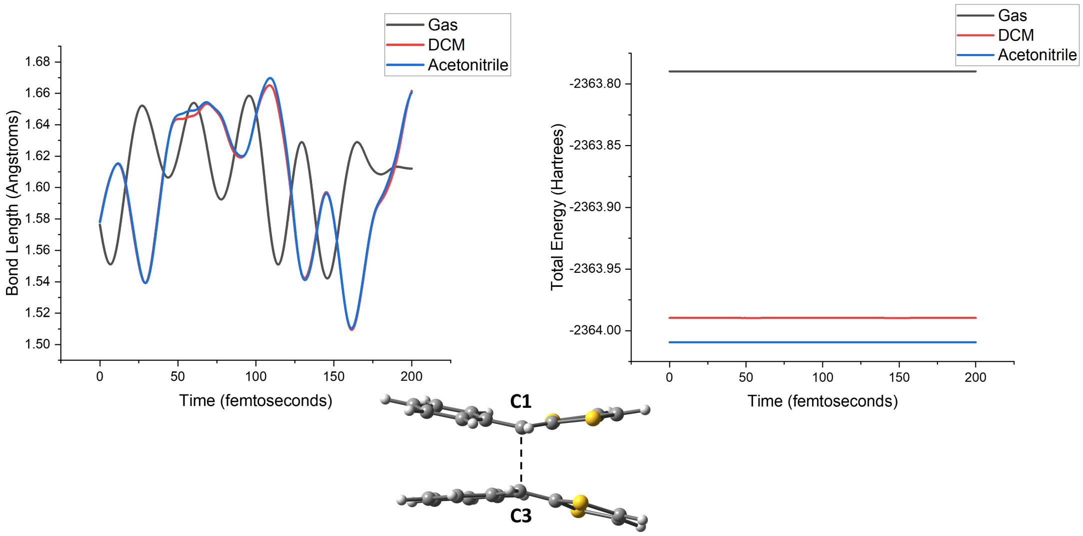

Figure 4.13: Time dependency of the C_1-C_3 bond length and total energy of the product of the syn isomer of the dication dimer.

The mechanism for the anti isomer, however, is different. Molecular dynamics simulations of the bond distance between the two central carbons show that the transition state in the gas phase leads to separation of the two monomers. In contrast, we observed a decrease in terms of time in bond distance of the two central carbons in the anti isomer which shows that the anti isomer is the one which is kinetically favored over the syn isomer based on the ADMP calculations (Figure 4.14, left graph). The bond distance in the product of the anti isomer shows a lesser degree of fluctuations in the course of time (between 1.54 to 1.64 Å, which can be considered as a normal bond fluctuation), and we observed no separations of the two central carbons in a 200 fs time range (Figure 4.14, right graph).

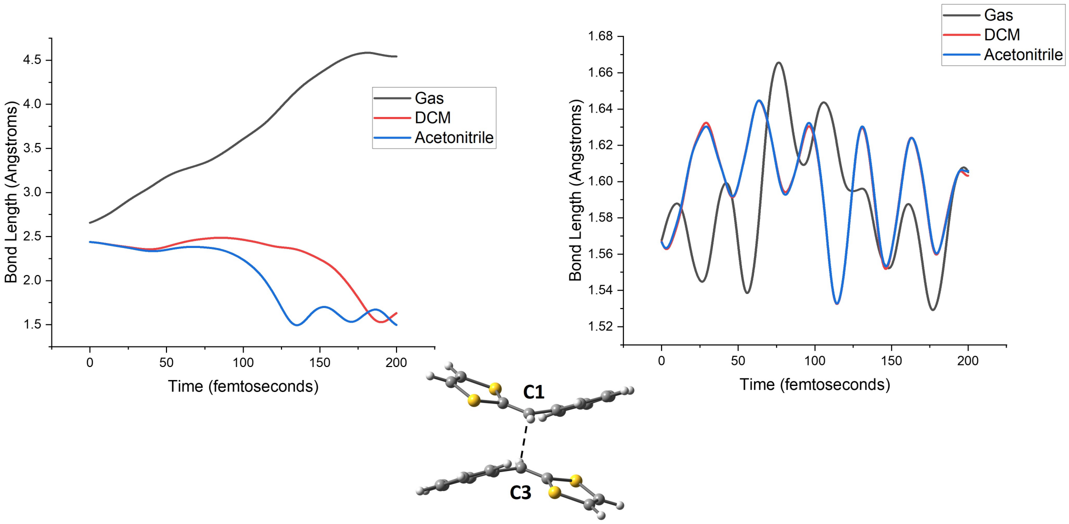

Figure 4.14: Time dependency of the C_1-C_3 bond length in the transition state (left) and product (right) of the anti isomer of the dication dimer.

4.3.3 Substituent effects on the Ph-DTF dimerization mechanisms

The addition of three electron-donating groups (i.e., amine, methoxy, and methyl) as well as five electron-withdrawing groups (i.e., nitrile, nitro, aldehyde, carboxylic acid, and acetophenone) to the *para* position of the benzene ring of the parent molecule have also been investigated. The impacts of the presence of different electron-withdrawing (EWG) and electron-donating groups (EDG) on the kinetics and thermodynamics of the dimerizatioon reaction have been studied (Figure 4.15). We found out that the presence of the electron-donating groups on the *para* position of the phenyl substituent has an adverse impact on the thermodynamics and kinetics of the dimerization reaction. On the other hand, while most of the electron-withdrawing groups don't have a significant impact on the dimerization reaction, carboxylic acid and aldehyde substituents have positive impacts on the reaction in both points of view. We have determined that the addition of either electron-withdrawing or electron-donating groups to the parent molecule causes little change in the dimerization pathway for the system. Solvent effects play a dominant role in the reaction.

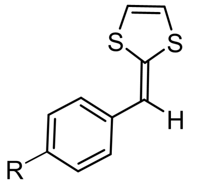

R = H, -OMe, -NH$_2$, -Me, -CN, -NO$_2$, -COMe, -CHO, -COOH

Figure 4.15: Schematic illustration of different substituents at the *para* position of the Ph-DTF.

Based on the results for the DC pathway (Table 4.1), the addition of EWG group to the *para* position of the phenyl moiety does not have any significant impact on the energy barrier of the transition state. Only nitro ($-\mathrm{NO_2}$) group significantly increases this barrier in the gas phase. Carboxyl group $-\mathrm{COOH}$ in acetonitrile significantly lowers the TS energy barrier. Generally speaking, EWG substituents increase the amount of Gibbs energy released in the dimerization reaction via the DC pathway, increasing the spontaneity of the reaction. (Figure 4.1).

The addition of EDG substituents will have adverse impacts on both kinetics and thermodynamics of the reaction in the DC pathway as they increase the amount of TS energy barrier as well as $\mathit{\Delta} G^{\circ}$ in all media. Particularly, the addition of $-\mathrm{NH_2}$ turns the dimerization reaction to a non-spontaneous one even in DCM and ACN solvents (Table 4.1).

Table 4.1: Comparison of thermodynamic and kinetic effects of substitution at the *para* position on the Ph-DTF dimerization in the DC pathway

	$\Delta G^{\ddagger}$ **(kcal/mol)**			ΔG° **(kcal/mol)**		
R	**Gas**	**DCM**	**ACN**	**Gas**	**DCM**	**ACN**
H	60.96	13.13	7.71	39.95	-6.66	-12.92
-OMe	60.49	15.10	8.85	48.06	-0.38	-5.98
-NH$_2$	63.25	22.67	16.44	52.99	12.21	6.31
-Me	61.29	14.91	9.84	43.92	-4.27	-10.45
-CN	66.49	15.23	8.65	44.15	-7.68	-14.44
-NO$_2$	69.32	18.25	9.68	44.67	-5.81	-14.72
-CHO	61.95	12.14	8.57	41.72	-11.47	-12.55
-COOH	61.05	13.31	5.74	39.54	-9.76	-16.65
-COMe	59.37	13.58	7.37	40.78	-7.75	-14.54

On the other hand, the addition of different EWG substituents has insignificant thermodynamic and kinetic influence on the dimerization reaction in mixed-valence pathway. In contrast, EDG substituents will increase the energy barrier of the transition state as well as the amount of released ΔG° in all media (Table 4.2).

Table 4.2: Comparison of thermodynamic and kinetic effects of substitution at the *para* position on the Ph-DTF dimerization in the MV pathway

	$\Delta G^{\ddagger}$(kcal/mol)			**ΔG^{o}(kcal/mol)**		
R	**Gas**	**DCM**	**ACN**	**Gas**	**DCM**	**ACN**
H	6.07	8.68	7.27	4.84	6.98	6.66
-OMe	11.24	12.71	14.57	11.08	10.64	12.00
-NH_2	12.89	18.96	17.98	12.29	15.48	16.70
-Me	8.80	9.05	9.76	7.61	8.90	8.91
-CN	8.17	7.51	8.46	6.85	7.35	6.73
-NO_2	7.82	8.65	9.08	6.45	7.95	6.56
-CHO	8.13	8.16	8.95	6.92	6.50	6.09
-COOH	7.77	8.38	8.21	6.28	6.10	5.76
-COMe	7.57	8.55	7.55	6.34	7.29	6.34

4.3.4 Frontier molecular orbital properties

In the complex and the transition state of the mixed-valence π-dimer, the Singly Occupied Molecular Orbital (SOMO) is predominantly spread around the two sulfurs as well as the two central carbon atoms in the DTF units and also on the two bridge carbons between the phenyl and the DTF unit. However, the share of the bridge carbons in the SOMO decreases to near zero in the product of the MV σ-dimer, which means that the new bond between the two central carbons will prevent their involvement in the radical delocalization over the supramolecular system. The other important observation is that except for a small contribution in the CX_{MV}, there is no SOMO electron density over the aromatic sector in all the species of the MV system. On the other hand, for the Lowest Unoccupied Molecular Orbital (LUMO), the electron density contributions of the two sulfurs have shifted to the *ortho* and *para* positions of the benzene rings in the π-dimer complex and there are no contributions to the LUMO associated with the benzene rings in the TS and σ-dimer product. The interesting point for the LUMO contours in the TS and σ-dimer product in the MV system is that there is no significant electron density on the two bridge carbons but precisely on the prospective bond between the two atoms. In addition, as we go from the complex to the product, the SOMO–LUMO gap decreases, which shows the system's higher reactivity and lower stability as the two bridge carbons get closer to each other (Figure 4.16).

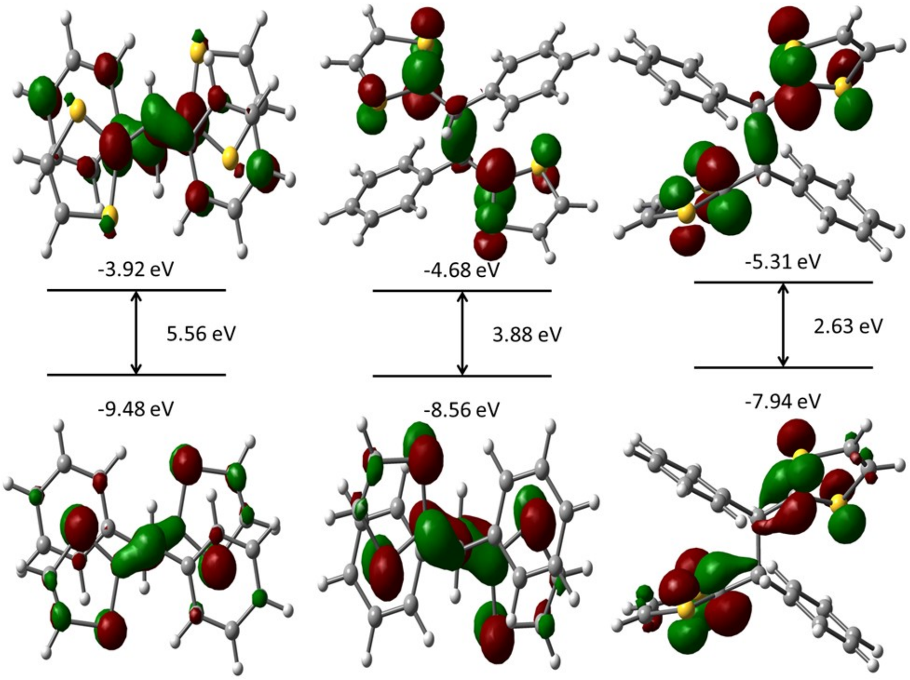

Figure 4.16: Contours and eigenvalues of the SOMO (bottom pictures) and LUMO (top pictures) of the CX (left), TS (middle), and product (right) of the mixed-valence system (isovalue = 0.05).

For the CX_{DC}, the HOMO is spread all over the system, with the majority on and between the middle carbon of DTF and the two bridge carbon atoms (figure 4.17). The LUMO distribution is the same as the HOMO but with the opposite phases on each atom. Interestingly, we can see a significant amount of the HOMO of the TS on and between the two bridge carbons with negative phase lobes on the atoms and positive ones between them. For the HOMO of the product, however, almost all of the HOMO is spread on the *ortho* and *meta* positions of only one phenyl ring with a planar node between them. On the other hand, both phenyl groups and the two bridge carbons have no electron density in the LUMO of both TS and σ-dimer in the DC pathway. In contrast to the MV system, the HOMO–LUMO gap increases as we go forward along the reaction pathway, which demonstrates greater product stability compared to the two separate monomers (Figure 4.17).

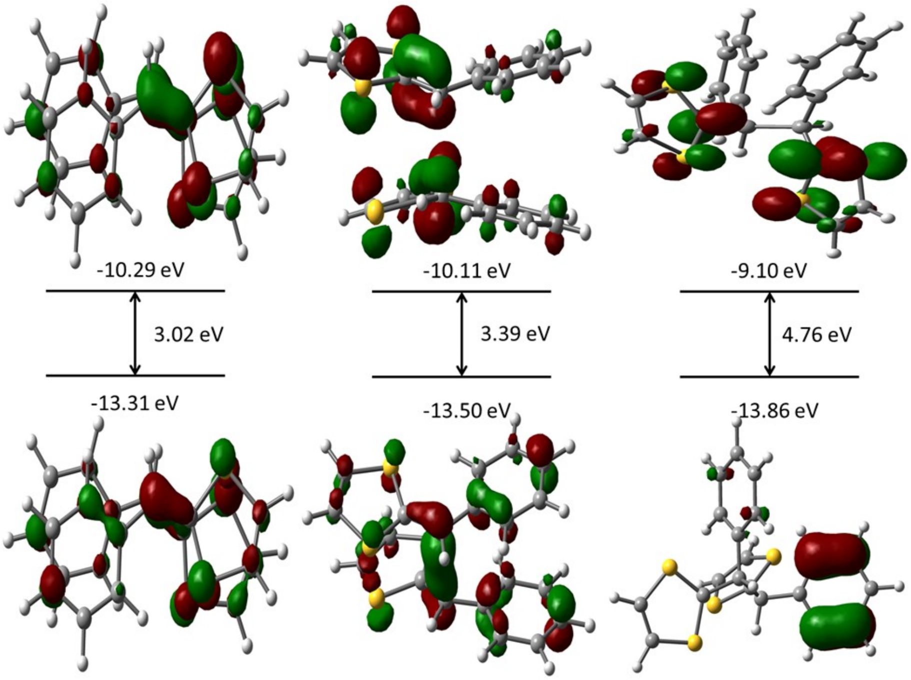

Figure 4.17: Contours and eigenvalues of the HOMO (bottom pictures) and LUMO (top pictures) of the CX (left), TS (middle), and product (right) of the dication system (isovalue = 0.05).

4.3.5 Spin density

After one neutral and one radical cation species get close enough to each other to form the CX_{MV}, one can see that the unpaired electron has already been delocalized on both monomers, which is the main reason for the stability of the complex comparing to the separate monomers (Figure 4.18). Another remarkable result is how the spin density is distributed on the system as we go forward along the reaction pathway.

At first, the spin density is only distributed on the two bridge carbons and only two sulfurs with the C_2 symmetry. Once we reach the TS, we can see that the spin density shifts toward the DTF units rather than the aromatic sectors with distribution on the central carbons and all four sulfurs of the two DTF units. Finally, in the protonated product, the majority of the spin density is present on the two central carbons of the DTFs, and only a small portion is found on the sulfurs. It is noteworthy that the unpaired electron will not be present on its origin, which is one of the two bridge carbons anymore.

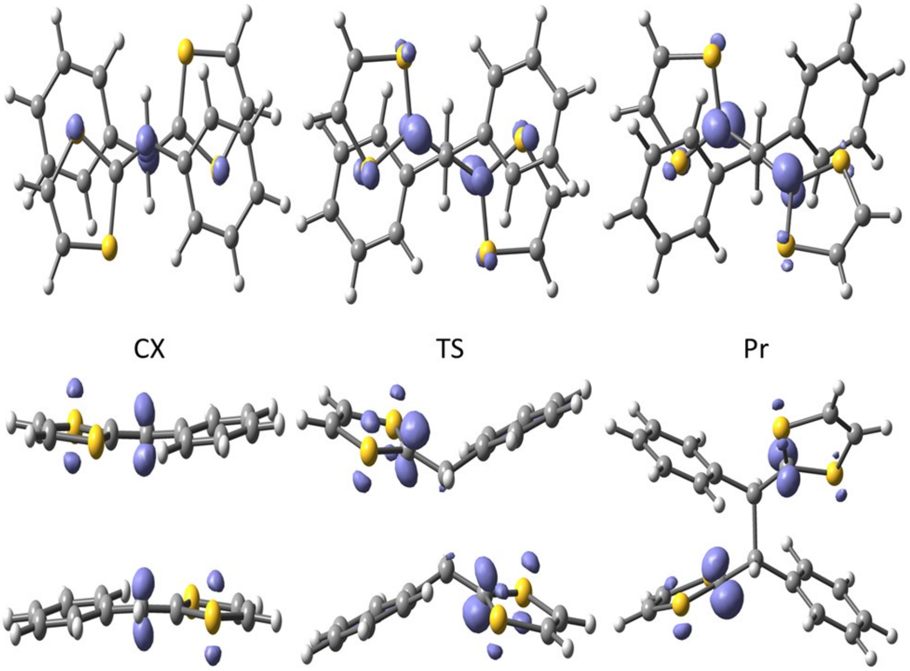

Figure 4.18: Contours of the spin density distribution of the top view (top) and side view (bottom) of the CX (left), TS (middle), and product (Pr) (right) of the mixed-valence system (isovalue = 0.01).

4.3.6 Oxidation potentials

We have also calculated the oxidation potential of the mixed-valence product directly to that of the dication system in the parent molecule as well as its derivatives with the aforementioned variety of electron-donating and electron-withdrawing groups at the *para* position of the benzene ring. In this regard, we have used the following equations based on the Nernst equation,[266]

$$nFE^{\circ}_{O/R} = \mathit{\Delta} G_{ox} = [G_{O,soln} - G_{R,soln}] + G_{e^-,gas} \tag{4.1}$$

where O/R is the oxidized/reduced species, G is the Gibbs free energy obtained from the calculated results of each system. F is the Faraday constant that is equal to 96485.33212 C/mol, and $E_{O/R}$ is the oxidation potential. It is noteworthy that 1 Hartree = 2625500 J/mol and also $G_{e^-,gas}$ = -3616.0 J/mol.[267,268] Therefore, we have

$$E^{\circ}_{O/R} = \frac{((G_{O,soln} - G_{R,soln}) \times 2625500) - 3616}{96485.33212}. \tag{4.2}$$

Several trials have been carried out to determine the absolute potential of the standard hydrogen electrode (SHE).[269–274] This measurement has been further recalculated by Gennaro *et al.* with the aid of the Gibbs free energy of solvation of the proton rather than its potential as well as the application of the latest thermodynamic data.[275] Gennaro *et al.* obtained $E^{abs}_{H^+/H_2} = 4.281$ V at $T = 298.15$ K and $P_{H_2} = 1$ bar. This amount is in line with the Fermi–Dirac electron convention.

Based on the results shown in Table 4.3, as the polarity of the solvent increases, the oxidation potential decreases, which means that the system needs less energy to be oxidized in polar solvents. This observation can be rationalized based on the fact that the permanent dipolar molecules are more stable in more polar solvents. In addition, these results show that the EDG substituents at the *para* position including methyl, methoxy, and amino decrease the value of $E_{O/R}$. In contrast, the EWG substituents including nitrile, nitro, aldehyde, acid, and acetophenone increase $E_{O/R}$ relative to that of the parent molecule. This can be explained by the inductive effect of an EWG on a more positive system which makes it harder to get oxidized. Therefore, the presence of an EDG substituent makes the Ph-DTF more stable by decreasing the total dipole moment of the molecule. On the other hand, the introduction of an EWG substituent will lead to a more positive charge and a more significant dipole moment of the system. As a result, the oxidation happens in more $E_{O/R}$ values. Based on this rationalization, one can conclude that the more the electron pushing of the EDG substituent, the less the value of $E_{O/R}$ will be. In contrast, the more electron-withdrawing an EWG substituent is, the greater the value of $E_{O/R}$ is (see Table 4.3).

Table 4.3: Calculated oxidation potentials of the product of the mixed-valence pathway to the product of the dication pathway in different media. Values have been obtained based on the Nernst Equation (relative to SHE in Volts).

R	**Gas**	**DCM**	**ACN**
H	4.47	0.43	0.02
-OMe	4.26	0.34	-0.02
-Me	4.36	0.36	-0.06
-NH$_2$	4.06	0.32	-0.07
-CN	4.89	0.57	0.17
-NO$_2$	4.97	0.61	0.14
-CHO	4.72	0.46	0.16
-COOH	4.60	0.48	0.09
-COMe	4.63	0.49	0.07

Furthermore, we have calculated the oxidation potentials of the monomer of Ph-DTF and eight of its derivatives in the gas phase, as well as in dichloromethane and acetonitrile (Table 4.4). Similar to what has been observed in the dimer, $E_{O/R}$ values decrease as the solvent's polarity increases. Moreover, the same as in dimer (table 4.3), electron-donating groups causes the $E_{O/R}$ value to decrease while the electron-withdrawing groups lead to the increment of the oxidation potential compared to that of the parent molecule. This observation can be attributed to the inductive effect in the *para* position of the benzene. In fact, the imposed positive charge on the DTF group (upon oxidation) will get more stable by the presence of an EDG on the *para* position of benzene not only by means of the inductive effect, but also with the aid of the resonance effect.

Table 4.4: Calculated oxidation potentials of the Ph-DTF monomer derivatives in different media vs SHE (in Volts).

R	**Gas**	**DCM**	**ACN**
H	2.60	1.03	0.85
-OMe	2.28	0.82	0.68
-Me	2.42	0.93	0.77
-NH_2	1.99	0.46	0.37
-CN	4.24	1.22	1.05
-NO_2	3.03	1.21	1.06
-CHO	2.85	1.20	0.97
-COOH	2.77	1.17	1.03
-COMe	2.77	1.14	0.98

4.3.7 TD-DFT analysis

Time-dependent density functional theory (TD-DFT) calculations have also been performed on the complex of both the MV and DC systems. It is noteworthy that the SOMO–LUMO gap determined from TD-DFT calculations is different from that calculated by time independent DFT. This is because that the former calculates the energy of the molecular orbitals in an N-electron system in the excited state, and the latter deals with the same N-electron system in the ground state.[276] In the UV-Vis absorbance spectrum of the MV complex, the most intense peak is found between 300 to 350 nm, which is mainly due to the SOMO to LUMO+1 electronic transition. Another absorption peak in the UV-Vis region is observed between 500 to 550 nm and it is due to the SOMO-1 to LUMO electronic excitation in all media. In addition, we can see a bathochromic shift as the polarity of the solvent increases (Figure 4.19). We have also observed a small peak at about 1822, 2276, and 1430 nm in vacuum, DCM, and CH_3CN, respectively (inset in Figure 4.19). Based on our TD-DFT calculations, the SOMO to LUMO transition is responsible for these peaks.

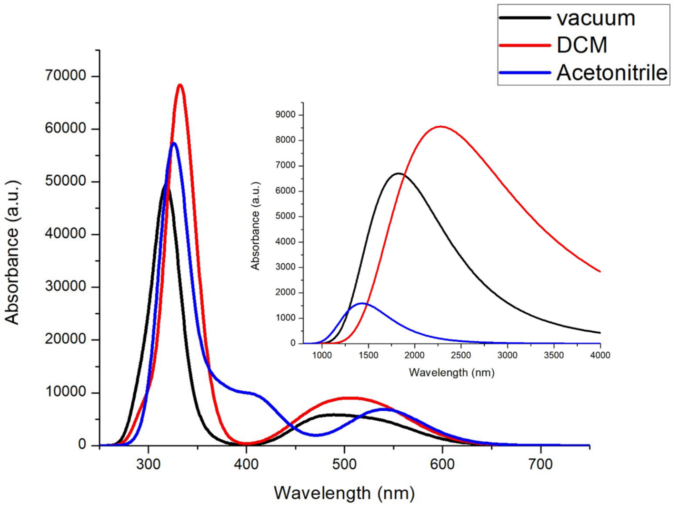

Figure 4.19: TD-DFT results of the complex in the mixed-valence system in different media calculated at the CAM-B3LYP/6-311++G(d,2p) level.

The TD-DFT results for the complex of the DC system reveal that, unlike the MV system, there is a hypsochromic shift with increasing solvent polarity. However, there is little change in the intensity of the peaks as a result of changing the medium polarity (Figure 4.20). Indeed, λ_{max} occurs at 677, 696, and 655 nm (HOMO to LUMO transition) in the gas phase and in DCM and acetonitrile, respectively. The second UV-Vis absorption is observed at 468, 472, and 478 nm (related to HOMO-1 to LUMO transition), and another is seen at 338, 351, and 346 nm, which is due to the HOMO to LUMO+1 electronic transition.

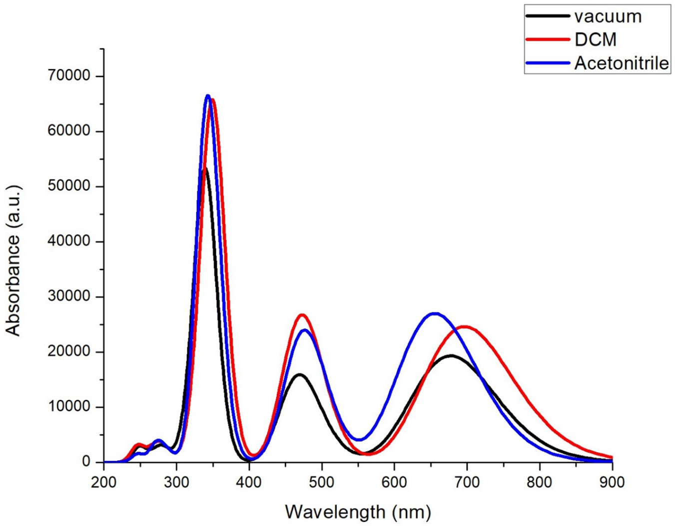

Figure 4.20: TD-DFT results for the complex in the dication system in different media calculated at the CAM-B3LYP/6-311++G(d,2p) level.

4.4 Conclusions

In this chapter, the reaction pathways of the oxidative dimerization of phenyl-substituted dithiafulvene (Ph-DTF) in vacuum, dichloromethane, and acetonitrile have been for the first time systematically investigated using DFT calculations. A Ph-DTF radical cation forms a stable mixed-valence π-dimer with a neutral Ph-DTF molecule, but the resulting mixed-valence σ-dimer product is thermodynamically disfavored (endergonic). Direct dimerization of two Ph-DTF radical cations is disfavored in the gas phase due to strong electrostatic repulsion, but under solvation the repulsion is mitigated and the dimerization becomes possible, particularly in polar solvents. The effects of different electron-withdrawing and electron-donating groups on the kinetics and thermodynamics of the dimerization reaction have been studied as well. Our computational results indicate that the presence of the electron-donating groups in the *para* position of the phenyl group has an adverse impact on the thermodynamics and kinetics of the dimerization reaction. On the other hand, while most of the electron-withdrawing groups do not have significant impacts on the dimerization reaction, carboxylic acid and aldehyde substituents make the reaction both kinetically and thermodynamically more favored. Moreover, the study of the oxidation potentials of the monomer and dimer of Ph-DTFs with EDG and EWGs present at the *para* position of the phenyl group confirms that the addition of an EDG decreases the oxidation potential and the addition of EWGs increases the oxidation potential of both monomer and dimer of Ph-DTF in all media compared to the parent molecule. Other properties of such systems including spin density distribution, TD-DFT results, and frontier molecular orbitals have also been investigated in this chapter.

Chapter 5

Quantum Chemical Calculations of Molecular Structure and Electronic Properties of Dithiafulvene-substituted Polycyclic Aromatic Hydrocarbons

5.1 Introduction

Polycyclic aromatic hydrocarbons (PAHs) are organic aromatic compounds that contain two or more fused benzene rings but do not include heteroatoms. Light PAHs are defined as having up to four rings in their molecular structures, whereas heavy PAHs are those comprised of more than four rings.[277–282] Compared to light PAHs, heavy PAHs are more stable but more toxic.[283,284] The sole components of PAHs are carbon and hydrogen, which form a variety of simple to complex ring structures and exhibit a wide range of physical, chemical, and toxicological properties. In the systems such as linear anthracenes or the pericondensed pyrenes, the ring linkage patterns exist where the tertiary carbon atoms are the centers of two or three interconnected rings. However, the majority of PAHs are hybrids that combine different structural elements, for example, naphthalene, acenaphthylene, acenaphthene, fluorene, phenanthrene, anthracene, fluoranthene, pyrene, chrysene, and so on. The hydrophobicity and electrochemical stability of a PAH molecule often grow in tandem with its size and angularity.[285,286]

Sulfur-containing heterocyclic compounds have been employed in various applications in diverse aspects of chemistry, including synthetic materials, biological and medicinal chemistry.[1–3] A fascinating example of these compounds is tetrathiafulvalene (TTF), one of the most investigated organic π-conjugated systems in the literature.[4–10] Since the first studies of this compound,[12,287] many research efforts have been made on TTF-based functional π-conjugated materials and molecular devices. TTF consists of two non-aromatic 1,3-dithiole rings, which can be either sequentially or simultaneously transformed into aromatic dithiolium rings via oxidation. The gain of aromaticity associated with oxidation makes TTF possesses excellent electron-donating capability. As such, TTF has been popularly used as a suitable π-electron donor in many redox-active π-conjugated materials, and molecular electronic devices,[76,288–291] rotors,[186] compounds with remarkable surface areas,[181] organic dyes with intramolecular charge transfer ability[292] and nonlinear optic-phores.[80] The half structure of TTF, 1,4-dithiafulvene (DTF), is also a very appealing heterocyclic functional group. The first studies of the unsubstituted parent DTF molecule, which is 2-methylene-1,3-dithiole, were only carried out theoretically in terms of its structural and ionization energies[29] as well as its thermochemical properties.[30] Early studies based on nucleus-independent chemical shift (NICS) and isomerization stabilization energy (ISE) calculations suggested that the 1,3-dithiole ring in unsubstituted DTF is a good organic π-electron donor.[31] Later, experimental results have demonstrated that extension of the π-conjugation of DTF works as an effective design strategy for improving the stability, synthetic accessibility, electronic properties, and redox activities of DTF derivatives. According to a literature survey,[47] a DTF group can be integrated in various π-conjugation systems through three main connection patterns (see Scheme 5.1).[47] In patterns 1 and 2, a DTF group is directly linked to a π-conjugated system via covalent linkages at the vinylidene position, while in pattern 3, π-extension is achieved through the fusion of the 1,3-dithiole ring with other conjugated structures.[47]

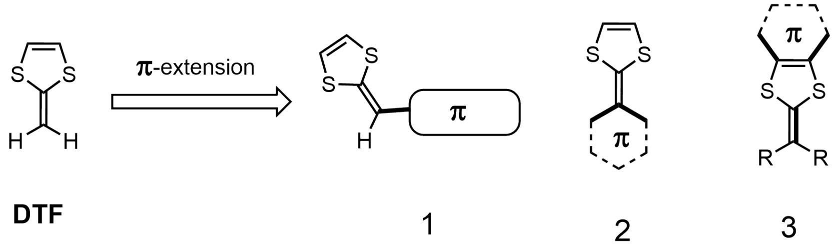

Scheme 5.1: Three main patterns for integrating the DTF unit into π-conjugated systems. Scheme adapted from M. F. Abdollahi, Y. Zhao, *New J. Chem.* **2020**, *44*, 4681–4693 with permission.

To the best of our knowledge, there have been no comprehensive studies of DTF functionalized polycyclic aromatic hydrocarbons (DTF-PAH) in terms of the interplay between PAH conjugation patterns with electronic and redox properties. In this work, we chose DTF-PAH assembled in pattern 1 as models for a systematic computational analysis based on DFT calculations. A total of 14 DTF-PAH compounds have been examined in their neutral and oxidized (radical cation) states. Beside the gas-phase properties, we have also taken solvent effects into account, analyzing their molecular properties in three solvent media, including hexanes, dichloromethane (DCM), and dimethylsulfoxide (DMSO). These solvents represent the range from non-polar to strongly polar solvents, so that the DFT calculated results can be reasonably linked to experimentally established data. Our DFT studies have examined various molecular properties, including molecular structures, vertical electronic transitions (via TD-DFT), oxidation potentials, charge and spin density analysis as well as frontier molecular orbitals.

5.2 Methodologies

DFT calculations were carried out using the Gaussian 16 software package.[188] The geometries of all calculated compounds were initially optimized via the semi-empirical PM6 method[189] and then reoptimized using the University of Minnesota's hybrid functional (M06-2X)[129,190] with the Karlsruhe basis set of def2-SVP.[191,192] Following the optimization, each structure was subjected to vibrational analysis at the same level of theory to verify that it is a global energy minimum (no imaginary frequencies). Atomic charge populations were calculated by different methods: (1) The Mulliken charge analysis method proposed by Mulliken and Ermler,[293–295] (2) The Hirshfeld atomic charge method,[296] (3) The Löwdin atom and basis function population method,[297,298] (4) The atomic dipole moment corrected Hirshfeld (ADCH) population method proposed by Lu and Chen,[193] (5) The charge model 5 (CM5) method proposed by Truhlar et al.[299] Solvent effects were analyzed using the continuum solvation model based on the charge density (SMD) developed by Truhlar et al.[195] In addition, visualization of molecular structures and molecular orbitals was carried out using the CYLview[196], and the GaussView 6 software packages,[197] respectively. Topological analysis of electron density and its visualization were performed using the Multiwfn program[198] with the VMD software package.[199] The energies of excitation and calculated excited-state properties, as well as calculations of UV-Vis absorption spectra, were performed using time-dependent density functional theory (TD-DFT)[142] at the M06-2X/6-311++G(d,2p) level. We considered only singlet to singlet transitions in the TD-DFT calculations in order to save computational costs while maintaining the precision of the results. Simulated UV-Vis absorption spectra were generated by the GaussSum[200] program and plotted using the OriginPro 8 software package.[201] All the DFT calculations have been done at the temperature of 298.15 K and the pressure of 1.00 Atm.

5.3 Results and discussion

To obtain deeper understanding of the nature of the changes that happen in the geometry and electronic distribution of arene substituted dithiafulvenes (Ar–DTFs) upon oxidation to their radical cation counterparts, 14 different compounds have been studied and compared with each other (Figure 5.1). We considered s-*cis* and s-*trans* conformers for three of our compounds (**2**, **5**, and **9**), since different spatial arrangements have influence on their structural and electronic properties.

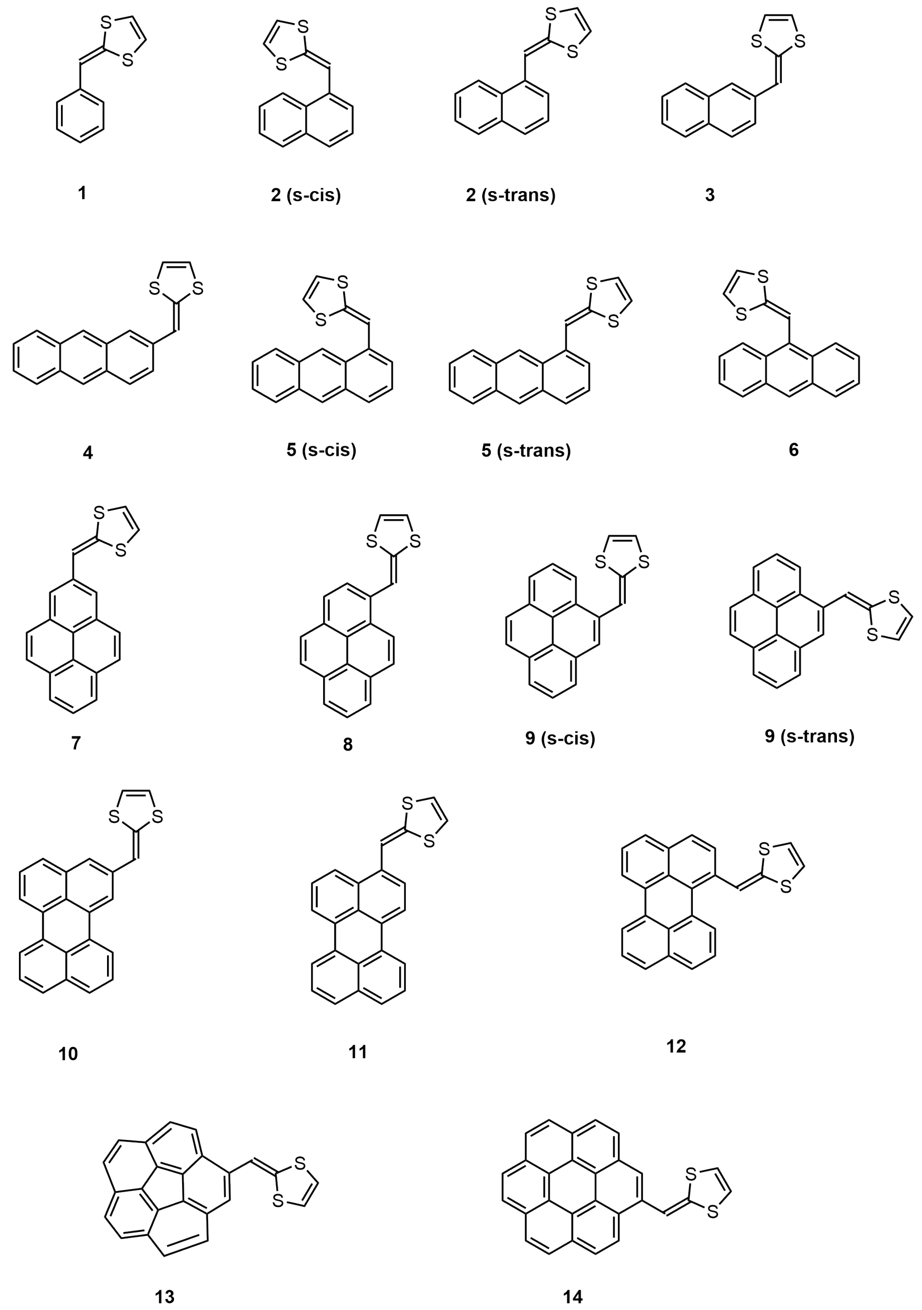

Figure 5.1: The compounds studied at the M06-2X/Def2-SVP level of theory. For **2**, **5**, and **9**, both s-*cis* and s-*trans* conformers have been studied.

5.3.1 Geometric analysis

It is obvious that the radical cation (RC) species are less stable than their neutral (N) form because of having a doublet spin multiplicity. Table 5.1 shows the torsion angle of each compound in its two oxidation states. In this work, the torsion angle is defined as the dihedral angle between the planes of the two cyclic π-moieties, arene (AS) and DTF, in each compound. For the sake of clarification, the geometrical parameters applied in this work are illustrated in Scheme 5.2.

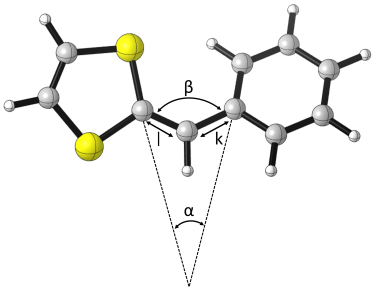

Scheme 5.2: Schematic illustration of torsion angle (α), C_{DTF}-C-C_{AS} bond angle (β), C_{DTF}-C bond length (l), and C-C_{AS} bond length (k).

In all of our systems studied, it shows that the Ar–DTFs tend to be closer to the linear geometry upon oxidation (Table 5.1). This linearity makes it more suitable for molecular orbitals to have a more efficient interaction through space in order to share the imposed positive charge (hole) and unpaired electron over the constituent atoms. Interestingly, our data demonstrate that the bigger the system is, the more significantly the positive charge and unpaired electron are delocalized. It can be further illustrated by comparing the oxidation potentials of each group of systems. Two exceptions to this trend (**13** and **14**) will be discussed further.

Table 5.1: Torsion angles (α in degrees) of the compounds studied in their neutral and radical cation oxidation states.

Compound	**Neutral**	**Radical Cation**
1	20.87	0.03
2 (s-*cis*)	38.42	31.71
2 (s-*trans*)	38.50	19.83
3	21.09	0.68
4	21.31	0.00
5 (s-*cis*)	59.04	29.68
5 (s-*trans*)	38.01	18.57
6	65.03	34.89
7	22.10	0.00
8	37.91	13.52
9 (s-*cis*)	38.19	21.70
9 (s-*trans*)	38.24	21.70
10	21.92	5.47
11	37.55	31.52
12	42.95	23.13
13	29.38	26.57
14	38.57	19.50

Regarding the relative stability of the RC species upon oxidation, the extent of the stability is dependent on the position and spatial orientation of the substituted DTF moiety and the solvent in which oxidation occurs. For the DTF-naphthalene group (i.e., **2** and **3**), 1-DTF naphthalene is more stable when compared to 2-DTF naphthalene. In dichloromethane, however, 2-DTF naphthalene possesses the more stable RC species. In the case of those compounds with s-*cis* and s-*trans* geometric isomers (**2**, **5**), the s-*trans* isomer is the more stable RC species in all media. In contrast, while the starting geometries of s-*cis* and s-*trans* in **9** were different in space, the final optimized geometries reached different geometric isomers with the same energies so that the oxidation potentials were the same in all media. This can be seen by comparing their twist angle, HOMO–LUMO gap, and other structural and electronic properties (for the optimized geometries, please refer to the Supporting Information in Appendix).

Once Ar–DTFs are oxidized, three main phenomena occur, and all of these observations are considered as a kind of adaptation that the system takes to accommodate the imposed positive charge and unpaired electron. Firstly, the torsion angle decreases as the system is oxidized (Table 5.1). This phenomenon sets the stage for the molecular orbitals to have a more efficient overlap with each other. This allows the system to improve the interaction between its orbitals in order to distribute the electron density (including that electron-hole) over the whole molecule. We will discuss this observation in the charge and spin population analysis section. The second point is the increase of the central bond angle (C_{DTF}-C-C_{AS}, denoted as β) upon oxidation (Table 5.2). Indeed, the DTF group is the source of the positive charge upon oxidation in the system, and this central bond is a bridge between the positive section (i.e., DTF group) and π-moiety of the molecule. This increase in β will again improve the molecular orbital overlap between these two parts, which can be considered as an effect of widening the bridge for a more efficient π-electron transfer between the two aforementioned parts of the molecule, which in turn increases the stability of the system.

Table 5.2: Central bond angle (C_{DTF}-C-C_{AS}, β) in degrees.

Compound	β **(N)**	β **(RC)**	**Variance**
1	129.34	131.58	+2.24
2-*cis*	126.60	130.66	+4.06
2-*trans*	126.59	129.97	+3.38
3	129.02	131.77	+2.75
4	128.89	131.54	+2.65
5-*cis*	125.37	131.22	+5.85
5-*trans*	126.65	130.08	+3.43
6	124.24	129.83	+5.59
7	129.15	131.46	+2.31
8	126.81	130.55	+3.74
9-*cis*	126.49	129.79	+3.30
9-*trans*	126.48	129.79	+3.31
10	128.79	131.17	+2.38
11	126.61	131.14	+4.53
12	127.15	129.93	+2.78
13	128.12	128.71	+0.59
14	126.53	130.07	+3.54

The third observation upon oxidation is related to the bond length of the central bridge of the Ar–DTF molecules (Table 5.3). Once these molecules are oxidized in the gas phase, the bond length of C_{DTF}-C (denoted as l in scheme 5.2) increases from *ca.* 1.35 Å to *ca.* 1.39 Å. On the other hand, we observed a decrease in the bond length of C-C_{AS} (denoted as k in Scheme 5.2) from *ca.* 1.47 Å to *ca.* 1.42 Å. This means that once the system is neutral, the bond length of C_{DTF}-C is almost equal to that of C=C in sp^2 hybridized systems, and the bond length of C-C_{AS} approaches the C–C bond in sp^3 hybridized systems (with an acceptable approximation). Upon oxidation, however, both bonds tend to get closer to each other in terms of their lengths for a better and more efficient interaction and π-delocalization, which will lead to a more effective distribution of the imposed spin density and positive charge between the two segments of the molecule, resulting in better stability.

Table 5.3: Central bond lengths in Å. k and l are the C-C_{AS}, and C_{DTF}-C bond lengths, respectively.

Compound	**l (N)**	**l (RC)**	**Variance**	**k (N)**	**k (RC)**	**Variance**
1	1.35	1.39	+0.04	1.46	1.43	-0.03
2-*cis*	1.35	1.40	+0.05	1.47	1.42	-0.05
2-*trans*	1.35	1.39	+0.04	1.47	1.42	-0.05
3	1.35	1.39	+0.04	1.46	1.42	-0.04
4	1.35	1.39	+0.04	1.46	1.42	-0.04
5-*cis*	1.35	1.39	+0.04	1.48	1.42	-0.06
5-*trans*	1.35	1.39	+0.04	1.47	1.42	-0.05
6	1.34	1.40	+0.06	1.48	1.42	-0.06
7	1.35	1.39	+0.04	1.46	1.42	-0.04
8	1.35	1.39	+0.04	1.47	1.42	-0.05
9-*cis*	1.35	1.39	+0.04	1.47	1.42	-0.05
9-*trans*	1.35	1.39	+0.04	1.47	1.42	-0.05
10	1.35	1.38	+0.03	1.46	1.43	-0.03
11	1.35	1.39	+0.04	1.47	1.42	-0.05
12	1.35	1.39	+0.04	1.47	1.42	-0.05
13	1.35	1.40	+0.05	1.46	1.42	-0.04
14	1.35	1.39	+0.04	1.47	1.42	-0.05

5.3.2 Dipole moment and oxidation potentials

The general trend in the dipole moment values of the Ar–DTF molecules is observed as follows. For a given molecule, the dipole moment of the RC form is greater than that of the N species, which is expected due to the introduction of a positive charge after the oxidation process. In addition, the dipole moment increases with the increase of the dielectric constant of the solvent due to the better charge separation in a medium with more distinct unlike charges (i.e., solvents with more dielectric constant values). As aforementioned, our results show that the RC species are more planar than their N counterparts. In addition to this, the vector nature of dipole moment causes the RCs to possess larger dipole moments than those of their neutral counterparts, as it contributes to increasing the dipole moment value. For the dipole moment values, please refer to the Supporting Information in the Appendix.

5.3.2.1 Redox potential calculation method

In order to calculate the oxidation potential of the compounds investigated, the following equation derived by J. W. Gibbs and W. Ostwald[300,301] is applied with the understanding that as the work has been done on the system during the oxidation process, the sign will be positive:

$$\Delta G_{ox}^{\Theta} = +nFE^{\circ}_{O/R} \tag{5.1}$$

where ΔG_{ox}^{Θ} is the standard Gibbs free energy change for the oxidation process, n is the number of electrons transferred in the process (equal to 1 in this case), F is the Faraday constant and $E^{\circ}_{O/R}$ is the standard oxidation potential. By considering the Gibbs free energy of an electron in the gas phase, we will have,[266]

$$\Delta G^{\Theta}_{ox} = [G_{O,soln} - G_{R,soln}] + G_{e^-,gas} \tag{5.2}$$

By combining Equations 5.1 and 5.2, and converting Hartree to J/mol (1 Hartrees = 2625500 J/mol),[302] and having the value of $G_{e^-,gas}$ = -3616.0 J/mol,[268] we have,

$$[G_{O,soln} - G_{R,soln}] + G_{e^-,gas} = FE^{\circ}_{O/R} \tag{5.3}$$

therefore,

$$E^{\circ}_{O/R} = [(((G_{O,soln} – G_{R,soln})2625500) - 3616)/96485.33212] \tag{5.4}$$

Therefore, we have calculated the oxidation potentials of the Ar–DTFs investigated using Equation 5.4. Detailed data are compared in Figure 5.2. The results demonstrate that by enhancing the polarity of the solvent, the redox potential decreases in all compounds. These results can be explained by the lower energy level of the ground states in the charged species (RC) in a more polar medium.

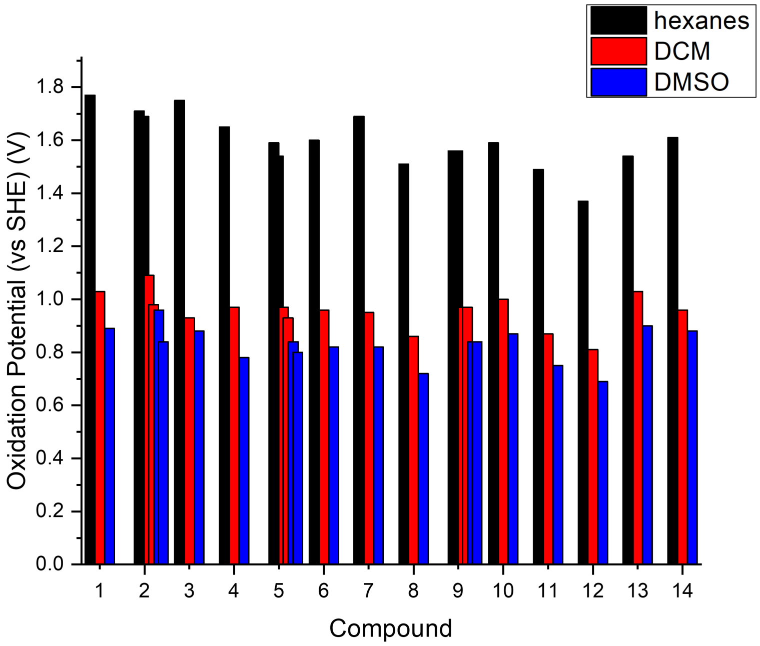

Figure 5.2: Calculated oxidation potentials (vs. SHE). For compounds **2**, **5**, and **9**, the set of columns on the left refer to the *s-cis* isomer, and the ones on the right refer to the *s-trans* isomer.

As previously mentioned, the s-*trans* isomers of **2** and **5** show better RC stability, and hence less oxidation potential than their s-*cis* isomers. However, our calculations for the s-*cis* and s-*trans* isomers of **9** led to different optimized geometries with the same Gibbs free energies and therefore the same oxidation potentials and other properties. The reason behind this behavior could be attributed to the hyperconjugation effect between the DTF and arene sections, which leads to better electron-hole distribution in s-*trans* isomers compared to their s-*cis* counterparts. More studies are needed in order to fully understand the reasons for this phenomenon. Figure 5.2 shows that as the arene system becomes larger, the oxidation potential decreases due to the existence of more π-conjugation (i.e. higher number of available degenerate resonance structures) in larger π moieties. A comparison of DTF-naphthalene molecules (**2** and **3**) shows that 2-DTF naphthalene (**3**) has the lower oxidation potential in dichloromethane while in hexanes and DMSO, s-*trans* 1-DTF naphthalene (**2**) has the lower oxidation potential. For DTF-anthracene molecules (**4**, **5**, and **6**), s-*trans* 1-DTF anthracene (**5**) possesses the lowest oxidation potential in hexanes and DCM. In DMSO, however, 2-DTF anthracene (**4**) has the lowest oxidation potential. For DTF-pyrene molecules (**7**, **8**, and **9**) and DTF-perylene molecules (**10**, **11**, and **12**), the 1-substituted compounds (**8** and **12**, respectively) demonstrate the lowest oxidation potentials among the others in all solvents. Although the arene moieties are larger in **13** and **14**, the oxidation potential values increase in these compounds compared to the systems with smaller π-moieties. DTF-corannulene has a saddle-shaped structure in which there is less π-delocalization and interactions between the molecular orbitals than in the other Ar–DTFs. The second piece of evidence supporting a modest intramolecular π-delocalization between DTF and arene moieties in this particular compound is the fact that we did not observe a substantial torsion angle decrease following oxidation in this molecule. The case with DTF-coronene (**14**) is different. The shape of the π-moiety in DTF-coronene is planar, demonstrating highly effective π-delocalization in the neutral form. However, the planarity of the system is altered as a result of oxidation. To overcome this relative perfection and steadiness, and to disrupt the strong π-delocalization, it thus requires greater energy.

5.3.3 Optical properties

The electronic absorption spectra were obtained using Time-Dependent Density Functional Theory (TD-DFT) calculations. To the best of our knowledge, there are not any comprehensive reports on the absorption spectroscopy of the compounds studied (UV-Vis spectra of all the compounds are available in the Supporting Information Appendix). Table 5.4 shows the maximum absorption wavelength of each compound in its N and RC forms in four different media. Based on our UV-Vis results, a red shift is observed by increasing the size of π-moiety in Ar–DTFs in both their neutral and radical cation forms. This is due to the fact that the HOMO–LUMO gap in Ar–DTFs decreases with the π-expansion. There are again two exceptions to this trend (**13** and **14**) due to the system's greater relative stability and lower relative reactivity. In addition, for a given compound in neutral form, the maximum absorption wavelength will increase as the polarity of the solvent rises.

Table 5.4: Maximum absorption wavelength (in nm) of all compounds studied in both N and RC forms in four different media. G, H, D, and S denote gas phase, hexane, DCM, and DMSO, respectively.

System	**G(N)**	**H(N)**	**D(N)**	**S(N)**	**G(RC)**	**H(RC)**	**D(RC)**	**S(RC)**
1	307	314	324	324	528	538	524	519
2-*cis*	342	350	352	353	819	828	783	765
2-*trans*	342	350	352	353	762	772	736	721
3	335	345	348	349	894	857	769	743
4	381	390	393	394	1216	1250	1117	1067
5-*cis*	373	378	381	382	1068	1104	1039	1012
5-*trans*	387	395	398	398	1035	1071	998	971
6	385	391	394	395	929	967	970	969
7	329	335	338	338	658	648	593	577
8	375	387	390	391	867	902	888	878
9-*cis*	359	367	370	371	1125	1138	1015	971
9-*trans*	359	367	370	371	1125	1138	1015	971
10	400	411	411	411	2395	3036	1978	1644
11	438	453	455	455	1080	1153	1156	1150
12	433	445	448	449	1064	1115	1087	1070
13	377	387	392	393	682	703	662	648
14	360	368	371	372	986	999	889	849

In the RC form, the maximum absorption wavelength decreases with increasing solvent polarity. Compounds **6** and **11** are the exceptions, in which the λ_{max} remains almost constant by changing the polarity of the solvent both in the N and RC forms. In addition, the λ_{max} increases significantly upon oxidation, which is expected as the HOMO–LUMO gap decreases once oxidation takes place which could also be relevant to the remarkable reactivity enhancement of the RC counterparts. In some cases, including **4**, **5**, **9**, **10**, **11**, and **12**, the maximum absorption peak appears at more than 1000 nm (Figure 5.3), demonstrating how reactive the radical cation of each one becomes when oxidation occurs.

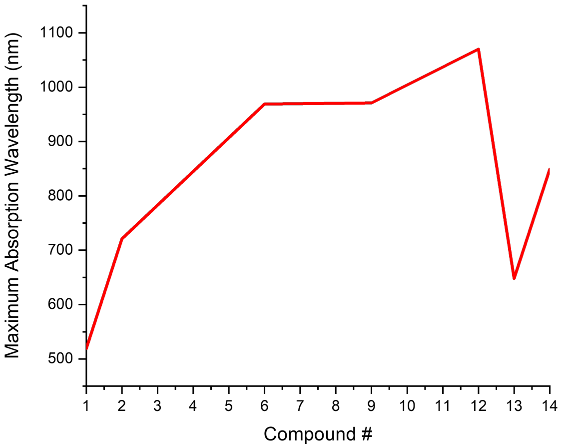

Figure 5.3: Calculated maximum absorption wavelength of the radical cation forms in DMSO.

5.3.4 Charge and spin density population analysis

Charge population analysis has also been done via five different methods (Table 5.5) in the gas phase and in dichloromethane. Scheme 5.3 illustrates our definition of DTF and π-sectors of an Ar–DTF molecule.

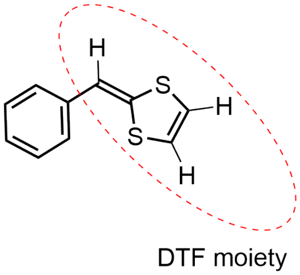

Scheme 5.3: The DTF moiety of the Ar–DTF molecule.

Based on charge population analysis, the DTF moiety is slightly positive, and the π-moiety is slightly negative when the Ar–DTFs are neutral. In the solution phase, the positive magnitude of the DTF sector increases relative to the gas phase. However, once oxidation occurs, the majority of the positive charge is found on the DTF moiety in the gas phase. Again, the positive charge distribution in the RC form is more significant in the solution phase than in the gas phase. This is expected as the DTF part tends to keep the positive charge in order to preserve its aromaticity. Indeed, the results based on different charge population methods have produced almost the same results. In some cases, the ADCH method showed some discrepancies, which could be ignored as the other methods showed very similar charge distributions. Generally speaking, the DTF moiety is the positive part, and the π-sector is the negative part of the molecule, and once the system gets solvated and/or becomes oxidized, the amount of positive charge distributed on the DTF moiety increases (Table 5.5).

Table 5.5: Charge population analysis using five different calculation methods. The numbers show the charge contribution of the DTF moiety in each compound in the gas phase and in dichloromethane (DCM). M, H, L, A, and C denote Mulliken, Hirshfeld, Lowdin, ADCH, and CM5 charge population analysis methods.

		M		**H**		**L**		**A**		**C**	
Entry	**State**	**(N)**	**(RC)**	**(N)**	**(RC)**	**(N)**	**(RC)**	**(N)**	**(RC)**	**(N)**	**(RC)**
1	**Gas**	0.030	0.682	0.036	0.704	0.047	0.730	-0.001	0.706	0.034	0.702
	DCM	0.046	0.755	0.044	0.755	0.055	0.783	-0.012	0.759	0.042	0.753
2-*cis*	**Gas**	0.024	0.591	0.030	0.624	0.040	0.651	0.027	0.604	0.029	0.624
	DCM	0.037	0.676	0.038	0.690	0.047	0.719	0.042	0.676	0.037	0.689
2-*trans*	**Gas**	0.024	0.580	0.030	0.613	0.040	0.620	0.028	0.611	0.029	0.612
	DCM	0.037	0.664	0.038	0.683	0.047	0.710	0.042	0.680	0.037	0.682
3	**Gas**	0.044	0.619	0.043	0.638	0.055	0.661	0.008	0.639	0.041	0.636
	DCM	0.060	0.718	0.055	0.717	0.065	0.719	-0.001	0.721	0.053	0.716
4	**Gas**	0.049	0.512	0.048	0.529	0.060	0.543	0.015	0.528	0.046	0.527
	DCM	0.067	0.623	0.061	0.626	0.072	0.645	0.008	0.628	0.059	0.625
5-*cis*	**Gas**	0.011	0.488	0.034	0.520	0.037	0.539	0.013	0.500	0.033	0.519
	DCM	0.022	0.573	0.040	0.592	0.042	0.615	0.015	0.577	0.038	0.591
5-*trans*	**Gas**	0.032	0.483	0.032	0.516	0.043	0.532	0.028	0.510	0.031	0.515
	DCM	0.045	0.576	0.041	0.597	0.051	0.617	0.043	0.589	0.039	0.596
6	**Gas**	0.004	0.430	0.038	0.491	0.035	0.507	0.026	0.475	0.036	0.491
	DCM	0.020	0.487	0.046	0.538	0.043	0.557	0.034	0.529	0.044	0.538
7	**Gas**	0.041	0.609	0.042	0.631	0.054	0.658	0.007	0.633	0.040	0.630
	DCM	0.057	0.730	0.054	0.732	0.064	0.761	-0.001	0.737	0.052	0.731
8	**Gas**	0.028	0.462	0.036	0.506	0.044	0.523	0.036	0.499	0.034	0.505
	DCM	0.043	0.543	0.046	0.574	0.054	0.594	0.054	0.565	0.045	0.573
9-*cis*	**Gas**	0.033	0.503	0.035	0.535	0.046	0.553	0.030	0.534	0.034	0.533
	DCM	0.046	0.625	0.045	0.642	0.055	0.664	0.046	0.638	0.044	0.640
9-*trans*	**Gas**	0.034	0.503	0.035	0.535	0.046	0.553	0.030	0.534	0.034	0.533
	DCM	0.046	0.625	0.045	0.642	0.055	0.664	0.046	0.639	0.044	0.640
10	**Gas**	0.043	0.387	0.047	0.405	0.058	0.413	0.142	0.379	0.045	0.403
	DCM	0.061	0.620	0.060	0.627	0.070	0.646	0.004	0.602	0.058	0.625
11	**Gas**	0.035	0.394	0.038	0.428	0.047	0.439	0.032	0.410	0.036	0.427
	DCM	0.050	0.456	0.049	0.479	0.057	0.492	0.048	0.463	0.048	0.478
12	**Gas**	0.006	0.407	0.034	0.448	0.034	0.461	0.033	0.415	0.031	0.447
	DCM	0.024	0.489	0.046	0.520	0.045	0.536	0.047	0.490	0.043	0.519
13	**Gas**	0.030	0.577	0.044	0.600	0.058	0.629	0.039	0.606	0.043	0.600
	DCM	0.050	0.693	0.060	0.696	0.073	0.728	0.052	0.701	0.059	0.696
14	**Gas**	0.033	0.486	0.036	0.521	0.046	0.542	0.034	0.519	0.035	0.520
	DCM	0.048	0.632	0.048	0.652	0.057	0.677	0.052	0.649	0.047	0.650

In addition, we have calculated the spin population analysis of the Ar–DTFs via three different methods (Table 5.6). Indeed, these results demonstrate greater spin density distribution on the DTF moiety of Ar–DTFs compared to the π-sector. While the Becke spin population method shows less distribution of the spin density on the DTF moiety, it still reveals the same trend as the other two in terms of the greater spin contribution of the DTF sector. Similar to the charge population results, moreover, the spin distribution on DTF increases even more upon solvation, indicating that solvation stabilizes spin delocalization on the DTF part of the system.

Table 5.6: Spin density population analysis using three different calculation methods. The numbers show the spin density distribution on the DTF moiety in each compound in the gas phase and in dichloromethane (DCM).

Compound	**State**	**Mulliken**	**Lowdin**	**Becke**
1	**gas**	0.770	0.747	0.739
	DCM	0.809	0.781	0.771
2-*cis*	**gas**	0.682	0.664	0.660
	DCM	0.744	0.720	0.714
2-*trans*	**gas**	0.637	0.620	0.616
	DCM	0.705	0.680	0.674
3	**gas**	0.674	0.656	0.651
	DCM	0.745	0.719	0.711
4	**gas**	0.483	0.474	0.473
	DCM	0.596	0.578	0.574
5-*cis*	**gas**	0.519	0.511	0.511
	DCM	0.600	0.586	0.584
5-*trans*	**gas**	0.475	0.467	0.467
	DCM	0.567	0.551	0.549
6	**gas**	0.462	0.455	0.457
	DCM	0.509	0.498	0.498
7	**gas**	0.700	0.684	0.679
	DCM	0.785	0.759	0.751
8	**gas**	0.497	0.492	0.492
	DCM	0.561	0.550	0.547
9-*cis*	**gas**	0.514	0.503	0.502
	DCM	0.633	0.612	0.608
9-*trans*	**gas**	0.514	0.503	0.502
	DCM	0.633	0.612	0.608
10	**gas**	0.307	0.299	0.299
	DCM	0.614	0.596	0.591
11	**gas**	0.389	0.390	0.394
	DCM	0.443	0.440	0.443
12	**gas**	0.442	0.441	0.442
	DCM	0.515	0.508	0.507
13	**gas**	0.659	0.644	0.641
	DCM	0.738	0.714	0.707
14	**gas**	0.537	0.529	0.529
	DCM	0.671	0.650	0.646

5.3.5 Frontier molecular orbitals studies

The frontier molecular orbitals of the Ar–DTF systems have also been evaluated. Table 5.7 shows the HOMO and LUMO properties in the N form and Table 5.8 shows the HOMO and LUMO properties in the RC form of the Ar–DTFs in DMSO. According to our calculations, as the π moiety expands, the HOMO–LUMO gap decreases which explains the reactivity increase in the Ar–DTFs due to the enhancement in the π delocalization.

Table 5.7: The energy levels of the frontier molecular orbitals of the Ar–DTFs studied and their energy gap in the neutral form in DMSO.

Entry	**HOMO(Hartree)**	**LUMO(Hartree)**	**Gap(Hartree)**	**Gap(ev)**	**Gap(kcal/mol)**
1	-0.23139	-0.00841	0.22298	6.07	139.92
2-*cis*	-0.23146	-0.02566	0.2058	5.60	129.14
2-*trans*	-0.23146	-0.02565	0.20581	5.60	129.15
3	-0.23084	-0.02584	0.205	5.58	128.64
4	-0.22775	-0.04634	0.18141	4.94	113.84
5-*cis*	-0.23368	-0.04505	0.18863	5.13	118.37
5-*trans*	-0.22846	-0.04619	0.18227	4.96	114.38
6	-0.23328	-0.04682	0.18646	5.07	117.00
7	-0.2311	-0.03819	0.19291	5.25	121.05
8	-0.22606	-0.04489	0.18117	4.93	113.69
9-*cis*	-0.23075	-0.04168	0.18907	5.14	118.64
9-*trans*	-0.23074	-0.04168	0.18906	5.14	118.64
10	-0.22891	-0.05575	0.17316	4.71	108.66
11	-0.22219	-0.05866	0.16353	4.45	102.62
12	-0.22245	-0.05692	0.16553	4.50	103.87
13	-0.23173	-0.04861	0.18312	4.98	114.91
14	-0.23044	-0.04324	0.1872	5.09	117.47

There are two exceptions to the aforementioned phenomenon (i.e. **13** and **14**) in which the HOMO–LUMO gap increases compared to the other smaller arene systems. In addition, the energy gap between the frontier molecular orbitals can be seen to decrease upon oxidation which, as expected, indicating an increase in the reactivity of the Ar–DTFs after oxidation.

Table 5.8: The energy levels of the frontier molecular orbitals of the Ar–DTFs studied and their energy gap in the radical cation form in DMSO.

Compound	SOMO(Hartrees)	LUMO(Hartrees)	Gap(Hartrees)	Gap(ev)	Gap(kcal/mol)
1	-0.27085	-0.054	0.21685	5.90	136.07
2-*cis*	-0.26151	-0.0631	0.19841	5.40	124.50
2-*trans*	-0.26064	-0.06524	0.1954	5.32	122.61
3	-0.26414	-0.06315	0.20099	5.47	126.12
4	-0.2527	-0.07568	0.17702	4.82	111.08
5-*cis*	-0.24873	-0.07615	0.17258	4.70	108.29
5-*trans*	-0.24931	-0.0766	0.17271	4.70	108.38
6	-0.24659	-0.08234	0.16425	4.47	103.07
7	-0.26117	-0.05901	0.20216	5.50	126.86
8	-0.24349	-0.07556	0.16793	4.57	105.38
9-*cis*	-0.25385	-0.07272	0.18113	4.93	113.66
9-*trans*	-0.25385	-0.07272	0.18113	4.93	113.66
10	-0.24405	-0.07714	0.16691	4.54	104.74
11	-0.23633	-0.08667	0.14966	4.07	93.91
12	-0.2381	-0.08304	0.15506	4.22	97.30
13	-0.26056	-0.07565	0.18491	5.03	116.03
14	-0.24948	-0.07112	0.17836	4.85	111.92

5.4 Conclusion

The research results reported in this chapter provide a computational perspective on the molecular structure and electronic properties of arene-substituted dithiafulvene (Ar–DTF) compounds. By increasing the size of the π-system in Ar–DTFs, the radical cation counterpart gains more stability upon oxidation which results in a decrease in the oxidation potential of this type of molecule. The reason for this trend is that the system becomes more π-delocalized, so that the electron-hole pair on the molecule becomes increasingly separated from each other. In our study, there are two exceptions to this general trend (i.e., **13** and **14**). Compound **13** possesses a saddle shape π moiety in which the extent of π-delocalization and molecular orbital interactions is less than those of the other Ar–DTF compounds. In addition, we did not observe a significant decrease in twist angle upon oxidation in this molecule, which is the second piece of evidence for weak intramolecular delocalization between the DTF and arene moieties in this specific compound. The situation for **14** is different. In coronene-DTF, the geometry of the π-moiety is planar, resulting in very efficient π-delocalization in the neutral form. After oxidation, the perfection of the system is changed, and the very efficient π-delocalization of the neutral form is reduced. That is why more energy is needed to overcome this relative perfection and stability. The charge transfer phenomenon has also been calculated via five different population analyses. We have found that as the π-moiety gets larger in size, the stability of the molecule increases due to a more efficient electron-hole distribution throughout the structure of the molecule. This effect causes the oxidation potential to decrease, making the compound more oxidizable.

Chapter 6

A Combined TD-DFT, UV–Vis And Fluorescence Spectroscopic Studies of A Novel Organic Fluorophore Derived From Self-Condensation of Pyrene-4,5-dione

6.1 Introduction

Pyrene is categorized in the group of polycyclic aromatic hydrocarbons (PAHs) and exhibits attracting photophysical characteristics. Its exceptional properties such as high charge carrier mobility[303] and remarkable luminescence efficiency[304] have resulted in its widespread use in various technological applications including organic photovoltaics,[305] organic field-effect transistors,[306] and organic light-emitting diodes (OLEDs).[306] Pyrene is characterized by its extended π-conjugated system, which enables efficient electron delocalization and light absorption over a broad range of wavelengths. Consequently, the synthesis of pyrene and its derivatives with multiple substituents have emerged as popular molecular building blocks for the development of advanced organic optoelectronic materials due to their unique electronic and photophysical properties.[306–308] Additionally, pyrene derivatives exhibit high thermal and chemical stability, making them suitable candidates for a wide range of applications in various fields.

The development of new functionalized pyrenes has been an area of active research as they serve as useful precursors for the preparation of advanced π-conjugated materials.[304,307,309] Pyrene-4,5-dione is one such functionalized pyrene that has gained growing application in recent years. Furthermore, the development of an efficient large-scale synthesis method of pyrene-4,5-dione by the Bodwell group has led to an increase in its use as a precursor for the preparation of advanced π-conjugated materials.[310] Their synthetic method of pyrene-4,5-dione involves the oxidative cleavage of pyrene using suitable oxidizing agents, including ruthenium(III) chloride and sodium periodate under controlled conditions. This synthetic method enables the production of pyrene-4,5-dione in high yield and purity, making it a valuable starting material for the preparation of advanced π-conjugated materials.[311–318] The continuous development of new functionalized pyrenes has led to the discovery of new materials with enhanced electronic and photophysical properties, paving a way for the development of advanced optoelectronic devices. pyrene-4,5-dione is particularly interesting as it can undergo various reactions to yield more extended π-systems, including condensation reactions.[310,319,320] Condensation reactions have become an appealing approach to produce advanced π-conjugated materials from pyrene-4,5-dione due to their high efficiency and simplicity in operation. The resulting compound may exhibit enhanced electronic and optical features, such as increased emission of light and improved charge transport properties.[321]

6.1.1 Excimer formation

The present project is built on the exciplex formation of pyrene derivatives. Excimers, a short-lived dimeric system that is formed when two atoms or molecules interact in an excited state, are characterized by having a different electronic state and a shorter lifetime than their constituent atoms or molecules in their ground state.[322] Because excimer formation is dependent on a bimolecular interaction, it is promoted by high monomer density (higher concentrations). Low-density conditions produce excited monomers that decay to the ground state before they interact with an unexcited monomer to form an excimer.[322,323] The excimer state is a type of excited state in which two molecules form a complex and are bound together through weak van der Waals forces.[322] Usually, increased concentration will lead to the quenching of the fluorescence spectrum of one given compound. However, rather than quenching the fluorescence, excimers are responsible for redshifting of the emission spectrum of some organic compounds by increasing their concentration.[324] Excimers are typically formed through photoexcitation or electrical excitation in gases, liquids, or even solids.[325,326] They are often used in various applications, such as in the development of lasers,[327] light-emitting diodes,[328] and in photolithography for microchip manufacturing.[327] Among these compounds, pyrene and its derivatives has been investigated for their excimer formation for a long time.[322,329] Therefore, the study of pyrene excimers opens up new possibilities in understanding the behavior of systems in excited states. By elucidating the unique electronic states of excimers, this research aims to shed light on their intriguing properties and explore their potential applications. The investigation of pyrene derivatives in excimer formation further contributes to the existing body of knowledge in this area.

6.1.2 Complex formation using cyclodextrins

Cyclodextrins (CDs) are cyclic oligosaccharides which are typically composed of at least six glucose units, with the most prevalent varieties being α-CD, β-CD, and γ-CD, which contain six, seven, and eight units, respectively.[330,331] Their unique structural characteristics, including a hydrophilic outer surface and a hydrophobic cavity, make them versatile molecular hosts capable of forming inclusion complexes with a wide range of guest molecules.[332,333] The formation of inclusion complexes involves the encapsulation of guest molecules within the hydrophobic cavity of CDs, leading to the alteration of various physicochemical properties and the development of novel functional materials.[330,334]

CDs and their derivatives have been extensively investigated for their ability to form stable inclusion complexes leading to significant opportunities particularly in the field of pharmaceutical industries.[331] Various analytical techniques, including transmission electron microscopy (TEM) and dynamic light scattering (DLS), have been employed to examine the complexation and aggregation phenomena.[330,331,333,335–339] These studies collectively elucidate that the physical behaviors observed are governed by the interplay between the hydrophobic and hydrophilic properties of the involved constituents, as they strive to attain self-assembled complexes.[340] Consequently, the formed aggregates exhibit varying levels of complexity in terms of stability, size distribution, and solubility, which are intrinsically influenced by the nature of the CD molecule, attached functionalities, and the concentrations ratio of CDs and the guest molecules.[334,341]

6.1.3 Time-dependent DFT studies

The investigation of electronic transitions in organic molecules, specifically PAHs, has been increasingly applied Time-Dependent Density Functional Theory (TD-DFT) to comprehend their behavior in electronically excited states. TD-DFT accurately predicts excited-state properties by combining quantum mechanics with density functionals (see Chapter 2 for detailed information). This computational approach has been crucial in determining the optical properties, spectroscopic features, and excited-state behavior of PAHs. It aids in understanding processes like energy transfer, charge transfer, and excited-state relaxation. Furthermore, TD-DFT studies facilitate the design and optimization of PAH-based materials for applications such as OLEDs, solar cells, and sensors.[342–354] The study of charge transfer in pyrene complexes has also been extensively explored utilizing TD-DFT, which has provided valuable insights into the electronic properties and spectroscopic features of pyrene complexes, shedding light on their charge transfer dynamics and facilitating their design for various applications.[355–358] In addition, substantial investigations have been carried out to explore the influence of substituents on the photoluminescence properties of pyrene-core compounds and to understand their behavior on the excited-state dynamics, and photophysical properties of pyrene derivatives, paving the way for the rational design of these compounds with tailored photoluminescence characteristics.[359,360]

The study of pyrene derivatives absorption and emission spectra in a water-ice matrix has also been conducted to comprehend its behavior in this unique environment, exploring their applications in astrochemistry. Through experimental techniques and theoretical modeling, the interaction between pyrene-core compounds and the water-ice matrix have been studied, elucidating the spectral shifts, electronic transitions, and photophysical properties that occur in this context.[350,361] These findings contribute to our understanding of the spectroscopic behavior of PAHs in complex matrices and provide valuable information for applications in astrochemistry and environmental science. Furthermore, the utilization of pyrene derivatives in organic light emitting diode (OLED) devices has been investigated with the aid of TD-DFT leading to design and optimization of these compounds for enhanced OLED device performance, offering promising avenues for the development of efficient and sustainable organic optoelectronic devices.[362]

TD-DFT has also been utilized to investigate the formation of excimers in PAHs. By simulating the excited state interactions, it enables the understanding of the factors influencing PAH excimer formation such as molecular geometry, intermolecular interactions, and electronic transitions. These studies provide insights into the excited-state behavior of PAHs and contribute to the development of advanced materials for optoelectronic applications.[346,363–368]

In this chapter, we have studied the excimer formation in a pyrene-core PAH and validated it through the use of inclusion complexation with β and γ-CDs. Different excimer formation influential factors including molecular geometry, intermolecular interactions, and electronic transitions have also been studied via spectroscopic analyses and computational modeling. Furthermore, the validation using CD inclusion complexes provides experimental confirmation of our theoretical predictions. This chapter also tries to enhance the understanding of the excited-state behavior of pyrene-core PAHs, paving the way for the development of novel strategies for controlling and manipulating excimer formation with potential applications in areas such as optoelectronic devices and materials science.

6.2 Methodology

6.2.1 Experimental

The chemicals and reagents used in this study were acquired from commercial vendors and were utilized without further purification. All reactions were executed in customary, dry glass apparatus under inert atmosphere (N_2). The evaporation and concentration were accomplished using a rotary evaporator. Flash column chromatography was performed using 240-400 mesh silica gel, while thin-layer chromatography (TLC) was performed using silica gel F254 coated on plastic sheets and viewed under ultraviolet (UV) light. Pyrene-4,5-dione (**1**) was synthesized based on the literature[310,321,369] with some modifications. UV-Vis absorption spectra were recorded using a Cary 6000i spectrophotometer. Fluorescence spectra were obtained using a Photon Technology International (PTI) quantamaster spectrofluorometer. The determination of relative fluorescence quantum yields (Φ) in solution was carried out following established protocols[370,371] employing quinine sulfate (Φ = 0.546) as the standard.[371] For the calculation of Φ in the H_2O/DMF mixture (in the case of complexation with β- and γ-CDs), where the molar fraction of water is 0.89 (H_2O/DMF, 2:1 v/v), the refractive index of the mixture was assumed to be that of pure water at 20°C ($n_{H_2O} = 1.3330$).[372] For single-crystal X-ray diffraction (SCXRD) analysis, data were collected at a temperature of 100(2) K on a XtaLAB Synergy-S, Dualflex, HyPix-6000HE diffractometer, utilizing Cu Kα radiation (λ = 1.5406 Å). The crystals were mounted onto nylon CryoLoops with Paraton-N, and data collection and reduction were conducted within CrysAlisPro (Rigaku OD, 2019). A multi-scan absorption correction was applied to the collected reflections. The structure was solved using the ShelXT structure solution program[373] with Intrinsic Phasing, and then refined using the ShelXL refinement package[374] with Least Squares minimization in the Olex2[375] software. Anisotropic refinement was performed on all non-hydrogen atoms, while organic hydrogen atoms were geometrically generated.

Synthesis of 6*H*-phenanthro[4,5-*cde*]pyreno[4',5':4,5]imidazo[1,2-*a*]azepin-6-one (2). A 150 mL round-bottomed flask was filled with pyrene-4,5-dione (**1**) (1.000 g, 4.306 mmol), ammonium acetate (3.990 g, 51.763 mmol), and glacial acetic acid (99.7%, 55 mL). The mixture was stirred at 115 °C for 48 hours to yield a opaque brown solution containing a yellowish precipitate. The reaction mixture was then cooled down to room temperature. 60 mL of water was added to the solution and the mixture was stirred for 5 minutes. The resultant brown-yellow solid was then suction filtered and washed with water and methanol successively. The resulting residue was subjected to flash column chromatography with solvent system starting from ethyl acetate/hexane (1:19, v:v), gradually increased to end with ethyl acetate/hexane (12:8, v:v). Compound **2** (1.378 g, 3.100 mmol, 72%) was the final pure compound that was obtained as a yellow solid.

Preparation of inclusion complex. The initial concentration of **2** in DMF was 1.0×10^{-3} M, and the initial concentration of either β or γ-CD was 5.0×10^{-3} M in water. In a 5 mL glass vial, one mL of **2** in DMF was poured, and next, one mL of either β- or γ-CD aqueous solution was added to the vial. The mixture was then subjected to a 2-hour bath sonication. Finally, the sonicated solution was passed through a PTFE syringe filter with the pore size of 0.22 μm in order to separate the undissolved particles and make a clear 1:1 DMF–H_2O (v:v) inclusion complex solution. Water was added to further dilute the solution to make 1:2 DMF–H_2O (v:v) to 1:6 DMF–H_2O (v:v) solutions. After each dilution, a 2-hour bath sonication was also applied to each set of solutions.

6.2.2 Computational modelling and visualization methods

Time-dependent density functional theory (TD-DFT) calculations[142] have been conducted using the Gaussian 16 software package.[188] Both singlet and triplet (the first 20 of each) transition states have been considered for the calculations. The initial structures of monomer and both π- and T-dimers have been directly derived from the X-ray single crystal structure and crystalline packing pattern of compound

2. The applied TD-DFT methods include the hybrid functional, M06-2X,[129,190] in conjunction with the Karlsruhe basis set, def2-SVP,[191,192] as well as Coulomb-attenuating method (CAM-B3LYP)[250] functional with 6-311++G(d,2p) basis set. Solvent effects were analyzed using the Polarizable Continuum Model (PCM)[376–379] applying the integral equation formalism variant.[380] In addition, visualization of molecular structures was carried out using the CYLview software package.[196] Simulated UV-Vis absorption and fluorescence emission spectra were generated by the GaussSum[200] and plotted using the OriginPro 8 software package.[201]

The conformer–rotamer ensemble sampling tool (CREST)[381,382] calculations have also been carried out to obtain all the possible supramolecular conformers of **2** in the gas phase. CREST applies GFN2-xtb semiempirical functional.[383] The initial geometries of CREST calculations obtained from π- and T-dimers of the X-ray single crystal structure and crystalline packing pattern of compound **2**. CREST output provided a total number of 29 conformers, each of which was further optimized by DFT calculations at the M06-2X/def2-SVP level in the gas phase. All the DFT calculations have been done at the temperature of 298.15 K and the pressure of 1.00 Atm.

6.3 Results and discussion

The self-condensation reaction of pyrene-4,5-dione (**1**) to yield 6*H*-phenanthro[4,5-*cde*]pyreno[4’,5’:4,5]imidazo[1,2-*a*]azepin-6-one (**2**) has been discovered earlier in our group.[321] With some modifications in reaction conditions as well as in the separation process, we succeeded in increasing the reaction yield remarkably (Scheme 6.1).

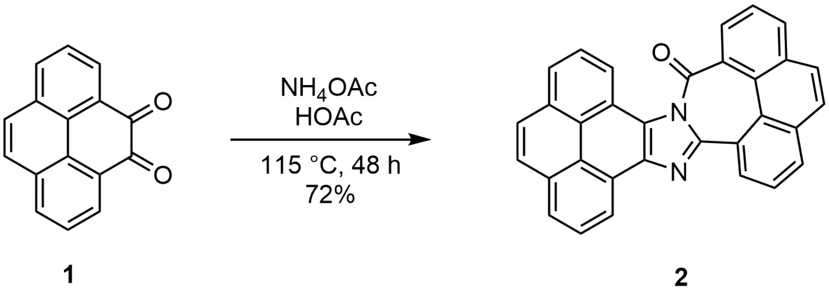

Scheme 6.1: Synthesis of **2** via self-condensation of pyrene-4,5-dione.

The molecular structure of product **2** was verified by X-ray single crystallographic analysis (Figure 6.1A). In contrast to what was observed previously in the crystalline packing of the derivatives of **2**,[321] the packing pattern of the parent compound shows that each monomer interacts with its neighboring molecules in two ways. The first one is the $\pi - \pi$ interaction leading to co-facially stacked dimers (π-dimers). On the other hand, each molecule is engaged with the neighboring molecules towards its tip forming T-dimers (Figures 6.1B and 6.1C).

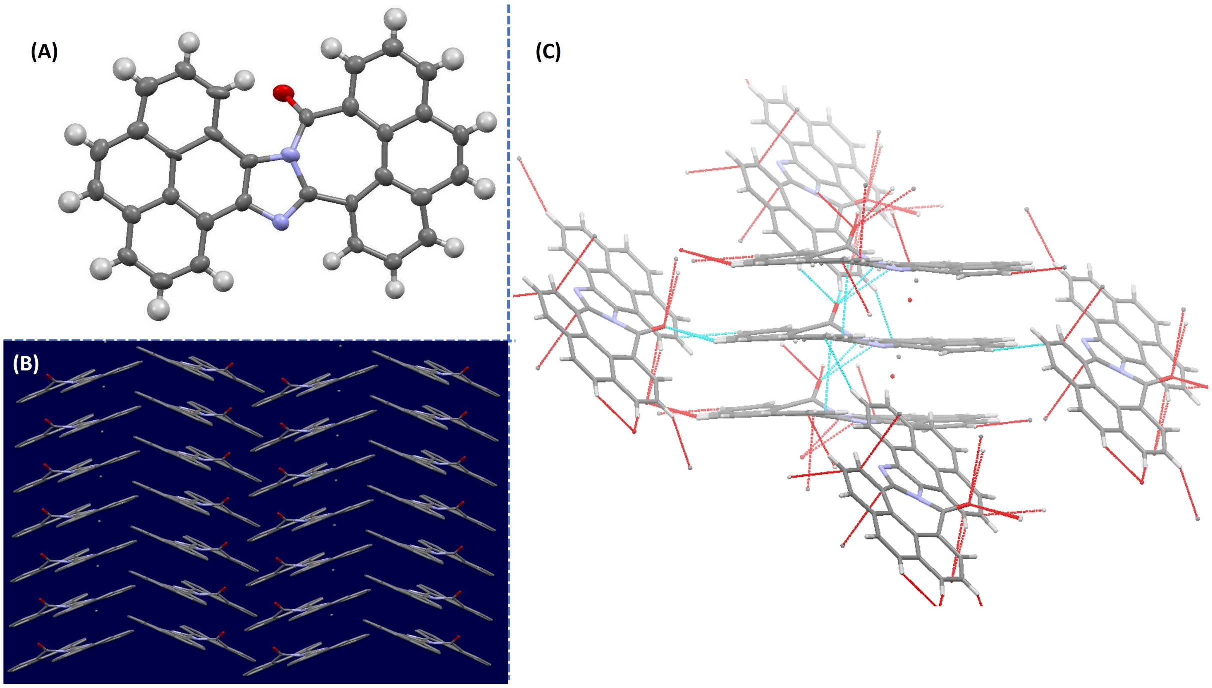

Figure 6.1: (A) ORTEP drawing (50% probability) and (B) general packing diagram and (C) two different packing patterns (π- and T-dimers) of **2** in the crystalline state.

6.3.1 Electronic transition analysis

The UV-Vis absorption spectroscopy was employed to investigate the behavior of **2** in various organic solvents. The analysis revealed that compound **2** gives its lowest-energy absorption peak ($\pi \rightarrow \pi^*$) within the wavelength range of 381 nm to 388 nm when dissolved in dichloromethane (DCM), chloroform ($CHCl_3$), *N*,*N*-dimethylformamide (DMF), and dimethylsulfoxide (DMSO). Interestingly, a bathochromic shift of approximately 20 nm was observed in the λ_{max} of **2** when dissolved in ethyl acetate, resulting in a value of 408 nm. The subsequent sections will provide an in-depth examination of the electronic transitions exhibited by the system.

6.3.1.1 Dichloromethane (DCM)

The UV-Vis absorbance behavior of **2** in DCM exhibits a distinct characteristic. At concentrations below ca. 1.0×10^{-4} M, the λ_{max} of the system remains constant at 388 nm. However, intriguingly, at higher concentrations, a new λ_{max} emerges at 459 nm, indicating the potential presence of an excimer in the solution (Figure 6.2A). Moreover, the intensity of this peak displays an increment with increasing concentration, which can be attributed to the enhanced abundance of the excimer species within the solution. These findings suggest that the formation of excimers induces a redshift in the UV-Vis absorption spectrum, attributable to alterations in the electronic properties of compound **2** in the excimeric state.

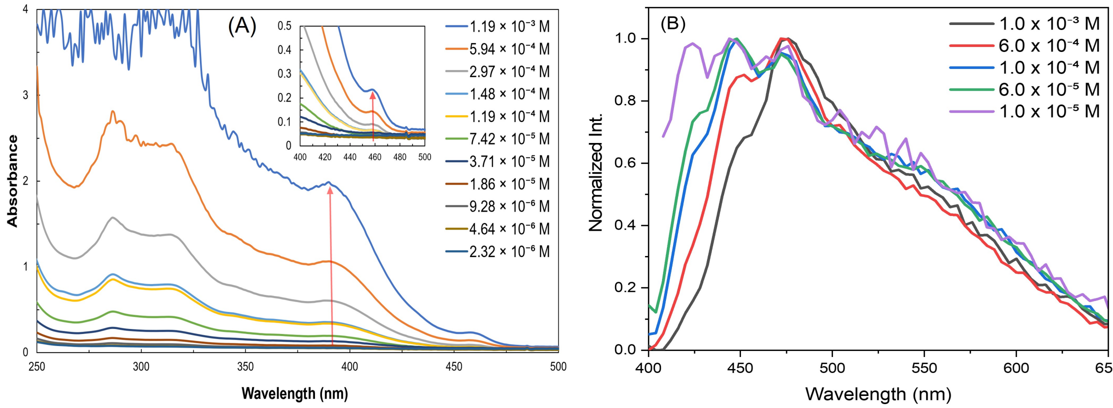

Figure 6.2: (A) UV-Vis absorption spectra of **2** measured at different concentrations in DCM. The inset is showing the same spectra between 400 to 500 nm. (B) Normalized fluorescence spectra of **2** (in DCM) measured at different concentrations ($\lambda_{ex} = 380$ nm).

Figure 6.2B displays the emission spectroscopy results of **2** in DCM. The spectrum exhibits two distinct peaks at 448 nm and 476 nm, respectively. The fluorescence quantum yield of **2** in DCM was observed as $\Phi = 0.096$. Notably, the intensity of the peak at the higher wavelength demonstrates a direct correlation with the concentration of **2**, while the intensity of the peak at the lower wavelength exhibits an inverse relationship with the compound's concentration in DCM. At a concentration of 1.0×10^{-3} M, the emission corresponding to the peak at 448 nm appears as a shoulder (Figure 6.2B). This observed dual emissive behavior suggests the potential presence of an excimer species. Indeed, this observation suggests that at low concentrations, the monomeric form of **2** dominates the system, whereas at higher concentrations, the excimeric form of **2** becomes the predominant luminescent species in the system.

6.3.1.2 Chloroform

The UV-Vis spectral examination of **2** in a chloroform medium exhibits a λ_{max} absorption at 387 nm, but only when the concentration is $\leq 1.0 \times 10^{4}$ M. At higher concentrations, a minor additional absorption feature, known as an excimeric absorption, manifests itself as a slight shoulder around 460 nm (see Figure 6.3A).

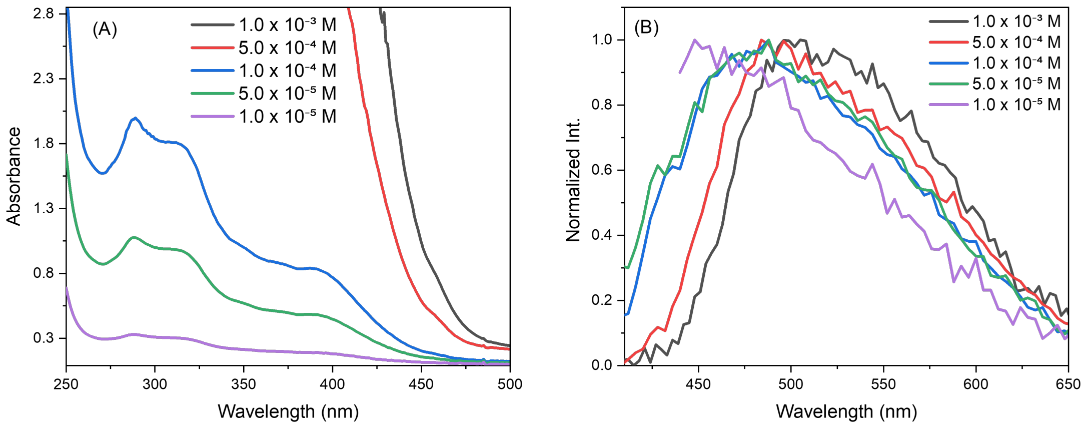

Figure 6.3: (A) UVVis absorption and (B) normalized fluorescence spectra of **2** measured at different concentrations in $CHCl_3$ ($\lambda_{ex} = 380$ nm).

In Figure 6.3B, the fluorescence emission of compound **2** in chloroform is presented across a range of concentrations, from low to high. When the concentration of **2** does not exceed 1.0×10^4 M, the emission spectrum exhibits a relatively narrow distribution centered around 466 nm. Upon increasing the concentration by a factor of five, a secondary peak emerges at 475 nm, resulting in a double-peak spectrum. Furthermore, doubling the concentration once more (i.e., 1.0×10^3 M) causes the lower-wavelength peak to disappear entirely, leaving behind a single, broad peak spanning from 493 to 544 nm. These findings confirm that the monomeric state of **2** predominates at lower concentrations. However, as the concentration increases, a competition arises between the monomeric and excimeric forms of **2**. In concentrated solutions, the prevailing species is the excimeric form. It is noteworthy that the fluorescence quantum yield of **2** in chloroform (Φ) is equal to 0.122 which is higher than that in DCM.

6.3.1.3 Ethyl acetate

The investigation of the absorption properties of compound **2** in ethyl acetate (EtOAc) demonstrates distinct behavior compared to other solvents. As previously mentioned, the absorption peak at λ_{max} is observed at 408 nm, with additional peaks occurring below 350 nm (Figure 6.4A).

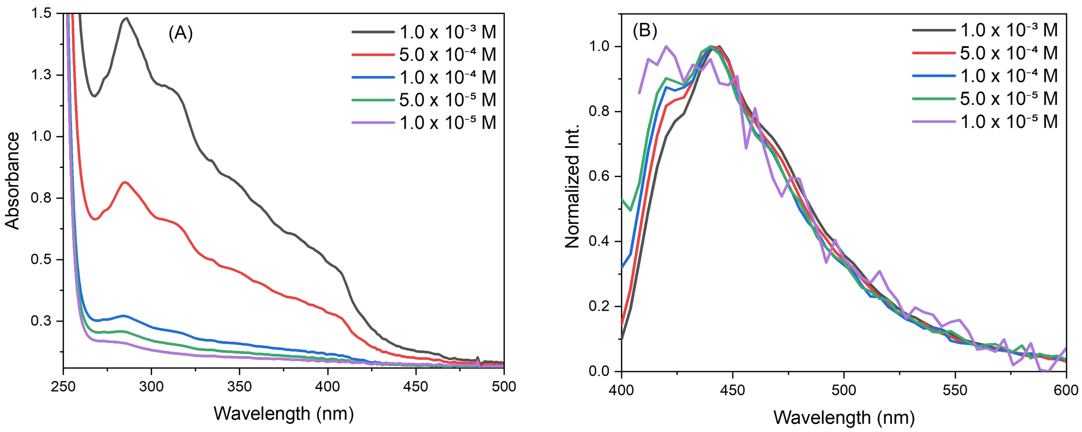

Figure 6.4: (A) UV-Vis absorption and (B) normalized fluorescence spectra of **2** measured at different concentrations in ethyl acetate ($\lambda_{ex} = 380$ nm).

Remarkably, the fluorescence analysis of **2** in EtOAc displays minimal dependence on concentration, characterized by a prominent peak at 440 nm and two smaller peaks at 420 nm and 468 nm. In Figure 6.4B, it is evident that the main peak remains unaffected by changes in concentration. However, the higher-wavelength shoulder exhibits a hyperchromic shift when the concentration increases, while the lower-wavelength shoulder undergoes a hyperchromic shift as the concentration decreases. Despite slight variations in the two shoulders with changes in concentration, the results obtained from UV-Vis and emission spectroscopic investigations of **2** in EtOAc do not provide conclusive evidence for the presence of exciplex, even at relatively higher concentrations. In addition, the quantum yield in ethyl acetate $\Phi = 0.233$, which is the highest value observed in all the studied solvents in this work.

6.3.1.4 ***N*,*N*-dimethylformamide (DMF)**

The UV-Vis absorption spectroscopy of compound **2** in DMF reveals the presence of a small shoulder-like peak at approximately 460 nm, along with a prominent peak at 388 nm. Interestingly, while the shoulder at 460 nm becomes more noticeable at higher concentrations, it persists even at lower concentrations, as depicted in Figure 6.5A.

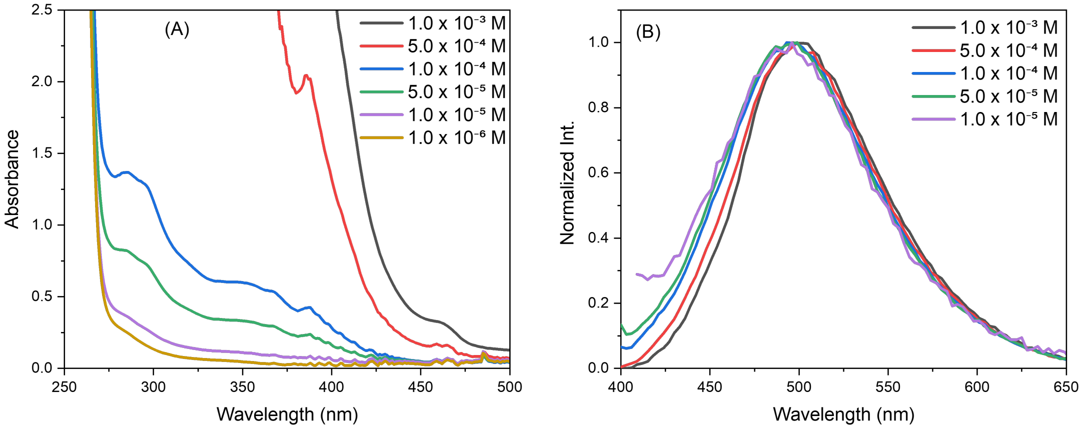

Figure 6.5: (A) UV-Vis absorption and (B) normalized fluorescence spectra of **2** measured at different concentrations in DMF ($\lambda_{ex} = 380$ nm).

Furthermore, the fluorescence emission of **2** in DMF exhibits a broad peak spanning approximately 470 nm to 515 nm across the entire range of studied concentrations, from 1.0×10^5 M to 1.0×10^3 M (Figure 6.5B). This observation indicates that the wavelength of emission remains independent of the concentration of the chromophore. Based on these findings, it can be inferred that the presence of excimeric forms can be observed even at low concentrations in DMF. Moreover, the observed quantum yield of **2** in DMF (Φ) is 0.217, which is the third highest value (after EtOAc with $\Phi = 0.233$, and DMSO with $\Phi = 0.224$) among the studied solvents in this work.

6.3.1.5 Dimethylsulfoxide (DMSO)

The UV-Vis spectroscopy of the system in DMSO reveals a maximum absorption peak at 382 nm, accompanied by a negligible shoulder at around 460 nm (see Figure 6.6A). The emission spectra, on the other hand, display a broad peak ranging from approximately 470 nm to 515 nm for concentrations exceeding 1.0×10^{5} M. However, at lower concentrations, a blueshift in the emission spectrum can be observed (see Figure 6.6B).

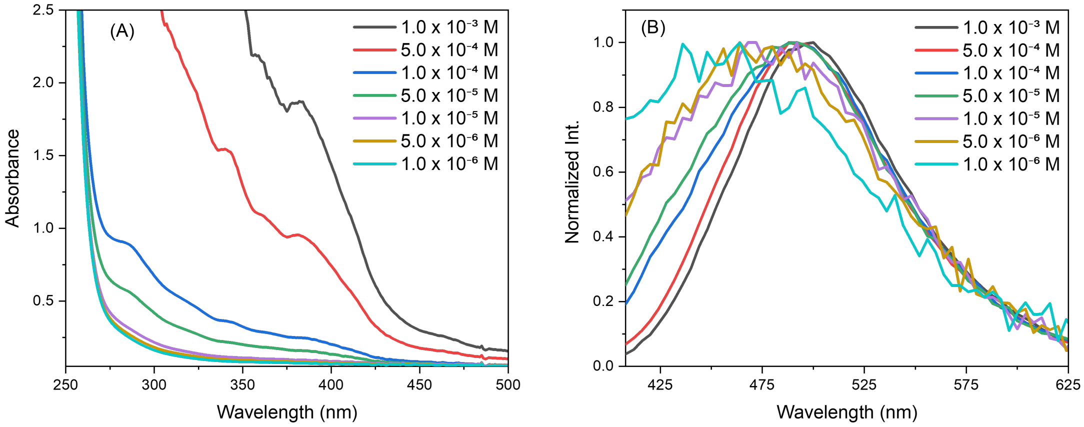

Figure 6.6: (A) UVVis absorption and (B) normalized fluorescence spectra of **2** measured at different concentrations in DMSO ($\lambda_{ex} = 380$ nm).

The concentration-dependent effect on the presence of an excimer in each solvent was examined. In DCM and chloroform, an excimer emerged at higher concentrations, suggesting its formation and abundance. However, in ethyl ethanoate, no conclusive evidence of exciplex formation was found, even at relatively higher concentrations. In contrast, fluorescence results demonstrated that the molecules of **2** exhibit a high tendency to aggregate so as to form the exciplex in polar solvents such as DMF and DMSO especially at higher concentrations. These observations indicate that the concentration plays a crucial role in the formation and stability of excimeric species in different organic solvents. Understanding the concentration-dependent behavior of excimers is essential for elucidating the photophysical properties and potential applications of the studied compound in various solvent environments.

6.3.2 Complexation with β- and γ-cyclodextrins

In order to obtain a deeper understanding of the emission behavior of **2**, the complexes of **2** with two naturally occurring CDs, which usually play the host roles in the literature,[172,330–336,338–341] β- and γ-CDs (Figure 6.7) have been formed. The evaluation of the interaction of **2** with β-CD and γ-CD using fluorescence spectroscopy will be discussed in the following sections.

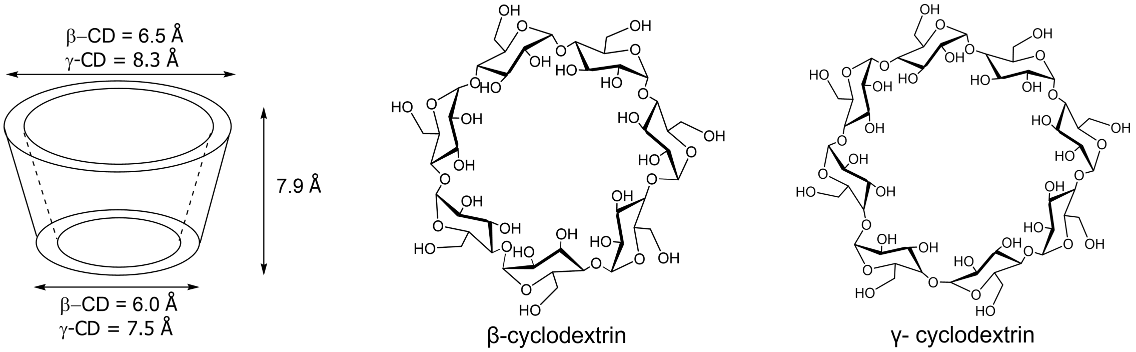

β-cyclodextrin

γ- cyclodextrin

Figure 6.7: The molecular structures, dimensions and schematic geometry of β- and γ-CDs.

6.3.2.1 β-Cyclodextrins

The UV-Vis absorption analysis of the complex formed between compound **2** and β-CD elucidated notable changes in the absorption properties. The effects of this complex formation as well as dilution with water on the UV-Vis absorption of **2** has been investigated and shown in Figure 6.8A. In the presence of β-CD, the peak at approximately 460 nm, observed in DMF, undergoes complete disappearance. Additionally, the peak observed at 388 nm in DMF experiences a blueshift by 7 nm upon complexation with β-CD.

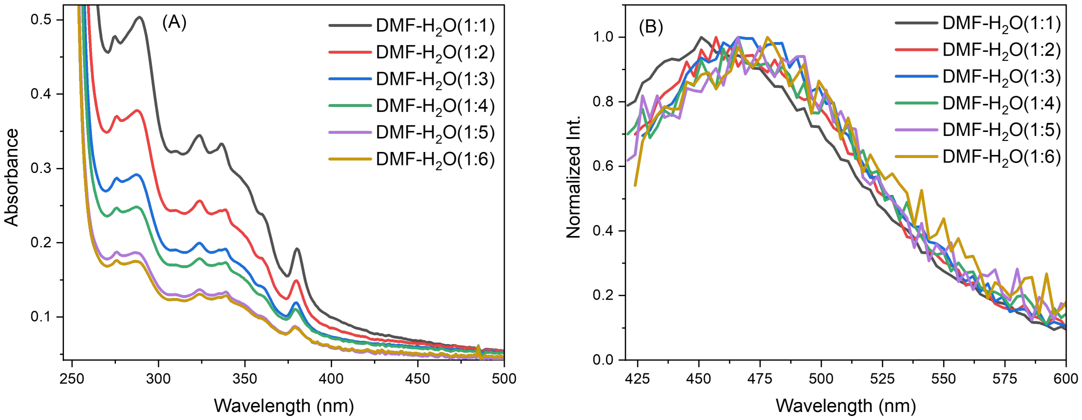

Figure 6.8: (A) UV-Vis absorption, and (B) Normalized fluorescence spectra of the complex of **2** (1.0×10^{-3} M) with β-CD (5.0×10^{-3} M) measured at different DMF/water v/v ratios ($\lambda_{ex} = 380$ nm).

The fluorescence studies of **2**/β-CD complex has been illustrated in Figure 6.8B. The complex shows a narrower (compared to that of **2** in DMF) emission spectrum starting from 430 to 475 nm. In addition, it shows a slightly red-shift upon dilution of DMF solution with water from 1:1 (v/v) to 1:6 (v/v) that can be attributed to the quenching effect of water. As it can be seen in Figure 6.8, diluting with water had no significant impact on the electronic transition properties of the system, confirming the formation of the inclusion complex of **2** with β-CD. The results demonstrate that β-CD only hosts one molecule of **2** rather than the excimer, as the **2**/β-CD emits light at much lower wavelength compared to pure **2** in DMF. Furthermore, the MALDI-TOF MS analysis showed that the **2**/β-CD complex formation ratio is 1:1 confirming the hosting of one molecule of **2** within the β-CD cavity (See the MALDI-TOF MS analysis results in supporting information of Chapter 6 in Appendix.).

6.3.2.2 γ-Cyclodextrins

The UV-Vis absorption investigation of the complex formed between compound **2** and γ-CD revealed similarities to the **2**/β-CD complex. The absorption spectrum of **2**/γ-CD, as depicted in Figure 6.9A, exhibited a maximum absorption peak at 380 nm, which is blue-shifted by 8 nm compared to the absorption peak of **2** in DMF. This blue-shift suggests alterations in the electronic structure and environment of **2** induced by the complexation with γ-CD. Furthermore, the dilution of **2**/γ-CD in a DMF/water (1:1, v/v) mixture did not demonstrate any significant impact on the UV-visible absorption study of the system. These observations indicate that the interaction between **2** and γ-CD, similar to β-CD, influences the absorption properties of **2** in terms of peak position but remains unaffected by dilution with water. The findings contribute to the understanding of the host-guest interactions between **2** and cyclodextrins with different cavity sizes and their effects on the photophysical behavior of the system.

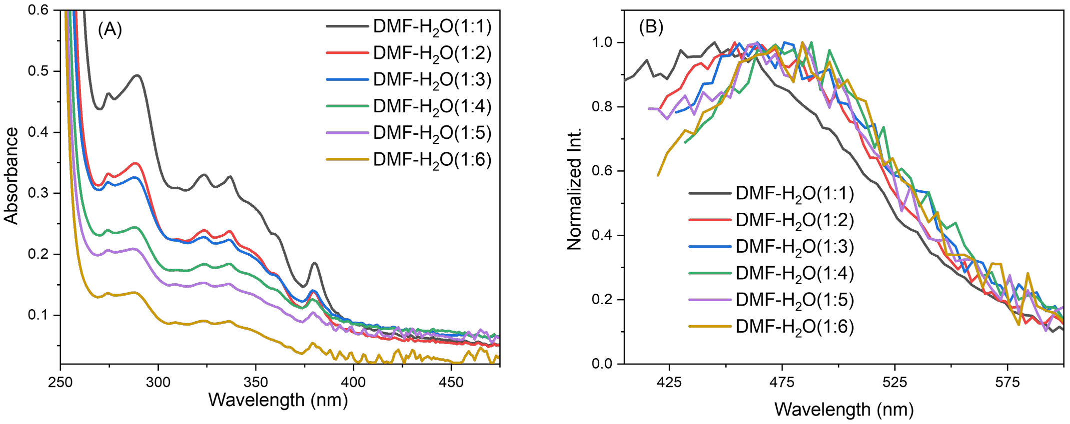

Figure 6.9: (A) UV-Vis absorption and (B) normalized fluorescence spectra of the complex of **2** (1.0×10^{-3} M) with γ-CD (5.0×10^{-3} M) measured at different DMF/water v/v ratios ($\lambda_{ex} = 380$ nm).

The emission behavior of the **2**/γ-CD complex was investigated, as depicted in Figure 6.9B. Similar to **2**/β-CD, the emission peak of **2**/γ-CD displayed a blue-shift compared to **2** in DMF, with a very broad peak ranging from approximately 410 nm to 475 nm. Dilution with water had a minimal impact, resulting in a slight red-shift towards longer wavelengths. This also confirms the formation of **2**/γ-CD inclusion complex, as diluting with water had no significant influences on the UV-Vis and fluorescence spectroscopies of the system. The quantum yield (Φ) of **2** in **2**/γ-CD is higher than that in **2**/β-CD with $\Phi = 0.103$ and $\Phi = 0.073$, respectively. The fluorescence results of the **2**/γ-CD indicated the presence of only one molecule of compound **2** inside the cavity of γ-CD as the host. These findings suggest that the 1.8 nm-difference between the cavity entrance of β-CD and γ-CD (refer to Scheme 6.7) is insufficient for the latter to accommodate the excimeric form of **2** within its cavity. This result has also been confirmed via the MALDI-TOF MS analysis showing the 1:1 ratio of **2**/γ-CD complex (refer to the supporting information of Chapter 6 in Appendix).

6.3.3 Theoretical studies

The UV-Vis absorption spectrum of product **2** has been examined through TD-DFT calculations utilizing M06-2X and CAM-B3LYP methods (Figure 6.10). The M06-2X calculations reveal an excellent agreement with the experimental data in the gas phase, DCM, chloroform, and DMF with simulated λ_{max} at 387, 392, 393, and 391 nm, respectively. In ethyl acetate, the maximum wavelength of **2** was calculated at 431 nm, while its second absorption peak was observed at 377 nm, which is close to its experimental λ_{max}. The detailed analysis of each absorption transition in different solvents reveals that in all cases, the HOMO to LUMO+1 transition has a higher oscillator strength compared to that of the HOMO to LUMO transition. This implies that the maximum absorption peak observed in the UV-Vis spectrum of compound **2** is mainly due to the HOMO to LUMO+1 transition, whereas the contribution of the HOMO-LUMO transition is relatively small. Even in ethyl acetate, where the calculated absorption at 377 nm is close to the experimental value, the absorption is predominantly due to the HOMO-LUMO+1 transition.

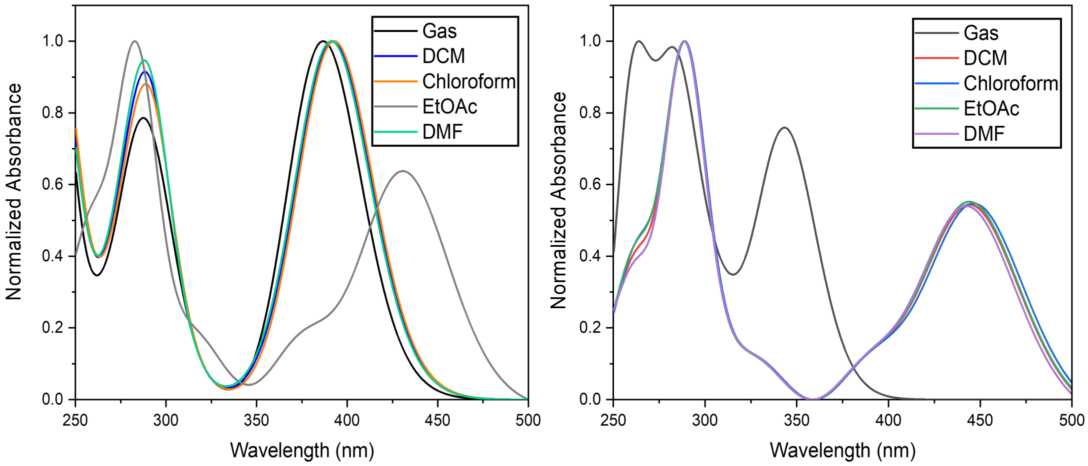

Figure 6.10: Simulated absorbance spectra of **2** calculated via M06-2X (left) and CAM-B3LYP (right) methods.

The maximum absorption wavelength of compound **2** as calculated through CAM-B3LYP was found to be between 443 nm and 447 nm in all the studied solvents. However, the second maximum wavelengths (observed as a shoulder in Figure 6.10 (right graph) between 392 nm in DMF to 394 nm in $CHCl_3$) were found to be consistent with the results obtained through M06-2X. Again, our CAM-B3LYP calculations indicate that the HOMO to LUMO+1 transition is the primary contributor to this absorption peak, which supports the conclusion that the experimental peak observed at around 390 nm is primarily due to this electronic transition.

Furthermore, to determine the fluorescence spectroscopic characteristics of product **2**, the M06-2X and CAM-B3LYP methods were employed. The results of the former method, presented in Figure 6.11, revealed emission λ_{max} values for the monomer in the gas phase at 462 nm. Notably, in $CHCl_3$, DMF, and DMSO solvents, the emissive λ_{max} was determined to be 445 nm, while in the ethyl acetate solvent system, the maximum emission was observed at 441 nm. These calculated values exhibit a high degree of agreement with the experimental results. However, a discrepancy was observed in DCM, where the calculated maximum emission was found to be 432 nm, differing from the experimentally observed value. Despite this discrepancy in DCM, the overall consistency between the calculated and experimental values using the M06-2X method suggests the reliability of the computational approach in predicting the fluorescence characteristics of **2** in various solvents.

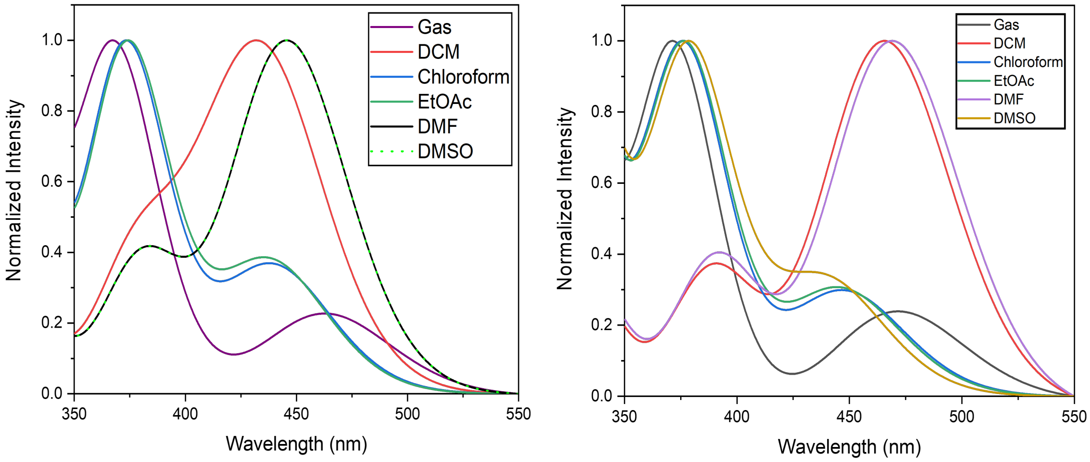

Figure 6.11: Simulated fluorescence spectra of **2** calculated via M06-2X (left) and CAM-B3LYP (right) methods.

The fluorescence spectroscopic characteristics of compound **2** were further investigated using the CAM-B3LYP method (Figure 6.11). The calculated emission λ_{max} values for the monomer in the gas phase appeared at 471 nm. In different solvents, the calculated maximum emission wavelengths were as follows: in DCM, 467 nm; in ethyl acetate, 451 nm; in DMF, 468 nm; in DMSO, 445 nm; and in chloroform, the calculated emissive peak was at 452 nm. Remarkably, the calculated λ_{max} in chloroform and DMF were found to be in excellent agreement with the experimental results. However, while the calculated values for the rest of the solvents did not exactly match the experimental values, they provided an overview of where the monomer emissive λ_{max} might be in those solvents.

6.3.3.1 Excimer formation analysis

In order to gain a more profound comprehension of the luminescence behavior of compound **2** in relation to its interaction, a TD-DFT analysis of its two distinct dimers in diverse spatial arrangements has been undertaken. The two dimer configurations, namely the π-dimer and T-dimer, have been identified with reference to the single crystal structure of the compound (Scheme 6.2).

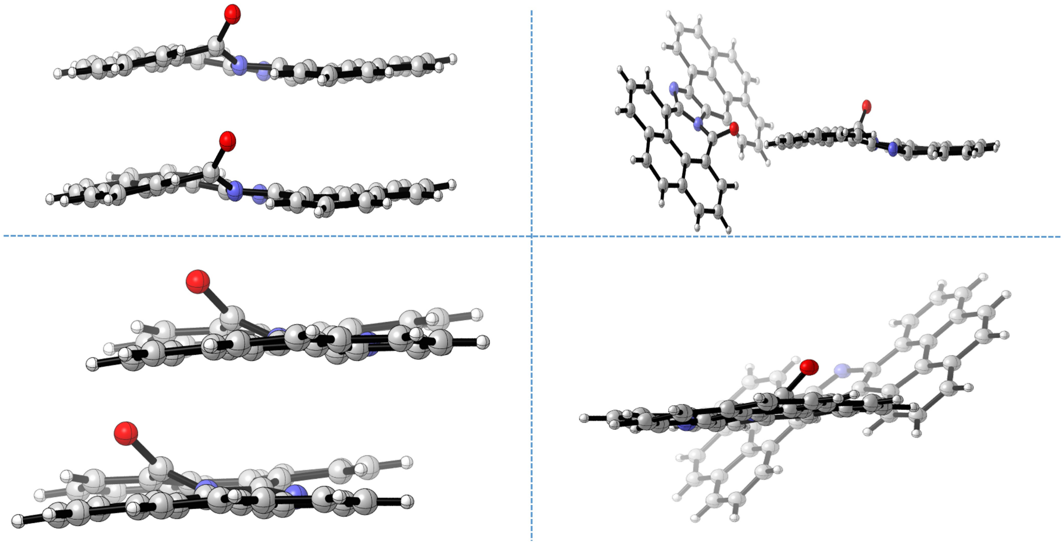

Scheme 6.2: Schematic illustration of π-dimer (left pictures) and T-dimer (right pictures) from different perspectives. The geometries have been originated from the crystalline packing pattern of **2**.

The computational results are summarized in Table 6.1. As stated earlier, the TD-DFT calculations conducted on the monomeric compound exhibited favorable agreement with the experimental data, particularly in chloroform, ethyl acetate, and DMF solvents. Since we have previously compared the theoretical fluorescence calculations with the experimental results for the monomer, we will now focus on the comparison between the theoretical (dimer) and the experimental (excimer) results (TD-DFT calculation results of π- and T-dimers are available in the Supporting Information of Chapter 6 in the Appendix).

In DCM, the experimental emission peak observed at 476 nm, while the theoretical emission peaks for the π-dimer and T-dimer were calculated at 445 nm and 426 nm, respectively. This indicates that the theoretical π-dimer prediction is in closer agreement with the experimental results compared to the T-dimer prediction.

Similarly, in chloroform, the experimental emission peak spanned from 487 to 544 nm, whereas the theoretical emission peaks for the π-dimer and T-dimer were calculated at 490 nm and 455 nm, respectively. The theoretical π-dimer emission peak aligns well with the experimental results, suggesting the accuracy of the computational approach in predicting the fluorescence behavior of the π-dimer species. In ethyl acetate, the experimental emission peak was observed from 440 to 460 nm, and the theoretical emission peaks for the π-dimer and T-dimer were calculated at 470 nm and 449 nm, respectively. Both π- and T-dimer predictions demonstrate good agreement with the experimental results. In DMF, the experimental emission peak was distributed from 475 to 529 nm, while the theoretical emission peaks for the π-dimer and T-dimer were calculated at 465 nm and 431 nm, respectively. Again, the calculated π-dimer emission peak closely matches the experimental data, and finally, in DMSO, the experimental emission peak was observed from 476 to 536 nm, while the theoretical emission peaks for the π-dimer and T-dimer were calculated at 543 nm and 430 nm, respectively. The theoretical π-dimer prediction, once again, displays a reasonable agreement with the experimental results, supporting the accuracy of the computational method in predicting the fluorescence properties. Overall, the comparison between the experimental and theoretical fluorescence results reveals that the π-dimer predictions generally provide a better agreement with the experimental data in most of the studied solvents. Therefore, our TD-DFT calculations demonstrate that the π-dimer spatial arrangement is responsible for the excimeric emission, as the fluorescence spectrum of this type of dimer emerges in a higher wavelength than that of the monomer in all solvents and aligns completely with the experimental excimeric emissions in chloroform and DMSO. Conversely,

Table 6.1: The comparison of the experimental and theoretical results of the fluorescence spectroscopy of compound **2**. The default calculations method is M06-2X. Numbers in parenthesis represent the results calculated in CAM-B3LYP method.

	Experimental results (nm)		**Theoretical results (nm)**		
	Monomer	**Excimer**	**Monomer**	**π-dimer**	**T-dimer**
DCM	448	476	432 (467)	445	426
$CHCl_3$	442-484	487-544	443 (452)	490	455
EtOAc	420-440	440-460	441 (451)	470	449
DMF	466-526	475-529	445 (468)	465	431
DMSO	456-532	476-536	445 (445)	543	430

the results show that the T-dimer interaction results in a decrease in the maximum emissive wavelength relative to that of the monomer, which serves as sufficient reason to discard the hypothesis that the T-dimer leads to excimeric emission.

6.3.3.2 CREST studies

In this section, a new program called CREST (the Grimme group's conformer rotamer ensemble sampling tool) which is designed for generating conformational ensembles of different types of molecules ranging from small to supramolecules will be introduced.[381] Unlike knowledge-based algorithms, CREST employs a direct sampling approach at a semiempirical quantum mechanical level, offering reasonable conformational energies for various chemical species.[384] Although CREST may not compete with chemoinformatics-driven methods in terms of computation final accuracy, its advantage lies in providing reliable conformational energies for any chemical system.[381,382] The program's algorithms are broadly applicable and can be used with any quantum chemical level, but semiempirical methods, such as GFNn-xTB,[384–386] are preferred due to their favorable accuracy-to-cost ratio.[384] Overall, CREST offers a valuable tool for exploring the chemical space and gaining insights into molecular conformations which is quite useful for the present study. In order to maintain the reliability of the output data coming from CREST calculations, we then applied DFT calculations on each one of the output conformer.

The CREST studies for $(\mathbf{2})_2$ starting from π-dimer provides us with 14 different conformers, while that of T-dimer offered 15 diverse ones. Next, the results for all the 29 conformers have been reoptimized by the DFT calculations using M06-2X/def2-SVP in the gas phase. The final results are summarized in Table 6.2.

Table 6.2: Relative conformational energies of $(\mathbf{2})_2$ calculated by the CREST method.

Compound	**Relative Gibbs Free Energy (kcal/mol)**
1	0.00
2	1.64
3	1.76
4	2.48
5	2.49
6	3.10
7	3.31
8	3.32
9	3.90
10	4.01
11	4.09
12	4.11
13	4.12
14	4.14
15	4.44
16	4.50
17	4.74
18	4.75
19	4.84
20	4.97
21	5.41
22	5.78
23	5.92
24	6.94

In the investigation of various output dimers for the studied compound, it was observed that the most stable conformer corresponds to a π-dimer (Figure 6.12). This finding is consistent with the TD-DFT fluorescence results, where the π-dimer exhibited higher maximum emission wavelengths compared to the T-dimer in all studied solvent environments. Furthermore, the simulated maximum fluorescence peaks for the π-dimer in all solvents were found to be in good agreement with the experimental results. Once again, our CREST study reaffirms that the π-dimer represents the thermodynamically favorable dimeric form of the studied compound. The calculated binding energy of the most stable conformer is determined to be –16.83 kcal/mol, providing compelling evidence that the formation of the π-dimer is thermodynamically favored. The structures of the second to fifth most stable conformers obtained from the CREST calculations are available in the Supporting Information of Chapter 6 in the Appendix.

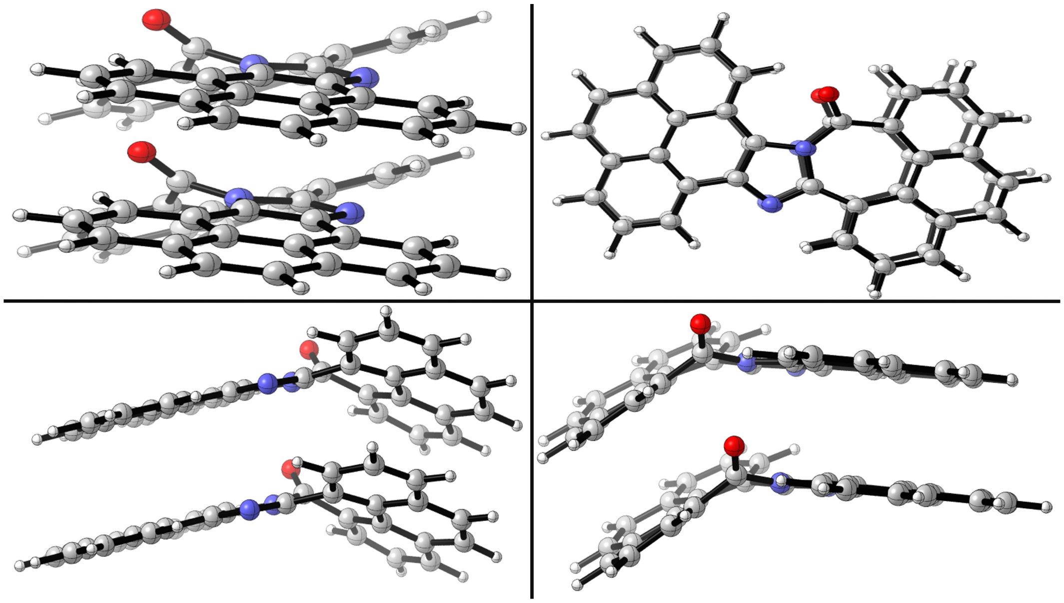

Figure 6.12: The geometry of the most stable conformer of $(\mathbf{2})_2$, represented from different views. The conformer was initially obtained using the CREST method and subsequently reoptimized in the gas phase using the M06-2X/def2-SVP method.

TD-DFT calculations were performed on the most stable conformer obtained from the CREST method in the gas phase (Figure 6.13). The maximum wavelength in the UV-Vis absorbance spectrum of the dimer was found to occur at 333 nm (black graph in Figure 6.13), and the λ_{max} of the fluorescence spectrum of the dimer was observed at 528 nm (red graph in Figure 6.13).

Indeed, it should be noted that while the fluorescence emission value is consistent with the experimentally observed range (refer to Table 6.1), the absorption value for the dimer deviates significantly from reality. According to the TD-DFT results of the most stable CREST dimer and those of the monomer, it can be concluded that the observed λ_{max} in the experimental UV-Vis spectroscopy is primarily due to light absorption by the monomer species, whereas the experimental emission λ_{max}

originates from either the exciplex formation of compound **2** in higher concentrations (Figure 6.13) or the monomer of **2** in diluted solutions (6.11). These findings shed light on the complex photophysical behavior of the compound and highlight the significance of exciplex formation in the observed fluorescence emission.

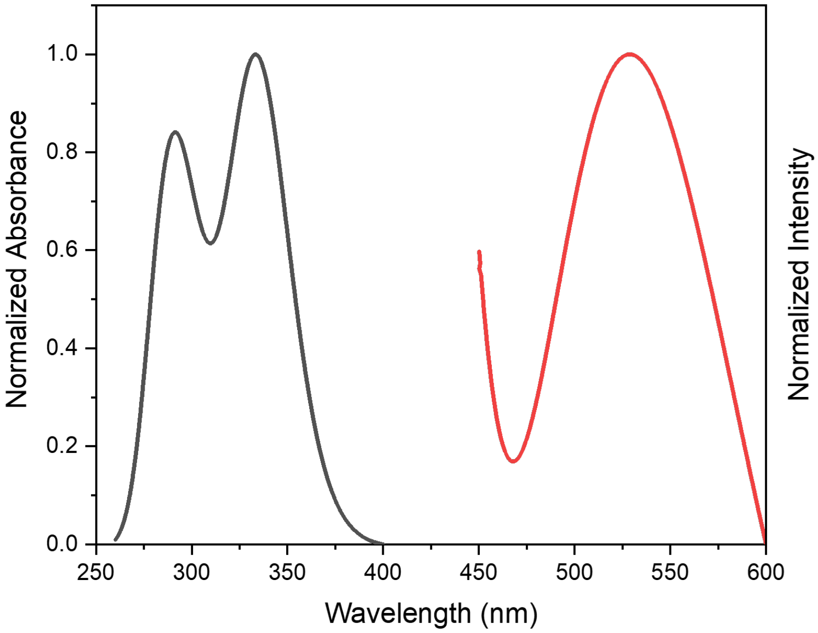

Figure 6.13: simulated normalized absorbance (black graph) and emission (red graph) spectra of the most stable conformer of $(\mathbf{2})_2$ calculated via M06-2X/def2-SVP method in the gas phase.

6.3.3.3 Effects of protonation on fluorescence properties

In this study, the effect of protonation on the emission behavior of **2** utilizing M06-2X and CAM-B3LYP methods was also investigated. Protonation specifically takes

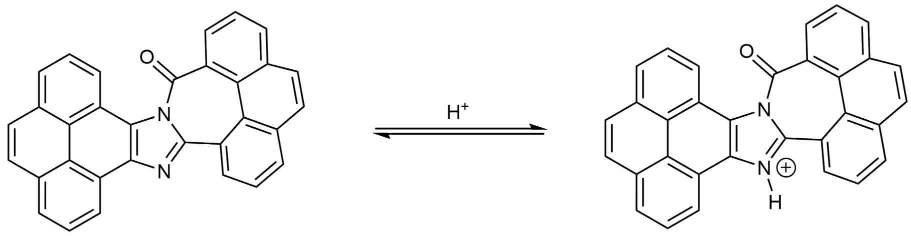

2 [**2** + H+]

Scheme 6.3: Protonation reaction of **2**.

place at the imidazolyl nitrogen position, considering it as the most basic site within the molecule, as depicted in Scheme 6.3. Experimental confirmation of this nitrogen atom being protonated in an acidic solution has been previously demonstrated in the tetra tert-butylated derivative of **2**.[321]

The fluorescence spectra of neutral **2** were obtained using both methods, by which similar λ_{max} values (463 nm in M06-2X vs. 471 nm in CAM-B3LYP) have been gained. Our calculations indicated that protonation would cause a redshift in the emission spectrum of the studied compound. Figure 6.14 shows that M06-2X calculations resulted in a 22 nm bathochromic shift (485 nm), while using the CAM-B3LYP method, we observed a 50 nm red-shift (521 nm) due to protonation. These observations, particularly the latter, agrees extensively with the experimental data of the tetra tert-butylated derivative of **2** discovered in 2019 in our group in which the protonation has led to the redshift of the emission spectrum from 513 nm in the neutral compound up to 530 nm upon the addition of ca. 3100 molar equivalence of trifluoroacetic acid.[321]

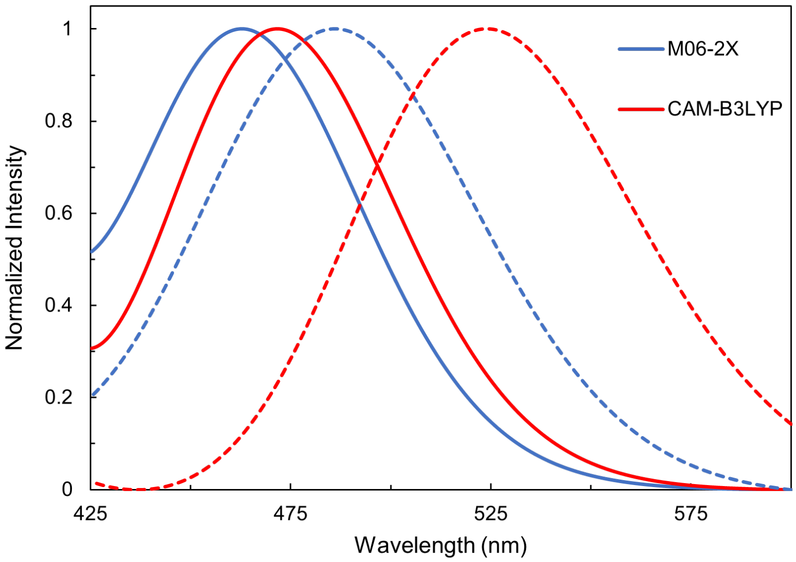

Figure 6.14: Simulated fluorescence spectra of **2** in neutral (solid lines) and protonated (dashed lines) states in gas phase.

6.4 Conclusion

In this study, a modified synthetic method has been developed to produce a π-conjugated compound from pyrene-4,5-dione via self-condensation reaction. The compound exhibited promising excimeric emissions in different organic solvents, including DCM, chloroform, ethyl acetate, DMF, and DMSO as confirmed by UV-Vis and fluorescence analyses. Additionally, the compound was successfully solubilized in the aqueous phase with the aid of β- and γ-CDs to form fluorescent host-guest complexes. It was found that while γ-CD possesses a larger cavity volume with a wider opening, both β- and γ-CDs can only host one molecule of the studied compound, resulting in only monomeric emissions in both complexes. However, the fluorescence spectroscopic analysis of both complexes showed a significant blueshift compared to that of pure chromophore, confirming the exciplex formation at higher concentrations in various organic solvents.

Moreover, X-ray single crystallographic studies were conducted to investigate the molecular structural and solid-state packing properties of this compound. The CREST calculations demonstrated that the π-stacked dimer is more stable than the T-dimer to be formed. Moreover, TD-DFT calculations showed that the experimental emission behavior of the chromophore at higher concentrations is due to the presence of the excimer in π-stacked format rather than in T-dimer pattern.

Overall, this new pyrene derivative has promising potential in the applications of chemical sensing and optoelectronics. The successful solubilization of the compound in aqueous media and the formation of fluorescent host-guest complexes suggest potential applications in biological and environmental sensing. The findings of this study pave the way for further research on the development and optimization of the chromophore for various optoelectronic applications.

Chapter 7

Conclusions and Future Work

7.1 Conclusions

This PhD dissertation presents the successful accomplishment of four projects. Three of these projects were carried out mainly via computational studies and analyses including density functional theory, time-dependent-DFT and other quantum mechanical methods included in the Gaussian suite of programs. These studies focused on a wide range of applicability involving the attractive and/or repulsive interactions of the redox-active dithiafulvene (DTF) and its derivatives with their neighboring molecules as well as the study of the mechanism of these interactions. In addition, the redox activity and electronic properties of different polycyclic aromatic hydrocarbon-substituted DTFs have been reported in this thesis. Moreover, the electronic adsorption and emission behaviour of a modified self-condensed pyrene-4,5-dione product via a combined experimental and theoretical investigations has been brought in this thesis. Throughout this thesis work, significant steps in understanding the fundamental mechanisms and interactions that underlie the behavior of the aforementioned compounds have been taken.

In Chapter 3, the utility of DTF derivatives in reducing Au(III) species to generate AuNPs in organic environments has been experimentally validated. Nevertheless, prior to the DFT studies presented in Chapter 3, theoretical investigations into key aspects remained unexplored. These aspects encompass the surface charge properties of AuNPs, the nature of Au–DTF cluster interactions, and the influence of solvents. We presented pioneering systematic examinations of the interactions between AuNPs and a representative DTF molecule in this chapter. Our findings demonstrated that DTF binds to the AuNP surface predominantly as a radical cation rather than in its neutral form. Notably, the sulfur and oxygen atoms within the DTF moiety emerge as the primary active binding sites for Au surface interactions. Additionally, our TD-DFT calculations revealed that electronic transitions within the AuNP component predominantly govern the UV–Vis absorption spectra of AuNP/DTF complexes. Furthermore, we explored the impact of open-shell and closed-shell configurations on the UV–Vis absorption of Au_n/DTF complexes. Lastly, our investigations underscore the critical role of solvents in influencing the stability of AuNP/DTF assemblies, emphasizing their significance in practical experiments.

Chapter 4 investigated the oxidative dimerization pathways of 1,4-dithiolene, 5-phenylmethylene in various media, which is considered a pioneering analysis in this context. Notably, a stable mixed-valence π-dimer forms between a neutral phenyl dithiafulvene (Ph-DTF) molecule and a Ph-DTF radical cation, whereas the ensuing mixed-valence σ-dimer product proves thermodynamically unfavorable. While direct dimerization of two Ph-DTF radical cations faces electrostatic repulsion in the gas phase, solvation in polar solvents mitigates this hindrance, enabling dimerization (i.e., thermodynamically favored). The impact of electron-withdrawing and electron-donating groups on dimerization kinetics and thermodynamics was also explored. *para*-positioned electron-donating groups adversely affect both aspects, in contrast to carboxylic acid and aldehyde substituents, which have beneficial effects. Additionally, the oxidation potential of 1,4-dithiolene, 5-phenylmethylene monomer and dimer with *para*-positioned electron-withdrawing and electron-donating groups was examined. Results indicated that electron-donating groups lower oxidation potential, while electron-withdrawing groups raise it across all media compared to the parent molecule. This chapter demonstrated the significant influence of solvation on dimerization reactions, highlighting the intricate interplay between solvent environments and reaction energetics.

In Chapter 5, the molecular structure and electronic properties of arene-substituted dithiafulvene (Ar–DTF) compounds were explored, revealing a trend where an increase in the size of the π-system leads to enhanced stability upon oxidation. It also showed that linearity is preferred upon oxidation in all studied Ar–DTFs which could be attributed to more efficient electron-hole distribution over the system. In addition, the central C_{DTF}–C–C_{AS} bond lengths tend to shift towards more sp^2 hybridized characteristics upon oxidation while the central bond angle shifts to increase for a better orbital overlap to have a more efficient electron mobility after oxidation. Exceptions to this trend were identified, highlighting the significance of specific molecular geometries in influencing oxidation potentials. Furthermore, our studies revealed that the size of π moiety is inversely proportional to the oxidation potential in Ar–DTFs. Compounds **13** and **14** are excluded from this trend due to their structural limitations. The study of optical properties also revealed the direct relationship between π moiety size and the increase in the maximum absorption wavelength. These results also proved that the chemical reactivity of Ar–DTFs will significantly impacted directly by increase in the π moiety size. Charge transfer calculations were conducted using five different population analysis methods. Our findings revealed that as the π moiety of the molecule increases in size, it becomes more stable as the electron-hole is distributed more efficiently throughout the molecule structure. This phenomenon leads to a reduction in the oxidation potential, making the compound more prone to oxidation. The study of spin density over the whole Ar–DTF systems showed greater quota for the DTF moiety compared to the π moiety of the system both in gas and solution phases. Moreover, the charge distribution analysis demonstrated that the DTF moiety carries a positive charge, while the π sector bears a negative charge within the molecule. When the system undergoes solvation and/or oxidation, the positive charge on the DTF moiety tends to increase, while the negative charge on the π moiety decreases. The investigation in the gap between the frontier molecular orbitals showed an indirect relationship with the π moiety size in Ar–DTFs both in neutral and radical cation oxidation states.

Finally, in Chapter 6, a modified synthetic method to produce a π-conjugated compound from pyrene-4,5-dione self-condensation reaction was reported, demonstrating promising excimeric emissions in various organic solvents and aqueous media. The compound was also effectively rendered soluble in the aqueous phase by utilizing β- and γ-CDs to form fluorescent host-guest complexes. X-ray single crystallographic studies and TD-DFT calculations provided deeper insights into the molecular structural and solid-state packing properties, supporting the formation of excimers in π-

stacked formats. CREST analysis demonstrated that the π-stacked dimer was more stable than the T-dimer configuration. Moreover, TD-DFT calculations indicated that the observed emission behavior at higher concentrations stemmed from excimer presence in a π-stacked arrangement, rather than a T-dimer pattern.

7.2 Future works

The findings in Chapter 3 serve as essential guidance for further experimental exploration of AuNPs with controlled size, morphology, and novel functionalities arising from DTF ligands. Building upon the results in this chapter, there remains ample room for further exploration into the interactions between π-conjugated ligands and AuNPs. The effect of different ligand structures, electronic properties, and steric configurations on the binding affinity and stability of ligand-AuNP assemblies necessitates systematic investigation. In particular, understanding the interplay between ligand-induced electronic changes and their impact on AuNP properties can facilitate the rational design of multifunctional AuNPs tailored for specific applications, such as catalysis, sensing, and biomedicine. In this chapter, the elucidation of the intricate mechanism underlying the stabilization of AuNPs through DTF derivatives has been a central focus. Nevertheless, it is imperative to acknowledge that certain gaps persist within this domain. Primarily, owing to the inherent constraints of computational methodologies, particularly with respect to time and cost resources, the imperative to extend our investigations to encompass larger AuNPs remains evident. In fact, to authentically mimic the conditions encountered in experimental settings, an imperative requirement emerges for the execution of computational simulations entailing AuNP systems comprising more than 100 Au atoms encapsulated by multiple DTF molecules. Furthermore, it is noteworthy to highlight that our computational analyses, particularly in the context of certain Au_n/DTFs, notably Au_7/DTF and Au_8/DTF, have encountered irregularities and errors in specific solution calculations. The thorough examination of these anomalies is commanding, thereby necessitating further, meticulous examination to resolve these issues. The investigation of such larger clusters not only holds the promise of enriching our understanding of the intricate interplay between theory and experimentation but also sets the stage for demanding comparisons between theoretical predictions and experimental observations, thereby advancing the field of gold nanoparticle interactions.

In spite of our systematic computational investigations on the properties of various Ph-DTF dimers, both in the mixed-valence radical cation and dication states in Chapter 4, it is important to acknowledge that certain gaps continue to persist in our comprehension of the different derivatives of Ph-DTF dimerization. This ongoing endeavor has been principally facilitated through the application of DFT, ADMP, and molecular dynamics simulations. However, it is imperative to recognize that these studies represent only the initial steps towards a more profound comprehension of the attractive and repulsive forces that scheme the dimerization phenomenon. Prospective avenues of research beckon us to delve deeper into the field of Ph-DTF dimerization, fortified by a synergistic compound of advanced computational methodologies and experimental techniques. Future research could focus deeper into the role of different solvents and their properties in facilitating and modulating various chemical reactions involving π-conjugated compounds. Advanced computational methodologies and experimental techniques can provide valuable insights into solvent and other DTF derivatives effects on reaction pathways, equilibria, and kinetics, thereby charting new views in the realm of TTF chemistry.

In addition, the exploration of arene-substituted dithiafulvene (Ar–DTF) compounds in Chapter 5 has led to significant findings regarding the interplay between molecular structure, electronic properties, and oxidation stability. It was discovered that an increase in the size of the π-system generally leads to enhanced stability upon oxidation. This is attributed to larger π moieties promoting efficient electron-hole distribution, thereby reducing oxidation potential. However, exceptions to this trend were identified, emphasizing the role of specific molecular geometries in influencing oxidation potentials. Overall, the systematic exploration of the structure–property relationships of Ar–DTF compounds holds promise for tailoring their electronic and optical properties. The knowledge gained from this study can be leveraged to design and engineer Ar–DTF compounds with desired electronic properties leading to the discovery of new Ar–DTF compounds with unique functionalities and applications in optoelectronics, photonics, and molecular sensing. While this work has contributed to the advancement of the understanding in this area, several promising avenues for future research and remaining gaps in the field can be identified. Primarily, a detailed investigation in the exceptions to the trends identified in our study, particularly compounds **13** and **14**. Understanding the structural limitations and unique properties of these compounds can provide a deeper insight into the factors governing oxidation potentials.

Furthermore, exploration of Ar–DTF compounds with even larger π-systems to corroborate and refine the observed trends is also missing. This could involve synthesizing and characterizing new compounds with varying π moiety sizes. Also, the study of how the optical properties of Ar–DTFs are affected by different environmental conditions, such as varying solvents or temperatures can be beneficial. This can help elucidate the practical applicability of these compounds in different contexts. Future research can also delve into the specific mechanisms of charge transfer in Ar–DTF compounds in order to investigate how different structural elements influence charge transfer and stability, shedding light on potential applications in molecular electronics or sensing.

Moreover, the study of the effects of functionalization or modification of Ar–DTF compounds on their electronic properties can be a future research topic. This could open up avenues for tailoring these compounds for specific applications. The exploration of advanced quantum chemistry methods or computational techniques to gain deeper insights into the electronic properties, charge distribution, and orbital characteristics of Ar–DTF compounds will also be an interesting research topic. By addressing these future research directions and remaining gaps, one can contribute further to the comprehensive understanding and potential applications of Ar–DTFs in various scientific and technological domains.

Finally, the potential of the pyrene derivative introduced in Chapter 6 extends to chemical sensing and optoelectronics applications. Successful solubilization in aqueous media and the creation of fluorescent host-guest complexes suggest potential roles in biological and environmental sensing. To develop these findings, further investigations could encompass the exploration of other similar chromophores and their potential for excimer formation. A broader range of host molecules and environments could be considered to expand the applicability of these excimeric systems in sensing and materials science. Indeed, there are several promising directions for future research and remaining gaps in this field. Firstly, the excimer formation can be investigated more comprehensively, exploring various factors such as temperature, pressure, and the presence of different solutes. This can provide a deeper understanding of the conditions that optimize excimeric emissions. On the other hand, the selection of a host with a larger cavity opening than that of $\beta-$ and $\gamma-$CDs can set the stage for a more effective understanding of exciemric behavior of the chromophore. As previously mentioned, given the successful solubilization in aqueous media, this can be led to the compound potential applications in biological sensing, such as fluorescence-based assays for biomolecules or cellular imaging.

Bibliography

[1] Zhu, H.; Dronamraju, V.; Xie, W.; More, S. S. Sulfur-containing therapeutics in the treatment of Alzheimer's disease. *Med. Chem. Res.* **2021**, *30*, 305–352.

[2] Gomtsyan, A. Heterocycles in drugs and drug discovery. *Chem. Heterocycl. Compd.* **2012**, *48*, 7–10.

[3] Broughton, H. B.; Watson, I. A. Selection of heterocycles for drug design. *J. Mol. Graph. Model.* **2004**, *23*, 51–58.

[4] Jørgensen, T.; Hansen, T. K.; Becher, J. Tetrathiafulvalenes as building-blocks in supramolecular chemistry. *Chem. Soc. Rev.* **1994**, *23*, 41–51.

[5] Bryce, M. R.; Murphy, L. C. Organic metals. *Nature* **1984**, *309*, 119–126.

[6] Nielsen, M. B.; Lomholt, C.; Becher, J. Tetrathiafulvalenes as building blocks in supramolecular chemistry II. *Chem. Soc. Rev.* **2000**, *29*, 153–164.

[7] Bryce, M. R. Functionalised tetrathiafulvalenes: new applications as versatile π-electron systems in materials chemistry. *J. Mater. Chem.* **2000**, *10*, 589–598.

[8] Iyoda, M.; Hasegawa, M.; Miyake, Y. Bi-TTF, bis-TTF, and related TTF oligomers. *Chem. Rev.* **2004**, *104*, 5085–5114.

[9] Perez, E. M.; Illescas, B. M.; Herranz, M. Á.; Martin, N. Supramolecular chemistry of π-extended analogues of TTF and carbon nanostructures. *New J. Chem.* **2009**, *33*, 228–234.

[10] Martín, N. Tetrathiafulvalene: the advent of organic metals. *Chem. Commun.* **2013**, *49*, 7025–7027.

[11] Bendikov, M.; Wudl, F.; Perepichka, D. F. Tetrathiafulvalenes, oligoacenenes, and their buckminsterfullerene derivatives: The brick and mortar of organic electronics. *Chem. Rev.* **2004**, *104*, 4891–4946.

[12] Wudl, F.; Smith, G.; Hufnagel, E. Bis-1,3-dithiolium chloride: an unusually stable organic radical cation. *J. Chem. Soc. D, Chem. Commun.* **1970**, 1453–1454.

[13] Rovira, C. Bis (ethylenethio) tetrathiafulvalene (BET-TTF) and related dissymmetrical electron donors: from the molecule to functional molecular materials and devices (OFETs). *Chem. Rev.* **2004**, *104*, 5289–5318.

[14] Yamada, J.; Sugimoto, T. *TTF chemistry: fundamentals and applications of tetrathiafulvalene*; Springer: Berlin Heidelberg, 2004.

[15] Canevet, D.; Sallé, M.; Zhang, G.; Zhang, D.; Zhu, D. Tetrathiafulvalene (TTF) derivatives: key building-blocks for switchable processes. *Chem. Commun.* **2009**, 2245–2269.

[16] Segura, J. L.; Martín, N. New concepts in tetrathiafulvalene chemistry. *Angew. Chem. Int. Ed.* **2001**, *40*, 1372–1409.

[17] Carlier, R.; Hapiot, P.; Lorcy, D.; Robert, A.; Tallec, A. Electrosynthesis and redox behavior of vinylogous TTF displaying strong conformational changes associated with electron transfers. *Electrochim. Acta* **2001**, *46*, 3269–3277.

[18] Spruell, J. M. et al. Highly stable tetrathiafulvalene radical dimers in [3]catenanes. *Nat. Chem.* **2010**, *2*, 870–879.

[19] Logtenberg, H.; van der Velde, J. H.; de Mendoza, P.; Areephong, J.; Hjelm, J.; Feringa, B. L.; Browne, W. R. Electrochemical switching of conductance with diarylethene-based redox-active polymers. *J. Phys. Chem. C* **2012**, *116*, 24136–24142.

[20] Sauvage, J.-P.; Duplan, V.; Niess, F. In *Macrocyclic and Supramolecular Chemistry: How Izatt–Christensen award winners shaped the field*; Izatt, R. M., Ed.; Wiley Online Library, 2016; Chapter 22, pp 444–464.

[21] Izatt, R. M.; Bradshaw, J. S.; Izatt, S. R.; Harrison, R. G. *Macrocyclic and Supramolecular Chemistry*; John Wiley Sons, Ltd, 2016; Chapter 1, pp 1–9.

[22] Stoddart, J. F. The master of chemical topology. *Chem. Soc. Rev.* **2009**, *38*, 1521–1529.

[23] Peplow, M. The tiniest Lego: a tale of nanoscale motors, rotors, switches and pumps. *Nature* **2015**, *525*, 18–21.

[24] Chen, G.; Mahmud, I.; Dawe, L. N.; Zhao, Y. Acetylenic phenyldithiafulvene: a versatile synthon for TTFV-Based macromolecules. *Org. Lett.* **2010**, *12*, 704–707.

[25] Solovyeva, V.; Keller, K.; Huth, M. Organic charge transfer phase formation in thin films of the BEDT-TTF/TCNQ donor–acceptor system. *Thin Solid Films* **2009**, *517*, 6671–6676.

[26] Massue, J.; Ghilane, J.; Bellec, N.; Lorcy, D.; Hapiot, P. Facile electrochemical generation of polyoxyethyl-vinylogous tetrathiafulvalene films. *Electrochem. Commun.* **2007**, *9*, 677–682.

[27] Simonsen, K. B.; Becher, J. Tetrathiafulvalene thiolates: important synthetic building blocks for macrocyclic and supramolecular chemistry. *Synlett* **1997**, *1997*, 1211–1220.

[28] Bryce, M. R. Current trends in tetrathiafulvalene chemistry: towards increased dimensionality. *J. Mater. Chem.* **1995**, *5*, 1481–1496.

[29] Kao, J.; Eyermann, C.; Southwick, E.; Leister, D. A systematic approach to calculate molecular properties of organosulfur compounds containing the carbon-sulfur (Csp2-S) bond. *J. Am. Chem. Soc.* **1985**, *107*, 5323–5332.

[30] Benassi, R.; Taddei, F. Ground-state molecular stabilization of substituted ethylenes. A theoretical mo ab-initio thermochemical study. *J. Mol. Struc. Theochem* **2001**, *572*, 169–183.

[31] Nielsen, M. B.; Sauer, S. P. On the aromaticity of tetrathiafulvalene cations. *Chem. Phys. Lett.* **2008**, *453*, 136–139.

[32] Kirmse, W.; Horner, L. Über lichtreaktionen VIII. Photolyse von 1.2.3-thiodiazolen. *Justus Liebigs Ann. Chem.* **1958**, *614*, 4–18.

[33] Mayer, R.; Kröber, H. Oxydative dimerisierung von 1,4-dithiafulvenen (2-methylen-1,3-dithiolen). *J. Prakt. Chem.* **1974**, *316*, 907–912.

[34] Ohta, A.; Yamashita, Y. Oxidative intramolecular cyclization of 2,2-bis (1,4-dithiafulven-6-yl)-3,3-bithienyls affording novel bis (1,3-dithiole) electron donors. *J. Chem. Soc., Chem. Commun.* **1995**, 1761–1762.

[35] Yamashita, Y.; Tomura, M.; Badruz Zaman, M. Synthesis and properties of novel tetrathiafulvalene vinylogues. *Chem. Commun.* **1998**, 1657–1658.

[36] Müller, H.; Salhi, F.; Divisia-Blohorn, B. Bis-substituted tetrathiapentalenes—novel building blocks for extended tetrathiafulvalenes and conducting polymers. *Tetrahedron Lett.* **1997**, *38*, 3215–3218.

[37] Massue, J.; Bellec, N.; Guerro, M.; Bergamini, J.-F.; Hapiot, P.; Lorcy, D. Crown ether vinylogous tetrathiafulvalene receptors: Complexation interference on the molecular movements triggered by electron transfer. *J. Org. Chem.* **2007**, *72*, 4655–4662.

[38] Lakshmikantham, M.; Cava, M. P.; Carroll, P. J. Novel oxidative rearrangement of o-xylene-. alpha.,. alpha.'-diylidenebis (4,5-dicarbomethoxy-1,3-dithiole). *J. Org. Chem.* **1984**, *49*, 726–728.

[39] Frère, P.; Gorgues, A.; Jubault, M.; Riou, A.; Gouriou, Y.; Roncali, J. Electrochemically induced intramolecular cyclization of 1,2-bis (1,4-dithiafulven-6-yl) benzenes. *Tetrahedron Lett.* **1994**, *35*, 1991–1994.

[40] Guerro, M.; Roisnel, T.; Pellon, P.; Lorcy, D. Redox-active dithiaful-

venyldiphenylphosphine as a mono-or bidentate ligand: intramolecular coupling reaction in the coordination sphere of a metal carbonyl fragment. *Inorg. Chem.* **2005**, *44*, 3347–3355.

[41] Guerro, M.; Pham, N. H.; Massue, J.; Bellec, N.; Lorcy, D. New redox active ligands involving a tetrathiafulvalene vinylogue backbone. *Tetrahedron* **2008**, *64*, 5285–5290.

[42] Gontier, E.; Bellec, N.; Brignou, P.; Gohier, A.; Guerro, M.; Roisnel, T.; Lorcy, D. Pyridyldithiafulvenes as precursors of coordination-driven self-assembled redox active macrocycle. *Org. Lett.* **2010**, *12*, 2386–2389.

[43] Benahmed-Gasmi, A.; Frère, P.; Roncali, J.; Elandaloussi, E.; Orduna, J.; Garin, J.; Jubault, M.; Gorgues, A. Oxidative dimerization of 2-(1,4-dithiafulven-6-yl) thiophenes: an alternative route towards extensively π-conjugated tetrathiafulvalene analogs. *Tetrahedron Lett.* **1995**, *36*, 2983–2986.

[44] Lorcy, D.; Carlier, R.; Robert, A.; Tallec, A.; Le Maguerès, P.; Ouahab, L. Electrochemical synthesis of extended TTF. *J. Org. Chem.* **1995**, *60*, 2443–2447.

[45] Hascoat, P.; Lorcy, D.; Robert, A.; Carlier, R.; Tallec, A.; Boubekeur, K.; Batail, P. Formation of attractive π-redox cyclophanes. *J. Org. Chem.* **1997**, *62*, 6086–6089.

[46] Hapiot, P.; Lorcy, D.; Tallec, A.; Carlier, R.; Robert, A. Mechanism of dimerization of 1,4-dithiafulvenes into TTF vinylogues. *J. Phys. Chem.* **1996**, *100*, 14823–14827.

[47] Abdollahi, M. F.; Zhao, Y. Recent advances in dithiafulvenyl-functionalized organic conjugated materials. *New J. Chem.* **2020**, *44*, 4681–4693.

[48] Hartzler, H. D. 2-Benzylidene-1,3-dithioles. Remarkably rapid Wittig reaction. *J. Am. Chem. Soc.* **1971**, *93*, 4961–4962.

[49] Guerro, M.; Lorcy, D. A simple route to novel functionalized tetrathiafulvalene vinylogues. *Tetrahedron Lett.* **2005**, *46*, 5499–5502.

[50] Lakshmikantham, M.; Cava, M. P. Some novel transformations of 1,4-dithiafulvenes. *J. Org. Chem.* **1981**, *46*, 3246–3249.

[51] Sarhan, A. A.; Bolm, C. Iron (III) chloride in oxidative C–C coupling reactions. *Chem. Soc. Rev.* **2009**, *38*, 2730–2744.

[52] Shahrokhi, F.; Abdollahi, M. F.; Zhao, Y. A comparative study of redox-active dithiafulvenyl-functionalized 1,3,6,8-tetraphenylpyrene derivatives. *J. Org. Chem.* **2021**, *86*, 12723–12736.

[53] Spies, H.; Gewald, K.; Mayer, R. Zur reaktion von natriumphenylacetylid mit schwefel oder selen und heterokumulenen. *J. Prakt. Chem.* **1971**, *313*, 804–810.

[54] Mulla, K.; Zhao, Y. When dithiafulvenyl functionalized π-conjugated oligomers meet fullerenes and single-walled carbon nanotubes. *J. Mater. Chem. C* **2013**, *1*, 5116–5127.

[55] Fu, H.; Zhao, B.; Zhu, W. Elemental iodine mediated synthesis of thiadiazole-based dithiafulvalene donors via C (sp2)–S formation. *Tetrahedron Lett.* **2019**, *60*, 124–128.

[56] Wang, Y.; Zhao, Y. Dithiafulvenyl-substituted phenylacetylene derivatives: synthesis and structure–property–reactivity relationships. *Org. Biomol. Chem.* **2015**, *13*, 9575–9579.

[57] Wang, C.; Flinn, C.; Zhao, Y. Intramolecular alkyne–dithiolium cycloaddition: a joint experimental and DFT mechanistic study. *RSC Adv.* **2017**, *7*, 36623–36631.

[58] Alévêque, O.; Leriche, P.; Cocherel, N.; Frère, P.; Cravino, A.; Roncali, J. Star-shaped conjugated systems derived from dithiafulvenyl-derivatized triphenylamines as active materials for organic solar cells. *Sol. Energy Mater. Sol. Cells* **2008**, *92*, 1170–1174.

[59] Guo, K.; Yan, K.; Lu, X.; Qiu, Y.; Liu, Z.; Sun, J.; Yan, F.; Guo, W.; Yang, S. Dithiafulvenyl unit as a new donor for high-efficiency dye-sensitized solar cells: synthesis and demonstration of a family of metal-free organic sensitizers. *Org. Lett.* **2012**, *14*, 2214–2217.

[60] Wu, Y.; Zhang, Q.; Li, J.; Tian, X.; Li, D.; Lu, X.; Xu, B.; Wu, Y.; Guo, K. Regulation of dithiafulvene-based molecular shape and aggregation on TiO_2 for high efficiency dye-sensitized solar cells. *J. Mater. Chem. C* **2019**, *7*, 1974–1981.

[61] Wu, M.; Li, J.; Zhang, R.; Tian, X.; Han, Z.; Lu, X.; Guo, K.; Liu, Z.; Wang, Z. Synthesis and properties of dithiafulvenyl functionalized spiro [fluorene-9, 9-xanthene] molecules. *Org. Lett.* **2018**, *20*, 780–783.

[62] Bumm, L.; Arnold, J. J.; Cygan, M.; Dunbar, T.; Burgin, T.; Jones, L.;

Allara, D. L.; Tour, J. M.; Weiss, P. Are single molecular wires conducting? *Science* **1996**, *271*, 1705–1707.

[63] Yaliraki, S.; Kemp, M.; Ratner, M. A. Conductance of molecular wires: influence of molecule-electrode binding. *J. Am. Chem. Soc.* **1999**, *121*, 3428–3434.

[64] Leary, E.; La Rosa, A.; González, M. T.; Rubio-Bollinger, G.; Agraït, N.; Martín, N. Incorporating single molecules into electrical circuits. The role of the chemical anchoring group. *Chem. Soc. Rev.* **2015**, *44*, 920–942.

[65] Perrin, M. L.; Burzurí, E.; van der Zant, H. S. Single-molecule transistors. *Chem. Soc. Rev.* **2015**, *44*, 902–919.

[66] Xiang, D.; Wang, X.; Jia, C.; Lee, T.; Guo, X. Molecular-scale electronics: from concept to function. *Chem. Rev.* **2016**, *116*, 4318–4440.

[67] Sørensen, J. K.; Vestergaard, M.; Kadziola, A.; Kilså, K.; Nielsen, M. B. Synthesis of oligo (phenyleneethynylene)-tetrathiafulvalene cruciforms for molecular electronics. *Org. Lett.* **2006**, *8*, 1173–1176.

[68] Vestergaard, M.; Jennum, K.; Sørensen, J. K.; Kilså, K.; Nielsen, M. B. Synthesis and characterization of cruciform-conjugated molecules based on tetrathiafulvalene. *J. Org. Chem.* **2008**, *73*, 3175–3183.

[69] Jennum, K.; Vestergaard, M.; Pedersen, A. H.; Fock, J.; Jensen, J.; Santella, M.; Led, J. J.; Kilså, K.; Bjørnholm, T.; Nielsen, M. B. Synthesis of

oligo (phenyleneethynylene) s with vertically disposed tetrathiafulvalene units. *Synthesis* **2011**, *2011*, 539–548.

[70] Jennum, K.; Nielsen, M. B. Tetrathiafulvalene-based cruciform molecules. *Chem. Lett.* **2011**, *40*, 662–667.

[71] Schou, S. S.; Parker, C. R.; Lincke, K.; Jennum, K.; Vibenholt, J.; Kadziola, A.; Nielsen, M. B. On the phosphite-mediated synthesis of dithiafulvenes and π-extended tetrathiafulvalenes. *Synlett* **2013**, *24*, 231–235.

[72] Wei, Z.; Hansen, T.; Santella, M.; Wang, X.; Parker, C. R.; Jiang, X.; Li, T.; Glyvradal, M.; Jennum, K.; Glibstrup, E., et al. Molecular heterojunctions of oligo (phenylene ethynylene)s with linear to cruciform framework. *Adv. Funct. Mater.* **2015**, *25*, 1700–1708.

[73] Parker, C. R.; Leary, E.; Frisenda, R.; Wei, Z.; Jennum, K. S.; Glibstrup, E.; Abrahamsen, P. B.; Santella, M.; Christensen, M. A.; Della Pia, E. A., et al. A comprehensive study of extended tetrathiafulvalene cruciform molecules for molecular electronics: synthesis and electrical transport measurements. *J. Am. Chem. Soc.* **2014**, *136*, 16497–16507.

[74] Lissau, H.; Frisenda, R.; Olsen, S. T.; Jevric, M.; Parker, C. R.; Kadziola, A.; Hansen, T.; Van Der Zant, H. S.; Brøndsted Nielsen, M.; Mikkelsen, K. V. Tracking molecular resonance forms of donor–acceptor push–pull molecules by single-molecule conductance experiments. *Nat. Commun.* **2015**, *6*, 1–8.

[75] Khadem, M.; Walsh, J. C.; Bodwell, G. J.; Zhao, Y. A macrocyclization of 1,8-bis(dithiafulvenyl)pyrenes. *Org. Lett.* **2016**, *18*, 2403–2406.

[76] Khadem, M.; Zhao, Y. Multivalent dithiafulvenyl functionalization of dendritic oligo(phenylene vinylene)s with an anthraquinodimethane core. *Chem. Commun.* **2017**, *53*, 1821–1824.

[77] Shahrokhi, F.; Zhao, Y. A tetrathiafulvalene vinylogue-based double-layer polymer thin film as a highly sensitive and selective TNT sensor. *New J. Chem.* **2019**, *43*, 5277–5281.

[78] Moreno-Mañas, M.; Pleixats, R.; Andreu, R.; Garín, J.; Orduna, J.; Villacampa, B.; Levillain, E.; Sallé, M. The first 1,3-dithiol-2-ylidene donor–π–acceptor chromophores containing an azine spacer: synthesis, electrochemical and nonlinear optical properties. *J. Mater. Chem.* **2001**, *11*, 374–380.

[79] Andreu, R.; Aramburo, J.; Cerdán, M. A.; Garín, J.; Orduna, J.; Villacampa, B. Highly polarized dithiafulvenes: synthesis and nonlinear optical properties. *Tetrahedron Lett.* **2006**, *47*, 661–664.

[80] Alías, S.; Andreu, R.; Blesa, M. J.; Franco, S.; Garín, J.; Gragera, A.; Orduna, J.; Romero, P.; Villacampa, B.; Allain, M. Synthesis, structure, and optical properties of 1,4-dithiafulvene-based nonlinear optic-phores. *J. Org. Chem.* **2007**, *72*, 6440–6446.

[81] Zhou, P.; Wan, Z.; Liu, Y.; Jia, C.; Weng, X.; Xie, J.; Deng, L. Synthesis and electrochromic properties of a novel conducting polymer film based on dithiafulvenyl-triphenylamine-di (N-carbazole). *Electrochim. Acta* **2016**, *190*, 1015–1024.

[82] Guo, K.; Yang, J.; Shi, X.; Lu, X.; Cheng, J.; Wu, Y.; Guo, Y.; Wang, H. A π-extended tetrathiafulvene derivative: synthesis and photoluminescence properties. *Mater. Chem. Phys.* **2014**, *146*, 193–197.

[83] Fong, D.; Adronov, A. Recent developments in the selective dispersion of single-walled carbon nanotubes using conjugated polymers. *Chem. Sci.* **2017**, *8*, 7292–7305.

[84] Wang, H.; Mei, J.; Liu, P.; Schmidt, K.; Jiménez-Osés, G.; Osuna, S.; Fang, L.; Tassone, C. J.; Zoombelt, A. P.; Sokolov, A. N., et al. Scalable and selective dispersion of semiconducting arc-discharged carbon nanotubes by dithiafulvalene/thiophene copolymers for thin film transistors. *ACS Nano* **2013**, *7*, 2659–2668.

[85] Liang, S.; Chen, G.; Peddle, J.; Zhao, Y. Reversible dispersion and releasing of single-walled carbon nanotubes by a stimuli-responsive TTFV-phenylacetylene polymer. *Chem. Commun.* **2012**, *48*, 3100–3102.

[86] Liang, S.; Chen, G.; Zhao, Y. Conformationally switchable TTFV–phenylacetylene polymers: synthesis, properties, and supramolecular interactions with single-walled carbon nanotubes. *J. Mater. Chem. C* **2013**, *1*, 5477–5490.

[87] Liang, S.; Zhao, Y.; Adronov, A. Selective and reversible noncovalent functionalization of single-walled carbon nanotubes by a pH-responsive vinylogous tetrathiafulvalene–fluorene copolymer. *J. Am. Chem. Soc.* **2014**, *136*, 970–977.

[88] Liang, S.; Subrahmanyam, A. V.; Khadem, M.; Zhao, Y.; Adronov, A. Selective dispersion of single-walled carbon nanotubes with electron-rich fluorene-based copolymers. *RSC Adv.* **2016**, *6*, 25733–25740.

[89] Khadem, M.; Zhao, Y. Tetrathiafulvalene vinylogue–fluorene co-oligomers: synthesis, properties, and supramoleclar interactions with carbon nanotubes. *J. Org. Chem.* **2015**, *80*, 7419–7429.

[90] Khan, M. Z. H.; Alrawashdeh, A. I.; Aljohani, S.; Zhao, Y.; Lagowski, J. B. DFT investigation of the interaction between single-walled carbon nanotubes and fluorene-based conjugated oligomers. *Phys. Chem. Chem. Phys.* **2017**, *19*, 28071–28082.

[91] Aljohani, S.; Alrawashdeh, A. I.; Khan, M. Z. H.; Zhao, Y.; Lagowski, J. B. Dispersion of single-walled carbon nanotubes with oligo (p-phenylene ethynylene)s: a DFT study. *J. Phys. Chem. C* **2017**, *121*, 4692–4702.

[92] Alrawashdeh, A. I.; Lagowski, J. B. The role of the solvent and the size of the nanotube in the non-covalent dispersion of carbon nanotubes with short organic oligomers–a DFT study. *RSC Adv.* **2018**, *8*, 30520–30529.

[93] Frens, G. Controlled nucleation for the regulation of the particle size in monodisperse gold suspensions. *Nat. Phys. Sci.* **1973**, *241*, 20–22.

[94] Yonezawa, T.; Kunitake, T. Practical preparation of anionic mercapto ligand-stabilized gold nanoparticles and their immobilization. *Colloids Surf. A Physicochem. Eng. Asp.* **1999**, *149*, 193–199.

[95] Brust, M.; Walker, M.; Bethell, D.; Schiffrin, D. J.; Whyman, R. Synthesis of thiol-derivatised gold nanoparticles in a two-phase liquid–liquid system. *J. Chem. Soc., Chem. Commun.* **1994**, 801–802.

[96] Uehara, A.; Booth, S. G.; Chang, S. Y.; Schroeder, S. L. M.; Imai, T.; Hashimoto, T.; Mosselmans, J. F. W.; Dryfe, R. A. W. Electrochemical insight into the Brust–Schiffrin synthesis of Au nanoparticles. *J. Am. Chem. Soc.* **2015**, *137*, 15135–15144.

[97] Zhou, Y.; Itoh, H.; Uemura, T.; Naka, K.; Chujo, Y. Synthesis of novel stable nanometer-sized metal (M= Pd, Au, Pt) colloids protected by a π-conjugated polymer. *Langmuir* **2002**, *18*, 277–283.

[98] Zhou, Y.; Itoh, H.; Uemura, T.; Naka, K.; Chujo, Y. Preparation of π-conjugated polymer-protected gold nanoparticles in stable colloidal form. *Chem. Commun.* **2001**, 613–614.

[99] Lanterna, A. E.; Coronado, E. A.; Granados, A. M. Synthesis of gold nanoparticles using electron-donating dithiafulvene units. *Tetrahedron Lett.* **2015**, *56*, 4871–4876.

[100] Cai, K.; Zhang, L.; Astumian, R. D.; Stoddart, J. F. Radical-pairing-induced molecular assembly and motion. *Nat. Rev. Chem.* **2021**, *5*, 447–465.

[101] Broløs, L.; Kilde, M. D.; Brock-Nannestad, T.; Nielsen, M. B. Dimeric indenofluorene-extended tetrathiafulvalene motif for enhanced intramolecular complexation. *Eur. J. Org. Chem.* **2021**, *2021*, 3537–3544.

[102] Xu, J.; Guo, J.; Li, S.; Yang, Y.; Lai, W.; Keoingthong, P.; Wang, S.; Zhang, L.; Dong, Q.; Zeng, Z., et al. Dual charge transfer generated from stable mixed-valence radical crystals for boosting solar-to-thermal conversion. *Adv. Sci.* **2023**, 2300980.

[103] Schrödinger, E. An undulatory theory of the mechanics of atoms and molecules. *Phys. Rev.* **1926**, *28*, 1049.

[104] Born, M.; Oppenheimer, R. Zur quantentheorie der molekeln. *Ann. Phys.* **1927**, *389*, 457–484.

[105] Fock, V. Näherungsmethode zur lösung des quantenmechanischen mehrkörperproblems. *Z. Phys.* **1930**, *61*, 126–148.

[106] Slater, J. C. Note on Hartree's method. *Phys. Rev.* **1930**, *35*, 210.

[107] Lennard-Jones, J. E. The electronic structure of some diatomic molecules. *Trans. Faraday Soc.* **1929**, *25*, 668–686.

[108] Szabo, A.; Ostlund, N. S. Modern quantum chemistry: Introduction to advanced electronic structure theory. 1989.

[109] Sherrill, C. D.; Schaefer III, H. F. *Advances in quantum chemistry*; Elsevier, 1999; Vol. 34; pp 143–269.

[110] Møller, C.; Plesset, M. S. Note on an approximation treatment for many-electron systems. *Phys. Rev.* **1934**, *46*, 618.

[111] Čížek, J. On the correlation problem in atomic and molecular systems. Calculation of wavefunction components in Ursell-type expansion using quantum-field theoretical methods. *J. Chem. Phys.* **1966**, *45*, 4256–4266.

[112] Engel, T. *Quantum chemistry* & *spectroscopy*, 3rd ed.; Pearson Education, USA, 2013.

[113] Thomas, L. H. The calculation of atomic fields. *Math. Proc. Cambridge Philos. Soc.* **1927**, *23*, 542–548.

[114] Fermi, E. Eine statistische methode zur bestimmung einiger eigenschaften des atoms und ihre anwendung auf die theorie des periodischen systems der elemente (The statistical deduction of some properties of the atom and their application on the theory of the periodic system of elements). *Z. Phys.* **1928**, *48*, 73–79.

[115] Tsuneda, T. Density functional theory in quantum chemistry. **2014**,

[116] Mardirossian, N.; Head-Gordon, M. Thirty years of density functional theory in computational chemistry: an overview and extensive assessment of 200 density functionals. *Mol. Phys.* **2017**, *115*, 2315–2372.

[117] Hohenberg, P.; Kohn, W. Inhomogeneous electron gas. *Phys. Rev.* **1964**, *136*, B864.

[118] Kohn, W.; Sham, L. J. Self-consistent equations including exchange and correlation effects. *Phys. Rev.* **1965**, *140*, A1133.

[119] Vosko, S. H.; Wilk, L.; Nusair, M. Accurate spin-dependent electron liquid

correlation energies for local spin density calculations: a critical analysis. *Can. J. Phys.* **1980**, *58*, 1200–1211.

[120] Perdew, J. P.; Burke, K.; Ernzerhof, M. Generalized gradient approximation made simple. *Phys. Rev. Lett.* **1996**, *77*, 3865.

[121] Becke, A. D. Density-functional exchange-energy approximation with correct asymptotic behavior. *Phys. Rev. A* **1988**, *38*, 3098.

[122] Perdew, J. P.; Chevary, J. A.; Vosko, S. H.; Jackson, K. A.; Pederson, M. R.; Singh, D. J.; Fiolhais, C. Atoms, molecules, solids, and surfaces: Applications of the generalized gradient approximation for exchange and correlation. *Phys. Rev. B* **1992**, *46*, 6671.

[123] Lee, C.; Yang, W.; Parr, R. G. Development of the Colle-Salvetti correlation-energy formula into a functional of the electron density. *Phys. Rev. B* **1988**, *37*, 785.

[124] Stephens, P. J.; Devlin, F. J.; Chabalowski, C. F.; Frisch, M. J. Ab initio calculation of vibrational absorption and circular dichroism spectra using density functional force fields. *J. Phys. Chem.* **1994**, *98*, 11623–11627.

[125] Becke, A. Density-functional thermochemistry. III. The role of exact exchange. *J. Chem. Phys.* **1993**, *98*, 5648–5652.

[126] Perdew, J. P.; Ernzerhof, M.; Burke, K. Rationale for mixing exact exchange with density functional approximations. *J. Chem. Phys.* **1996**, *105*, 9982–9985.

[127] Adamo, C.; Barone, V. Toward reliable density functional methods without adjustable parameters: The PBE0 model. *J. Chem. Phys.* **1999**, *110*, 6158–6170.

[128] Becke, A. D. Density-functional thermochemistry. V. Systematic optimization of exchange-correlation functionals. *J. Chem. Phys.* **1997**, *107*, 8554–8560.

[129] Zhao, Y.; Truhlar, D. G. The M06 suite of density functionals for main group thermochemistry, thermochemical kinetics, noncovalent interactions, excited states, and transition elements: two new functionals and systematic testing of four M06-class functionals and 12 other functionals. *Theor. Chem. Acc.* **2008**, *120*, 215–241.

[130] Dykstra, C.; Frenking, G.; Kim, K.; Scuseria, G. *Theory and applications of computational chemistry: the first forty years*; Elsevier, 2011.

[131] Fan, X.; Chen, L.; Borodin, O.; Ji, X.; Chen, J.; Hou, S.; Deng, T.; Zheng, J.; Yang, C.; Liou, S.-C., et al. Non-flammable electrolyte enables Li-metal batteries with aggressive cathode chemistries. *Nat. Nanotechnol.* **2018**, *13*, 715–722.

[132] Légaré, M.-A.; Bélanger-Chabot, G.; Dewhurst, R. D.; Welz, E.; Krummenacher, I.; Engels, B.; Braunschweig, H. Nitrogen fixation and reduction at boron. *Science* **2018**, *359*, 896–900.

[133] Meng, G.; Lam, N. Y.; Lucas, E. L.; Saint-Denis, T. G.; Verma, P.; Chekshin, N.; Yu, J.-Q. Achieving site-selectivity for C–H activation processes

based on distance and geometry: a carpenter's approach. *J. Am. Chem. Soc.* **2020**, *142*, 10571–10591.

[134] Mancuso, J. L.; Mroz, A. M.; Le, K. N.; Hendon, C. H. Electronic structure modeling of metal–organic frameworks. *Chem. Rev.* **2020**, *120*, 8641–8715.

[135] Pan, Q.; Abdellah, M.; Cao, Y.; Lin, W.; Liu, Y.; Meng, J.; Zhou, Q.; Zhao, Q.; Yan, X.; Li, Z., et al. Ultrafast charge transfer dynamics in 2D covalent organic frameworks/Re-complex hybrid photocatalyst. *Nat. Commun.* **2022**, *13*, 1–13.

[136] Liu, S.-J.; Chen, Z.-H.; Chen, J.-Y.; Ni, S.-F.; Zhang, Y.-C.; Shi, F. Rational design of axially chiral styrene-based organocatalysts and their application in catalytic asymmetric (2+4) cyclizations. *Angew. Chem.* **2022**, *134*, e202112226.

[137] Chai, J.-D.; Head-Gordon, M. Systematic optimization of long-range corrected hybrid density functionals. *J. Chem. Phys.* **2008**, *128*, 084106.

[138] Grimme, S. Semiempirical GGA-type density functional constructed with a long-range dispersion correction. *J. Comput. Chem.* **2006**, *27*, 1787–1799.

[139] Goerigk, L.; Grimme, S. A thorough benchmark of density functional methods for general main group thermochemistry, kinetics, and noncovalent interactions. *Phys. Chem. Chem. Phys.* **2011**, *13*, 6670–6688.

[140] Grimme, S.; Antony, J.; Ehrlich, S.; Krieg, H. A consistent and accurate ab initio parametrization of density functional dispersion correction (DFT-D) for the 94 elements H-Pu. *J. Chem. Phys.* **2010**, *132*, 154104.

[141] de la Roza, A. O.; DiLabio, G. A. *Non-covalent interactions in quantum chemistry and physics: Theory and applications*; Elsevier, 2017.

[142] Runge, E.; Gross, E. K. Density-functional theory for time-dependent systems. *Phys. Rev. Lett.* **1984**, *52*, 997.

[143] Marques, M. A.; Maitra, N. T.; Nogueira, F. M.; Gross, E. K.; Rubio, A. *Fundamentals of time-dependent density functional theory*; Springer, 2012; Vol. 837.

[144] Management Association, I. R., Ed. *Biomedical engineering: concepts, methodologies, tools, and applications*; IGI Global, 2018.

[145] Alivisatos, A. P. Semiconductor clusters, nanocrystals, and quantum dots. *Science* **1996**, *271*, 933–937.

[146] Brust, M.; Kiely, C. J. Some recent advances in nanostructure preparation from gold and silver particles: a short topical review. *Colloids Surf. A Physicochem. Eng. Asp.* **2002**, *202*, 175–186.

[147] Hache, F.; Ricard, D.; Flytzanis, C.; Kreibig, U. The optical kerr effect in small metal particles and metal colloids: The case of gold. *Appl. Phys. A* **1988**, *47*, 347–357.

[148] Andres, R. P.; Bein, T.; Dorogi, M.; Feng, S.; Henderson, J. I.; Kubiak, C. P.; Mahoney, W.; Osifchin, R. G.; Reifenberger, R. Coulomb staircase at room temperature in a self-assembled molecular nanostructure. *Science* **1996**, *272*, 1323–1325.

[149] Pelizzetti, E. *Fine particles science and technology: from micro to nanoparticles*, softcover reprint of the original 1st ed. 1996 edition ed.; Springer: Italy, 2011.

[150] Beesley, J. E. *Colloidal gold. A new perpective for cytochemical marking;*; Royal Microscopical Society Handbook 17; Oxford Science Publication, Oxford University Press: Oxford, 1989.

[151] Toshima, N.; Yonezawa, T. Bimetallic nanoparticles—novel materials for chemical and physical applications. *New J. Chem.* **1998**, *22*, 1179–1201.

[152] Fendler, J. H. Self-assembled nanostructured materials. *Chem. Mater.* **1996**, *8*, 1616–1624.

[153] Henglein, A. Physicochemical properties of small metal particles in solution: "microelectrode" reactions, chemisorption, composite metal particles, and the atom-to-metal transition. *J. Phys. Chem.* **1993**, *97*, 5457–5471.

[154] Belloni, J. Metal nanocolloids. *Curr. Opin. Colloid Interface Sci.* **1996**, *1*, 184–196.

[155] Saha, K.; Agasti, S. S.; Kim, C.; Li, X.; Rotello, V. M. Gold nanoparticles in chemical and biological sensing. *Chem. Rev.* **2012**, *112*, 2739–2779.

[156] Wagner, F. E.; Haslbeck, S.; Stievano, L.; Calogero, S.; Pankhurst, Q. A.; Martinek, K. P. Before striking gold in gold-ruby glass. *Nature* **2000**, *407*, 691–692.

[157] Daniel, M.-C.; Astruc, D. Gold nanoparticles: assembly, supramolecular

chemistry, quantum-size-related properties, and applications toward biology, catalysis, and nanotechnology. *Chem. Rev.* **2004**, *104*, 293–346.

[158] Perrault, S. D.; Chan, W. C. W. Synthesis and surface modification of highly monodispersed, spherical gold nanoparticles of 50200 nm. *J. Am. Chem. Soc.* **2009**, *131*, 17042–17043.

[159] Yu,; Chang, S.-S.; Lee, C.-L.; Wang, C. R. C. Gold nanorods: electrochemical synthesis and optical properties. *J. Phys. Chem. B* **1997**, *101*, 6661–6664.

[160] Braun, G. B.; Pallaoro, A.; Wu, G.; Missirlis, D.; Zasadzinski, J. A.; Tirrell, M.; Reich, N. O. Laser–activated gene silencing *via* gold nanoshell–siRNA conjugates. *ACS Nano* **2009**, *3*, 2007–2015.

[161] Xia, Y.; Li, W.; Cobley, C. M.; Chen, J.; Xia, X.; Zhang, Q.; Yang, M.; Cho, E. C.; Brown, P. K. Gold nanocages: from synthesis to theranostic applications. *Acc. Chem. Res.* **2011**, *44*, 914–924.

[162] Huang, X.; El-Sayed, M. A. Gold nanoparticles: optical properties and implementations in cancer diagnosis and photothermal therapy. *J. Adv. Res.* **2010**, *1*, 13–28.

[163] Eustis, S.; El-Sayed, M. A. Why gold nanoparticles are more precious than pretty gold: noble metal surface plasmon resonance and its enhancement of the radiative and nonradiative properties of nanocrystals of different shapes. *Chem. Soc. Rev.* **2006**, *35*, 209–217.

[164] Faraday, M. X. The Bakerian lecture. —Experimental relations of gold (and other metals) to light. *Phil. Trans. R. Soc.* **1857**, *147*, 145–181.

[165] Turkevich, J.; Stevenson, P. C.; Hillier, J. A study of the nucleation and growth processes in the synthesis of colloidal gold. *Discuss. Faraday Soc.* **1951**, *11*, 55.

[166] Perala, S. R. K.; Kumar, S. On the mechanism of metal nanoparticle synthesis in the Brust–Schiffrin method. *Langmuir* **2013**, *29*, 9863–9873.

[167] Shon, Y.-S.; Mazzitelli, C.; Murray, R. W. Unsymmetrical disulfides and thiol mixtures produce different mixed monolayer-protected gold clusters. *Langmuir* **2001**, *17*, 7735–7741.

[168] Chen, S.; Templeton, A. C.; Murray, R. W. Monolayer-protected cluster growth dynamics. *Langmuir* **2000**, *16*, 3543–3548.

[169] Turkevich, J.; Stevenson, P. C.; Hillier, J. A study of the nucleation and growth processes in the synthesis of colloidal gold. *Discuss. Faraday Soc.* **1951**, *11*, 55–75.

[170] Kimling, J.; Maier, M.; Okenve, B.; Kotaidis, V.; Ballot, H.; Plech, A. Turkevich method for gold nanoparticle synthesis revisited. *J. Phys. Chem. B* **2006**, *110*, 15700–15707.

[171] Sakai, T.; Alexandridis, P. Mechanism of gold metal ion reduction, nanoparticle growth and size control in aqueous amphiphilic block copolymer solutions at ambient conditions. *J. Phys. Chem. B* **2005**, *109*, 7766–7777.

[172] Male, K. B.; Li, J.; Bun, C. C.; Ng, S.-C.; Luong, J. H. Synthesis and stability of fluorescent gold nanoparticles by sodium borohydride in the presence of mono-6-deoxy-6-pyridinium-β-cyclodextrin chloride. *J. Phys. Chem. C* **2008**, *112*, 443–451.

[173] Deraedt, C.; Salmon, L.; Gatard, S.; Ciganda, R.; Hernandez, R.; Ruiz, J.; Astruc, D. Sodium borohydride stabilizes very active gold nanoparticle catalysts. *Chem. Commun.* **2014**, *50*, 14194–14196.

[174] Watson, K. J.; Zhu, J.; Nguyen, S. T.; Mirkin, C. A. Redox-active polymer-nanoparticle hybrid materials. *Pure Appl. Chem.* **2000**, *72*, 67–72.

[175] Leiva, A.; Fuentes, I.; Bossel, E.; Urzúa, M.; Méndez, M.; Pino, M.; Radić, D.; Márquez, V.; González-Nilo, F. D. Block copolymers in the synthesis of gold nanoparticles. Two new approaches: copolymer aggregates as reductants and stabilizers and simultaneous formation of copolymer aggregates and gold nanoparticles. *J. Polym. Sci., Part A: Polym. Chem.* **2014**, *52*, 3069–3079.

[176] Ray, D.; Aswal, V. K.; Kohlbrecher, J. Synthesis and characterization of high concentration block copolymer-mediated gold nanoparticles. *Langmuir* **2011**, *27*, 4048–4056.

[177] Goulet, P. J.; Lennox, R. B. New insights into Brust- Schiffrin metal nanoparticle synthesis. *J. Am. Chem. Soc.* **2010**, *132*, 9582–9584.

[178] Inagi, S.; Naka, K.; Chujo, Y. Functional polymers based on electron-donating TTF and derivatives. *J. Mater. Chem.* **2007**, *17*, 4122–4135.

[179] Zhu, M.; Wang, X.; Naka, K.; Zhou, X.; Chujo, Y. Self-organized nanocomposite of gold nanoparticles and π-electron organic molecules. *J. Macromol. Sci. A* **2006**, *43*, 1801–1805.

[180] Zhang, X.; Lu, Z.; Ye, L.; Zhan, C.; Hou, J.; Zhang, S.; Jiang, B.; Zhao, Y.; Huang, J.; Zhang, S., et al. A potential perylene diimide dimer-based acceptor material for highly efficient solution-processed non-fullerene organic solar cells with 4.03% efficiency. *Adv. Mater.* **2013**, *25*, 5791–5797.

[181] Wang, Y.; Zhao, Y. Carboxylated dithiafulvenes and tetrathiafulvalene vinylogues: synthesis, electronic properties, and complexation with zinc ions. *Beilstein J. Org. Chem.* **2015**, *11*, 957–965.

[182] Mulla, K.; Shaik, H.; Thompson, D. W.; Zhao, Y. TTFV-based molecular tweezers and macrocycles as receptors for fullerenes. *Org. Lett.* **2013**, *15*, 4532–4535.

[183] Lorcy, D.; Guerro, M.; Bergamini, J.-F.; Hapiot, P. Vinylogous tetrathiafulvalene based podands: complexation interferences on the molecular movements triggered by electron transfer. *J. Phys. Chem. B* **2013**, *117*, 5188–5194.

[184] Mulla, K.; Zhao, Y. TTFV molecular tweezers with phenylboronic acid and phenylboronate endgroups: modular synthesis and electrochemical responses to saccharides and fluoride ion. *Tetrahedron Lett.* **2014**, *55*, 382–386.

[185] Mulla, K.; Dongare, P.; Thompson, D. W.; Zhao, Y. Click synthesized dianthryl–TTFV: an efficient fluorescent turn-on probe for transition metal ions. *Org. Biomol. Chem.* **2012**, *10*, 2542–2544.

[186] Chen, G.; Zhao, Y. Redox-regulated rotary motion of a bis (9-triptycyl)-TTFV system. *Org. Lett.* **2014**, *16*, 668–671.

[187] Adows, H.; Zhao, Y. Redox interactions of Au (III) with carboxylated dithiafulvenes and tetrathiafulvalene analogues in polar organic media. *Chem. Commun.* **2016**, *52*, 13101–13104.

[188] M. J. Frisch, G. W. Trucks, H. B. Schlegel, G. E. Scuseria,, et al. Gaussian 16. 2016.

[189] Stewart, J. J. P. Optimization of parameters for semiempirical methods V: modification of NDDO approximations and application to 70 elements. *J. Mol. Model.* **2007**, *13*, 1173–1213.

[190] Zhao, Y.; Truhlar, D. G. Density functionals with broad applicability in chemistry. *Acc. Chem. Res.* **2008**, *41*, 157–167.

[191] Weigend, F.; Ahlrichs, R. Balanced basis sets of split valence, triple zeta valence and quadruple zeta valence quality for H to Rn: design and assessment of accuracy. *Phys. Chem. Chem. Phys.* **2005**, *7*, 3297.

[192] Weigend, F. Accurate Coulomb-fitting basis sets for H to Rn. *Phys. Chem. Chem. Phys.* **2006**, *8*, 1057–1065.

[193] Lu, T.; Chen, F. Atomic dipole moment corrected Hirshfeld population method. *J. Theor. Comput. Chem.* **2012**, *11*, 163–183.

[194] Hirshfeld, F. L. Bonded-atom fragments for describing molecular charge densities. *Theor. Chim. Acta* **1977**, *44*, 129–138.

[195] Marenich, A. V.; Cramer, C. J.; Truhlar, D. G. Universal solvation model based on solute electron density and on a continuum model of the solvent defined by the bulk dielectric constant and atomic surface tensions. *J. Phys. Chem. B* **2009**, *113*, 6378–6396.

[196] Legault, C. Y. CYLview, 1.0b. 2009-2012; http://www.cylview.org/.

[197] Gaussview software.

[198] Lu, T.; Chen, F. Multiwfn: a multifunctional wavefunction analyzer. *J. Comput. Chem.* **2012**, *33*, 580–592.

[199] Humphrey, W.; Dalke, A.; Schulten, K. VMD: visual molecular dynamics. *J. Mol. Graph.* **1996**, *14*, 33–38.

[200] O'boyle, N. M.; Tenderholt, A. L.; Langner, K. M. cclib: A library for package-independent computational chemistry algorithms. *J. Comput. Chem.* **2008**, *29*, 839–845.

[201] OriginPro 8. 2007; http://www.originlab.com.

[202] Lu, T.; Chen, Q. Shermo: A general code for calculating molecular thermochemistry properties. *Comput. Theor. Chem.* **2021**, *1200*, 113249.

[203] Liang, M.-X.; Zhao, L.; Jia, J.; Wu, H.-S. Au_n ($n = 1–16$) clusters on the ZrO_2 (111) surface: a DFT+U investigation. *Phys. Chem. Chem. Phys.* **2016**, *18*, 30491–30497.

[204] Liu, H.-T.; Xiong, X.-G.; Diem Dau, P.; Wang, Y.-L.; Huang, D.-L.; Li, J.;

Wang, L.-S. Probing the nature of gold–carbon bonding in gold–alkynyl complexes. *Nat. Commun.* **2013**, *4*, 2223.

[205] Li, D.-Z.; Li, S.-D. A density functional investigation on C_2Aun^+ (n= 1, 3, 5) and C_2Aun (n= 2, 4, 6): from gold terminals, gold bridges, to gold triangles. *J. Clust. Sci.* **2011**, *22*, 331–341.

[206] Bakar, M. A.; Sugiuchi, M.; Iwasaki, M.; Shichibu, Y.; Konishi, K. Hydrogen bonds to Au atoms in coordinated gold clusters. *Nat. Commun.* **2017**, *8*, 576.

[207] Schmidbaur, H.; Raubenheimer, H. G.; Dobrzańska, L. The gold–hydrogen bond, Au–H, and the hydrogen bond to gold, Au H–X. *Chem. Soc. Rev.* **2014**, *43*, 345–380.

[208] Lefebvre, C.; Khartabil, H.; Boisson, J.-C.; Contreras-García, J.; Piquemal, J.-P.; Hénon, E. The independent gradient model: a new approach for probing strong and weak interactions in molecules from wave function calculations. *Chemphyschem* **2018**, *19*, 724–735.

[209] Johnson, E. R.; Keinan, S.; Mori-Sánchez, P.; Contreras-García, J.; Cohen, A. J.; Yang, W. Revealing noncovalent interactions. *J. Am. Chem. Soc.* **2010**, *132*, 6498–6506.

[210] Pascoe, D. J.; Ling, K. B.; Cockroft, S. L. The origin of chalcogen-bonding interactions. *J. Am. Chem. Soc.* **2017**, *139*, 15160–15167.

[211] Bader, R. F. W. Atoms in molecules. *Acc. Chem. Res.* **1985**, *18*, 9–15.

[212] Cremer, D.; Kraka, E. Chemical bonds without bonding electron density—does the difference electron-density analysis suffice for a description of the chemical bond? *Angew. Chem. Int. Ed.* **1984**, *23*, 627–628.

[213] Bader, R. F. W. A quantum theory of molecular structure and its applications. *Chem. Rev.* **1991**, *91*, 893–928.

[214] Popelier, P. L. A.; Aicken, F.; O'Brien, S. *Atoms in molecules*; Prentice Hall Manchester, 2000; Vol. 188.

[215] Kumar, P. S. V.; Raghavendra, V.; Subramanian, V. Bader's theory of atoms in molecules (AIM) and its applications to chemical bonding. *J. Chem. Sci.* **2016**, *128*, 1527–1536.

[216] Bader, R. F. *Atoms in molecules. A quantum theory*; Clarendon Press. Oxford, 1990.

[217] Alkorta, I.; Barrios, L.; Rozas, I.; Elguero, J. Comparison of models to correlate electron density at the bond critical point and bond distance. *J. Mol. Struct. Theochem* **2000**, *496*, 131–137.

[218] Espinosa, E.; Molins, E.; Lecomte, C. Hydrogen bond strengths revealed by topological analyses of experimentally observed electron densities. *Chem. Phys. Lett.* **1998**, *285*, 170–173.

[219] Spackman, M. A. Hydrogen bond energetics from topological analysis of experimental electron densities: recognising the importance of the promolecule. *Chem. Phys. Lett.* **1999**, *301*, 425–429.

[220] Espinosa, E.; Souhassou, M.; Lachekar, H.; Lecomte, C. Topological analysis of the electron density in hydrogen bonds. *Acta. Crystallogr. B. Struct. Sci. Cryst.* **1999**, *55*, 563–572.

[221] Alkorta, I.; Elguero, J. Theoretical study of strong hydrogen bonds between neutral molecules: the case of amine oxides and phosphine oxides as hydrogen bond acceptors. *J. Phys. Chem. A* **1999**, *103*, 272–279.

[222] Knop, O.; Rankin, K. N.; Boyd, R. J. Coming to grips with N- H N bonds. 1. Distance relationships and electron density at the bond critical point. *J. Phys. Chem. A* **2001**, *105*, 6552–6566.

[223] Espinosa, E.; Alkorta, I.; Elguero, J.; Molins, E. From weak to strong interactions: a comprehensive analysis of the topological and energetic properties of the electron density distribution involving X–H F–Y systems. *J. Chem. Phys.* **2002**, *117*, 5529–5542.

[224] Ranganathan, A.; Kulkarni, G.; Rao, C. Understanding the hydrogen bond in terms of the location of the bond critical point and the geometry of the lone pairs. *J. Phys. Chem. A* **2003**, *107*, 6073–6081.

[225] Tang, T.-H.; Deretey, E.; Knak Jensen, S.; Csizmadia, I. Hydrogen bonds: relation between lengths and electron densities at bond critical points. *Eur. Phys. J. D* **2006**, *37*, 217–222.

[226] Vener, M.; Manaev, A.; Egorova, A.; Tsirelson, V. QTAIM study of strong H-bonds with the O- H A fragment (A= O, N) in three-dimensional periodical crystals. *J. Phys. Chem. A* **2007**, *111*, 1155–1162.

[227] Dominiak, P. M.; Makal, A.; Mallinson, P. R.; Trzcinska, K.; Eilmes, J.; Grech, E.; Chruszcz, M.; Minor, W.; Woźniak, K. Continua of interactions between pairs of atoms in molecular crystals. *Chem. Eur. J.* **2006**, *12*, 1941–1949.

[228] Grabowski, S. J.; Sokalski, W. A.; Dyguda, E.; Leszczyński, J. Quantitative classification of covalent and noncovalent H-bonds. *J. Phys. Chem. B* **2006**, *110*, 6444–6446.

[229] Tsirelson, V. G.; Ozerov, R. P. *Electron density and bonding in crystals: principles, theory and X-ray diffraction experiments in solid state physics and chemistry*; CRC Press, 2020.

[230] Rodríguez, J. I. An efficient method for computing the QTAIM topology of a scalar field: The electron density case. *J. Comput. Chem.* **2013**, *34*, 681–686.

[231] Klingsberg, E. The 1,3-dithiolium cation and some related dithioles. *J. Am. Chem. Soc.* **1964**, *86*, 5290–5292.

[232] Svenstrup, N.; Becher, J. The organic chemistry of 1,3-dithiole-2-thione-4,5-dithiolate (DMIT). *Synthesis* **1995**, *1995*, 215–235.

[233] Lozac'h, N.; Stavaux, M. In *The 1,2- and 1,3-dithiolium ions*; Katritzky, A., Boulton, A., Eds.; Adv. Heterocycl. Chem.; Academic Press, 1981; Vol. 27; pp 151–239.

[234] Roncali, J. Linearly extended π-donors: when tetrathiafulvalene meets conjugated oligomers and polymers. *J. Mater. Chem.* **1997**, *7*, 2307–2321.

[235] Jeppesen, J. O.; Nielsen, M. B.; Becher, J. Tetrathiafulvalene cyclophanes and cage molecules. *Chem. Rev.* **2004**, *104*, 5115–5132.

[236] Gorgues, A.; Hudhomme, P.; Sallé, M. Highly functionalized tetrathiafulvalenes: riding along the synthetic trail from electrophilic alkynes. *Chem. Rev.* **2004**, *104*, 5151–5184.

[237] Zhao, Y.; Chen, G.; Mulla, K.; Mahmud, I.; Liang, S.; Dongare, P.; Thompson, D. W.; Dawe, L. N.; Bouzan, S. Tetrathiafulvalene vinylogues as versatile building blocks for new organic materials. *Pure Appl. Chem.* **2012**, *84*, 1005–1025.

[238] Jana, A.; Ishida, M.; Park, J. S.; Bahring, S.; Jeppesen, J. O.; Sessler, J. L. Tetrathiafulvalene-(TTF-) derived oligopyrrolic macrocycles. *Chem. Rev.* **2017**, *117*, 2641–2710.

[239] Duvva, N.; Chilakamarthi, U.; Giribabu, L. Recent developments in tetrathiafulvalene and dithiafulvalene based metal-free organic sensitizers for dye-sensitized solar cells: a mini-review. *Sustain. Energy Fuels* **2017**, *1*, 678–688.

[240] Johnson, M. A.; Flinn, C.; Zhao, Y. Computational mechanistic analysis of intramolecular cycloadditions of the 1,3-dithiolium cation with adjacent alkene and allene functional groups. *ACS Omega* **2018**, *3*, 9770–9780.

[241] Bryce, M. R. Recent progress on conducting organic charge-transfer salts. *Chem. Soc. Rev.* **1991**, *20*, 355–390.

[242] Inagi, S.; Naka, K.; Chujo, Y. Synthesis and properties of an amphiphilic dithiafulvene oligomer. *J. Polym. Sci. A Polym. Chem.* **2007**, *45*, 3770–3775.

[243] Hou, Y.; Long, G.; Sui, D.; Cai, Y.; Wan, X.; Yu, A.; Chen, Y. Different donor–acceptor structures of dithiafulvalene-fused semiconducting polymers with different band gaps. *Chem. Commun.* **2011**, *47*, 10401–10403.

[244] Wudl, F.; Smith, G. M.; Hufnagel, E. J. Bis-1,3-dithiolium chloride: an unusually stable organic radical cation. *J. Chem. Soc. D* **1970**, 1453–1454.

[245] Devonport, W.; Blower, M. A.; Bryce, M. R.; Goldenberg, L. M. A redox-active tetrathiafulvalene [2]pseudorotaxane: spectroelectrochemical and cyclic voltammetric studies of the highly-reversible complexation/decomplexation process. *J. Org. Chem.* **1997**, *62*, 885–887.

[246] Schröder, H. V.; Schalley, C. A. Tetrathiafulvalene – a redox-switchable building block to control motion in mechanically interlocked molecules. *Beilstein J. Org. Chem.* **2018**, *14*, 2163–2185.

[247] Spanggaard, H.; Prehn, J.; Nielsen, M. B.; Levillain, E.; Allain, M.; Becher, J. Multiple-bridged bis-tetrathiafulvalenes: new synthetic protocols and spectro-electrochemical investigations. *J. Am. Chem. Soc.* **2000**, *122*, 9486–9494.

[248] Khodorkovsky, V.; Shapiro, L.; Krief, P.; Shames, A.; Mabon, G.; Gorgues, A.; Giffard, M. Do π-dimers of tetrathiafulvalene cation radicals really exist at room temperature? *Chem. Commun.* **2001**, 2736–2737.

[249] Yoshizawa, M.; Kumazawa, K.; Fujita, M. Room-temperature and solution-

state observation of the mixed-valence cation radical dimer of tetrathiafulvalene, [(TTF)2]+•, within a self-assembled cage. *J. Am. Chem. Soc.* **2005**, *127*, 13456–13457.

[250] Yanai, T.; Tew, D. P.; Handy, N. C. A new hybrid exchange–correlation functional using the Coulomb-attenuating method (CAM-B3LYP). *Chem. Phys. Lett.* **2004**, *393*, 51–57.

[251] Zhao, Y.; Chen, G.; Mulla, K.; Mahmud, I.; Liang, S.; Dongare, P.; Thompson, D. W.; Dawe, L. N.; Bouzan, S. Tetrathiafulvalene vinylogues as versatile building blocks for new organic materials. *Pure Appl. Chem.* **2012**, *84*, 1005–1025.

[252] Cotton, F. A. *Progress in inorganic chemistry. Volume 8 Volume 8*; Interscience: New York, 1967.

[253] Robin, M. B.; Day, P. *Advances in inorganic chemistry and radiochemistry*; Elsevier, 1968; Vol. 10; pp 247–422.

[254] Creutz, C.; Taube, H. Direct approach to measuring the Franck-Condon barrier to electron transfer between metal ions. *J. Am. Chem. Soc.* **1969**, *91*, 3988–3989, Publisher: ACS Publications.

[255] Creutz, C.; Taube, H. Binuclear complexes of ruthenium ammines. *J. Am. Chem. Soc.* **1973**, *95*, 1086–1094.

[256] Spruell, J. M. Molecular recognition and switching via radical dimerization. *Pure Appl. Chem.* **2010**, *82*, 2281–2294.

[257] Torrance, J. B.; Scott, B. A.; Welber, B.; Kaufman, F. B.; Seiden, P. E. Optical properties of the radical cation tetrathiafulvalenium (TTF+) in its mixed-valence and monovalence halide salts. *Phys. Rev. B* **1979**, *19*, 730–741.

[258] Bozio, R.; Zanon, I.; Girlando, A.; Pecile, C. Vibrational spectroscopy of molecular constituents of one-dimensional organic conductors. Tetrathiofulvalene (TTF), TTF+, and (TTF+)2 dimer. *J. Chem. Phys.* **1979**, *71*, 2282.

[259] Rosokha, S. V.; Kochi, J. K. Molecular and electronic structures of the long-bonded π-dimers of tetrathiafulvalene cation-radical in intermolecular electron transfer and in (solid-state) conductivity. *J. Am. Chem. Soc.* **2007**, *129*, 828–838.

[260] Hratchian, H. P.; Schlegel, H. B. In *Theory and applications of computational chemistry*; Dykstra, C. E., Frenking, G., Kim, K. S., Scuseria, G. E., Eds.; Elsevier: Amsterdam, 2005; pp 195–249.

[261] Fukui, K. The path of chemical reactions-the IRC approach. *Acc. Chem. Res.* **1981**, *14*, 363–368.

[262] Maeda, S.; Harabuchi, Y.; Ono, Y.; Taketsugu, T.; Morokuma, K. Intrinsic reaction coordinate: Calculation, bifurcation, and automated search. *Int. J. Quantum Chem.* **2015**, *115*, 258–269.

[263] Iyengar, S. S.; Schlegel, H. B.; Millam, J. M.; A. Voth, G.; Scuseria, G. E.; Frisch, M. J. Ab initio molecular dynamics: Propagating the density matrix with Gaussian orbitals. II. Generalizations based on mass-weighting, idempo-

tency, energy conservation and choice of initial conditions. *J. Chem. Phys.* **2001**, *115*, 10291–10302.

[264] Schlegel, H. B.; Millam, J. M.; Iyengar, S. S.; Voth, G. A.; Daniels, A. D.; Scuseria, G. E.; Frisch, M. J. Ab initio molecular dynamics: Propagating the density matrix with Gaussian orbitals. *J. Chem. Phys.* **2001**, *114*, 9758–9763.

[265] Schlegel, H. B.; Iyengar, S. S.; Li, X.; Millam, J. M.; Voth, G. A.; Scuseria, G. E.; Frisch, M. J. Ab initio molecular dynamics: Propagating the density matrix with Gaussian orbitals. III. Comparison with Born–Oppenheimer dynamics. *J. Chem. Phys.* **2002**, *117*, 8694–8704.

[266] Capobianco, A.; Velardo, A.; Peluso, A. DFT predictions of the oxidation potential of organic dyes for opto-electronic devices. *Comput. Theor. Chem.* **2015**, *1070*, 68–75.

[267] Zielinski, T. J.; Poirier, R. A.; Peterson, M. R.; Csizmadia, I. G. Conformational study of protonated, neutral, and deprotonated formamide. *J. Comput. Chem.* **1982**, *3*, 477–485.

[268] Fifen, J. J. Thermodynamics of the electron revisited and generalized. *J. Chem. Theory Comput.* **2013**, *9*, 3165–3169.

[269] Kelly, C. P.; Cramer, C. J.; Truhlar, D. G. Single-ion solvation free energies and the normal hydrogen electrode potential in methanol, acetonitrile, and dimethyl sulfoxide. *J. Phys. Chem. B* **2007**, *111*, 408–422.

[270] Trasatti, S. The absolute electrode potential: an explanatory note (recommendations 1986). *Pure Appl. Chem.* **1986**, *58*, 955–966.

[271] Fawcett, W. R. The ionic work function and its role in estimating absolute electrode potentials. *Langmuir* **2008**, *24*, 9868–9875.

[272] Donald, W. A.; Leib, R. D.; O'Brien, J. T.; Bush, M. F.; Williams, E. R. Absolute standard hydrogen electrode potential measured by reduction of aqueous nanodrops in the gas phase. *J. Am. Chem. Soc.* **2008**, *130*, 3371–3381.

[273] Donald, W. A.; Leib, R. D.; O'Brien, J. T.; Williams, E. R. Directly relating gas-phase cluster measurements to solution-phase hydrolysis, the absolute standard hydrogen electrode potential, and the absolute proton solvation energy. *Chem. Eur. J.* **2009**, *15*, 5926–5934.

[274] Donald, W. A.; Leib, R. D.; Demireva, M.; O'Brien, J. T.; Prell, J. S.; Williams, E. R. Directly relating reduction energies of gaseous Eu (H2O) n 3+, n= 55- 140, to aqueous solution: the absolute SHE potential and real proton solvation energy. *J. Am. Chem. Soc.* **2009**, *131*, 13328–13337.

[275] Isse, A. A.; Gennaro, A. Absolute potential of the standard hydrogen electrode and the problem of interconversion of potentials in different solvents. *J. Phys. Chem. B* **2010**, *114*, 7894–7899.

[276] Bredas, J.-L. Mind the gap! *Mater. Horiz.* **2014**, *1*, 17–19.

[277] Blumer, M.; Blumer, W.; Reich, T. Polycyclic aromatic hydrocarbons in soils

of a mountain valley: correlation with highway traffic and cancer incidence. *Environ. Sci. Technol.* **1977**, *11*, 1082–1084.

[278] Vichi, S.; Pizzale, L.; Conte, L. S.; Buxaderas, S.; López-Tamames, E. Simultaneous determination of volatile and semi-volatile aromatic hydrocarbons in virgin olive oil by headspace solid-phase microextraction coupled to gas chromatography/mass spectrometry. *J. Chromatogr. A* **2005**, *1090*, 146–154.

[279] Haritash, A.; Kaushik, C. Biodegradation aspects of polycyclic aromatic hydrocarbons (PAHs): a review. *J. Hazard. Mater.* **2009**, *169*, 1–15.

[280] Yan, J.; Ying, Y.; Xianming, Z. Review on the biodegradation and conversion mechanisms of typical polycyclic aromatic hydrocarbons. *Acta Petrol. Sin. (Petroleum Processing Section)* **2014**, *30*, 1137.

[281] Nguyen, T. C.; Loganathan, P.; Nguyen, T. V.; Vigneswaran, S.; Kandasamy, J.; Slee, D.; Stevenson, G.; Naidu, R. Polycyclic aromatic hydrocarbons in road-deposited sediments, water sediments, and soils in Sydney, Australia: comparisons of concentration distribution, sources and potential toxicity. *Ecotoxicol. Environ. Saf.* **2014**, *104*, 339–348.

[282] Sharma, T. In silico investigation of polycyclic aromatic hydrocarbons against bacterial 1-2 dioxygenase. *J. Chem. Pharm. Res.* **2014**, *6*, 873–877.

[283] Kuppusamy, S.; Thavamani, P.; Megharaj, M.; Naidu, R. Biodegradation of polycyclic aromatic hydrocarbons (PAHs) by novel bacterial consortia tolerant to diverse physical settings–assessments in liquid-and slurry-phase systems. *Int. Biodeterior. Biodegradation* **2016**, *108*, 149–157.

[284] Li, P.-h.; Wang, Y.; Li, Y.-h.; Wai, K.-m.; Li, H.-l.; Tong, L. Gas-particle partitioning and precipitation scavenging of polycyclic aromatic hydrocarbons (PAHs) in the free troposphere in southern China. *Atmos. Environ.* **2016**, *128*, 165–174.

[285] Zander, M. *Handbook of polycyclic aromatic hydrocarbons*; Marcel Dekker New York, 1983; Vol. 1; pp 1–25.

[286] Harvey, R. G. *Polycyclic aromatic hydrocarbons: chemistry and carcinogenicity*; CUP Archive, 1991.

[287] Coffen, D. L.; Chambers, J. Q.; Williams, D. R.; Garrett, P.; Canfield, N. Tetrathioethylenes. *J. Am. Chem. Soc.* **1971**, *93*, 2258–2268.

[288] Woolridge, K.; Goncalves, L. C.; Bouzan, S.; Chen, G.; Zhao, Y. Aryl-substituted dithiafulvenes: synthesis, electronic properties, and redox reactivity. *Tetrahedron Lett.* **2014**, *55*, 6362–6366.

[289] Bouzan, S.; Dawe, L. N.; Zhao, Y. Bromophenyl substituted dithiafulvenes and tetrathiafulvalene vinylogues: synthesis, structure, and electronic properties. *Tetrahedron Lett.* **2013**, *54*, 4666–4669.

[290] Younes, E. A.; Williams, K.-L. M.; Walsh, J. C.; Schneider, C. M.; Bodwell, G. J.; Zhao, Y. A TTFV–pyrene-based copolymer: synthesis, redox properties, and aggregation behaviour. *RSC Adv.* **2015**, *5*, 23952–23956.

[291] Yoshimura, A.; Kimura, H.; Kagawa, K.; Yoshioka, M.; Itou, T.; Vasu, D.; Shirahata, T.; Yorimitsu, H.; Misaki, Y. Synthesis and properties of tetrathia-

fulvalenes bearing 6-aryl-1,4-dithiafulvenes. *Beilstein J. Org. Chem.* **2020**, *16*, 974–981.

[292] Rachi, Y.; Yamakado, R.; Okada, S. Synthesis of dyes with a sulfur-containing heterocyclic donor and a pyrroline-type acceptor. *Dyes Pigm.* **2018**, *159*, 345–351.

[293] Mulliken, R. S. Electronic population analysis on LCAO–MO molecular wave functions. I. *J. Chem. Phys.* **1955**, *23*, 1833–1840.

[294] Mulliken, R. S.; Ermler, W. C. *Diatomic molecules: results of ab initio calculations*; Academic Press: New York, 1977.

[295] Mulliken, R. S. Electronic structures of molecules XI. Electroaffinity, molecular orbitals and dipole moments. *J. Chem. Phys.* **1935**, *3*, 573–585.

[296] Hirshfeld, F. L. Bonded-atom fragments for describing molecular charge densities. *Theor. Chim. Acta* **1977**, *44*, 129–138.

[297] Löwdin, P.-O. On the non-orthogonality problem connected with the use of atomic wave functions in the theory of molecules and crystals. *J. Chem. Phys.* **1950**, *18*, 365–375.

[298] Löwdin, P.-O. *Advances in quantum chemistry*; Elsevier, 1970; Vol. 5; pp 185–199.

[299] Marenich, A. V.; Jerome, S. V.; Cramer, C. J.; Truhlar, D. G. Charge model 5: an extension of Hirshfeld population analysis for the accurate description

of molecular interactions in gaseous and condensed phases. *J. Chem. Theory Comput.* **2012**, *8*, 527–541.

[300] Gibbs, J. W. *Scientific papers of Josiah Willard Gibbs, Volume 1, thermodynamics*; 1906.

[301] Gibbs, J. W.; Ostwald, W. *Thermodynamische studien*; W. Engelmann Leipzig, 1892.

[302] Zielinski, T. J.; Poirier, R. A.; Peterson, M. R.; Csizmadia, I. G. Conformational study of protonated, neutral, and deprotonated formamide. *J. Comput. Chem.* **1982**, *3*, 477–485.

[303] Wang, L.; Dai, J.; Song, Y. Theoretical investigations of the substituent effect on the electronic and charge transport properties of butterfly molecules. *New J. Chem.* **2019**, *43*, 12440–12452.

[304] Feng, X.; Hu, J.-Y.; Redshaw, C.; Yamato, T. Functionalization of pyrene to prepare luminescent materials—typical examples of synthetic methodology. *Chem. Eur. J.* **2016**, *22*, 11898–11916.

[305] Anant, P.; Lucas, N. T.; Ball, J. M.; Anthopoulos, T. D.; Jacob, J. Synthesis and characterization of pyrene-centered oligothiophenes. *Synth. Met.* **2010**, *160*, 1987–1993.

[306] Figueira-Duarte, T. M.; Mullen, K. Pyrene-based materials for organic electronics. *Chem. Rev.* **2011**, *111*, 7260–7314.

[307] Casas-Solvas, J. M.; Howgego, J. D.; Davis, A. P. Synthesis of substituted pyrenes by indirect methods. *Org. Biomol. Chem.* **2014**, *12*, 212–232.

[308] Li, J.; Chen, S.; Wang, Z.; Zhang, Q. Pyrene-fused acenes and azaacenes: synthesis and applications. *Chem. Rec.* **2016**, *16*, 1518–1530.

[309] Mateo-Alonso, A. Pyrene-fused pyrazaacenes: from small molecules to nanoribbons. *Chem. Soc. Rev.* **2014**, *43*, 6311–6324.

[310] Walsh, J. C.; Williams, K.-L. M.; Lungerich, D.; Bodwell, G. J. Synthesis of pyrene-4,5-dione on a 15 g scale. *Eur. J. Org. Chem.* **2016**, *2016*, 5933–5936.

[311] Jadhav, T.; Dhokale, B.; Mobin, S. M.; Misra, R. Aggregation induced emission and mechanochromism in pyrenoimidazoles. *J. Mater. Chem. C* **2015**, *3*, 9981–9988.

[312] Tabasi, Z. A.; Younes, E. A.; Walsh, J. C.; Thompson, D. W.; Bodwell, G. J.; Zhao, Y. Pyrenoimidazolyl-benzaldehyde fluorophores: synthesis, properties, and sensing function for fluoride anions. *ACS Omega* **2018**, *3*, 16387–16397.

[313] Rao, H. S. P.; Vijjapu, S. Synthesis and photochromic properties of benzofuran–phenanthrene and benzofuran–pyrene hybrids. *RSC Adv.* **2014**, *4*, 25747–25758.

[314] Fan, Q.; Liu, Y.; Xiao, M.; Tan, H.; Wang, Y.; Su, W.; Yu, D.; Yang, R.; Zhu, W. Donor–acceptor copolymers based on benzo [1,2-b: 4,5-b] dithiophene and pyrene-fused phenazine for high-performance polymer solar cells. *Org. Electron.* **2014**, *15*, 3375–3383.

[315] Gu, P.-Y.; Zhang, J.; Long, G.; Wang, Z.; Zhang, Q. Solution-processable thiadiazoloquinoxaline-based donor–acceptor small molecules for thin-film transistors. *J. Mater. Chem. C* **2016**, *4*, 3809–3814.

[316] Liu, Y.; Bai, Q.; Li, J.; Zhang, S.; Zhang, C.; Lu, F.; Yang, B.; Lu, P. Efficient pyrene-imidazole derivatives for organic light-emitting diodes. *RSC Adv.* **2016**, *6*, 17239–17245.

[317] Karthik, S.; Ajantha, J.; Nagaraja, C.; Easwaramoorthi, S.; Gandhi, T. Synthesis and photophysics of extended π-conjugated systems of substituted 10-aryl-pyrenoimidazoles. *Org. Biomol. Chem.* **2016**, *14*, 10255–10266.

[318] Mardanya, S.; Karmakar, S.; Mondal, D.; Baitalik, S. An imidazolyl-pyrenoimidazole conjugate as a cyanide sensor and a set–reset memorized sequential logic device. *Dalton Trans.* **2015**, *44*, 15994–16012.

[319] Young, E. R.; Funk, R. L. A practical synthesis of pyrene-4,5-dione. *J. Org. Chem.* **1998**, *63*, 9995–9996.

[320] Qian, C.-G.; Xiao, B. 4,5-Disubstituted pyrenes from phenangermoles. *Org. Chem. Front.* **2023**,

[321] Shahrokhi, F.; Zhao, Y. Self-condensation of pyrene-4,5-dione: an approach to generate functional organic fluorophores. *Org. Lett.* **2019**, *21*, 9306–9310.

[322] Winnik, F. M. Photophysics of preassociated pyrenes in aqueous polymer solutions and in other organized media. *Chem. Rev.* **1993**, *93*, 587–614.

[323] De Silva, A. P.; Gunaratne, H. N.; Gunnlaugsson, T.; Huxley, A. J.; McCoy, C. P.; Rademacher, J. T.; Rice, T. E. Signaling recognition events with fluorescent sensors and switches. *Chem. Rev.* **1997**, *97*, 1515–1566.

[324] Förster, T. Excimers. *Angew. Chem. Int. Ed.* **1969**, *8*, 333–343.

[325] Stevens, B. Some effects of molecular orientation on fluorescence emission and energy transfer in crystalline aromatic hydrocarbons. *Spectrochim. Acta* **1962**, *18*, 439–448.

[326] Cohen, M. D. Excimers in crystals. *Mol. Cryst. Liq. Cryst.* **1979**, *50*, 1–10.

[327] Wang, J.; Niino, H.; Yabe, A. One-step microfabrication of fused silica by laser ablation of an organic solution. *Appl. Phys. A* **1999**, *68*.

[328] Kwon, H.; Kang, S.; Park, S.; Lee, H.; Park, J. Optimized triple core blue emitters based on anthracene–pyrene–anthracene chromophores for organic light-emitting diodes. *Dyes Pigm.* **2023**, *209*, 110931.

[329] Förster, T.; Kasper, K. Ein konzentrationsumschlag der fluoreszenz des pyrens. *Z. Elektrochem.* **1955**, *59*, 976–980.

[330] Kurkov, S. V.; Loftsson, T. Cyclodextrins. *Int. J. Pharm.* **2013**, *453*, 167–180.

[331] Loftsson, T.; Duchene, D. Cyclodextrins and their pharmaceutical applications. *Int. J. Pharm.* **2007**, *329*, 1–11.

[332] He, Y.; Fu, P.; Shen, X.; Gao, H. Cyclodextrin-based aggregates and characterization by microscopy. *Micron* **2008**, *39*, 495–516.

[333] Saokham, P.; Couto, A. S.; Ryzhakov, A.; Loftsson, T. The self-assemble of natural cyclodextrins in aqueous solutions: application of miniature permeation studies for critical aggregation concentration (cac) determinations. *Int. J. Pharm.* **2016**, *505*, 187–193.

[334] Toydemir, C.; Hall, S.; Demirel, E.; Elmaci, D. N.; Gol, D.; Vlaisavljevich, E.; Yuksel Durmaz, Y. Bioconjugated β-cyclodextrin–perfluorohexane nanocone clusters as functional nanoparticles for nanoparticle-mediated histotripsy. *Biomacromolecules* **2022**, *23*, 5297–5311.

[335] Ryzhakov, A.; Do Thi, T.; Stappaerts, J.; Bertoletti, L.; Kimpe, K.; Couto, A. R. S.; Saokham, P.; Van den Mooter, G.; Augustijns, P.; Somsen, G. W., et al. Self-assembly of cyclodextrins and their complexes in aqueous solutions. *J. Pharm. Sci.* **2016**, *105*, 2556–2569.

[336] Kaymaz, B.; Mustafa, W.; Hall, S.; Vlaisavljevich, E.; Sensoy, O.; Yuksel Durmaz, Y. Experimental and computational investigation of clustering behavior of cyclodextrin–perfluorocarbon inclusion complexes as effective histotripsy agents. *Mol. Pharm.* **2022**, *19*, 2907–2921.

[337] Gaitano, G. G.; Brown, W.; Tardajos, G. Inclusion complexes between cyclodextrins and triblock copolymers in aqueous solution: a dynamic and static light-scattering study. *J. Phys. Chem. B* **1997**, *101*, 710–719.

[338] Polarz, S.; Smarsly, B.; Bronstein, L.; Antonietti, M. From cyclodextrin assemblies to porous materials by silica templating. *Angew. Chem. Int. Ed.* **2001**, *40*, 4417–4421.

[339] Zaman, H.; Bright, A. G.; Adams, K.; Goodall, D. M.; Forbes, R. T. Characterisation of aggregates of cyclodextrin-drug complexes using Taylor dispersion analysis. *Int. J. Pharm.* **2017**, *522*, 98–109.

[340] Arora, P.; Dhingra, N. *Cyclodextrin: a versatile ingredient*; BoD–books on demand, 2018.

[341] Duchene, D.; Bochot, A. Thirty years with cyclodextrins. *Int. J. Pharm.* **2016**, *514*, 58–72.

[342] Hirata, S.; Lee, T. J.; Head-Gordon, M. Time-dependent density functional study on the electronic excitation energies of polycyclic aromatic hydrocarbon radical cations of naphthalene, anthracene, pyrene, and perylene. *J. Chem. Phys.* **1999**, *111*, 8904–8912.

[343] Lu, H.; Wang, Q.; Li, Z.; Lai, G.; Jiang, J.; Shen, Z. A specific chemodosimeter for fluoride ion based on a pyrene derivative with trimethylsilylethynyl groups. *Org. Biomol. Chem.* **2011**, *9*, 4558–4562.

[344] Chi, W.-J.; Li, Z.-S. The theoretical investigation on the 4-(4-phenyl-4-α-naphthylbutadieny)-triphenylamine derivatives as hole transporting materials for perovskite-type solar cells. *Phys. Chem. Chem. Phys.* **2015**, *17*, 5991–5998.

[345] Mardanya, S.; Karmakar, S.; Das, S.; Baitalik, S. Anion and cation triggered modulation of optical properties of a pyridyl-imidazole receptor rigidly linked to pyrene and construction of INHIBIT, OR and XOR molecular logic gates: a combined experimental and DFT/TD-DFT investigation. *Sens. Actuators B Chem.* **2015**, *206*, 701–713.

[346] Basheer, S. M.; Willis, A. C.; Sreekanth, A. Spectroscopic and TD-DFT studies on the dual mode fluorescent chemosensors based on pyrene thiosemicarbazones, and its application as molecular-scale logic devices. *J. Lumin.* **2017**, *183*, 266–280.

[347] Wazzan, N.; El-Shishtawy, R. M.; Irfan, A. DFT and TD–DFT calculations of the electronic structures and photophysical properties of newly designed pyrene-core arylamine derivatives as hole-transporting materials for perovskite solar cells. *Theor. Chem. Acc.* **2018**, *137*, 1–15.

[348] Kerkines, I. S.; Petsalakis, I. D.; Theodorakopoulos, G.; Klopper, W. Low-lying absorption and emission spectra of pyrene, 1, 6-dithiapyrene, and tetrathiafulvalene: a comparison between ab initio and time-dependent density functional methods. *J. Chem. Phys.* **2009**, *131*, 224315.

[349] Roos, M. K.; Reiter, S.; de Vivie-Riedle, R. Ultrafast relaxation from 1La to 1Lb in pyrene: a theoretical study. *Chem. Phys.* **2018**, *515*, 586–595.

[350] Freidzon, A. Y.; Valiev, R.; Berezhnoy, A. Ab initio simulation of pyrene spectra in water matrices. *RSC Adv.* **2014**, *4*, 42054–42065.

[351] D'Abramo, M.; Aschi, M.; Amadei, A. Theoretical calculation of the pyrene emission properties in different solvents. *Chem. Phys. Lett.* **2015**, *639*, 17–22.

[352] Bito, Y.; Shida, N.; Toru, T. Ab initio MRSD-CI calculations of the ground and the two lowest-lying excited states of pyrene. *Chem. Phys. Lett.* **2000**, *328*, 310–315.

[353] Bredas, J.; Street, G. Theoretical studies of the complexes of benzene and pyrene with water and of benzene with formic acid, ammonia, and methane. *J. Chem. Phys.* **1989**, *90*, 7291–7299.

[354] Estévez-Fregoso, M.; Hernández-Trujillo, J. Electron delocalization and electron density of small polycyclic aromatic hydrocarbons in singlet excited states. *Phys. Chem. Chem. Phys.* **2016**, *18*, 11792–11799.

[355] Kınal, A.; Acar, N. A DFT and TD-DFT study on intermolecular charge transfer complexes of pyrene with phenothiazine and promazine. *J. Mol. Struct. Theochem* **2010**, *949*, 36–40.

[356] Fihey, A.; Maurel, F.; Perrier, A. Modeling the absorbance properties of a pyrene chromophore grafted onto a Au25 nanocluster: a TD-DFT study. *J. Phys. Chem. C* **2014**, *118*, 4444–4453.

[357] Basheer, S. M.; Sreekanth, A. TD-DFT study on the fluoride and copper ion sensing mechanism of pyrene N (4) phenyl thiosemicarbazone. *Comput. Theor. Chem.* **2016**, *1085*, 31–39.

[358] Staněk, T.; Dvořák, M.; Almonasy, N.; Nepraš, M.; Šloufová, I.; Michl, M. Formation of planarized intramolecular charge-transfer state in dichlorotriazinyl-pyrene fluorescent probe: TD-DFT and resonance Raman study. *Dyes Pigm.* **2017**, *141*, 121–127.

[359] Niko, Y.; Hiroshige, Y.; Kawauchi, S.; Konishi, G.-i. Fundamental photoluminescence properties of pyrene carbonyl compounds through absolute fluores-

cence quantum yield measurement and density functional theory. *Tetrahedron* **2012**, *68*, 6177–6185.

[360] Örücü, H.; Acar, N. Effects of substituent groups and solvent media on pyrene in ground and excited states: a DFT and TDDFT study. *Comput. Theor. Chem.* **2015**, *1056*, 11–18.

[361] Graef, E. L.; Martins, J. B. Analysis of lowest energy transitions at TD-DFT of pyrene in vacuum and solvent. *J. Mol. Model.* **2019**, *25*, 1–9.

[362] Idzik, K. R.; Cywiński, P. J.; Kuznik, W.; Frydel, J.; Licha, T.; Ratajczyk, T. The optical properties and quantum chemical calculations of thienyl and furyl derivatives of pyrene. *Phys. Chem. Chem. Phys.* **2015**, *17*, 22758–22769.

[363] Amicangelo, J. C. Theoretical study of the benzene excimer using time-dependent density functional theory. *J. Phys. Chem. A* **2005**, *109*, 9174–9182.

[364] Boo, B. H.; Ryu, S. Y.; Yoon, M.; Koh, S. G.; Park, K. L. Fluorescence spectroscopic and time-dependent DFT studies for intramolecular excimer formation of di-9 H-fluoren-9-yldimethylsilane: dynamics and energetics for conformational change. *J. Phys. Chem. A* **2010**, *114*, 8969–8974.

[365] Kołaski, M.; Arunkumar, C.; Kim, K. S. Aromatic excimers: ab initio and TD-DFT study. *J. Chem. Theory Comput.* **2013**, *9*, 847–856.

[366] Hoche, J.; Schmitt, H.-C.; Humeniuk, A.; Fischer, I.; Mitrić, R.; Röhr, M. I. The mechanism of excimer formation: an experimental and theoretical study on the pyrene dimer. *Phys. Chem. Chem. Phys.* **2017**, *19*, 25002–25015.

[367] Hu, Y.; Paterno, G. M.; Wang, X.-Y.; Wang, X.-C.; Guizzardi, M.; Chen, Q.; Schollmeyer, D.; Cao, X.-Y.; Cerullo, G.; Scotognella, F., et al. π-extended pyrene-fused double [7] carbohelicene as a chiral polycyclic aromatic hydrocarbon. *J. Am. Chem. Soc.* **2019**, *141*, 12797–12803.

[368] Das, A.; Danao, A.; Banerjee, S.; Raj, A. M.; Sharma, G.; Prabhakar, R.; Srinivasan, V.; Ramamurthy, V.; Sen, P. Dynamics of anthracene excimer formation within a water-soluble nanocavity at room temperature. *J. Am. Chem. Soc.* **2021**, *143*, 2025–2036.

[369] Venkataramana, G.; Dongare, P.; Dawe, L. N.; Thompson, D. W.; Zhao, Y.; Bodwell, G. J. 1,8-Pyrenylene- ethynylene macrocycles. *Org. Lett.* **2011**, *13*, 2240–2243.

[370] Brouwer, A. M. Standards for photoluminescence quantum yield measurements in solution (IUPAC Technical Report). *Pure Appl. Chem.* **2011**, *83*, 2213–2228.

[371] Eaton, D. F. Reference materials for fluorescence measurement. *Pure Appl. Chem.* **1988**, *60*, 1107–1114.

[372] Aminabhavi, T. M.; Gopalakrishna, B. Density, viscosity, refractive index, and speed of sound in aqueous mixtures of N, N-dimethylformamide, dimethyl sulfoxide, N, N-dimethylacetamide, acetonitrile, ethylene glycol, diethylene glycol, 1, 4-dioxane, tetrahydrofuran, 2-methoxyethanol, and 2-ethoxyethanol at 298.15 K. *J. Chem. Eng. Data* **1995**, *40*, 856–861.

[373] Sheldrick, G. M. SHELXT–Integrated space-group and crystal-structure determination. *Acta Crystallogr. A Found. Adv.* **2015**, *71*, 3–8.

[374] Sheldrick, G. M. Crystal structure refinement with SHELXL. *Acta Crystallogr. C Struct. Chem.* **2015**, *71*, 3–8.

[375] Dolomanov, O. V.; Bourhis, L. J.; Gildea, R. J.; Howard, J. A.; Puschmann, H. OLEX2: a complete structure solution, refinement and analysis program. *J. Appl. Crystallogr.* **2009**, *42*, 339–341.

[376] Miertuš, S.; Scrocco, E.; Tomasi, J. Electrostatic interaction of a solute with a continuum. A direct utilizaion of ab initio molecular potentials for the prevision of solvent effects. *Chem. Phys.* **1981**, *55*, 117–129.

[377] Miertus, S.; Tomasi, J. Approximate evaluations of the electrostatic free energy and internal energy changes in solution processes. *Chem. Phys.* **1982**, *65*, 239–245.

[378] Pascual-ahuir, J.-L.; Silla, E.; Tunon, I. GEPOL: An improved description of molecular surfaces. III. A new algorithm for the computation of a solvent-excluding surface. *J. Comput. Chem.* **1994**, *15*, 1127–1138.

[379] Barone, V.; Cossi, M. Quantum calculation of molecular energies and energy gradients in solution by a conductor solvent model. *J. Phys. Chem. A* **1998**, *102*, 1995–2001.

[380] Mennucci, B.; Cances, E.; Tomasi, J. Evaluation of solvent effects in isotropic and anisotropic dielectrics and in ionic solutions with a unified integral equation method: theoretical bases, computational implementation, and numerical applications. *J. Phys. Chem. B* **1997**, *101*, 10506–10517.

[381] Pracht, P.; Bohle, F.; Grimme, S. Automated exploration of the low-energy chemical space with fast quantum chemical methods. *Phys. Chem. Chem. Phys.* **2020**, *22*, 7169–7192.

[382] King, N. J.; Brown, A. Intermolecular interactions of pyrene and its oxides in toluene solution. *J. Phys. Chem. A* **2022**, *126*, 4931–4940.

[383] Grimme, S. Exploration of chemical compound, conformer, and reaction space with meta-dynamics simulations based on tight-binding quantum chemical calculations. *J. Chem. Theory Comput.* **2019**, *15*, 2847–2862.

[384] Bannwarth, C.; Caldeweyher, E.; Ehlert, S.; Hansen, A.; Pracht, P.; Seibert, J.; Spicher, S.; Grimme, S. Extended tight-binding quantum chemistry methods. *Wiley Interdiscip. Rev. Comput. Mol. Sci.* **2021**, *11*, e1493.

[385] Grimme, S.; Bannwarth, C.; Shushkov, P. A robust and accurate tight-binding quantum chemical method for structures, vibrational frequencies, and noncovalent interactions of large molecular systems parametrized for all spd-block elements (Z= 1–86). *J. Chem. Theory Comput.* **2017**, *13*, 1989–2009.

[386] Bannwarth, C.; Ehlert, S.; Grimme, S. GFN2-xTB—An accurate and broadly parametrized self-consistent tight-binding quantum chemical method with multipole electrostatics and density-dependent dispersion contributions. *J. Chem. Theory Comput.* **2019**, *15*, 1652–1671.

Appendix A

Appendix

Supporting Information for Chapter 3

Bond type	*d* (Å)	ρ	$\nabla^2\rho$	$H_b(r)$	$G_b(r)$	$V_b(r)$
$Au_1 \ldots S_1$	2.542	0.062	0.171	-0.011	0.053	-0.064
$Au_2 \ldots S_2$	2.604	0.055	0.154	-0.008	0.046	-0.054
$Au_3 \ldots O_1$	2.463	0.037	0.183	0.001	0.045	-0.044
$Au_3 \ldots H_1$	2.598	0.013	0.039	0.000	0.009	-0.009

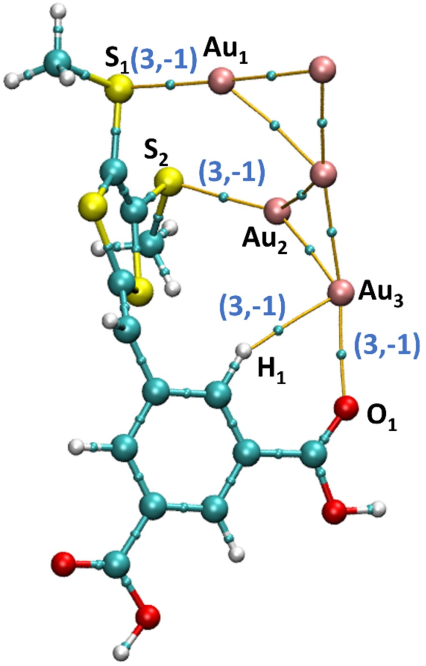

Figure A.1: Bond nature description based on the QTAIM analysis of the Au_5/DTF complex (calculated in DMSO).

Bond	d (Å)	ρ	$\nabla^2\rho$	H_b(r)	G_b(r)	V_b(r)	Bond Type
$Au_1 \ldots C_1$	3.459	0.008	0.022	0.001	0.005	-0.004	(3,-1)
$Au_2 \ldots O_1$	3.362	0.008	0.022	0.000	0.005	-0.005	(3,-1)
$Au_3 \ldots C_2$	3.108	0.014	0.043	0.001	0.010	-0.009	(3,-1)
$Au_3 \ldots S_1$	2.837	0.035	0.099	-0.003	0.027	-0.030	(3,-1)
$Au_3 \ldots H_2$	2.701	0.011	0.035	0.000	0.008	-0.008	(3,-1)
$Au_4 \ldots C_3$	3.759	0.006	0.013	0.000	0.003	-0.003	(3,-1)
$Au_5 \ldots S_2$	2.736	0.042	0.117	-0.004	0.034	-0.038	(3,-1)
$Au_5 \ldots H_3$	2.969	0.007	0.021	0.001	0.004	-0.004	(3,-1)
$S_1 \ldots H_1$	2.712	0.011	0.037	0.002	0.008	-0.006	(3,-1)

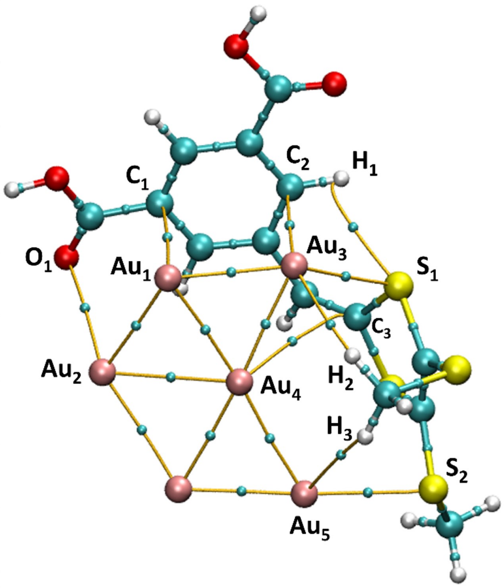

Figure A.2: Bond nature description based on the QTAIM analysis of the Au_6/DTF complex (calculated in DMSO).

Bond	d (Å)	ρ	$\nabla^2\rho$	H_b(r)	G_b(r)	V_b(r)	Bond Type
$Au_1 \ldots O_1$	3.223	0.010	0.030	0.000	0.007	-0.007	(3,-1)
$Au_1 \ldots H_1$	2.856	0.010	0.036	0.001	0.007	-0.006	(3,-1)
$Au_2 \ldots C_2$	3.953	0.004	0.009	0.000	0.002	-0.002	(3,-1)
$Au_2 \ldots S_3$	4.092	0.004	0.010	0.000	0.002	-0.002	(3,-1)
$Au_3 \ldots S_4$	3.239	0.017	0.046	0.000	0.012	-0.012	(3,-1)
$Au_4 \ldots S_2$	3.903	0.005	0.012	0.000	0.003	-0.003	(3,-1)
$Au_5 \ldots S_1$	2.578	0.057	0.159	-0.009	0.049	-0.058	(3,-1)
$Au_5 \ldots C_1$	3.066	0.015	0.046	0.001	0.010	-0.009	(3,-1)
$S_1 \ldots H_2$	2.588	0.013	0.046	0.002	0.010	-0.008	(3,-1)

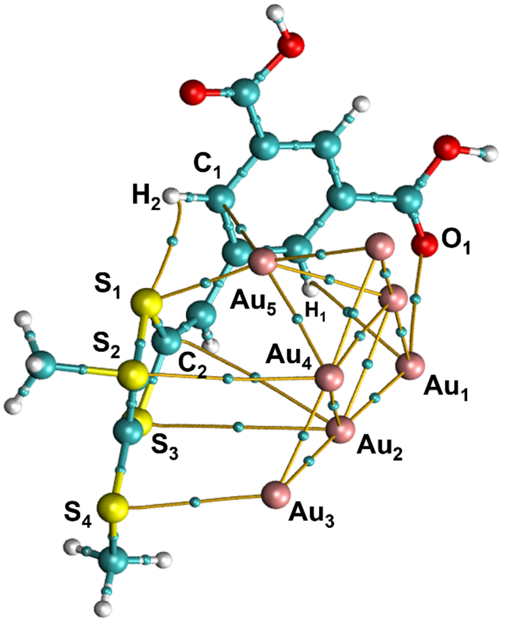

Figure A.3: Bond nature description based on the QTAIM analysis of the Au_7/DTF complex (calculated in DMSO).

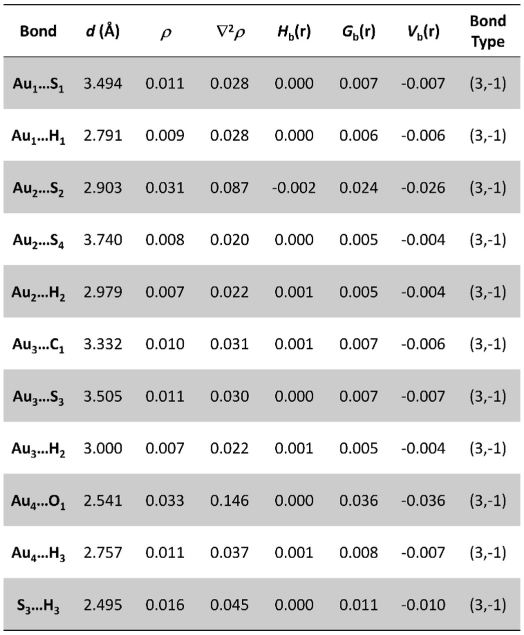

Bond	*d* (Å)	ρ	$\nabla^2\rho$	$H_b(r)$	$G_b(r)$	$V_b(r)$	Bond Type
$Au_1 \ldots S_1$	3.494	0.011	0.028	0.000	0.007	-0.007	(3,-1)
$Au_1 \ldots H_1$	2.791	0.009	0.028	0.000	0.006	-0.006	(3,-1)
$Au_2 \ldots S_2$	2.903	0.031	0.087	-0.002	0.024	-0.026	(3,-1)
$Au_2 \ldots S_4$	3.740	0.008	0.020	0.000	0.005	-0.004	(3,-1)
$Au_2 \ldots H_2$	2.979	0.007	0.022	0.001	0.005	-0.004	(3,-1)
$Au_3 \ldots C_1$	3.332	0.010	0.031	0.001	0.007	-0.006	(3,-1)
$Au_3 \ldots S_3$	3.505	0.011	0.030	0.000	0.007	-0.007	(3,-1)
$Au_3 \ldots H_2$	3.000	0.007	0.022	0.001	0.005	-0.004	(3,-1)
$Au_4 \ldots O_1$	2.541	0.033	0.146	0.000	0.036	-0.036	(3,-1)
$Au_4 \ldots H_3$	2.757	0.011	0.037	0.001	0.008	-0.007	(3,-1)
$S_3 \ldots H_3$	2.495	0.016	0.045	0.000	0.011	-0.010	(3,-1)

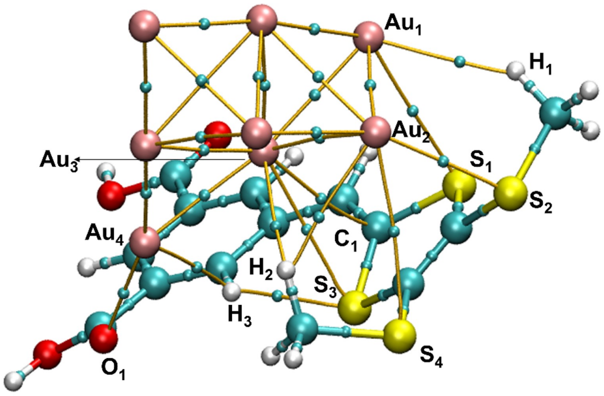

Figure A.4: Bond nature description based on the QTAIM analysis of the Au_8/DTF complex (calculated in DMSO).

Supporting Information for Chapter 5

Quantum Chemical Calculations of Molecular Structure and Electronic Properties of Dithiafulvene-substituted Polycyclic Aromatic Hydrocarbons

In this chapter, DFT and TD-DFT calculations have been done at M06-2X/Def2-SVP and M06-2X/6-311++g(d,2p) levels of theory, respectively.

A.1 Dithiafulvenylbenzene

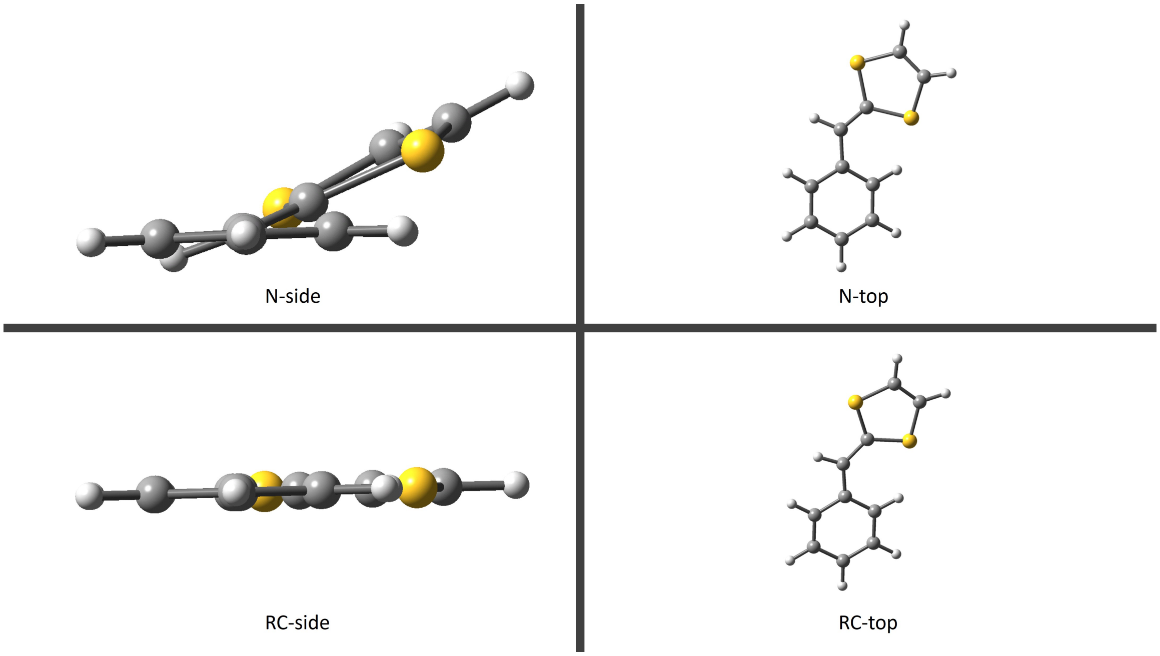

Figure A.5: Optimized geometry of dithiafulvenylbenzene **1**.

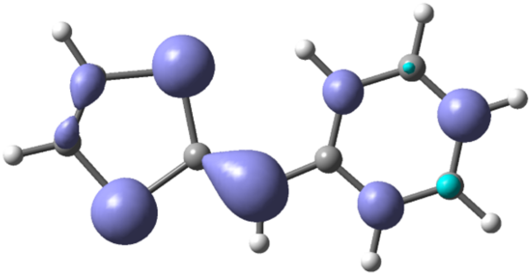

Figure A.6: Schematic illustration of spin density distribution over dithiafulvenylbenzene **1** (isovalue = 0.005).

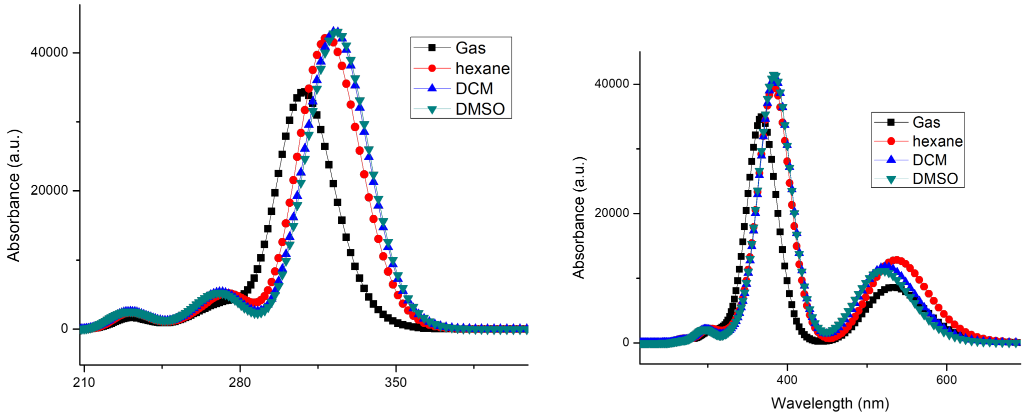

Figure A.7: UV-vis spectra of dithiafulvenylbenzene **1** in neutral (left) and radical cation (right) oxidation states.

Table A.1: Cartesian coordinates, energies, and dipole momentum of the optimized geometries of dithiafulvenylbenzene in N and RC oxidation states.

1-N in gas (E = -1181.502419 Hartree, μ = 1.612547 D) **1-N in hexanes** (E = -1181.514581 Hartree, μ = 1.800264 D) **1-N in DCM** (E = -1181.519172 Hartree, μ = 2.091700 D) **1-N in DMSO** (E = -1181.513321 Hartree, μ = 2.182971 D)				**1-RC in gas** (E = -1181.247463 Hartree, μ = 2.644097 D) **1-RC in hexanes** (E = -1181.292371 Hartree, μ = 3.269976 D) **1-RC in DCM** (E = -1181.324021 Hartree, μ = 4.295227 D) **1-RC in DMSO** (E = -1181.323779 Hartree, μ = 4.626912 D)			
C	-3.832719	-0.868974	-0.335819	C	-3.860184	-0.925776	0.000649
C	-2.525053	-1.330073	-0.244187	C	-2.541611	-1.345859	0.000448
C	-1.466644	-0.467022	0.097936	C	-1.474054	-0.407582	-0.00025
C	-1.779547	0.874954	0.376758	C	-1.792494	0.975834	-0.000794
C	-3.091868	1.33475	0.286242	C	-3.11305	1.386961	-0.000588
C	-4.123491	0.471423	-0.076867	C	-4.149287	0.442144	0.000147
H	-4.631594	-1.559646	-0.610448	H	-4.66752	-1.658015	0.00121
H	-2.304924	-2.38007	-0.448523	H	-2.310703	-2.412756	0.000854
H	-1.006245	1.567258	0.708349	H	-1.017418	1.740072	-0.001507
H	-3.308956	2.379943	0.51244	H	-3.348357	2.451321	-0.00103
H	-5.148719	0.836983	-0.148059	H	-5.187014	0.778664	0.000303
C	-0.115561	-1.029564	0.154122	C	-0.155813	-0.956176	-0.000234
H	-0.07157	-2.120158	0.224564	H	-0.117766	-2.05001	-0.00024
C	1.077635	-0.399827	0.088553	C	1.099875	-0.348486	-0.00015
C	3.083526	1.230972	-0.280039	C	3.157241	1.181787	0.000446
C	3.646924	0.028279	-0.132453	C	3.653036	-0.076546	0.000103
H	3.629869	2.153729	-0.471583	H	3.760016	2.090991	0.000777
H	4.7175	-0.165187	-0.188437	H	4.71442	-0.328333	0.000097
S	2.589379	-1.323127	0.189826	S	2.508258	-1.354694	-0.000387
S	1.340961	1.33673	-0.138813	S	1.443767	1.344086	0.000441

A.2 1-dithiafulvenylnaphthalene

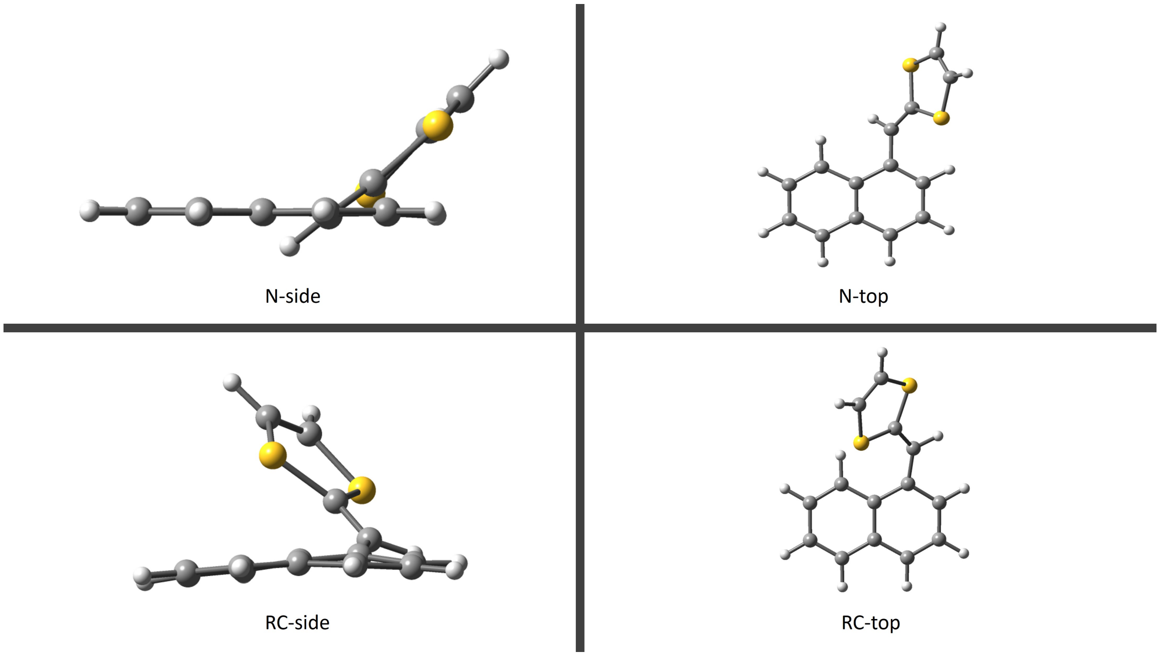

Figure A.8: Optimized geometry of 1-dithiafulvenylnaphthalene **2(s-cis)**.

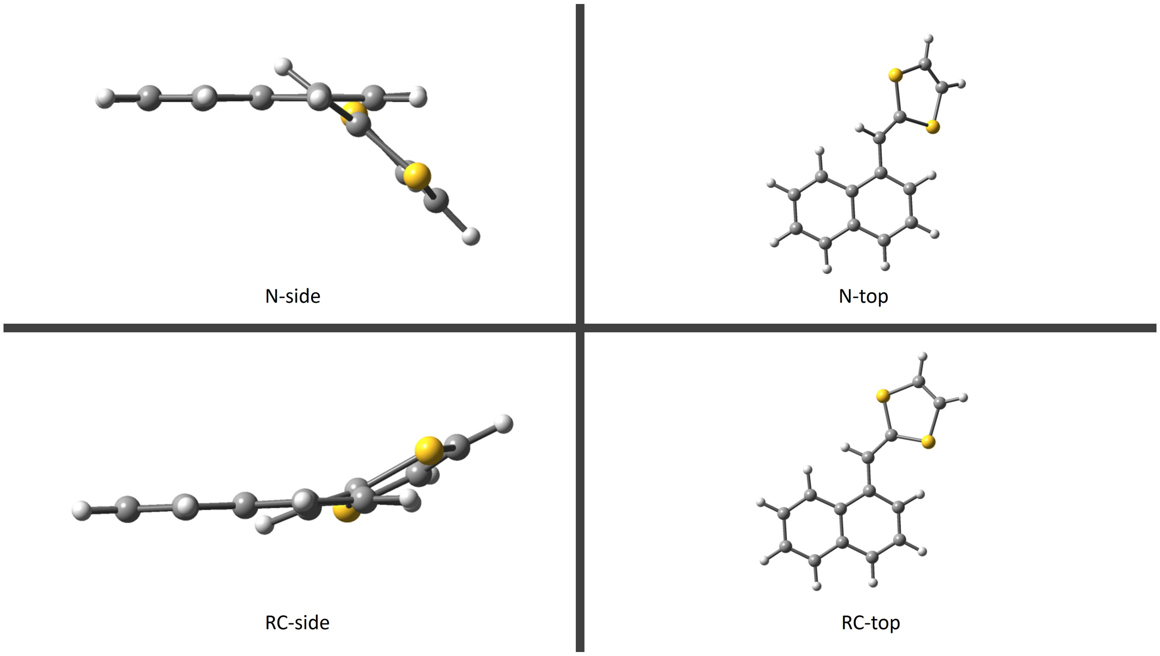

Figure A.9: Optimized geometry of 1-dithiafulvenylnaphthalene **2(s-trans)**.

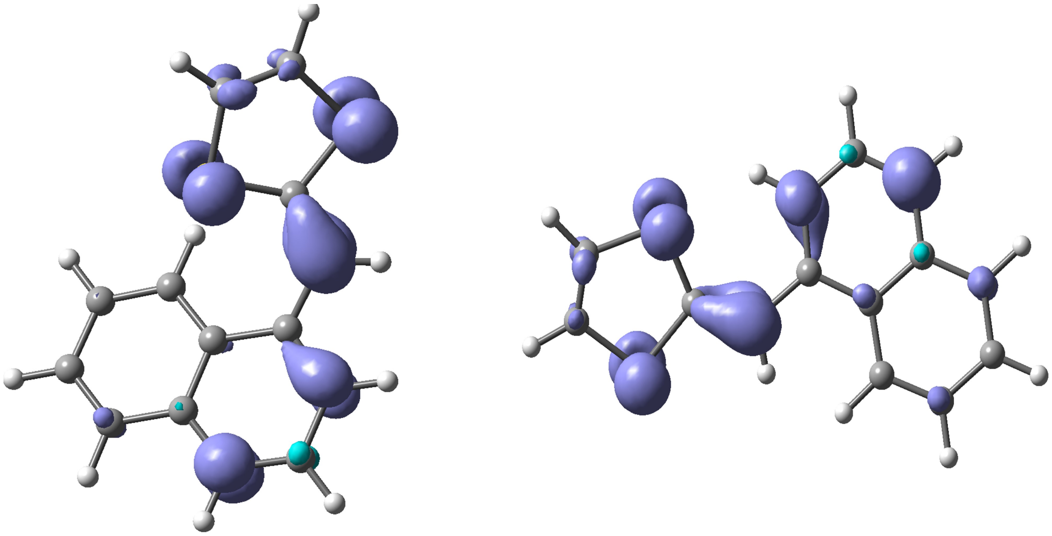

2 (s-cis) **2** (s-trans)

Figure A.10: Schematic illustration of spin density distribution over 1-dithiafulvenylnaphthalene **2** (isovalue = 0.005).

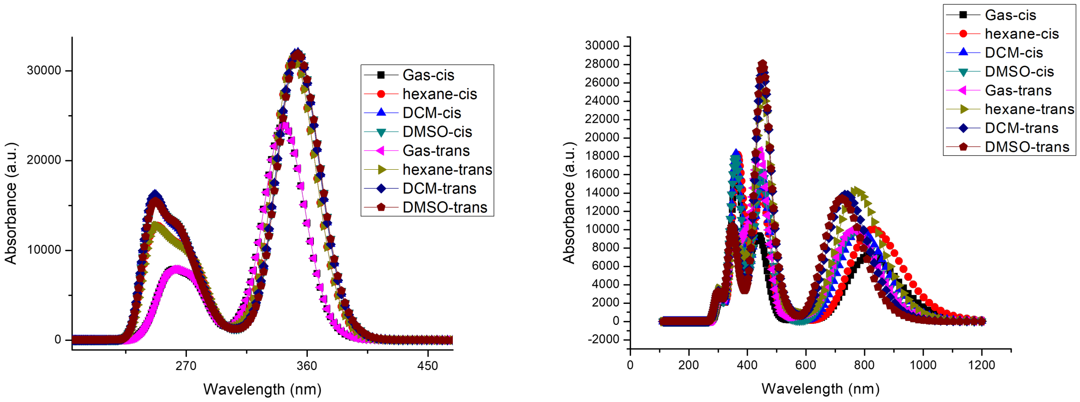

Figure A.11: UV-vis spectra of 1-dithiafulvenylnaphthalene **2** in neutral (left) and radical cation (right) oxidation states.

Table A.2: Cartesian coordinates, energies, and dipole momentum of the optimized geometries of 1-dithiafulvenylnaphthalene (s-cis) in N and RC oxidation states.

2-N (s-cis) in gas (E = -1334.972385 Hartree, μ = 1.494915 D) **2-N (s-cis) in hexanes** (E = -1334.988198 Hartree, μ = 1.800264 D) **2-N (s-cis) in DCM** (E = -1334.993677 Hartree, μ = 1.649704 D) **2-N (s-cis) in DMSO** (E = -1334.986338 Hartree, μ = 1.943071 D)				**2-RC (s-cis) in gas** (E = -1334.718136 Hartree, μ = 3.388147 D) **2-RC (s-cis) in hexanes** (E = -1334.764516 Hartree, μ = 4.079582 D) **2-RC (s-cis) in DCM** (E = -1334.795108 Hartree, μ = 5.370475 D) **2-RC (s-cis) in DMSO** (E = -1334.793122 Hartree, μ = 5.828776 D)			
C	4.382369	-1.364079	0.50731	C	3.085603	-2.318776	-0.222544
C	4.248738	-0.010099	0.324027	C	3.574339	-1.135378	0.285326
C	2.987252	0.565378	0.010449	C	2.795663	0.048074	0.232775
C	1.847588	-0.281835	-0.123955	C	1.470711	-0.002186	-0.293575
C	2.017345	-1.677218	0.091344	C	1.026562	-1.212195	-0.871335
C	3.249927	-2.205159	0.39475	C	1.814247	-2.346627	-0.830794
H	3.723809	2.605919	-0.049412	H	4.364879	1.313695	1.027408
H	5.356061	-1.793207	0.747825	H	3.692982	-3.223529	-0.189913
H	5.112677	0.650983	0.419229	H	4.578947	-1.085723	0.70878
C	2.843514	1.969811	-0.160314	C	3.350008	1.297061	0.624866
C	0.572686	0.301449	-0.45361	C	0.695605	1.220571	-0.315128
H	1.151515	-2.336751	0.034239	H	0.07241	-1.244805	-1.398264
H	3.355088	-3.278714	0.557981	H	1.457561	-3.267687	-1.293574
C	0.489304	1.672638	-0.616652	C	1.342726	2.441701	-0.032437
C	1.619271	2.508686	-0.462118	C	2.650988	2.479162	0.45393
H	-0.460454	2.121154	-0.913004	H	0.777997	3.3715	-0.125708
H	1.510272	3.585006	-0.60254	H	3.107128	3.433866	0.71451
C	-0.600634	-0.563718	-0.637422	C	-0.711871	1.319196	-0.521525
C	-1.868882	-0.288541	-0.267843	H	-1.058491	2.295488	-0.87639
C	-4.393338	-0.568012	0.334551	C	-1.744924	0.442466	-0.182914
C	-4.031413	0.591317	0.89188	C	-4.125435	-0.422986	0.262764
H	-5.383848	-1.013669	0.41759	C	-3.301201	-1.302957	0.870536
H	-4.687409	1.221641	1.491248	H	-5.213823	-0.489967	0.25081
S	-2.394829	1.154726	0.618372	H	-3.629091	-2.184046	1.423581
S	-3.19411	-1.413239	-0.616864	S	-3.375492	0.892292	-0.554036
H	-0.437043	-1.529866	-1.121646	S	-1.605048	-1.014888	0.741479

Table A.3: Cartesian coordinates, energies, and dipole momentum of the optimized geometries of 1-dithiafulvenylnaphthalene (s-trans) in N and RC oxidation states.

2-N (s-trans) in gas (E = -1334.972385 Hartree, μ = 1.495435 D) **2-N (s-trans) in hexanes** (E = -1334.988198 Hartree, μ = 1.650182 D) **2-N (s-trans) in DCM** (E = -1334.993676 Hartree, μ = 1.879028 D) **2-N (s-trans) in DMSO** (E = -1334.986338 Hartree, μ = 1.943493 D)				**2-RC (s-trans) in gas** (E = -1334.722376 Hartree, μ = 3.945403 D) **2-RC (s-trans) in hexanes** (E = -1334.768703 Hartree, μ = 4.857297 D) **2-RC (s-trans) in DCM** (E = -1334.799291 Hartree, μ = 6.422121 D) **2-RC (s-trans) in DMSO** (E = -1334.797146 Hartree, μ = 6.949366 D)			
C	-4.381726	-1.364528	0.507871	C	4.539352	-1.270184	0.272187
C	-4.248402	-0.01052	0.324556	C	4.333672	0.081823	0.119567
C	-2.987141	0.565207	0.010558	C	3.022183	0.600206	-0.035
C	-1.847363	-0.281802	-0.124265	C	1.900757	-0.283422	-0.040282
C	-2.016794	-1.677211	0.091055	C	2.145536	-1.662195	0.142386
C	-3.249164	-2.20539	0.394902	C	3.433664	-2.143092	0.286698
H	-3.724064	2.605637	-0.049056	H	3.691676	2.654464	-0.165454
H	-5.355264	-1.793822	0.748718	H	5.548258	-1.665824	0.389814
H	-5.112424	0.650416	0.420054	H	5.175348	0.776458	0.118876
C	-2.843702	1.969668	-0.160232	C	2.820035	1.996916	-0.171595
C	-0.572647	0.301686	-0.454308	C	0.569648	0.284733	-0.201119
H	-1.150834	-2.336553	0.033598	H	1.323916	-2.375468	0.191598
H	-3.354033	-3.278972	0.558149	H	3.593311	-3.213647	0.420697
C	-0.489606	1.672874	-0.617433	C	0.442307	1.684257	-0.339231
C	-1.61965	2.508734	-0.462469	C	1.548827	2.529455	-0.322783
H	0.459995	2.121557	-0.914065	H	-0.532443	2.127281	-0.540137
H	-1.510862	3.585073	-0.60293	H	1.413475	3.602737	-0.45411
C	0.600702	-0.563344	-0.638517	C	-0.556433	-0.579144	-0.274301
H	0.437383	-1.529066	-1.123705	H	-0.351427	-1.630436	-0.486576
C	1.868807	-0.288556	-0.268046	C	-1.913678	-0.298697	-0.109805
C	4.393249	-0.567541	0.334545	C	-4.246396	0.62506	0.449415
C	4.030983	0.591406	0.892442	C	-4.459251	-0.644016	0.044255
H	5.383893	-1.012991	0.417168	H	-5.024627	1.319917	0.767084
H	4.686762	1.221692	1.492082	H	-5.435813	-1.125961	-0.01339
S	2.394109	1.154235	0.619357	S	-3.069572	-1.55146	-0.412634
S	3.194277	-1.412803	-0.617105	S	-2.610615	1.176478	0.465711

A.3 2-dithiafulvenylnaphthalene

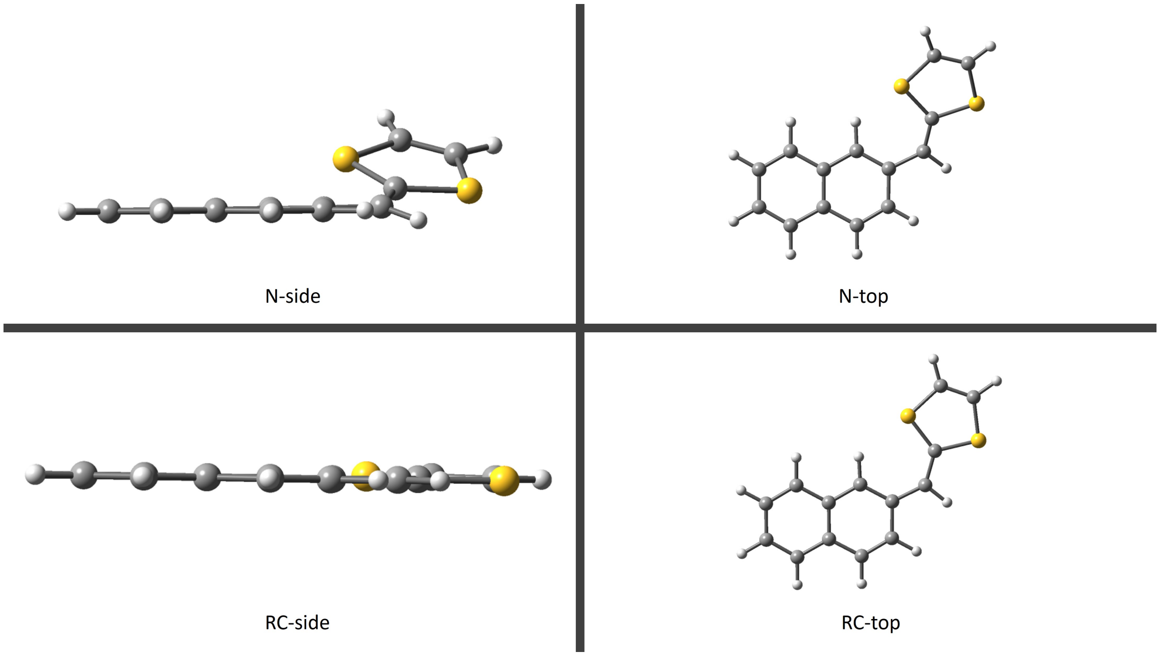

Figure A.12: Optimized geometry of 2-dithiafulvenylnaphthalene **3**.

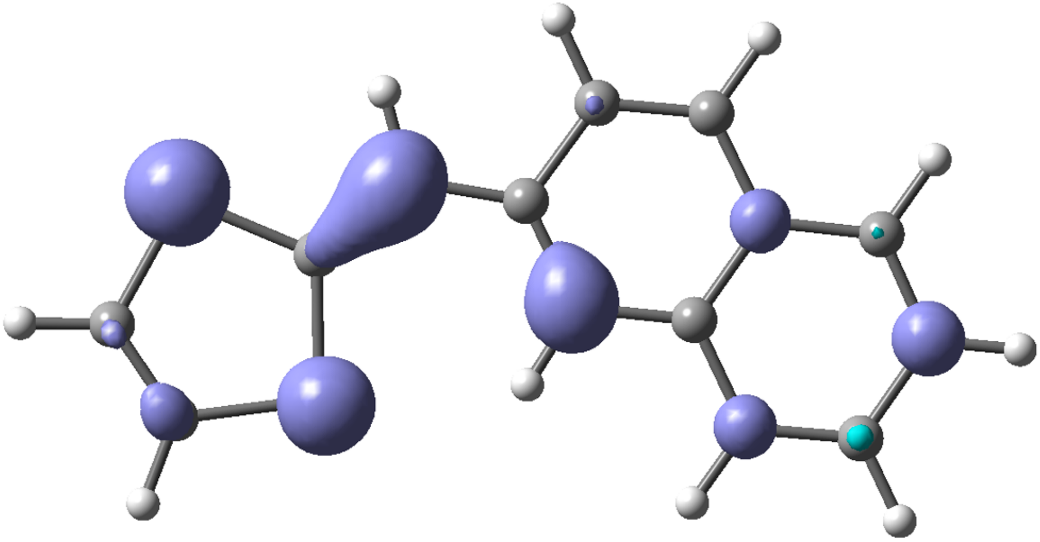

Figure A.13: Schematic illustration of spin density distribution over 2-dithiafulvenylnaphthalene **3** (isovalue = 0.005).

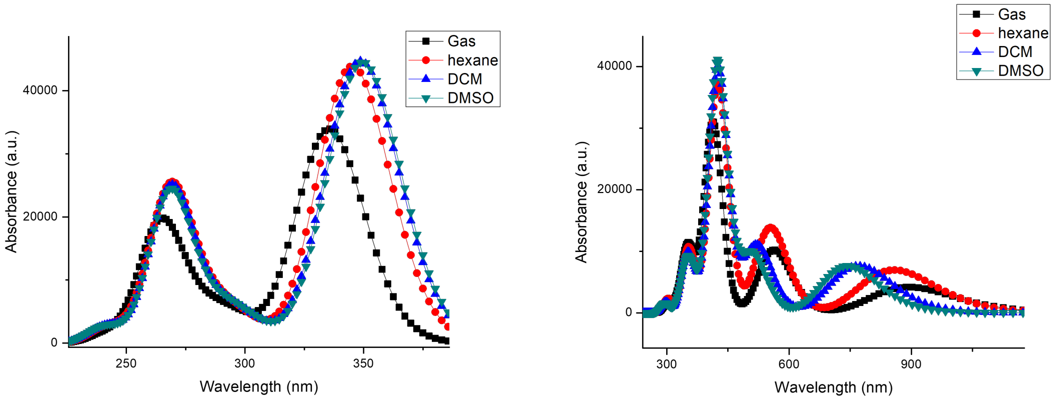

Figure A.14: UV-vis spectra of 2-dithiafulvenylnaphthalene **3** in neutral (left) and radical cation (right) oxidation states.

Table A.4: Cartesian coordinates, energies, and dipole momentum of the optimized geometries of 2-dithiafulvenylnaphthalene in N and RC oxidation states.

3-N in gas (E = -1334.974303 Hartree, μ = 1.772417 D) **3-N in hexanes** (E = -1334.990311 Hartree, μ = 1.972428 D) **3-N in DCM** (E = -1334.996026 Hartree, μ = 2.278959 D) **3-N in DMSO** (E = -1334.988686 Hartree, μ = 2.374174 D)				**3-RC in gas** (E = -1334.723801 Hartree, μ = 4.623221 D) **3-RC in hexanes** (E = -1334.770345 Hartree, μ = 5.747937 D) **3-RC in DCM** (E = -1334.801200 Hartree, μ = 7.628705 D) **3-RC in DMSO** (E = -1334.799103 Hartree, μ = 8.237497 D)			
C	5.0121	-0.689076	0.099139	C	5.031006	-0.674463	0.001073
C	4.443888	0.550224	0.272939	C	4.468293	0.587233	0.00864
C	3.04202	0.730162	0.139413	C	3.067061	0.741404	0.005156
C	2.223326	-0.392057	-0.174895	C	2.240088	-0.427757	-0.006104
C	2.840977	-1.66105	-0.353904	C	2.851427	-1.71706	-0.014183
C	4.20025	-1.806393	-0.219242	C	4.218615	-1.834946	-0.010486
H	3.038619	2.867159	0.526644	H	3.075078	2.917776	0.019022
H	6.09039	-0.817146	0.203905	H	6.116588	-0.781711	0.003807
H	5.063394	1.416317	0.515267	H	5.101978	1.475321	0.017072
C	2.417134	1.99923	0.296597	C	2.442556	2.028734	0.011182
C	0.819725	-0.219729	-0.30757	C	0.843274	-0.283106	-0.00939
H	2.212643	-2.520026	-0.598609	H	2.216053	-2.604597	-0.023099
H	4.661016	-2.785651	-0.357366	H	4.685613	-2.819948	-0.016511
C	0.220704	1.016258	-0.131687	C	0.235633	0.987695	-0.002072
C	1.06269	2.136268	0.161185	C	1.086642	2.150059	0.006806
H	0.234698	-1.093303	-0.59668	H	0.253543	-1.199121	-0.021494
H	0.599913	3.117312	0.286378	H	0.624398	3.138279	0.011294
C	-1.216735	1.267934	-0.229195	C	-1.166108	1.223522	-0.004765
H	-1.497295	2.313995	-0.381254	H	-1.449088	2.280706	-0.008592
C	-2.243125	0.396056	-0.113405	C	-2.25577	0.351218	-0.002199
C	-4.651694	-0.573522	0.169185	C	-4.690052	-0.47957	-0.001274
C	-3.83506	-1.604492	0.406624	C	-3.932001	-1.596321	0.012771
H	-5.738689	-0.61831	0.225072	H	-5.780571	-0.46604	-0.004693
H	-4.163055	-2.606193	0.681718	H	-4.318417	-2.616092	0.022151
S	-2.112617	-1.332153	0.243942	S	-2.221019	-1.375904	0.015552
S	-3.91981	0.946339	-0.281203	S	-3.852054	1.021877	-0.01367

A.4 2-dithiafulvenylanthracene

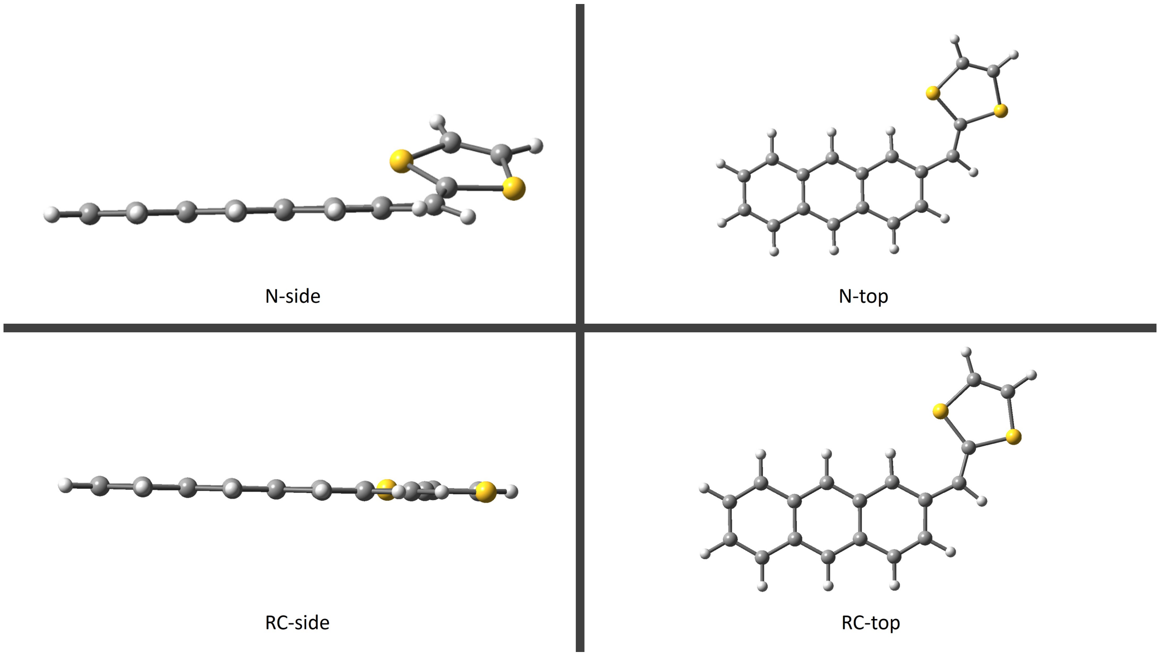

Figure A.15: Optimized geometry of 2-dithiafulvenylanthracene **4**.

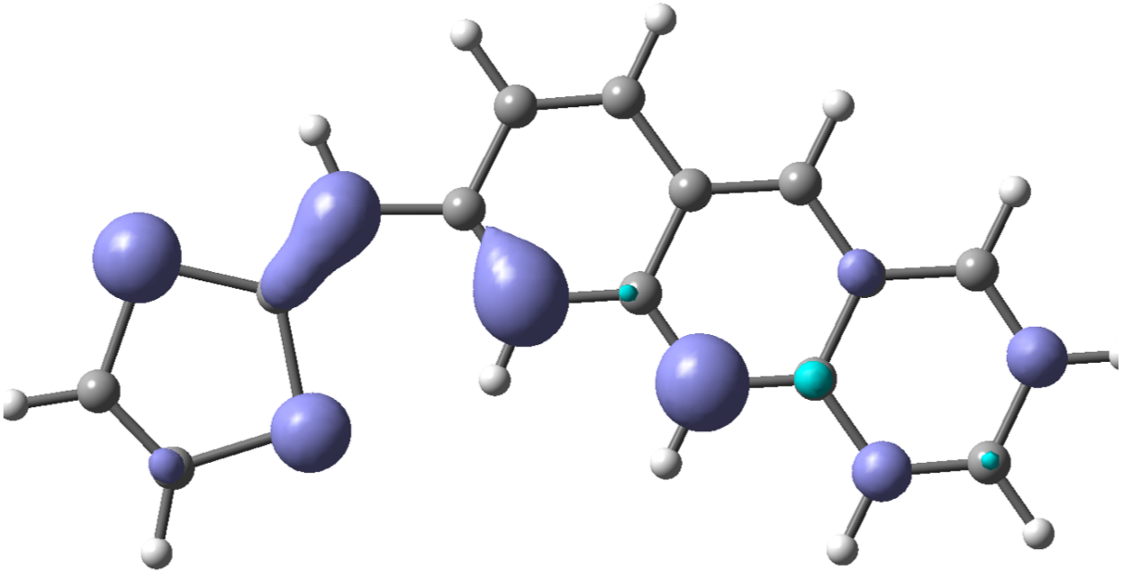

Figure A.16: Schematic illustration of spin density distribution over 2-dithiafulvenylanthracene **4** (isovalue = 0.005).

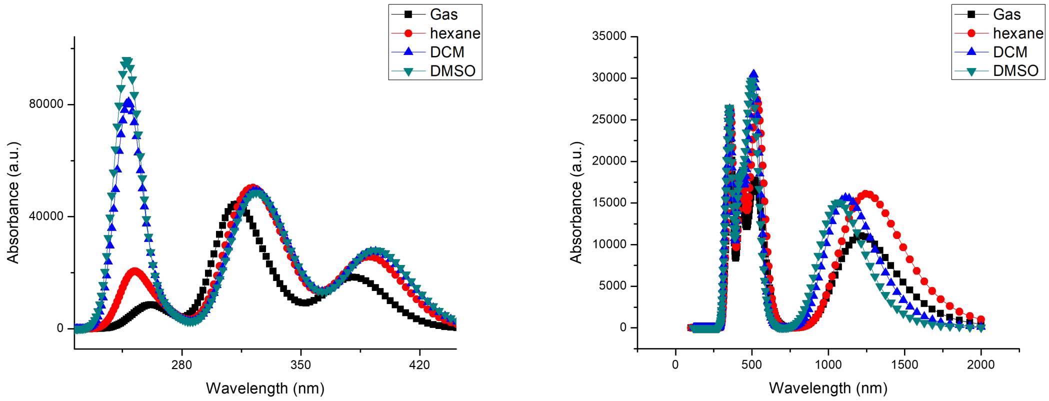

Figure A.17: UV-vis spectra of 2-dithiafulvenylanthracene **4** in neutral (left) and radical cation (right) oxidation states.

Table A.5: Cartesian coordinates, energies, and dipole momentum of the optimized geometries of 2-dithiafulvenylanthracene in N and RC oxidation states.

4-N in gas (E = -1488.438996 Hartree, μ = 1.915257 D) **4-N in hexanes** (E = -1488.458862 Hartree, μ = 2.121947 D) **4-N in DCM** (E = -1488.465677 Hartree, μ = 2.434055 D) **4-N in DMSO** (E = -1488.456815 Hartree, μ = 2.529568 D)				**4-RC in gas** (E = -1488.195408 Hartree, μ = 4.646864 D) **4-RC in hexanes** (E = -1488.243402 Hartree, μ = 6.108607 D) **4-RC in DCM** (E = -1488.273026 Hartree, μ = 9.007903 D) **4-RC in DMSO** (E = -1488.268950 Hartree, μ = 10.023291 D)			
C	6.142408	-0.665358	0.133723	C	-6.153716	-0.664457	0.000219
C	5.378554	0.459251	0.268088	C	-5.391921	0.482332	0.000206
C	3.955224	0.402229	0.124658	C	-3.976569	0.404308	0.000061
C	3.339687	-0.864459	-0.164316	C	-3.354005	-0.891318	-0.000077
C	4.176578	-2.019525	-0.297722	C	-4.17528	-2.058937	-0.000062
C	5.531472	-1.924142	-0.153744	C	-5.541959	-1.945544	0.000085
C	3.146974	1.538819	0.254636	C	-3.16603	1.566055	0.000056
C	1.948922	-0.933877	-0.305474	C	-1.956729	-0.973357	-0.000221
C	1.141118	0.200831	-0.169909	C	-1.154205	0.186988	-0.000195
C	1.760012	1.467002	0.112649	C	-1.785111	1.484752	-0.000077
C	0.91556	2.620249	0.226886	C	-0.939929	2.649169	-0.000069
H	1.377983	3.588318	0.429807	H	-1.410148	3.634021	-0.000079
C	-0.433552	2.516665	0.084394	C	0.412551	2.53741	-0.000081
C	-1.075383	1.250975	-0.175081	C	1.06474	1.246795	-0.000117
C	-0.280759	0.133816	-0.310274	C	0.248964	0.095579	-0.000215
H	3.612865	2.503624	0.470309	H	-3.648648	2.545966	0.000152
H	7.226108	-0.608366	0.24538	H	-7.242024	-0.591745	0.000334
H	5.841049	1.42376	0.487656	H	-5.868719	1.463797	0.000308
H	3.706037	-2.980048	-0.517461	H	-3.6972	-3.040024	-0.000167
H	6.156936	-2.811936	-0.257864	H	-6.166445	-2.839242	0.000098
H	1.48262	-1.897737	-0.524147	H	-1.477727	-1.955421	-0.000332
H	-1.060852	3.405636	0.17628	H	1.035565	3.432742	-0.000093
H	-0.707245	-0.834642	-0.573021	H	0.677213	-0.905901	-0.000305
C	-2.532789	1.258702	-0.276856	C	2.483484	1.243091	0.000001
H	-2.983419	2.237479	-0.463832	H	2.941514	2.23634	0.000058
C	-3.399937	0.232036	-0.125036	C	3.403918	0.198734	0.000035
C	-5.611335	-1.112858	0.215186	C	5.663578	-1.046436	0.000128
C	-4.633342	-1.982592	0.48642	C	4.728448	-2.01432	0.000058
H	-6.675476	-1.335937	0.282583	H	6.740239	-1.218332	0.000203
H	-4.788708	-3.012782	0.804591	H	4.931557	-3.085372	0.00006
S	-2.981214	-1.433792	0.295494	S	3.074898	-1.500378	-0.000064
S	-5.14406	0.487294	-0.303597	S	5.095318	0.58276	0.000149

A.5 1-dithiafulvenylanthracene

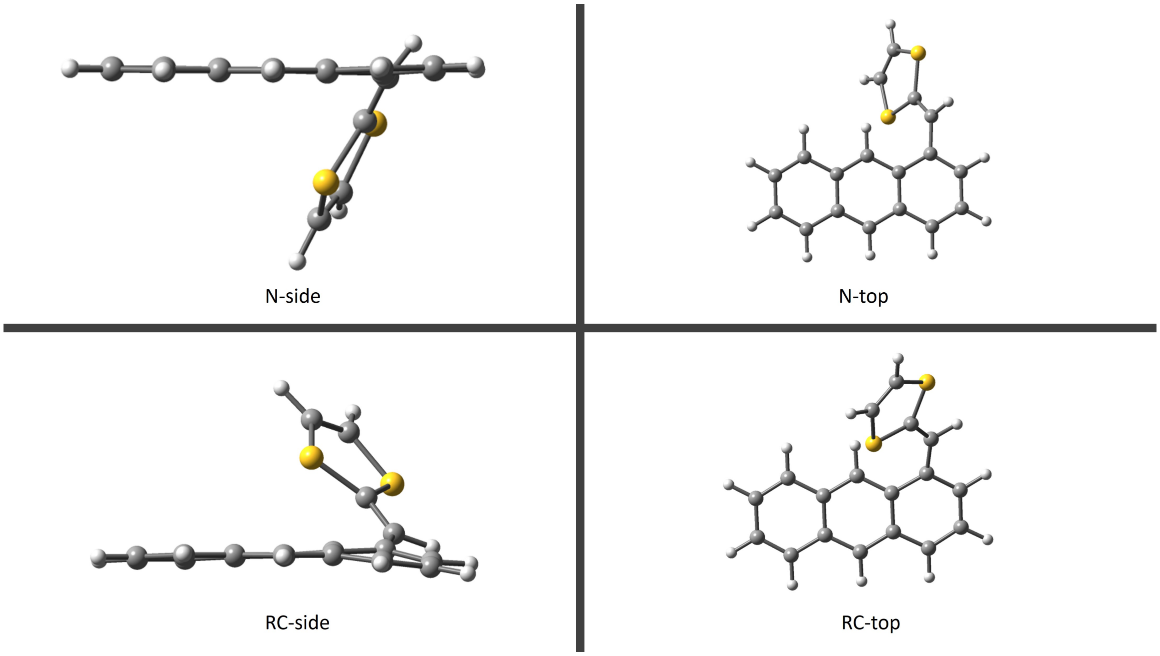
N-side

N-top

RC-side

RC-top

Figure A.18: Optimized geometry of 1-dithiafulvenylanthracene **5(s-cis)**.

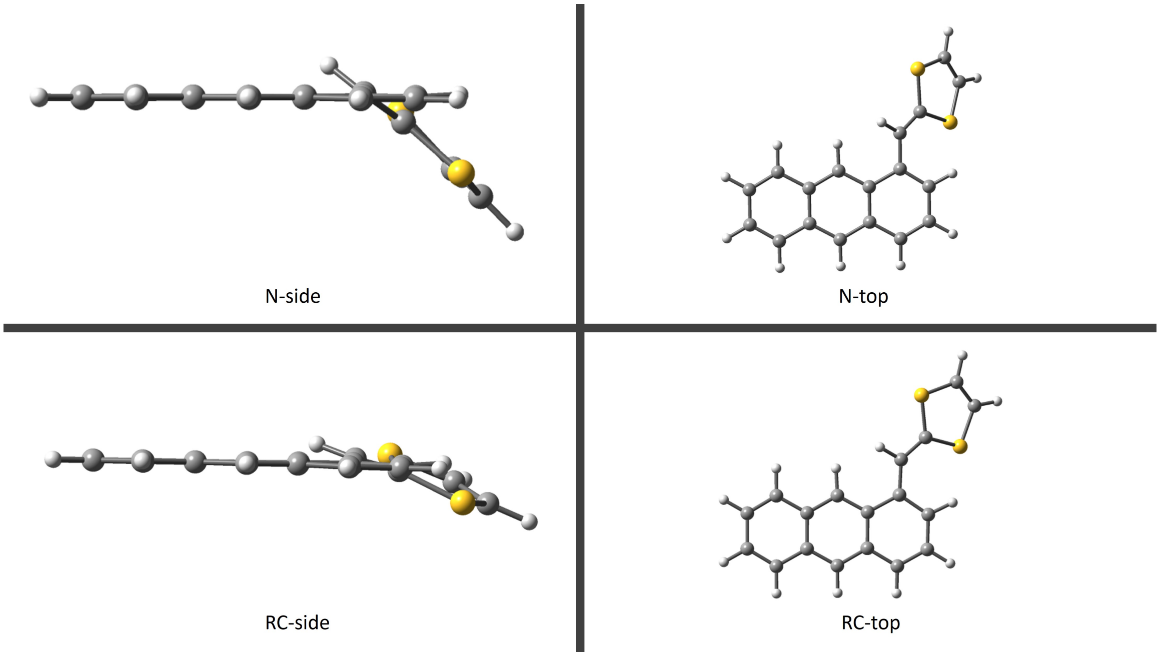

Figure A.19: Optimized geometry of 1-dithiafulvenylanthracene **5(s-trans)**.

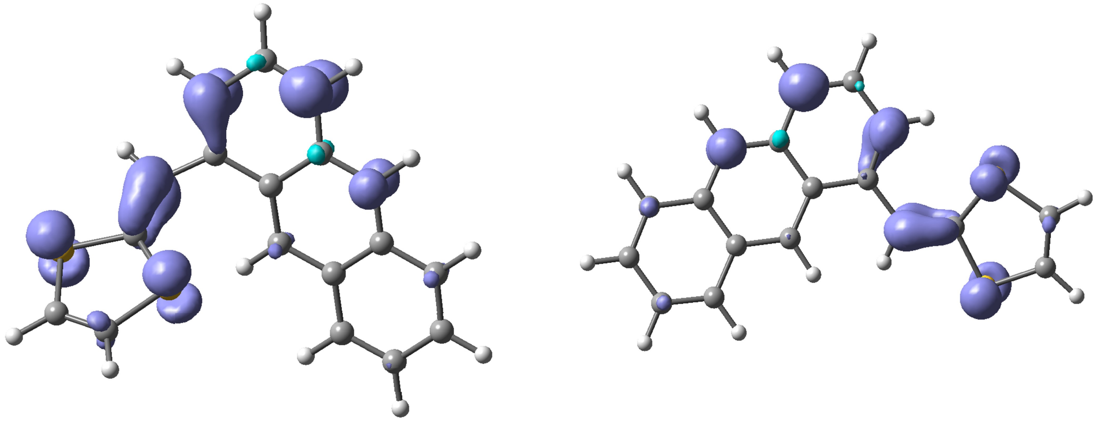

5 (s-cis)

5 (s-trans)

Figure A.20: Schematic illustration of spin density distribution over 1-dithiafulvenylanthracene **5** (isovalue = 0.005).

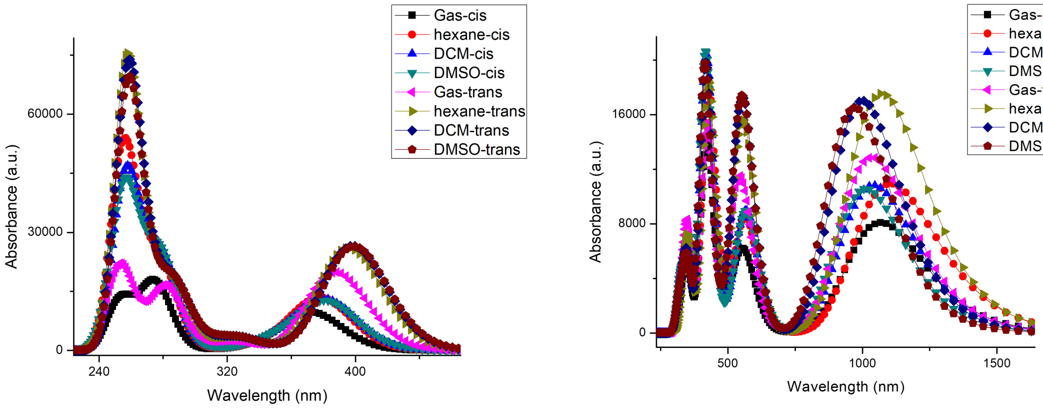

Figure A.21: UV-vis spectra of 1-dithiafulvenylanthracene **5** in neutral (left) and radical cation (right) oxidation states.

Table A.6: Cartesian coordinates, energies, and dipole momentum of the optimized geometries of 1-dithiafulvenylanthracene (s-cis) in N and RC oxidation states.

5-N (s-cis) in gas (E = -1488.434861 Hartree, μ = 1.517230 D) **5-N (s-cis) in hexanes** (E = -1488.454308 Hartree, μ = 1.659487 D) **5-N (s-cis) in DCM** (E = -1488.460606 Hartree, μ = 1.859360 D) **5-N (s-cis) in DMSO** (E = -1488.451780 Hartree, μ = 1.910383 D)				**5-RC (s-cis) in gas** (E = -1488.189566 Hartree, μ = 3.325122 D) **5-RC (s-cis) in hexanes** (E = -1488.237908 Hartree, μ = 4.160887 D) **5-RC (s-cis) in DCM** (E = -1488.267580 Hartree, μ = 5.818763 D) **5-RC (s-cis) in DMSO** (E = -1488.263596 Hartree, μ = 6.441500 D)			
C	-4.448968	-2.217925	0.032185	C	4.43754	-2.195332	0.028723
C	-4.324225	-0.894001	0.341876	C	4.295149	-0.889884	0.424686
C	-3.085824	-0.204929	0.129989	C	3.070346	-0.198026	0.195868
C	-1.973634	-0.93341	-0.414054	C	1.990369	-0.885036	-0.450733
C	-2.147473	-2.32052	-0.728454	C	2.178127	-2.233969	-0.860858
C	-3.343447	-2.942707	-0.511782	C	3.370382	-2.872023	-0.621587
C	-2.926975	1.153281	0.418764	C	2.901167	1.153354	0.540303
C	-0.756076	-0.276914	-0.622678	C	0.770872	-0.208988	-0.664704
C	-0.58364	1.075435	-0.303551	C	0.572796	1.097971	-0.240586
C	-1.7106	1.812439	0.20747	C	1.694366	1.82018	0.309167
C	-1.573262	3.213625	0.463063	C	1.585922	3.221871	0.520664
H	-2.436185	3.760716	0.847646	H	2.442862	3.757469	0.933871
C	-0.391743	3.85092	0.216307	C	0.439099	3.911846	0.163405
C	0.732531	3.121259	-0.264609	C	-0.671376	3.215264	-0.320568
C	0.673016	1.768014	-0.497554	C	-0.679683	1.808078	-0.427862
H	-3.775966	1.719652	0.809578	H	3.74137	1.705039	0.968234
H	-5.396794	-2.73217	0.197936	H	5.376517	-2.720711	0.205674
H	-5.16658	-0.336092	0.755971	H	5.115558	-0.363333	0.915129
H	-1.2986	-2.869252	-1.141324	H	1.360948	-2.753429	-1.364706
H	-3.462817	-4.000003	-0.75272	H	3.506426	-3.907635	-0.935482
H	0.07704	-0.837876	-1.049118	H	-0.01686	-0.733369	-1.208464
H	-0.293501	4.92156	0.40086	H	0.386608	4.99326	0.287553
H	1.677248	3.643757	-0.42742	H	-1.58895	3.763111	-0.544432
C	1.895068	1.064471	-0.947044	C	-1.957566	1.2156	-0.629859
H	2.409077	1.467855	-1.824363	C	-2.485865	0.000225	-0.195909
C	2.484365	0.037023	-0.304666	C	-3.138873	-2.160892	1.043706
C	3.230044	-1.781981	1.40572	C	-4.260461	-1.775673	0.406685
C	4.174622	-1.799107	0.460276	H	-3.050296	-3.046616	1.673465
H	3.2312	-2.416725	2.291182	H	-5.214282	-2.302551	0.441925
H	5.050633	-2.446512	0.470387	H	-2.70384	1.885458	-1.068554
S	1.885286	-0.678327	1.203458	S	-4.152541	-0.338231	-0.542041
S	3.979875	-0.710719	-0.895094	S	-1.724329	-1.188274	0.815325

Table A.7: Cartesian coordinates, energies, and dipole momentum of the optimized geometries of 1-dithiafulvenylanthracene (s-trans) in N and RC oxidation states.

5-N (s-trans) in gas (E = -1488.437070 Hartree, μ = 1.550463 D) **5-N (s-trans) in hexanes** (E = -1488.456722 Hartree, μ = 1.703208 D) **5-N (s-trans) in DCM** (E = -1488.463253 Hartree, μ = 1.919706 D) **5-N (s-trans) in DMSO** (E = -1488.454372 Hartree, μ = 1.976492 D)				**5-RC (s-trans) in gas** (E = -1488.193572 Hartree, μ = 4.444857 D) **5-RC (s-trans) in hexanes** (E = -1488.241711 Hartree, μ = 5.690538 D) **5-RC (s-trans) in DCM** (E = -1488.271381 Hartree, μ = 7.944062 D) **5-RC (s-trans) in DMSO** (E = -1488.267262 Hartree, μ = 8.726068 D)			
C	-5.544229	-1.316036	0.386699	C	-5.686846	-1.20905	0.188186
C	-5.051806	-0.042942	0.340204	C	-5.156051	0.052931	0.112613
C	-3.65376	0.195009	0.13963	C	-3.743973	0.235185	0.039453
C	-2.775527	-0.929685	-0.014807	C	-2.88652	-0.913077	0.046129
C	-3.330945	-2.2483	0.04394	C	-3.472013	-2.206122	0.129741
C	-4.67014	-2.436137	0.237046	C	-4.836477	-2.347751	0.197287
C	-3.112309	1.483939	0.099967	C	-3.158132	1.507142	-0.027179
C	-1.406081	-0.710458	-0.213367	C	-1.487077	-0.738023	-0.027631
C	-0.864459	0.577255	-0.274332	C	-0.901921	0.518561	-0.121612
C	-1.745261	1.702467	-0.09704	C	-1.769578	1.672628	-0.101037
C	-1.202384	3.027592	-0.111606	C	-1.211539	2.975203	-0.135206
H	-1.880533	3.871089	0.030626	H	-1.883123	3.835622	-0.116238
C	0.133899	3.224714	-0.301193	C	0.161059	3.162705	-0.201843
C	1.007633	2.117695	-0.501659	C	1.016894	2.063083	-0.239652
C	0.550049	0.819943	-0.492285	C	0.541924	0.733206	-0.207425
H	-3.772883	2.344573	0.231251	H	-3.797527	2.392754	-0.01426
H	-6.610954	-1.485682	0.540008	H	-6.767176	-1.345995	0.243516
H	-5.71529	0.816456	0.456185	H	-5.803017	0.931704	0.108128
H	-2.659448	-3.101706	-0.070647	H	-2.822998	-3.083496	0.137568
H	-5.08123	-3.445801	0.278354	H	-5.277141	-3.34345	0.259538
H	-0.753695	-1.580154	-0.302386	H	-0.877229	-1.641012	0.010313
H	0.545234	4.23489	-0.319385	H	0.575367	4.169461	-0.25237
H	2.059938	2.315211	-0.71286	H	2.079968	2.257799	-0.373094
C	1.44956	-0.316709	-0.721995	C	1.416951	-0.379344	-0.313555
C	2.719741	-0.44058	-0.282493	H	0.961522	-1.332476	-0.587753
C	5.02315	-1.470862	0.383148	C	2.793175	-0.459612	-0.117331
C	4.961005	-0.308996	1.040441	C	5.168628	-1.454825	0.056946
H	5.843449	-2.183607	0.458896	C	5.281709	-0.190687	0.503917
H	5.725431	0.056442	1.725258	H	5.987797	-2.171482	-0.006114
S	3.702206	-1.856654	-0.695719	H	6.204619	0.270993	0.855638
S	3.567457	0.715595	0.760091	S	3.838954	0.766817	0.518803
H	1.05657	-1.152225	-1.307051	S	3.598399	-1.958901	-0.453533

A.6 9-dithiafulvenylanthracene

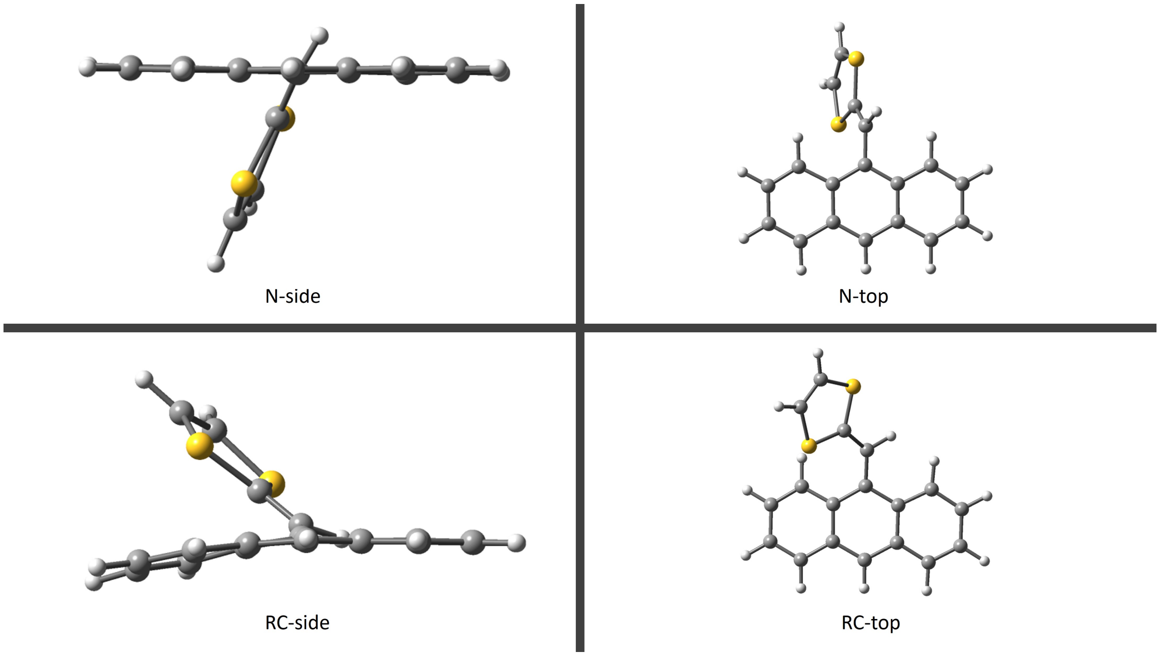

Figure A.22: Optimized geometry of 9-dithiafulvenylanthracene **6**.

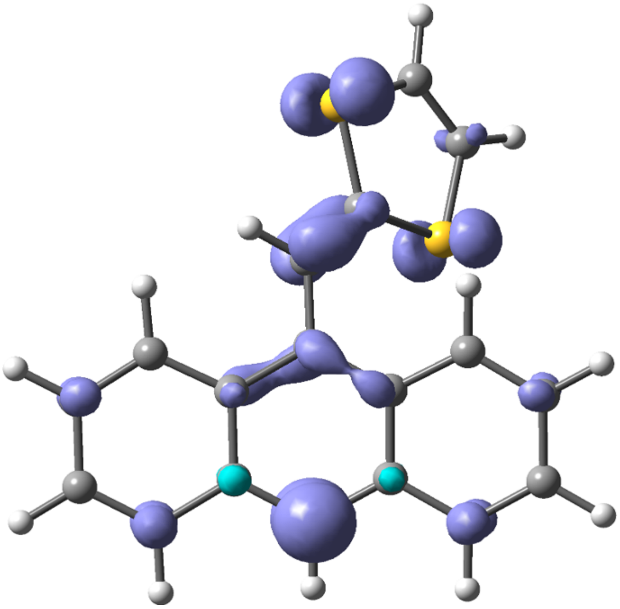

Figure A.23: Schematic illustration of spin density distribution over 9-dithiafulvenylanthracene **6** (isovalue = 0.005).

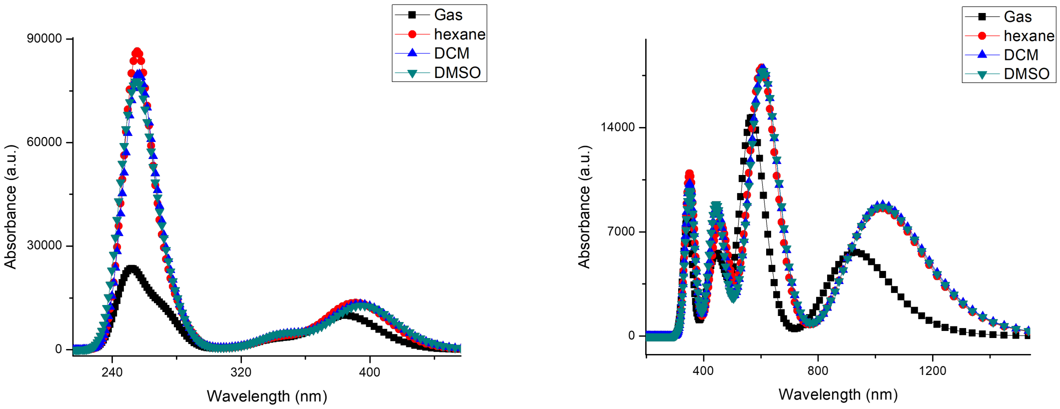

Figure A.24: UV-vis spectra of 9-dithiafulvenylanthracene **6** in neutral (left) and radical cation (right) oxidation states.

Table A.8: Cartesian coordinates, energies, and dipole momentum of the optimized geometries of 9-dithiafulvenylanthracene in N and RC oxidation states.

6-N in gas (E = -1488.434882 Hartree, μ = 1.527584 D) **6-N in hexanes** (E = -1488.454116 Hartree, μ = 1.652945 D) **6-N in DCM** (E = -1488.460319 Hartree, μ = 1.809050 D) **6-N in DMSO** (E = -1488.451591 Hartree, μ = 1.835750 D)				**6-RC in gas** (E = -1488.190194 Hartree, μ = 2.467604 D) **6-RC in hexanes** (E = -1488.238130 Hartree, μ = 2.887120 D) **6-RC in DCM** (E = -1488.267165 Hartree, μ = 3.790599 D) **6-RC in DMSO** (E = -1488.263000 Hartree, μ = 4.155304 D)			
C	3.64251	-2.871526	0.358127	C	-4.221409	-2.341986	0.339697
C	3.844833	-1.528394	0.49444	C	-4.128773	-0.987272	0.542935
C	2.80104	-0.592136	0.202156	C	-2.915491	-0.293678	0.27369
C	1.527029	-1.081857	-0.246116	C	-1.764719	-1.008301	-0.196359
C	1.35244	-2.50035	-0.356902	C	-1.894172	-2.407542	-0.367219
C	2.373469	-3.362762	-0.070611	C	-3.091685	-3.0505	-0.124388
C	2.992725	0.783597	0.356115	C	-2.840867	1.092379	0.488448
C	0.486831	-0.172089	-0.547302	C	-0.525135	-0.283504	-0.405591
C	0.70699	1.218528	-0.415742	C	-0.54879	1.160413	-0.365347
C	1.977664	1.695948	0.062035	C	-1.698303	1.837132	0.151658
C	2.183913	3.106777	0.210802	C	-1.709859	3.256509	0.235608
H	3.150998	3.450353	0.583573	H	-2.586132	3.749925	0.659532
C	1.202506	3.997785	-0.11057	C	-0.654064	3.992727	-0.247497
C	-0.048426	3.530267	-0.61568	C	0.431822	3.331815	-0.863839
C	-0.286738	2.193934	-0.765199	C	0.479819	1.953641	-0.926993
H	3.958106	1.153149	0.7105	H	-3.716607	1.614116	0.881738
H	4.445367	-3.574997	0.582992	H	-5.154245	-2.870098	0.537107
H	4.808354	-1.140205	0.830969	H	-4.984752	-0.418292	0.909656
H	0.38023	-2.88722	-0.663146	H	-1.052858	-3.009592	-0.704769
H	2.217758	-4.438725	-0.162112	H	-3.161725	-4.126438	-0.289004
H	1.371255	5.069287	0.005572	H	-0.670813	5.081514	-0.195588
H	-0.818696	4.251934	-0.891507	H	1.232617	3.91852	-1.315867
H	-1.241598	1.849696	-1.162472	H	1.303721	1.473329	-1.454537
C	-0.815643	-0.700437	-1.014883	C	0.665728	-1.025019	-0.606873
H	-0.831385	-1.280549	-1.942951	H	0.55447	-2.021873	-1.036933
C	-1.972286	-0.570641	-0.338967	C	1.968292	-0.758992	-0.178855
C	-3.814146	-0.088212	1.437686	C	4.461669	-1.146769	0.370789
C	-4.445681	-0.758521	0.468969	C	4.110146	-0.048623	1.063664
H	-4.287953	0.264235	2.353228	H	5.453783	-1.598445	0.370092
H	-5.501086	-1.027559	0.486924	H	4.776602	0.523442	1.709723
S	-3.507692	-1.227805	-0.932284	S	2.476391	0.503557	0.896321
S	-2.111403	0.259751	1.220927	S	3.227401	-1.875475	-0.594591

A.7 1-dithiafulvenylpyrene

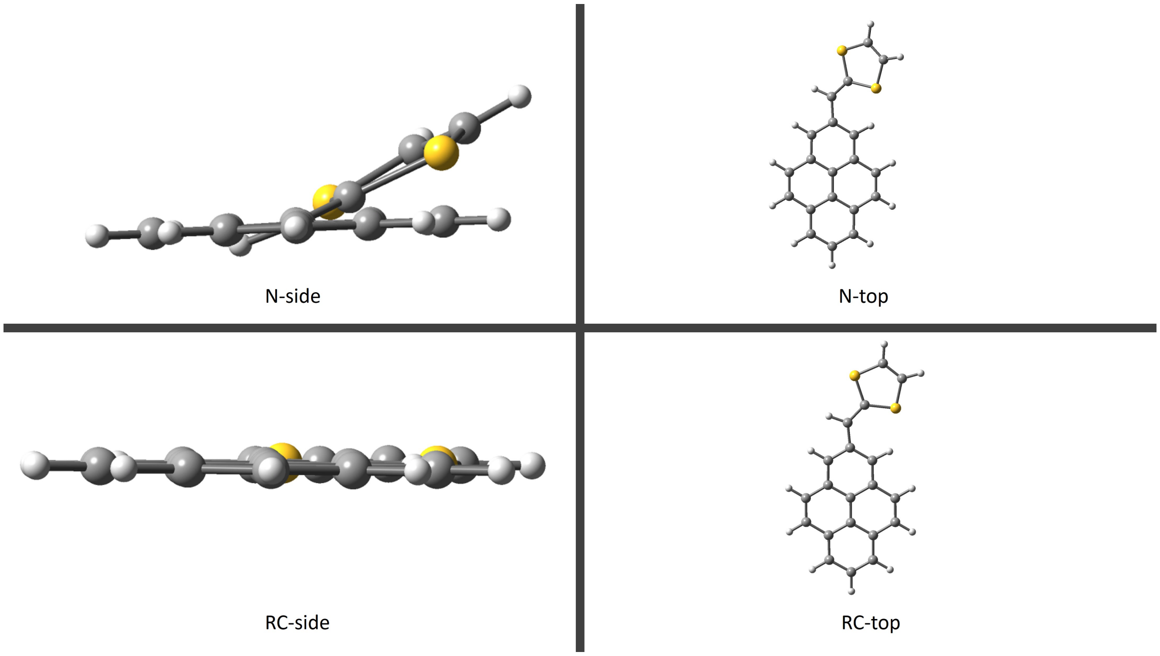

Figure A.25: Optimized geometry of 1-dithiafulvenylpyrene **7**.

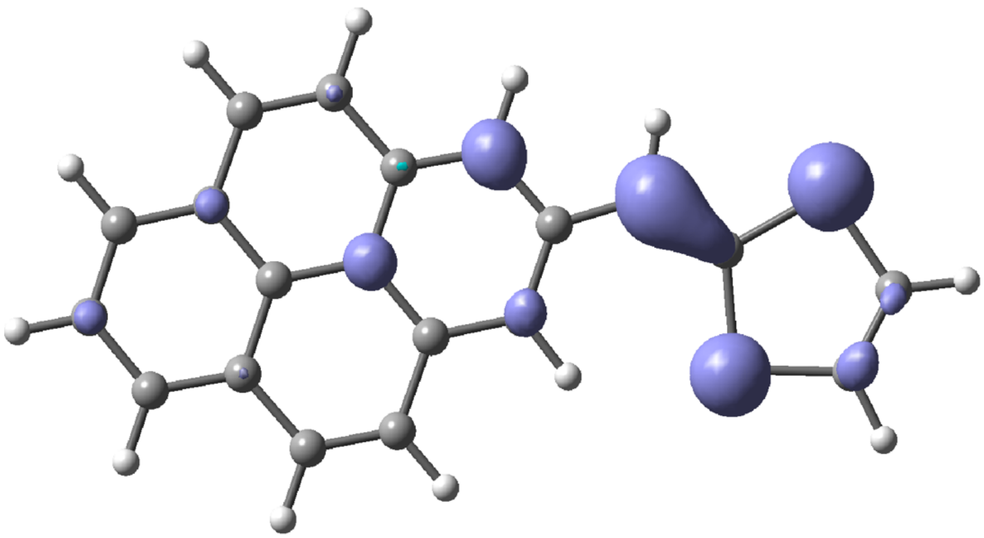

Figure A.26: Schematic illustration of spin density distribution over 1-dithiafulvenylpyrene **7** (isovalue = 0.005).

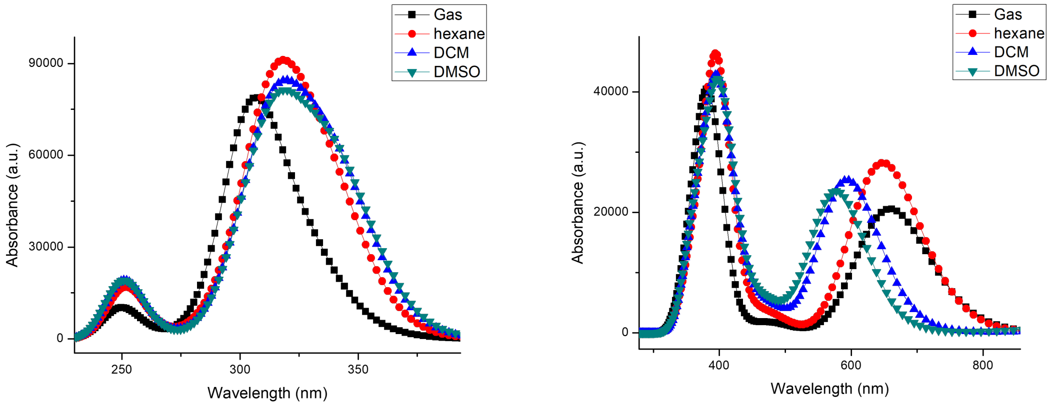

Figure A.27: UV-vis spectra of 1-dithiafulvenylpyrene **7** in neutral (left) and radical cation (right) oxidation states.

Table A.9: Cartesian coordinates, energies, and dipole momentum of the optimized geometries of 1-dithiafulvenylpyrene in N and RC oxidation states.

7-N in gas (E = -1564.601846 Hartree, μ = 1.793265 D)				**7-RC in gas** (E = -1564.353416 Hartree, μ = 8.376326 D)			
7-N in hexanes (E = -1564.623220 Hartree, μ = 1.966815 D)				**7-RC in hexanes** (E = -1564.403664 Hartree, μ = 10.270724 D)			
7-N in DCM (E = -1564.630096 Hartree, μ = 2.221502 D)				**7-RC in DCM** (E = -1564.434643 Hartree, μ = 13.223429 D)			
7-N in DMSO (E = -1564.620689 Hartree, μ = 2.295112 D)				**7-RC in DMSO** (E = -1564.430385 Hartree, μ = 14.150021 D)			
C	-5.866291	-0.644837	0.205683	C	5.893122	-0.612314	0.000093
C	-5.422848	0.673028	0.298003	C	5.448137	0.706485	0.000059
C	-4.058737	0.976537	0.199215	C	4.076726	0.99491	0.000006
C	-3.127195	-0.081933	0.004418	C	3.144426	-0.084375	-0.000009
C	-3.586474	-1.425265	-0.092954	C	3.610054	-1.432405	0.000021
C	-4.960105	-1.684403	0.011288	C	4.985494	-1.674352	0.000073
C	-3.56051	2.328328	0.284849	C	3.580721	2.348353	-0.000036
C	-1.732285	0.204471	-0.096424	C	1.750974	0.184778	-0.000044
C	-1.267654	1.54667	-0.010576	C	1.286767	1.536385	-0.000056
C	-2.235444	2.600388	0.182912	C	2.250285	2.610969	-0.000068
C	0.101201	1.801145	-0.11215	C	-0.081121	1.775342	-0.000038
H	0.452308	2.833607	-0.043692	H	-0.440232	2.806651	-0.000034
C	1.040077	0.7687	-0.284604	C	-1.026697	0.71245	-0.000021
C	0.568094	-0.54924	-0.389637	C	-0.551013	-0.623411	-0.000041
C	-0.796648	-0.846744	-0.295066	C	0.809902	-0.897974	-0.00005
C	-1.291577	-2.198289	-0.398961	C	1.310823	-2.253652	-0.000046
C	-2.616934	-2.472752	-0.300142	C	2.641809	-2.504375	-0.000006
H	-2.976447	-3.500859	-0.377272	H	3.010357	-3.531624	0.000006
H	-0.569373	-3.001893	-0.556301	H	0.590736	-3.073416	-0.000076
H	-4.28129	3.134974	0.433247	H	4.305331	3.164316	-0.000045
H	-6.932077	-0.863737	0.284803	H	6.963762	-0.820012	0.000135
H	-6.137986	1.484341	0.447805	H	6.16609	1.528154	0.000071
H	-5.313114	-2.714928	-0.06289	H	5.347759	-2.703693	0.0001
H	-1.874032	3.628578	0.24833	H	1.884441	3.638799	-0.000113
H	1.253983	-1.372431	-0.59121	H	-1.231248	-1.473328	-0.000039
C	2.454862	1.139975	-0.356364	C	-2.396021	1.103931	0.000009
H	2.647162	2.190197	-0.593084	H	-2.562506	2.185417	0.000036
C	3.548733	0.380803	-0.12711	C	-3.570285	0.35356	0.000011
C	5.299172	-1.409355	0.613121	C	-5.437117	-1.409814	-0.000012
C	6.025757	-0.330323	0.307489	C	-6.077033	-0.220833	0.000062
H	5.707504	-2.349323	0.982448	H	-5.927625	-2.383818	-0.000041
H	7.109869	-0.268521	0.394438	H	-7.160358	-0.095675	0.000098
S	3.564991	-1.313366	0.388432	S	-3.713008	-1.369502	-0.000057
S	5.173905	1.072026	-0.289968	S	-5.089882	1.18677	0.000086

A.8 2-dithiafulvenylpyrene

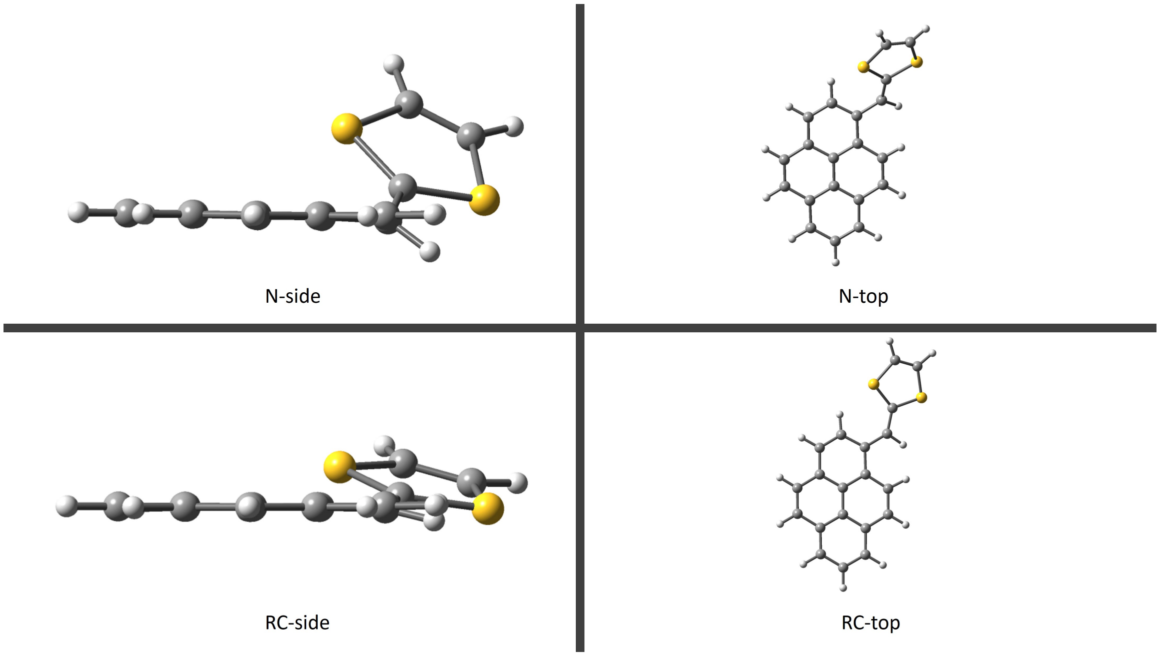

Figure A.28: Optimized geometry of 2-dithiafulvenylpyrene **8**.

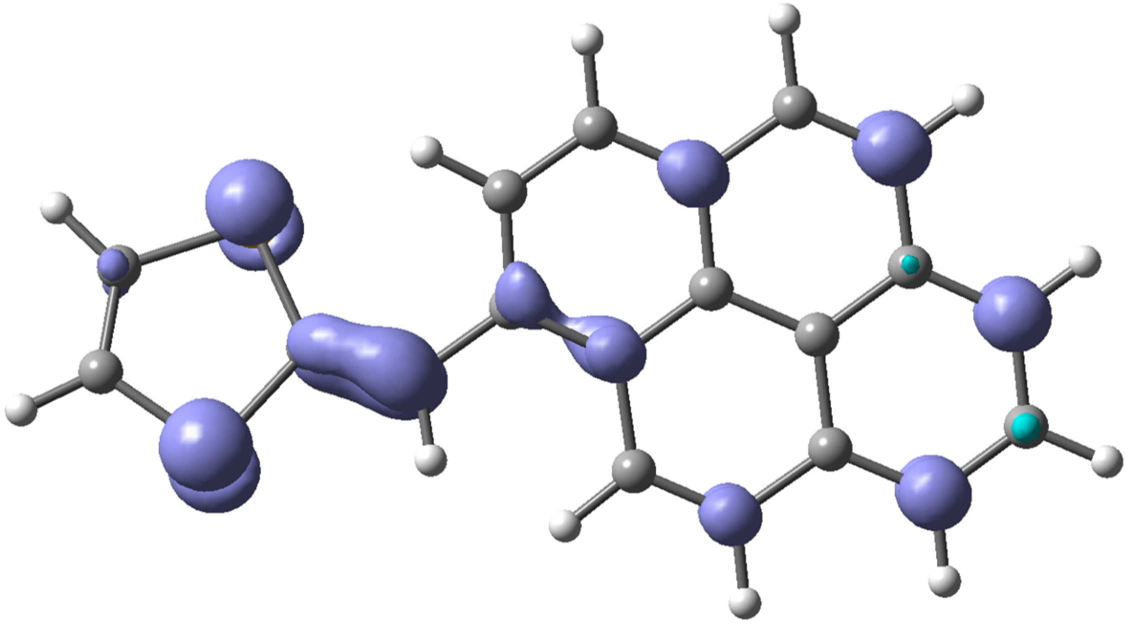

Figure A.29: Schematic illustration of spin density distribution over 2-dithiafulvenylpyrene **8** (isovalue = 0.005).

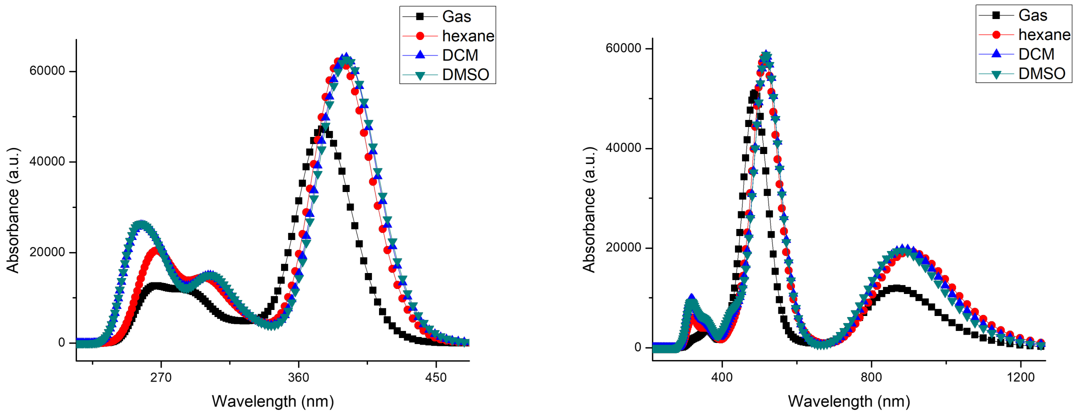

Figure A.30: UV-vis spectra of 2-dithiafulvenylpyrene **8** in neutral (left) and radical cation (right) oxidation states.

Table A.10: Cartesian coordinates, energies, and dipole momentum of the optimized geometries of 2-dithiafulvenylpyrene in N and RC oxidation states.

8-N in gas (E = -1564.600746 Hartree, μ = 1.688624 D) **8-N in hexanes** (E = -1564.621911 Hartree, μ = 1.852308 D) **8-N in DCM** (E = -1564.628608 Hartree, μ = 2.072890 D) **8-N in DMSO** (E = -1564.619257 Hartree, μ = 2.125880 D)				**8-RC in gas** (E = -1564.361375 Hartree, μ = 4.131613 D) **8-RC in hexanes** (E = -1564.409984 Hartree, μ = 5.112578 D) **8-RC in DCM** (E = -1564.438618 Hartree, μ = 7.108467 D) **8-RC in DMSO** (E = -1564.433645 Hartree, μ = 7.880783 D)			
C	-5.44203	-1.380062	0.448132	C	5.568066	-1.302205	-0.176227
C	-4.308419	-2.181694	0.351878	C	4.449151	-2.127157	-0.163813
C	-3.044725	-1.609815	0.144854	C	3.152089	-1.580111	-0.083579
C	-2.927913	-0.196722	0.032411	C	2.988858	-0.172206	-0.014407
C	-4.093025	0.616381	0.13641	C	4.138561	0.666853	-0.031509
C	-5.337091	0.005016	0.342742	C	5.415724	0.081798	-0.11163
C	-1.849188	-2.405022	0.052929	C	1.984505	-2.396987	-0.077743
C	-1.646344	0.404504	-0.182931	C	1.684075	0.396501	0.070107
C	-0.480936	-0.407861	-0.290749	C	0.530883	-0.44177	0.090094
C	-0.633506	-1.834732	-0.148831	C	0.730202	-1.851143	-0.00089
C	0.780715	0.202746	-0.514396	C	-0.783544	0.167519	0.174216
C	0.843891	1.601244	-0.616955	C	-0.862273	1.591079	0.240971
C	-0.288588	2.39481	-0.498236	C	0.254131	2.381364	0.222105
C	-1.547632	1.821269	-0.282936	C	1.553825	1.81452	0.129518
C	-2.741167	2.619356	-0.170955	C	2.71327	2.636153	0.11003
C	-3.955034	2.04694	0.027082	C	3.964619	2.083197	0.033147
H	-4.85374	2.661421	0.108645	H	4.849469	2.722212	0.019441
H	-2.644662	3.703935	-0.251578	H	2.589545	3.718925	0.1582
H	-1.938024	-3.487921	0.160523	H	2.100798	-3.48037	-0.142456
H	-6.418715	-1.838705	0.60895	H	6.565598	-1.73719	-0.237763
H	-4.391526	-3.266865	0.438039	H	4.564632	-3.211313	-0.217029
H	-6.228	0.631236	0.42106	H	6.294083	0.729894	-0.122679
H	0.253648	-2.466371	-0.184831	H	-0.118963	-2.530711	-0.024384
H	-0.206042	3.479347	-0.5927	H	0.15671	3.465289	0.299318
C	1.987545	-0.618588	-0.67253	C	-1.936351	-0.654027	0.218484
H	1.878316	-1.569582	-1.199838	H	-1.773169	-1.718571	0.387301
C	3.230257	-0.323581	-0.234202	C	-3.285255	-0.331435	0.077135
C	5.742161	-0.544864	0.44359	C	-5.84614	-0.627892	-0.079251
C	5.323602	0.57926	1.032567	C	-5.619883	0.662301	-0.387231
H	6.745677	-0.957891	0.538414	H	-6.828003	-1.100635	-0.04866
H	5.939693	1.209831	1.672618	H	-6.389278	1.391174	-0.642847
S	3.674092	1.090796	0.738571	S	-3.972393	1.194443	-0.372855
S	4.600067	-1.397424	-0.568697	S	-4.462192	-1.588603	0.295501
H	1.801403	2.076114	-0.836509	H	-1.825141	2.079746	0.372058

A.9 3-dithiafulvenylpyrene

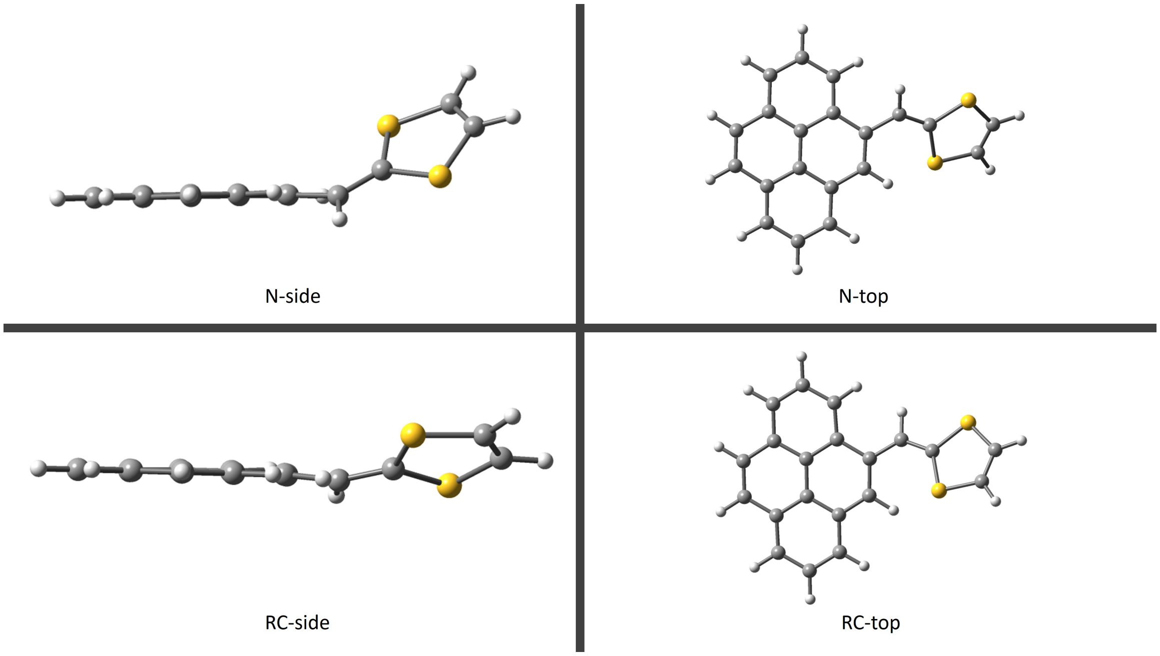

Figure A.31: Optimized geometry of 3-dithiafulvenylpyrene **9(s-cis)**.

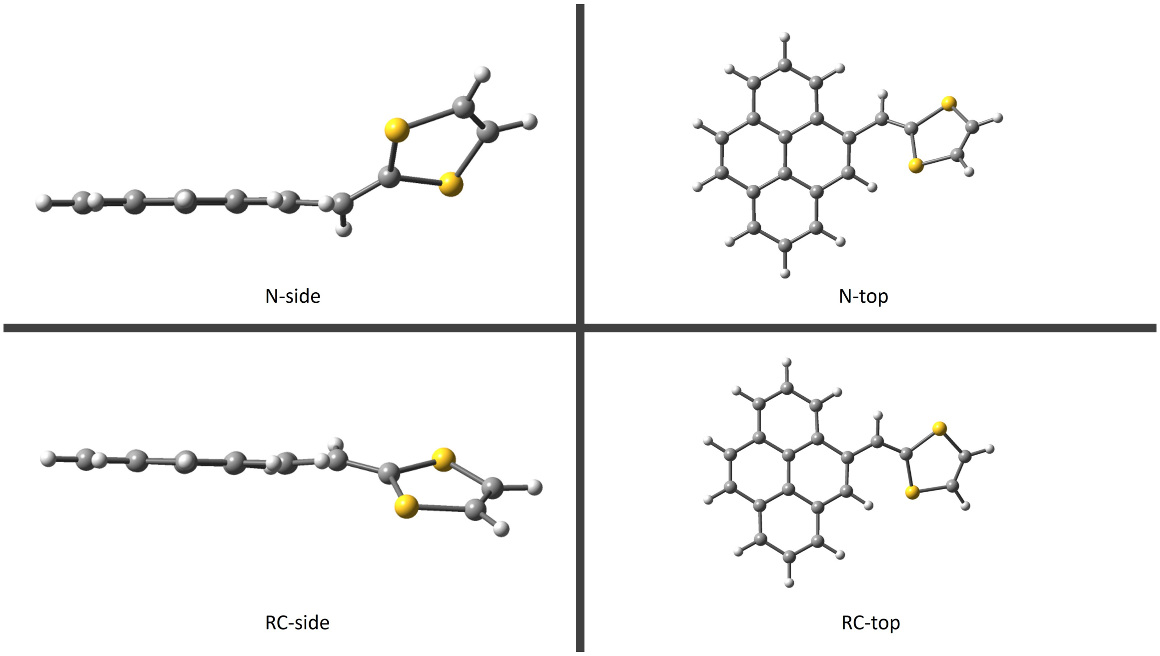

Figure A.32: Optimized geometry of 3-dithiafulvenylpyrene **9(s-trans)**.

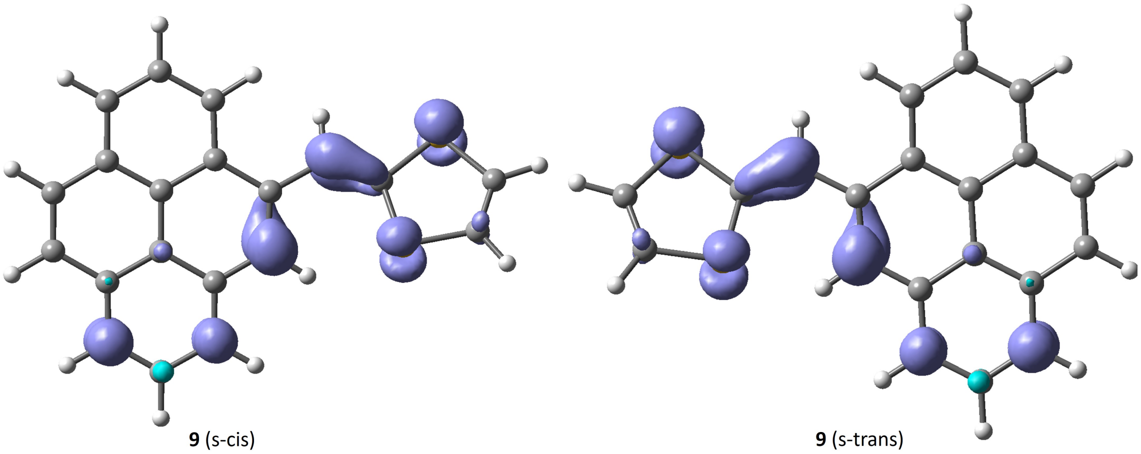

9 (s-cis)

9 (s-trans)

Figure A.33: Schematic illustration of spin density distribution over 3-dithiafulvenylpyrene **9** (isovalue = 0.005).

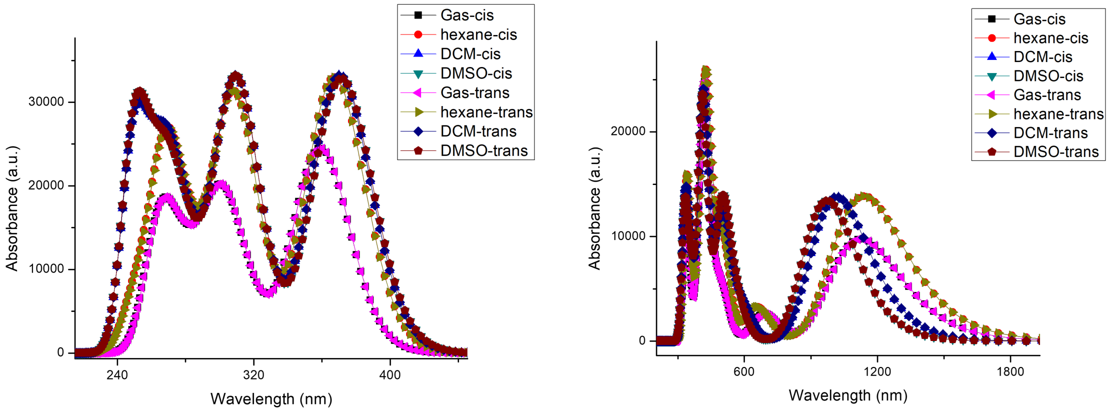

Figure A.34: UV-vis spectra of 3-dithiafulvenylpyrene **9** in neutral (left) and radical cation (right) oxidation states.

Table A.11: Cartesian coordinates, energies, and dipole momentum of the optimized geometries of 3-dithiafulvenylpyrene (s-cis) in N and RC oxidation states.

9-N (s-cis) in gas (E = -1564.601162 Hartree, μ = 1.607668 D) **9-N (s-cis) in hexanes** (E = -1564.622330 Hartree, μ = 1.765504 D) **9-N (s-cis) in DCM** (E = -1564.628979 Hartree, μ = 1.998091 D) **9-N (s-cis) in DMSO** (E = -1564.619592 Hartree, μ = 2.061319 D)				**9-RC (s-cis) in gas** (E = -1564.355030 Hartree, μ = 5.480676 D) **9-RC (s-cis) in hexanes** (E = -1564.404513 Hartree, μ = 6.867097 D) **9-RC (s-cis) in DCM** (E = -1564.434329 Hartree, μ = 9.463602 D) **9-RC (s-cis) in DMSO** (E = -1564.429799 Hartree, μ = 10.365568 D)			
C	2.770345	-3.37479	-0.262783	C	-2.634049	-3.448202	-0.207343
C	1.468878	-2.908857	-0.43218	C	-1.345921	-2.936624	-0.254661
C	1.18479	-1.538052	-0.351641	C	-1.126878	-1.540517	-0.173996
C	2.243816	-0.624065	-0.100354	C	-2.241427	-0.654286	-0.05896
C	3.570941	-1.106534	0.069694	C	-3.553366	-1.185991	-0.015233
C	3.81247	-2.485301	-0.013962	C	-3.723882	-2.583765	-0.087972
C	-0.144498	-1.024947	-0.536113	C	0.173892	-1.002312	-0.225711
C	1.965425	0.776366	-0.021373	C	-2.02635	0.753656	0.003278
C	0.6345	1.260418	-0.184973	C	-0.706575	1.295495	-0.039874
C	-0.438505	0.307993	-0.459944	C	0.428406	0.376661	-0.170511
C	0.403225	2.637127	-0.058985	C	-0.553196	2.680778	0.07685
H	-0.612083	3.024267	-0.13994	H	0.438074	3.132011	0.100535
C	1.449924	3.522988	0.191483	C	-1.660856	3.526112	0.191475
C	2.751838	3.057616	0.333184	C	-2.944221	3.005606	0.208637
C	3.029157	1.687256	0.23723	C	-3.150956	1.616339	0.124357
C	4.36601	1.171792	0.401189	C	-4.472636	1.053424	0.166002
C	4.625471	-0.1571	0.322089	C	-4.669992	-0.290141	0.098051
H	5.642238	-0.533734	0.450026	H	-5.677283	-0.708044	0.129847
H	5.170898	1.883594	0.595106	H	-5.321003	1.73365	0.256118
H	-0.92855	-1.741717	-0.789991	H	0.989859	-1.705161	-0.396269
H	2.974929	-4.444466	-0.326541	H	-2.798515	-4.524035	-0.265244
H	0.654407	-3.608592	-0.629396	H	-0.488504	-3.605316	-0.350223
H	4.831596	-2.854093	0.117566	H	-4.736598	-2.990346	-0.053117
H	1.240909	4.589732	0.28307	H	-1.507094	4.602123	0.274855
H	3.569724	3.753334	0.53054	H	-3.807236	3.667292	0.299288
C	-1.802961	0.807797	-0.668178	C	1.746264	0.893177	-0.312088
H	-1.911696	1.752127	-1.20754	H	1.829122	1.938764	-0.615003
C	-2.945321	0.218601	-0.25598	C	2.973661	0.267874	-0.115704
C	-4.773623	-1.142748	1.006622	C	4.979098	-1.21521	0.534612
C	-5.443152	-0.160053	0.396863	C	5.523596	-0.092214	0.029648
H	-5.226503	-1.888987	1.658464	H	5.540929	-2.06905	0.914092
H	-6.516181	0.006525	0.483431	H	6.593505	0.097976	-0.059223
S	-4.529371	0.917178	-0.634002	S	4.427821	1.125087	-0.514087
S	-3.049508	-1.260368	0.715495	S	3.250746	-1.293151	0.585287

Table A.12: Cartesian coordinates, energies, and dipole momentum of the optimized geometries of 3-dithiafulvenylpyrene (s-trans) in N and RC oxidation states.

9-N (s-trans) in gas (E = -1564.601162 Hartree, μ = 1.608525 D) **9-N (s-trans) in hexanes** (E = -1564.622330 Hartree, μ = 1.766406 D) **9-N (s-trans) in DCM** (E = -1564.628979 Hartree, μ = 1.999094 D) **9-N (s-trans) in DMSO** (E = -1564.619592 Hartree, μ = 2.062255 D)				**9-RC (s-trans) in gas** (E = -1564.355030 Hartree, μ = 5.480676 D) **9-RC (s-trans) in hexanes** (E = -1564.404513 Hartree, μ = 6.867097 D) **9-RC (s-trans) in DCM** (E = -1564.434329 Hartree, μ = 9.463603 D) **9-RC (s-trans) in DMSO** (E = -1564.429799 Hartree, μ = 10.365568 D)			
C	2.769995	-3.374866	0.26296	C	2.634053	-3.4482	-0.207349
C	1.468605	-2.908812	0.432634	C	1.345924	-2.936624	-0.254674
C	1.184604	-1.53799	0.352097	C	1.126879	-1.540518	-0.174006
C	2.243642	-0.624105	0.100441	C	2.241426	-0.654284	-0.058963
C	3.570681	-1.106711	-0.069947	C	3.553365	-1.185989	-0.015229
C	3.812129	-2.485495	0.013772	C	3.723884	-2.583762	-0.08797
C	-0.144591	-1.024754	0.536831	C	-0.173891	-1.002314	-0.225726
C	1.965363	0.776344	0.021419	C	2.026347	0.753657	0.003276
C	0.634512	1.260547	0.185259	C	0.706572	1.295494	-0.039882
C	-0.438491	0.308203	0.460509	C	-0.428407	0.37666	-0.170525
C	0.403387	2.637323	0.059521	C	0.55319	2.680777	0.076844
H	-0.61185	3.02454	0.140915	H	-0.438082	3.132007	0.100524
C	1.450116	3.523068	-0.191117	C	1.660848	3.526113	0.191475
C	2.751932	3.057535	-0.333255	C	2.944213	3.005609	0.208644
C	3.029141	1.687155	-0.237435	C	3.150951	1.616341	0.124363
C	4.36588	1.171542	-0.40174	C	4.472631	1.053428	0.166016
C	4.62521	-0.157385	-0.322683	C	4.669989	-0.290137	0.098064
H	5.641922	-0.534076	-0.450902	H	5.677281	-0.708038	0.129866
H	5.170855	1.883178	-0.5959	H	5.320997	1.733655	0.256138
H	-0.92871	-1.74143	0.790749	H	-0.989859	-1.705161	-0.396289
H	2.974473	-4.44456	0.326758	H	2.79852	-4.524033	-0.265251
H	0.654141	-3.608465	0.630162	H	0.488509	-3.605317	-0.350241
H	4.831186	-2.854367	-0.118033	H	4.7366	-2.990342	-0.053108
H	1.24127	4.589864	-0.282477	H	1.507084	4.602123	0.274855
H	3.569856	3.753151	-0.53081	H	3.807226	3.667295	0.299301
C	-1.803012	0.807952	0.668751	C	-1.746265	0.893174	-0.312106
C	-2.945186	0.218885	0.255825	C	-2.97366	0.26787	-0.115714
C	-4.77326	-1.143642	-1.005946	C	-5.523592	-0.09222	0.029659
C	-5.4431	-0.160892	-0.396578	C	-4.979089	-1.215209	0.534634
H	-5.226022	-1.890608	-1.657047	H	-6.593502	0.097967	-0.059207
H	-6.516244	0.005009	-0.482981	H	-5.540915	-2.069045	0.914129
H	-1.911951	1.752058	1.208456	H	-1.829124	1.93876	-0.615025
S	-3.048999	-1.260094	-0.715765	S	-4.427823	1.125079	-0.514093
S	-4.529393	0.917737	0.632841	S	-3.250736	-1.293146	0.585301

A.10 2-dithiafulvenylperylene

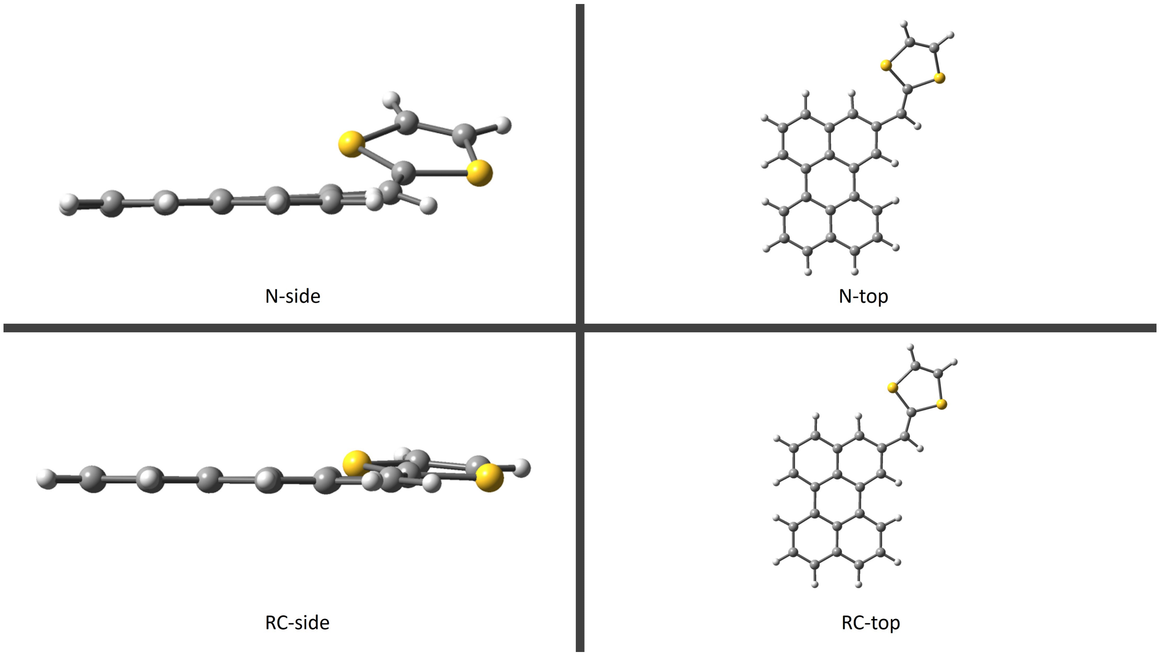

Figure A.35: Optimized geometry of 2-dithiafulvenylperylene **10**.

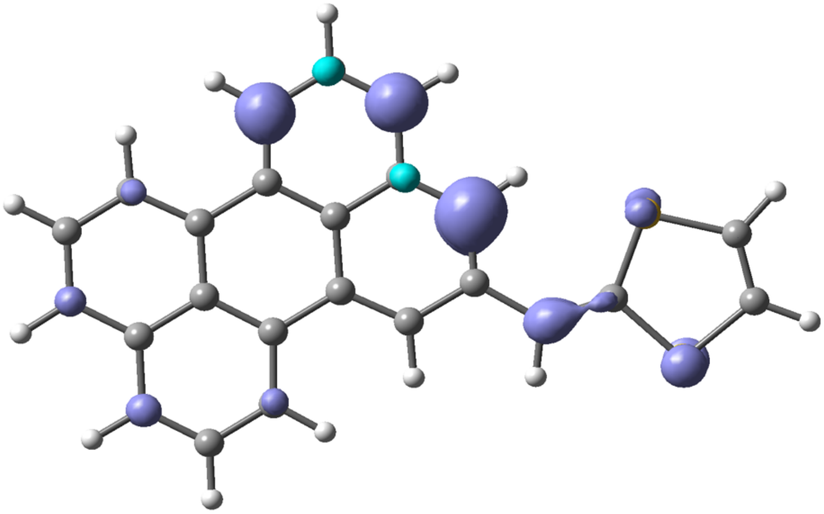

Figure A.36: Schematic illustration of spin density distribution over 2-dithiafulvenylperylene **10** (isovalue = 0.005).

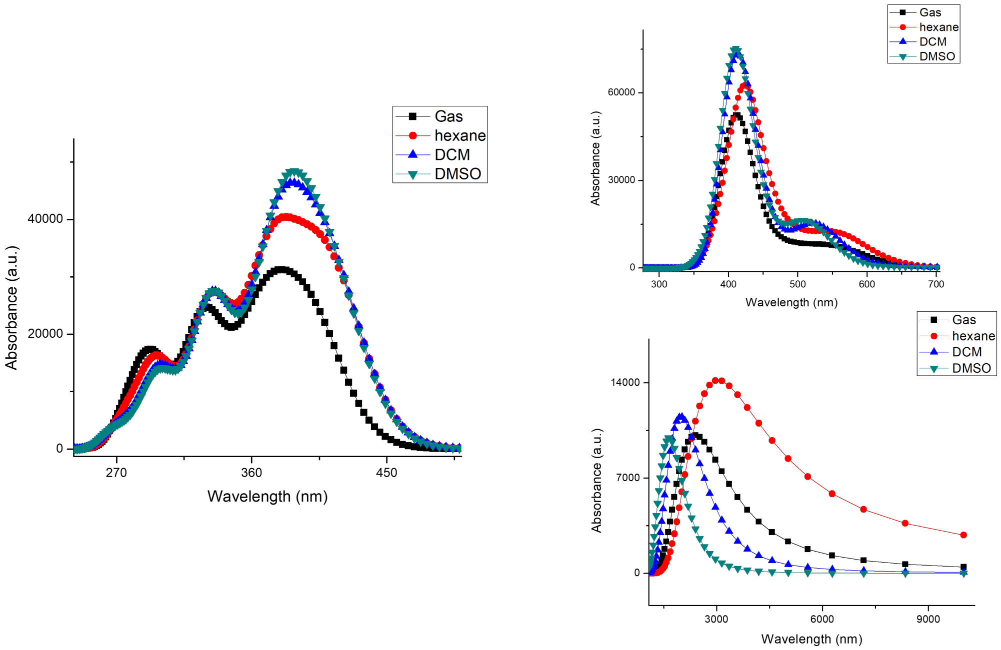

Figure A.37: UV-vis spectra of 2-dithiafulvenylperylene **10** in neutral (left) and radical cation (right) oxidation states.

Table A.13: Cartesian coordinates, energies, and dipole momentum of the optimized geometries of 2-dithiafulvenylperylene in N and RC oxidation states.

10-N in gas (E = -1718.065184 Hartree, μ = 1.873899 D)				**10-RC in gas** (E = -1717.821371 Hartree, μ = 3.938227 D)			
10-N in hexanes (E = -1718.090171 Hartree, μ = 2.044792 D)				**10-RC in hexanes** (E = -1717.872623 Hartree, μ = 5.591607 D)			
10-N in DCM (E = -1718.098298 Hartree, μ = 2.294430 D)				**10-RC in DCM** (E = -1717.901793 Hartree, μ = 13.204404 D)			
10-N in DMSO (E = -1718.087562 Hartree, μ = 2.367509 D)				**10-RC in DMSO** (E = -1717.895771 Hartree, μ = 15.400739 D)			
C	-1.111769	3.774667	-0.236994	C	-1.115958	3.780431	-0.069419
C	-2.291938	3.017337	-0.103003	C	-2.29089	3.026028	-0.033222
C	-2.268034	1.631426	-0.067276	C	-2.278721	1.617135	-0.019901
C	-1.008379	0.964403	-0.174814	C	-1.029287	0.954903	-0.042454
C	0.186867	1.732107	-0.300501	C	0.174276	1.724717	-0.075762
C	0.10614	3.149024	-0.333446	C	0.10929	3.143154	-0.091588
C	-3.501234	0.826169	0.074859	C	-3.515838	0.832915	0.013996
C	-0.911751	-0.465155	-0.170905	C	-0.932821	-0.483282	-0.038608
C	-2.148942	-1.271592	-0.065209	C	-2.170726	-1.268556	-0.011478
C	-3.409579	-0.603507	0.063117	C	-3.429886	-0.592699	0.016177
C	-2.128594	-2.656725	-0.082035	C	-2.159014	-2.66406	-0.010659
C	0.336427	-1.046659	-0.266863	C	0.321036	-1.07015	-0.059233
C	1.540572	-0.295138	-0.364225	C	1.528048	-0.324404	-0.076295
C	1.443888	1.084231	-0.397011	C	1.423959	1.08425	-0.093362
H	2.322849	1.712814	-0.540212	H	2.30579	1.721051	-0.140634
H	-1.175445	4.863296	-0.262748	H	-1.173377	4.868681	-0.080459
H	1.027155	3.725921	-0.435014	H	1.036861	3.717339	-0.11977
C	-4.748489	1.411974	0.217022	C	-4.773614	1.432405	0.043631
C	-5.922529	0.642089	0.340096	C	-5.954332	0.67359	0.074558
C	-5.855053	-0.727963	0.32051	C	-5.887501	-0.701393	0.075301
C	-4.601966	-1.379986	0.182338	C	-4.632061	-1.360259	0.04617
H	-6.883549	1.146296	0.449567	H	-6.918953	1.180323	0.097481
H	-6.756735	-1.336294	0.411821	H	-6.797572	-1.303305	0.098272
C	-3.308147	-3.419558	0.029376	C	-3.342133	-3.414784	0.017508
H	-3.244494	-4.508298	0.011187	H	-3.289651	-4.503421	0.016925
C	-4.523416	-2.796718	0.161928	C	-4.562757	-2.774524	0.046248
H	-1.184909	-3.190006	-0.183047	H	-1.214861	-3.205462	-0.032332
H	-3.237114	3.552545	-0.030727	H	-3.238809	3.560325	-0.017208
H	-4.845056	2.496123	0.237421	H	-4.868361	2.516803	0.043909
H	-5.444392	-3.375531	0.252692	H	-5.491132	-3.347903	0.069175
C	2.795323	-1.045057	-0.430192	C	2.76228	-1.050594	-0.090337
H	2.698922	-2.094215	-0.723246	H	2.650147	-2.136065	-0.157204
C	4.046782	-0.628985	-0.134907	C	4.071251	-0.618727	-0.022434
C	6.600686	-0.647376	0.410678	C	6.660508	-0.678598	0.05641
C	6.18275	0.57345	0.758428	C	6.339022	0.619592	0.171674
H	7.621468	-1.009528	0.527035	H	7.677389	-1.071115	0.052143
H	6.8147	1.345218	1.196241	H	7.05134	1.437974	0.274376
S	5.427208	-1.728463	-0.298632	S	5.351313	-1.801043	-0.096716
S	4.50126	0.970258	0.471242	S	4.646997	1.013344	0.158582
H	0.433429	-2.131812	-0.258556	H	0.413441	-2.15459	-0.056064

A.11 3-dithiafulvenylperylene

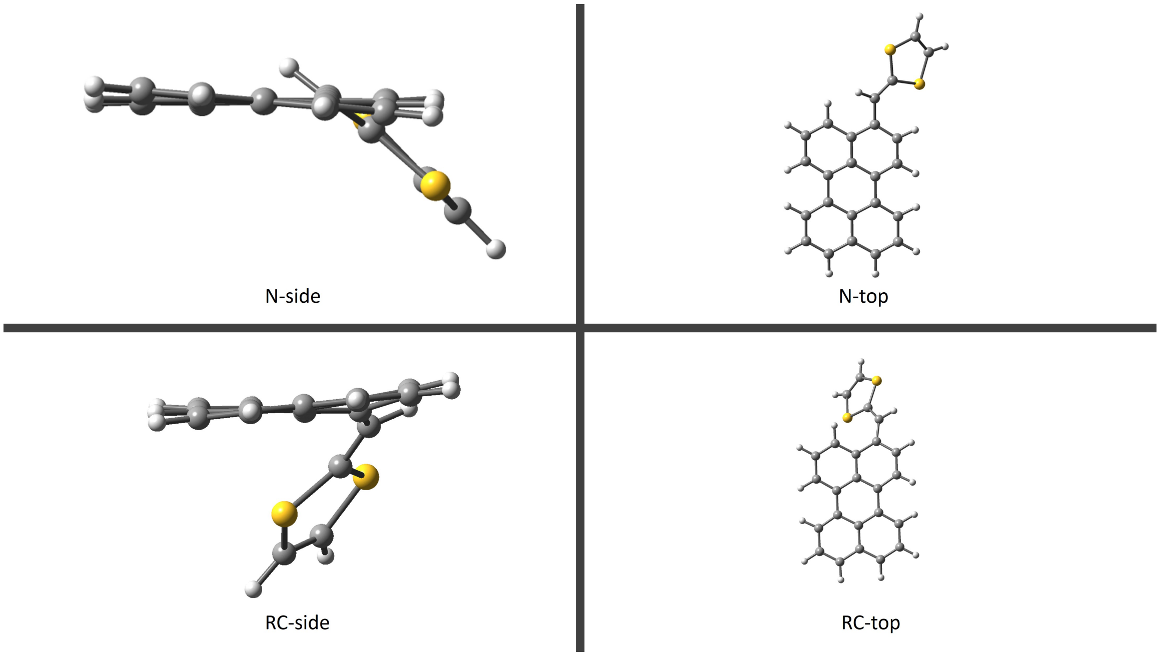

Figure A.38: Optimized geometry of 3-dithiafulvenylperylene **11**.

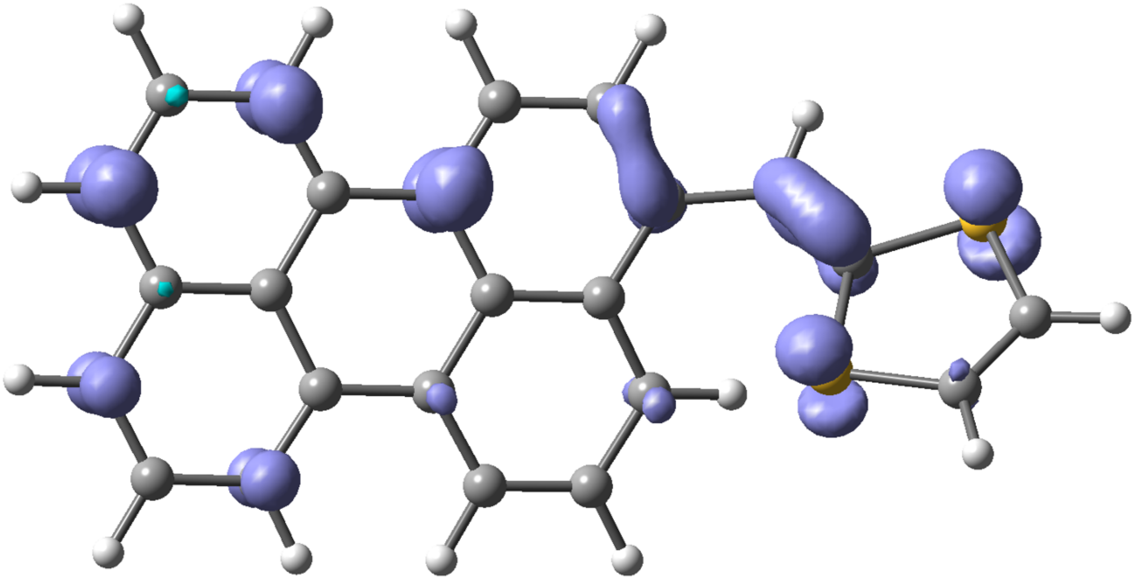

Figure A.39: Schematic illustration of spin density distribution over 3-dithiafulvenylperylene **11** (isovalue = 0.005).

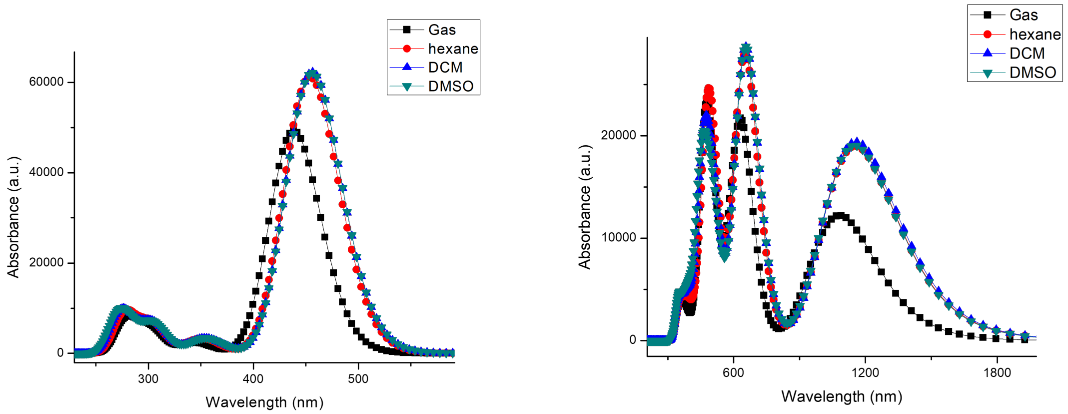

Figure A.40: UV-vis spectra of 3-dithiafulvenylperylene **11** in neutral (left) and radical cation (right) oxidation states.

Table A.14: Cartesian coordinates, energies, and dipole momentum of the optimized geometries of 3-dithiafulvenylperylene in N and RC oxidation states.

11-N in gas (E = -1718.063832 Hartree, μ = 1.718360 D) **11-N in hexanes** (E = -1718.088616 Hartree, μ = 1.876980 D) **11-N in DCM** (E = -1718.096511 Hartree, μ = 2.114164 D) **11-N in DMSO** (E = -1718.085779 Hartree, μ = 2.179015 D)				**11-RC in gas** (E = -1717.826116 Hartree, μ = 3.339364 D) **11-RC in hexanes** (E = -1717.877144 Hartree, μ = 4.030523 D) **11-RC in DCM** (E = -1717.904997 Hartree, μ = 5.831493 D) **11-RC in DMSO** (E = -1717.898237 Hartree, μ = 6.661704 D)			
C	5.702842	1.42959	0.322459	C	-4.932671	-2.351722	0.331982
C	3.297608	1.052808	0.120365	C	-2.807893	-1.222851	-0.10656
C	3.544841	-0.353286	0.021077	C	-3.438632	0.030093	0.135689
C	4.885613	-0.837205	0.101294	C	-4.825183	0.065345	0.467323
C	5.955378	0.082674	0.253041	C	-5.556628	-1.143665	0.558956
C	1.903517	1.548925	0.07952	C	-1.383013	-1.252025	-0.449924
C	2.471892	-1.283965	-0.15632	C	-2.708545	1.257546	0.047408
C	1.090269	-0.777193	-0.280905	C	-1.295972	1.223137	-0.277372
C	0.831168	0.625464	-0.145845	C	-0.637751	-0.034311	-0.464376
C	4.090967	-3.112522	-0.117454	C	-4.743532	2.49079	0.617866
C	5.133857	-2.232447	0.028758	C	-5.457415	1.311635	0.701687
H	6.163839	-2.587618	0.094937	H	-6.519564	1.323755	0.952972
H	4.277629	-4.186124	-0.165873	H	-5.232949	3.446287	0.80545
H	6.523184	2.140189	0.431451	H	-5.491802	-3.284262	0.407608
H	6.975539	-0.301394	0.309556	H	-6.617072	-1.102486	0.813265
C	0.281978	3.361041	0.214523	C	0.608447	-2.448812	-1.177072
C	-0.756084	2.49344	-0.023133	C	1.349938	-1.27774	-1.152663
C	-0.511993	1.110941	-0.226025	C	0.766831	-0.069026	-0.740405
H	0.083419	4.421006	0.378048	H	1.070187	-3.379303	-1.508358
H	-1.77977	2.865112	-0.031561	H	2.383998	-1.287553	-1.496648
C	-1.293354	-1.142359	-0.643224	C	0.81377	2.374975	-0.687225
H	-2.084818	-1.848569	-0.898542	H	1.363255	3.314109	-0.77261
C	-1.592632	0.199262	-0.491108	C	1.534537	1.157057	-0.703708
C	2.767955	-2.637313	-0.210442	C	-3.382624	2.461605	0.29596
H	1.970112	-3.368952	-0.32551	H	-2.848846	3.409133	0.254537
C	0.021227	-1.620642	-0.530421	C	-0.544139	2.406146	-0.464649
H	0.183532	-2.688104	-0.669144	H	-1.03059	3.377503	-0.412037
C	4.379132	1.908647	0.257713	C	-3.570259	-2.387375	0.002123
H	4.223987	2.984442	0.316829	H	-3.112277	-3.361264	-0.161666
C	1.605509	2.890514	0.256806	C	-0.732286	-2.440672	-0.79837
H	2.399691	3.60976	0.448149	H	-1.280474	-3.380265	-0.822379
C	-4.092563	0.075707	-0.220845	C	3.90338	0.438375	-0.048908
S	-5.690509	0.777599	-0.526793	S	5.569288	0.93608	-0.089471
S	-4.16175	-1.448492	0.68087	S	3.625542	-0.99847	0.891194
C	-6.574596	-0.36896	0.453239	C	6.170061	-0.310168	0.950262
H	-7.648486	-0.22308	0.563399	H	7.236091	-0.32406	1.176907
C	-5.883202	-1.374376	0.998208	C	5.27117	-1.197131	1.408139
H	-6.316224	-2.162406	1.613307	H	5.498978	-2.038726	2.062412
C	-2.965245	0.696962	-0.630098	C	2.950959	1.261928	-0.639108
H	-3.099993	1.665785	-1.117384	H	3.348485	2.226548	-0.969353

A.12 1-dithiafulvenylperylene

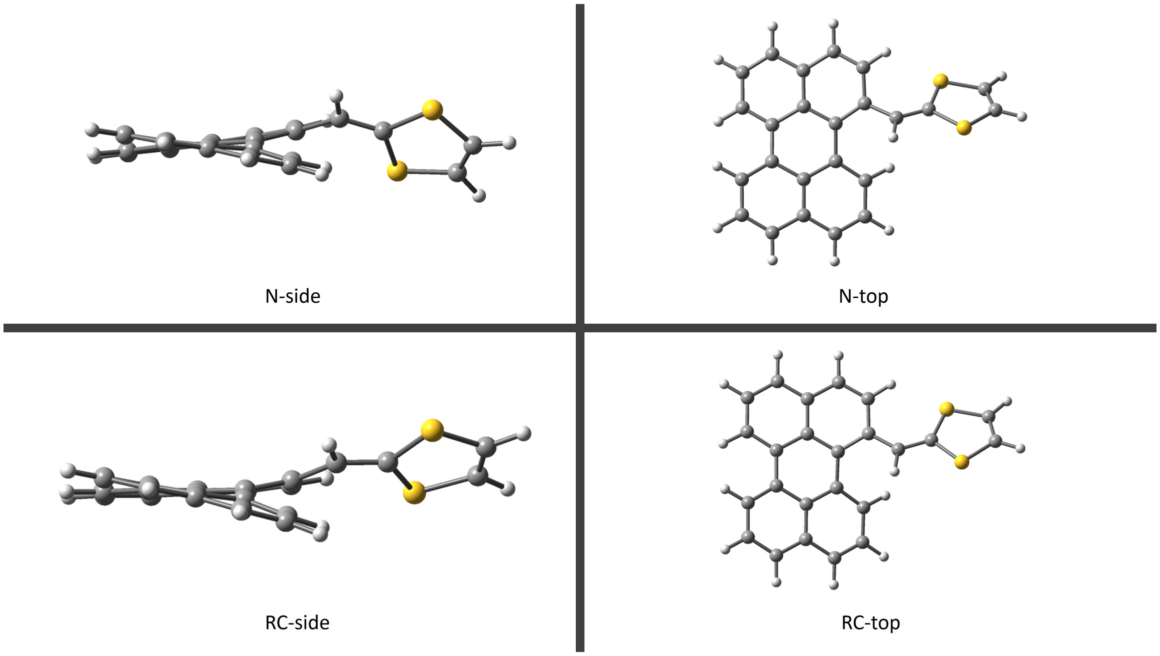

Figure A.41: Optimized geometry of 1-dithiafulvenylperylene **12**.

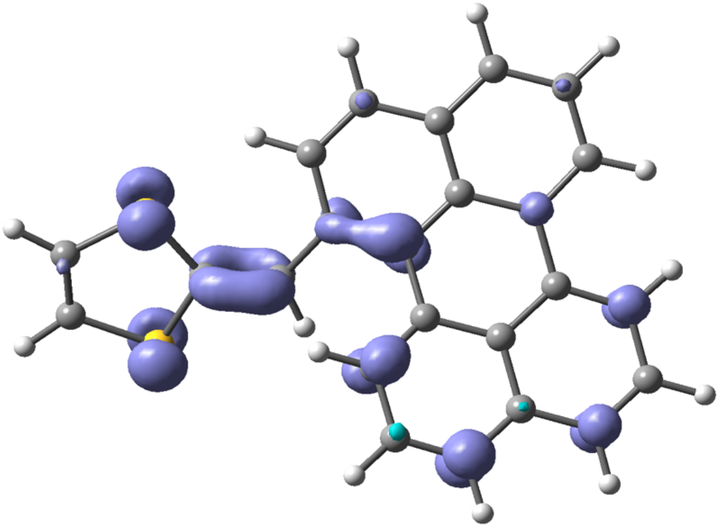

Figure A.42: Schematic illustration of spin density distribution over 1-dithiafulvenylperylene **12** (isovalue = 0.005).

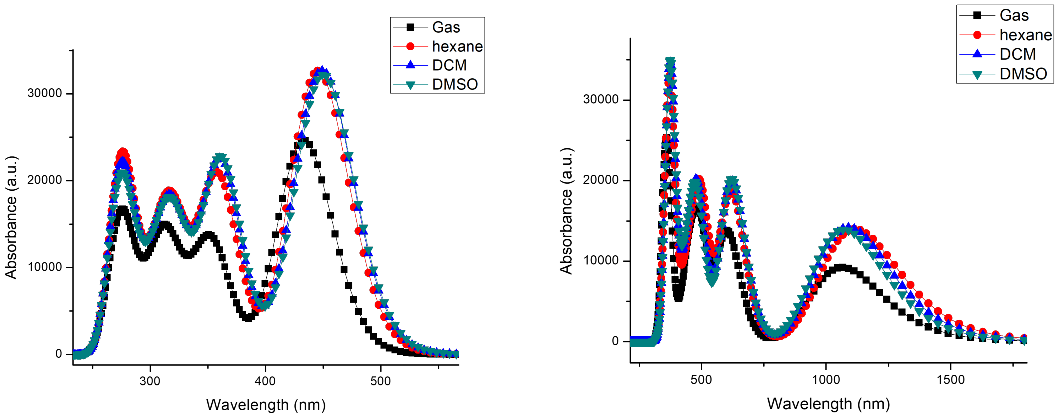

Figure A.43: UV-vis spectra of 1-dithiafulvenylperylene **12** in neutral (left) and radical cation (right) oxidation states.

Table A.15: Cartesian coordinates, energies, and dipole momentum of the optimized geometries of 1-dithiafulvenylperylene in N and RC oxidation states.

12-N in gas (E = -1718.058206 Hartree, μ = 1.530074 D) **12-N in hexanes** (E = -1718.082538 Hartree, μ = 1.662844 D) **12-N in DCM** (E = -1718.089662 Hartree, μ = 1.854206 D) **12-N in DMSO** (E = -1718.078820 Hartree, μ = 1.909804 D)				**12-RC in gas** (E = -1717.823331 Hartree, μ = 4.074782 D) **12-RC in hexanes** (E = -1717.874241 Hartree, μ = 4.974089 D) **12-RC in DCM** (E = -1717.902006 Hartree, μ = 6.969375 D) **12-RC in DMSO** (E = -1717.895255 Hartree, μ = 7.795064 D)			
C	-3.324301	3.559014	-0.207059	C	3.340351	3.57253	-0.064052
C	-3.7284	2.211463	-0.165501	C	3.750364	2.242481	-0.156347
C	-2.813299	1.178984	-0.025994	C	2.831076	1.189181	-0.111593
C	-1.416714	1.489813	0.030976	C	1.44384	1.497642	0.036807
C	-1.021778	2.859372	0.049958	C	1.034213	2.863159	0.093123
C	-1.994359	3.880759	-0.083692	C	1.99319	3.884907	0.056294
C	-3.242343	-0.228001	0.083825	C	3.241738	-0.209434	-0.218015
C	-0.424443	0.453843	0.095552	C	0.463633	0.461258	0.11689
C	-0.863013	-0.938029	-0.1491	C	0.919803	-0.897763	0.346236
C	-2.259241	-1.255496	-0.051807	C	2.289956	-1.223354	0.081258
C	0.011161	-1.956684	-0.507192	C	0.092369	-1.900878	0.878062
C	0.903895	0.807443	0.380346	C	-0.92588	0.803141	-0.009079
C	1.265014	2.18407	0.439122	C	-1.301175	2.182375	0.096891
C	0.348759	3.177717	0.23738	C	-0.362166	3.165331	0.166714
H	0.64864	4.226757	0.270796	H	-0.667303	4.212203	0.211158
H	2.297127	2.442519	0.680528	H	-2.348547	2.469243	0.028035
H	-4.074654	4.342115	-0.322571	H	4.08539	4.368096	-0.090415
H	-1.665609	4.921623	-0.083235	H	1.667884	4.924498	0.118675
C	-4.568432	-0.586792	0.270586	C	4.545968	-0.588659	-0.545816
C	-4.973077	-1.93596	0.270846	C	4.940291	-1.933022	-0.550347
C	-4.053561	-2.932521	0.051295	C	4.044095	-2.919072	-0.188658
C	-2.682751	-2.615323	-0.129833	C	2.712059	-2.58327	0.150696
H	-6.024936	-2.180096	0.424998	H	5.964207	-2.192266	-0.819656
H	-4.360297	-3.979291	0.009655	H	4.351485	-3.965614	-0.154479
C	-0.419652	-3.294136	-0.641207	C	0.525517	-3.228942	0.992246
H	0.307314	-4.060336	-0.913816	H	-0.145745	-3.981009	1.406763
C	-1.729865	-3.629107	-0.414215	C	1.799383	-3.576008	0.591333
H	1.055841	-1.731184	-0.706627	H	-0.896865	-1.640702	1.251707
H	-4.790706	1.986445	-0.251291	H	4.814851	2.033526	-0.248811
H	-5.325636	0.182016	0.41967	H	5.285261	0.167758	-0.805817
C	1.931261	-0.184069	0.731774	C	-1.870746	-0.19826	-0.378418
H	1.603413	-1.016972	1.36156	H	-1.455745	-1.088275	-0.857304
C	3.227621	-0.179217	0.361998	C	-3.254855	-0.19773	-0.276815
C	5.520634	0.150765	-0.837082	C	-5.708858	-0.990808	-0.436662
C	5.694852	-0.922737	-0.060543	C	-5.750041	0.136765	0.294174
H	6.28052	0.565823	-1.498248	H	-6.576609	-1.595272	-0.701016
H	6.615509	-1.502246	-0.003412	H	-6.654404	0.582373	0.708719
S	4.35488	-1.417378	0.948641	S	-4.241485	0.938795	0.591278
S	3.968365	0.960964	-0.779357	S	-4.153934	-1.500804	-0.996942
H	-2.066248	-4.665564	-0.479143	H	2.138092	-4.611843	0.653517

A.13 Dithiafulvenylcorannulene

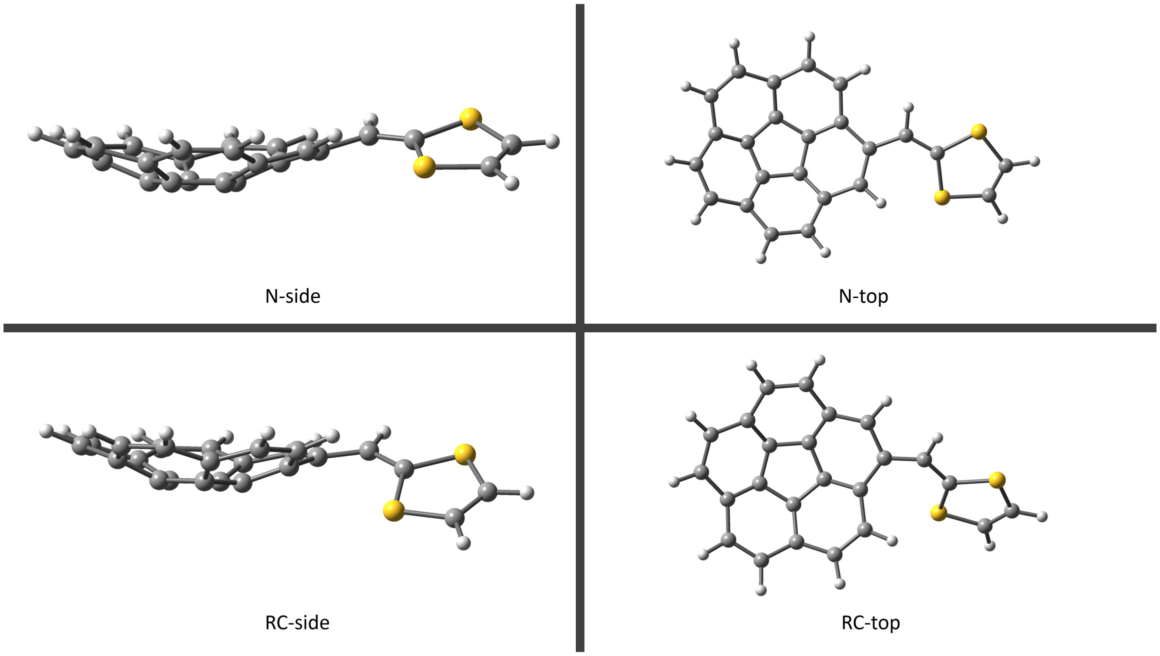

N-side

N-top

RC-side

RC-top

Figure A.44: Optimized geometry of dithiafulvenylcorannulene **13**.

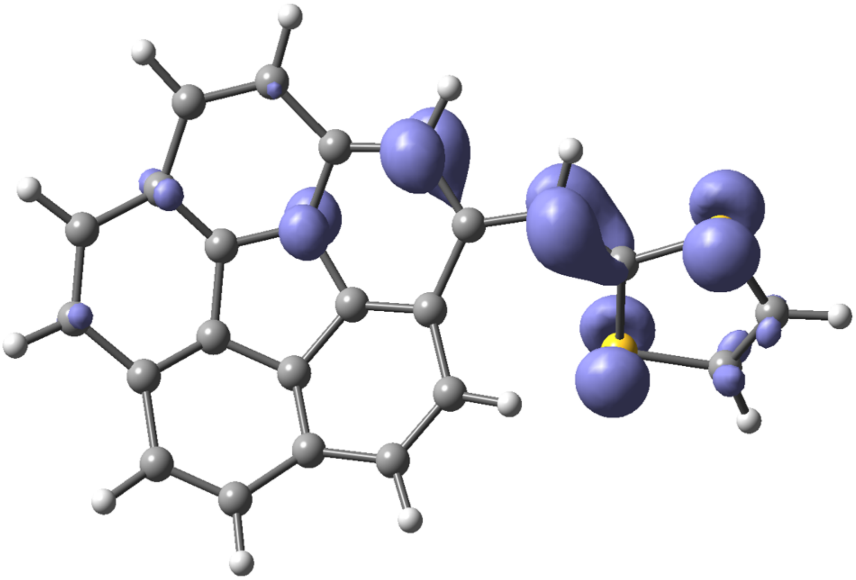

Figure A.45: Schematic illustration of spin density distribution over dithiafulvenylcorannulene **13** (isovalue = 0.005).

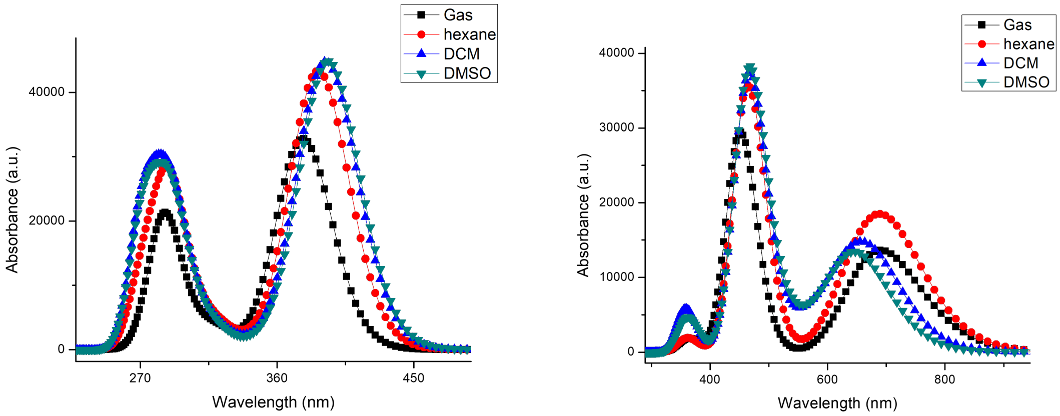

Figure A.46: UV-vis spectra of dithiafulvenylcorannulene **13** in neutral (left) and radical cation (right) oxidation states.

Table A.16: Cartesian coordinates, energies, and dipole momentum of the optimized geometries of dithiafulvenylcorannulene in N and RC oxidation states.

13-N in gas (E = -1716.820825 Hartree, μ = 2.680781 D) **13-N in hexanes** (E = -1716.845810 Hartree, μ = 3.012496 D) **13-N in DCM** (E = -1716.852913 Hartree, μ = 3.592237 D) **13-N in DMSO** (E = -1716.842167 Hartree, μ = 3.800978 D)				**13-RC in gas** (E = -1716.573909 Hartree, μ = 8.401129 D) **13-RC in hexanes** (E = -1716.626831 Hartree, μ = 10.075104 D) **13-RC in DCM** (E = -1716.657120 Hartree, μ = 12.804459 D) **13-RC in DMSO** (E = -1716.651440 Hartree, μ = 13.700652 D)			
C	0.090519	-2.578354	-0.023425	C	-0.835853	-1.550065	-0.603286
C	-0.083266	-1.166224	-0.292909	C	-0.51214	-0.252603	-0.052746
C	1.063075	-0.531125	-0.722103	C	0.741248	-0.171806	0.515328
C	2.341981	-1.144007	-0.696948	C	1.679756	-1.230543	0.484931
C	2.553114	-2.428502	-0.238301	C	1.440689	-2.424851	-0.166847
C	1.339856	-3.176464	0.005141	C	0.088621	-2.581831	-0.646045
C	1.252668	0.872237	-0.645715	C	1.477088	1.046564	0.625418
C	3.318306	-0.120802	-0.597963	C	2.980097	-0.673949	0.60478
C	2.643474	1.125758	-0.562641	C	2.849782	0.735168	0.698328
C	3.168656	2.244545	0.053661	C	3.8353	1.61225	0.277432
C	4.551051	2.108536	0.461481	C	5.096375	0.986391	-0.044732
C	5.211652	0.892233	0.422487	C	5.222275	-0.390123	-0.135357
C	4.558814	-0.320066	-0.026246	C	4.102785	-1.283082	0.085967
C	4.869637	-1.706014	0.258357	C	3.894067	-2.637449	-0.385377
C	3.918696	-2.706469	0.156804	C	2.62898	-3.180673	-0.50691
H	4.190272	-3.71683	0.470889	H	2.52519	-4.170249	-0.956022
H	5.856422	-1.963815	0.64964	H	4.747407	-3.217849	-0.741896
H	-0.770377	-3.192804	0.245911	H	-1.792196	-1.711805	-1.103176
H	1.40562	-4.225179	0.303555	H	-0.193019	-3.50385	-1.158958
H	5.067113	2.966585	0.898327	H	5.951743	1.608446	-0.314796
H	6.224103	0.83659	0.828773	H	6.175293	-0.802393	-0.473625
C	-1.198091	-0.273339	0.038358	C	-1.139006	1.057695	-0.288691
C	-0.979706	1.104619	0.137594	C	-0.348932	2.248186	-0.255003
C	0.302082	1.716942	-0.109818	C	1.012646	2.26645	0.148174
H	-1.776456	1.727584	0.548673	H	-0.827501	3.176008	-0.579999
C	2.183302	3.240924	0.41966	C	3.377159	2.959245	-0.004922
H	2.514281	4.186844	0.854478	H	4.107577	3.728955	-0.261603
C	0.824186	2.990619	0.343654	C	2.035432	3.274133	-0.068899
H	0.13333	3.747621	0.721669	H	1.742341	4.281657	-0.369149
C	-2.492238	-0.879007	0.342013	C	-2.516357	1.258645	-0.570086
H	-2.473047	-1.922209	0.665987	H	-2.780709	2.209585	-1.043229
C	-3.721721	-0.329126	0.216182	C	-3.606028	0.463566	-0.210326
C	-6.311522	-0.090594	0.003025	C	-5.269104	-1.145523	0.892321
C	-5.81836	1.057206	-0.471937	C	-6.0298	-0.307573	0.156888
H	-7.37012	-0.345766	0.033386	H	-5.654422	-1.965547	1.499357
H	-6.418886	1.868668	-0.881402	H	-7.116686	-0.351889	0.082145
S	-5.173007	-1.250289	0.643184	S	-3.561416	-0.897907	0.857958
S	-4.083196	1.288511	-0.403332	S	-5.195803	0.913507	-0.725525

A.14 Dithiafulvenylcoronene

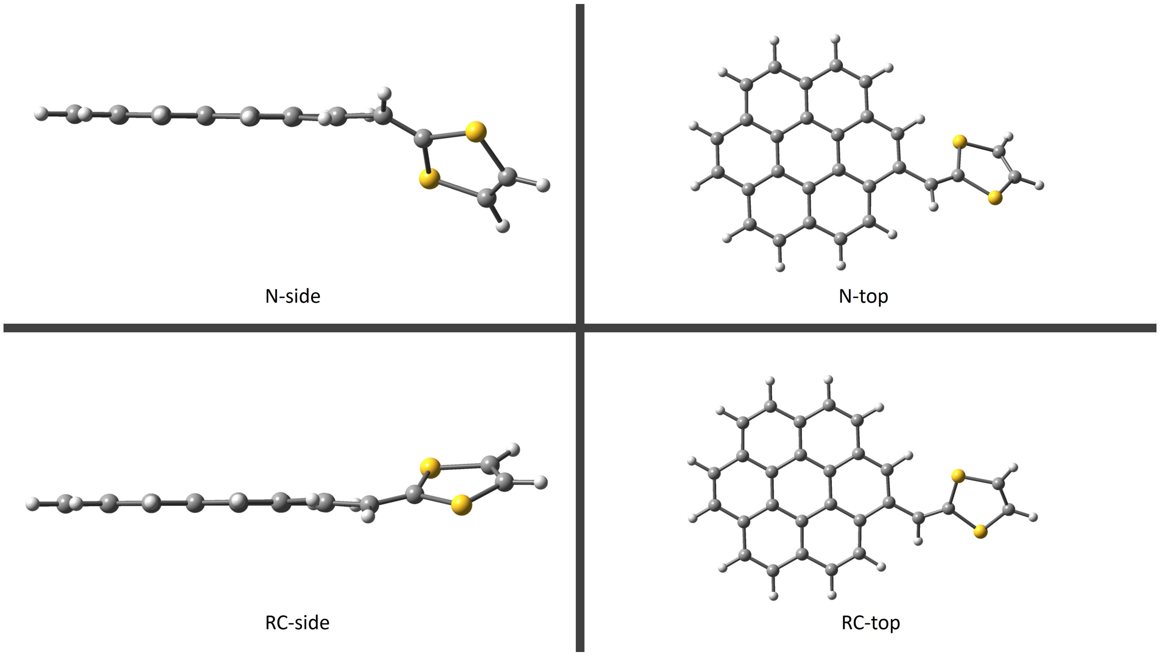

Figure A.47: Optimized geometry of dithiafulvenylcoronene **14**.

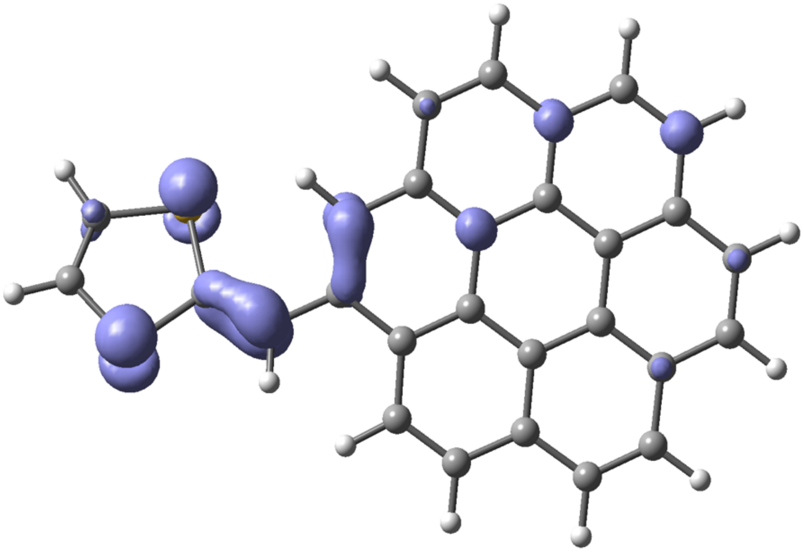

Figure A.48: Schematic illustration of spin density distribution over dithiafulvenylcoronene **14** (isovalue = 0.005).

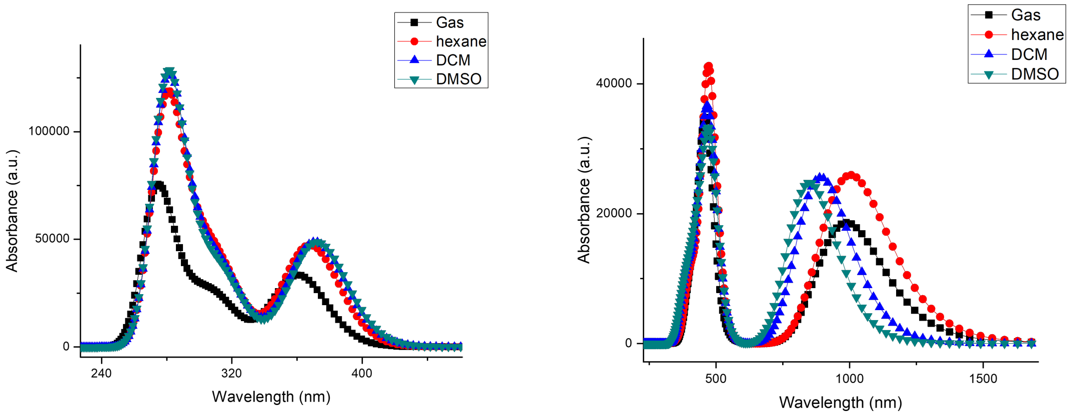

Figure A.49: UV-vis spectra of dithiafulvenylcoronene **14** in neutral (left) and radical cation (right) oxidation states.

Table A.17: Cartesian coordinates, energies, and dipole momentum of the optimized geometries of dithiafulvenylcoronene in N and RC oxidation states.

14-N in gas (E = -1870.395633 Hartree, μ = 1.684318 D)				**14-RC in gas** (E = -1870.152319 Hartree, μ = 8.219968 D)			
14-N in hexanes (E = -1870.423624 Hartree, μ = 1.832017 D)				**14-RC in hexanes** (E = -1870.206673 Hartree, μ = 10.373540 D)			
14-N in DCM (E = -1870.431516 Hartree, μ = 2.025147 D)				**14-RC in DCM** (E = -1870.236208 Hartree, μ = 14.309534 D)			
14-N in DMSO (E = -1870.419568 Hartree, μ = 2.067215 D)				**14-RC in DMSO** (E = -1870.228889 Hartree, μ = 15.645897 D)			
C	-5.471331	1.156957	0.38507	C	5.557045	-1.04484	-0.165024
C	-4.171826	1.73001	0.262762	C	4.271502	-1.653355	-0.128081
C	-3.058726	0.873802	0.092995	C	3.121238	-0.829716	-0.048911
C	-3.250513	-0.540239	0.049677	C	3.266148	0.584469	-0.009693
C	-4.549884	-1.084593	0.174464	C	4.553831	1.167506	-0.048202
C	-5.654048	-0.199042	0.342387	C	5.694938	0.318768	-0.126462
C	-1.744818	1.423289	-0.033075	C	1.821673	-1.416606	-0.007519
C	-2.126812	-1.404522	-0.118512	C	2.108642	1.414783	0.067517
C	-0.816248	-0.854362	-0.245747	C	0.816725	0.829491	0.105599
C	-0.617845	0.560499	-0.208888	C	0.659512	-0.591384	0.07664
C	0.294118	-1.710835	-0.414352	C	-0.333899	1.671638	0.185275
C	0.080391	-3.120441	-0.457512	C	-0.162415	3.096376	0.237612
C	-1.176346	-3.648042	-0.333832	C	1.080218	3.650347	0.196907
C	-2.313879	-2.806293	-0.161032	C	2.251918	2.828911	0.109595
C	-3.633938	-3.329647	-0.032593	C	3.552443	3.389552	0.069757
C	-4.711143	-2.500797	0.128878	C	4.665569	2.585367	-0.007193
H	-5.716496	-2.915296	0.225791	H	5.660852	3.032898	-0.036888
H	-3.771605	-4.412222	-0.066172	H	3.660076	4.474709	0.102112
H	-6.325512	1.824382	0.515163	H	6.438467	-1.685188	-0.225013
H	-6.655213	-0.623942	0.437792	H	6.686831	0.772988	-0.1557
H	0.943606	-3.775196	-0.591714	H	-1.04992	3.727524	0.306394
H	-1.326386	-4.72895	-0.36757	H	1.20513	4.733654	0.232331
C	-3.95909	3.139513	0.307826	C	4.10785	-3.072791	-0.168631
C	-2.702318	3.666737	0.192173	C	2.865737	-3.638123	-0.134135
C	-1.563977	2.824597	0.019589	C	1.691248	-2.825808	-0.053319
H	-4.8228	3.79426	0.439357	H	4.998678	-3.700011	-0.229501
H	-2.550653	4.747193	0.231304	H	2.749888	-4.72259	-0.168469
C	-0.245421	3.347148	-0.090367	C	0.393125	-3.385039	-0.029257
C	0.8343	2.520977	-0.255861	C	-0.728371	-2.5898	0.046814
C	0.683114	1.105297	-0.335012	C	-0.631382	-1.17811	0.120737
H	-0.103776	4.428068	-0.031044	H	0.284674	-4.469772	-0.080594
H	1.832943	2.953508	-0.309337	H	-1.700769	-3.078996	0.029419
C	1.588723	-1.142707	-0.556331	C	-1.600481	1.088692	0.229876
H	2.424534	-1.820652	-0.742758	H	-2.447925	1.760499	0.36574
C	1.807213	0.218236	-0.520482	C	-1.79796	-0.306257	0.204963
C	3.154422	0.778068	-0.692777	C	-3.095	-0.877869	0.313227
H	3.241357	1.700567	-1.27237	H	-3.142148	-1.927935	0.606579
C	4.304933	0.267929	-0.205123	C	-4.345671	-0.308445	0.095748
C	6.143175	-0.942273	1.191166	C	-6.906725	-0.0791	-0.115644
C	6.789788	0.042299	0.560069	C	-6.40729	1.078698	-0.587673
H	6.604384	-1.635618	1.893618	H	-7.967308	-0.325324	-0.059831
H	7.849926	0.263529	0.677375	H	-7.00284	1.908096	-0.969791
S	4.438325	-1.153579	0.845869	S	-5.764621	-1.246788	0.440778
S	5.86815	1.026766	-0.552918	S	-4.685047	1.250245	-0.584523

A.15 Oxidation potentials

Table A.18: Oxidation potential of the studied Ar-DTFs in 3 different solvents (vs. SHE).

Compound	**Hexanes**	**DCM**	**DMSO**
1	1.77	1.03	0.89
2-cis	1.71	1.09	0.96
2-trans	1.69	0.98	0.84
3	1.75	0.93	0.88
4	1.65	0.97	0.78
5-cis	1.59	0.97	0.84
5-trans	1.54	0.93	0.80
6	1.60	0.96	0.82
7	1.69	0.95	0.82
8	1.51	0.86	0.72
9-cis	1.56	0.97	0.84
9-trans	1.56	0.97	0.84
10	1.59	1.00	0.87
11	1.49	0.87	0.75
12	1.37	0.81	0.69
13	1.54	1.03	0.90
14	1.61	0.96	0.88

A.16 Frontier molecular orbitals

Table A.19: The energy levels of the studied Ar-DTFs' frontier molecular orbitals and their energy gap in the neutral form in gas.

Compound	HOMO(Hartrees)	LUMO(Hartrees)	Gap(Hartrees)	Gap(ev)	Gap(kcal/mol)
1	-0.23002	-0.0047	0.22532	6.13	141.39
2-cis	-0.23015	-0.02226	0.20789	5.66	130.45
2-trans	-0.23015	-0.02224	0.20791	5.66	130.46
3	-0.2295	-0.02192	0.20758	5.65	130.26
4	-0.22606	-0.04267	0.18339	4.99	115.08
5-cis	-0.232	-0.04122	0.19078	5.19	119.72
5-trans	-0.22693	-0.04301	0.18392	5.00	115.41
6	-0.23136	-0.04273	0.18863	5.13	118.37
7	-0.23023	-0.03457	0.19566	5.32	122.78
8	-0.22442	-0.04153	0.18289	4.98	114.76
9-cis	-0.22931	-0.03815	0.19116	5.20	119.95
9-trans	-0.2293	-0.03814	0.19116	5.20	119.95
10	-0.22642	-0.05203	0.17439	4.74	109.43
11	-0.21968	-0.0551	0.16458	4.48	103.27
12	-0.22039	-0.05335	0.16704	4.54	104.82
13	-0.23107	-0.04414	0.18693	5.09	117.30
14	-0.22923	-0.03939	0.18984	5.16	119.13

Table A.20: The energy levels of the studied Ar-DTFs' frontier molecular orbitals and their energy gap in the radical cation form in gas.

Compound	**SOMO(Hartrees)**	**LUMO(Hartrees)**	**Gap(Hartrees)**	**Gap(ev)**	**Gap(kcal/mol)**
1	-0.40163	-0.18452	0.21711	5.91	136.24
2-cis	-0.38298	-0.18467	0.19831	5.40	124.44
2-trans	-0.38062	-0.18579	0.19483	5.30	122.26
3	-0.38326	-0.18306	0.2002	5.45	125.63
4	-0.36198	-0.18586	0.17612	4.79	110.52
5-cis	-0.36141	-0.1896	0.17181	4.67	107.81
5-trans	-0.35974	-0.18809	0.17165	4.67	107.71
6	-0.3599	-0.19541	0.16449	4.48	103.22
7	-0.36068	-0.17019	0.19049	5.18	119.53
8	-0.35065	-0.18273	0.16792	4.57	105.37
9-cis	-0.36288	-0.18317	0.17971	4.89	112.77
9-trans	-0.36288	-0.18317	0.17971	4.89	112.77
10	-0.35248	-0.18339	0.16909	4.60	106.10
11	-0.33841	-0.18925	0.14916	4.06	93.60
12	-0.34118	-0.18641	0.15477	4.21	97.12
13	-0.36875	-0.18267	0.18608	5.06	116.77
14	-0.34721	-0.17107	0.17614	4.79	110.53

Table A.21: The energy levels of the studied Ar-DTFs' frontier molecular orbitals and their energy gap in the neutral form in hexanes.

Compound	**HOMO(Hartrees)**	**LUMO(Hartrees)**	**Gap(Hartrees)**	**Gap(ev)**	**Gap(kcal/mol)**
1	-0.2294	-0.00474	0.22466	6.11	140.98
2-cis	-0.22939	-0.02201	0.20738	5.64	130.13
2-trans	-0.22939	-0.022	0.20739	5.64	130.14
3	-0.22873	-0.02188	0.20685	5.63	129.80
4	-0.22538	-0.04256	0.18282	4.97	114.72
5-cis	-0.23139	-0.04104	0.19035	5.18	119.45
5-trans	-0.22617	-0.04263	0.18354	4.99	115.17
6	-0.23074	-0.04259	0.18815	5.12	118.07
7	-0.2292	-0.03427	0.19493	5.30	122.32
8	-0.2237	-0.04123	0.18247	4.96	114.50
9-cis	-0.22842	-0.03775	0.19067	5.19	119.65
9-trans	-0.2284	-0.03774	0.19066	5.19	119.64
10	-0.2258	-0.05166	0.17414	4.74	109.27
11	-0.21896	-0.0546	0.16436	4.47	103.14
12	-0.21965	-0.05296	0.16669	4.53	104.60
13	-0.22994	-0.04405	0.18589	5.06	116.65
14	-0.22821	-0.039	0.18921	5.15	118.73

Table A.22: The energy levels of the studied Ar-DTFs' frontier molecular orbitals and their energy gap in the radical cation form in hexanes.

Compound	**SOMO(Hartrees)**	**LUMO(Hartrees)**	**Gap(Hartrees)**	**Gap(ev)**	**Gap(kcal/mol)**
1	-0.33708	-0.12001	0.21707	5.91	136.21
2-cis	-0.32254	-0.12412	0.19842	5.40	124.51
2-trans	-0.32102	-0.12594	0.19508	5.31	122.41
3	-0.32401	-0.12348	0.20053	5.46	125.83
4	-0.30709	-0.13078	0.17631	4.80	110.64
5-cis	-0.30483	-0.13272	0.17211	4.68	108.00
5-trans	-0.30438	-0.13238	0.172	4.68	107.93
6	-0.30305	-0.1386	0.16445	4.47	103.19
7	-0.30925	-0.11507	0.19418	5.28	121.85
8	-0.29676	-0.12883	0.16793	4.57	105.38
9-cis	-0.30805	-0.12802	0.18003	4.90	112.97
9-trans	-0.30805	-0.12802	0.18003	4.90	112.97
10	-0.29943	-0.13087	0.16856	4.59	105.77
11	-0.28627	-0.13696	0.14931	4.063	93.69
12	-0.28878	-0.13391	0.15487	4.21	97.18
13	-0.31506	-0.1289	0.18616	5.06	116.82
14	-0.29736	-0.12074	0.17662	4.81	110.83

A Combined TD-DFT, UV–vis And Fluorescence Spectroscopic Studies of A Novel Organic Fluorophore Derived From Self-Condensation of Pyrene-4,5-dione

A.17 Structures obtained from the CREST calculations

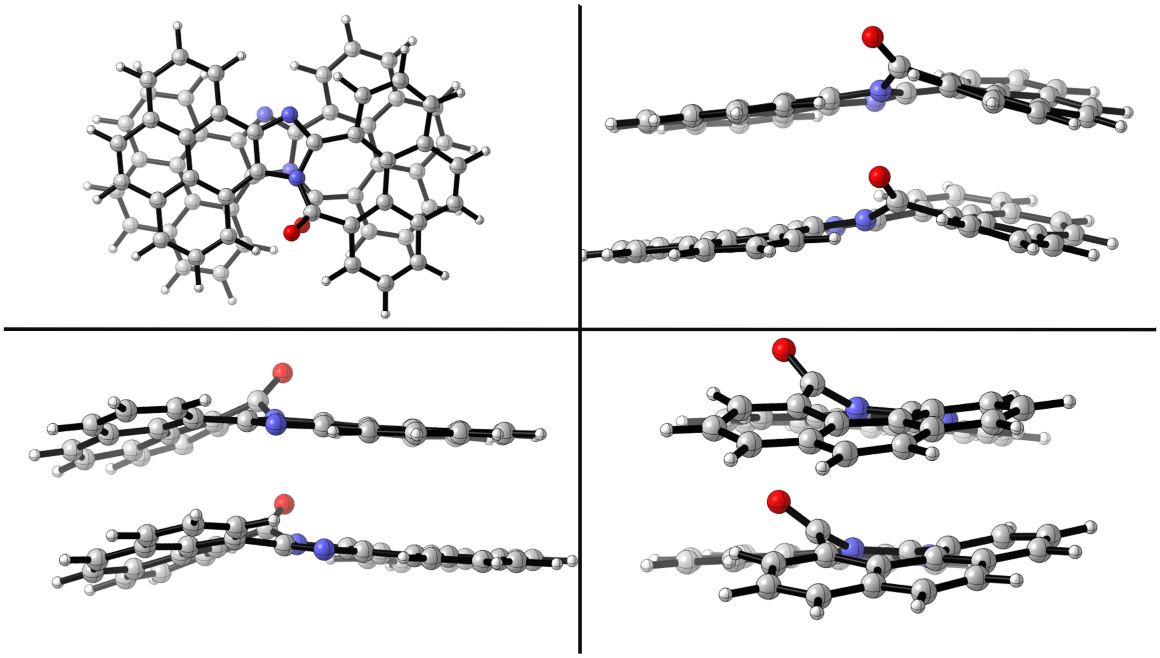

Figure A.50: The geometry of the second most stable conformer of (**2**)$_2$, represented from different views. The conformer was initially obtained using the CREST method and subsequently reoptimized in the gas phase using the M06-2X/def2-SVP method. This conformer is relatively 1.64 kcal/mol less stable than the most stable conformer.

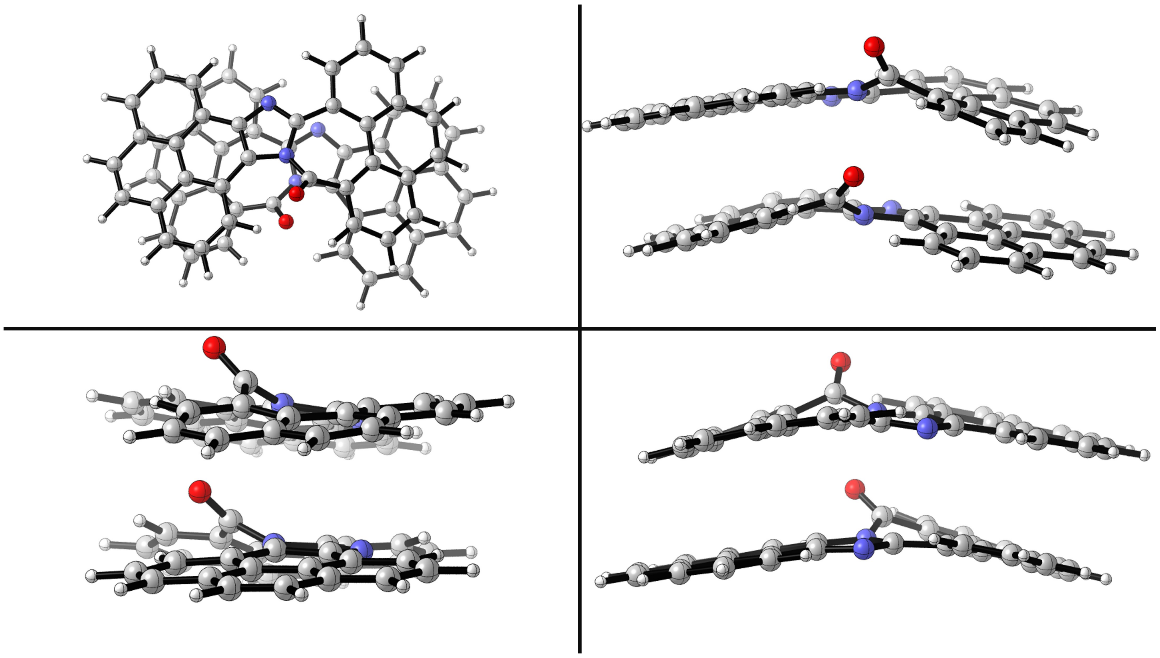

Figure A.51: The geometry of the third most stable conformer of $(\mathbf{2})_2$, represented from different views. The conformer was initially obtained using the CREST method and subsequently reoptimized in the gas phase using the M06-2X/def2-SVP method. This conformer is relatively 1.76 kcal/mol less stable than the most stable conformer.

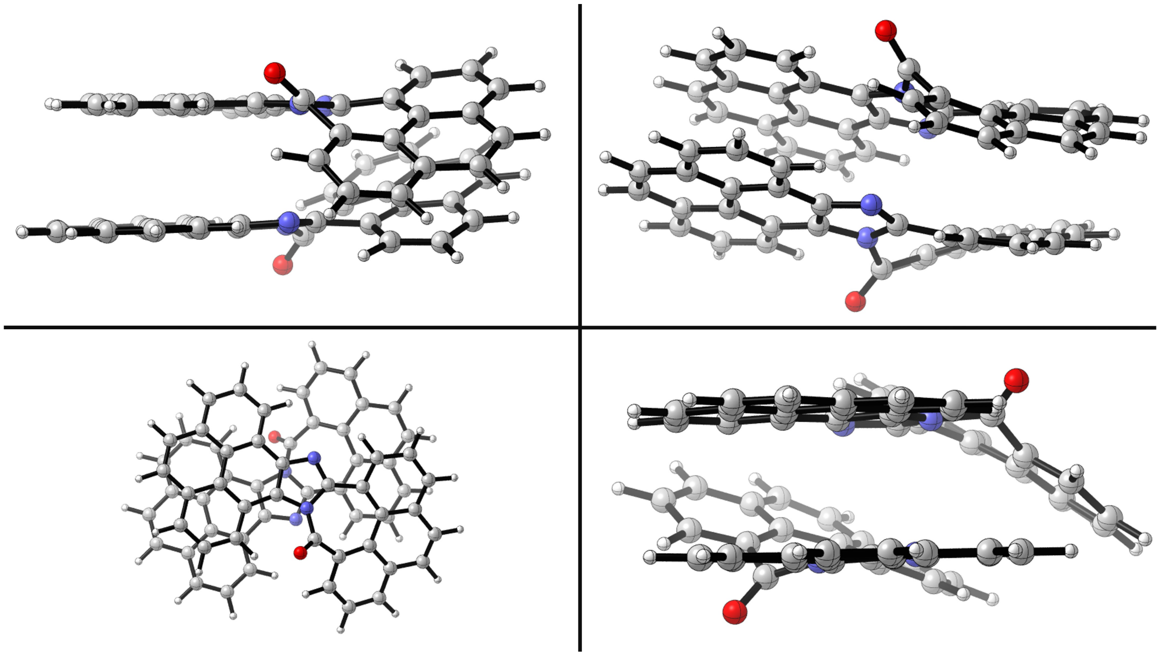

Figure A.52: The geometry of the fourth most stable conformer of $(\mathbf{2})_2$, represented from different views. The conformer was initially obtained using the CREST method and subsequently reoptimized in the gas phase using the M06-2X/def2-SVP method. This conformer is relatively 2.48 kcal/mol less stable than the most stable conformer.

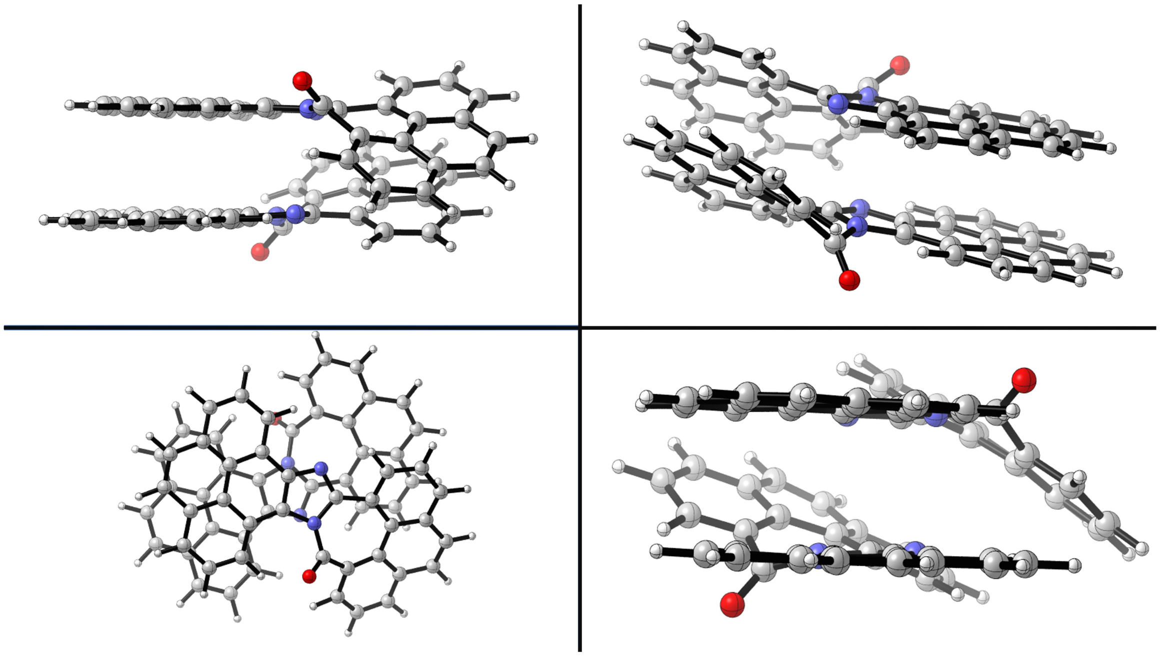

Figure A.53: The geometry of the fifth most stable conformer of $(\mathbf{2})_2$, represented from different views. The conformer was initially obtained using the CREST method and subsequently reoptimized in the gas phase using the M06-2X/def2-SVP method. This conformer is relatively 2.49 kcal/mol less stable than the most stable conformer.

A.18 MALDI-TOF MS analysis

Matrix-assisted laser desorption/ionization-time of flight (MALDI-TOF) mass spectrometry (MS) analysis was performed on both **2**/β-CD and **2**/γ-CD using 2,5-Dihyroxybenzoic acid (DHB) as the matrix. The results are shown in the following Figures.

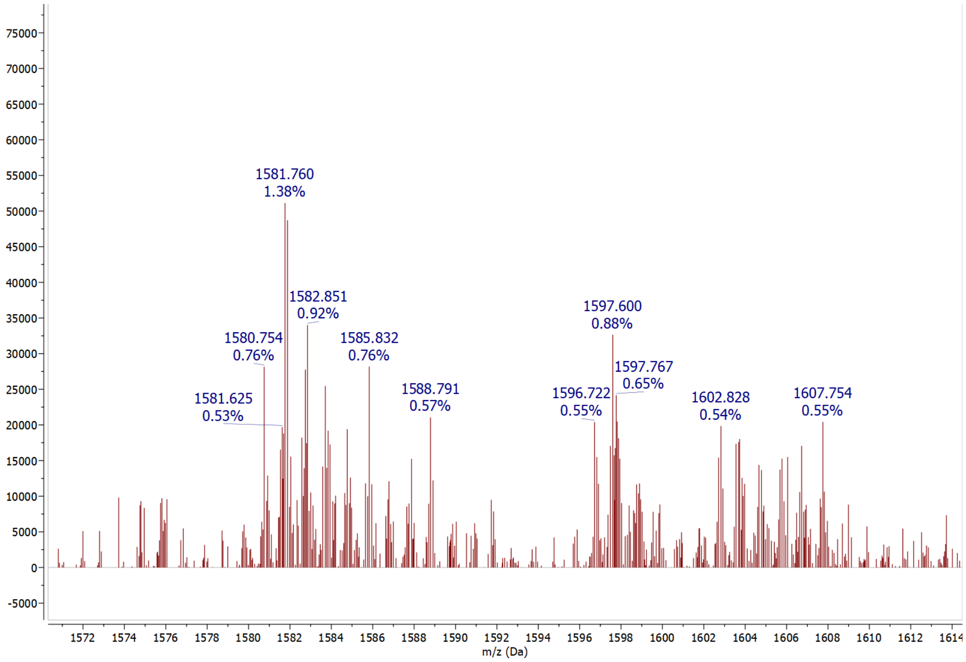

Figure A.54: MALDI-TOF MS result for **2**/β-CD. The peak at 1597.600 represents the presence of **2**/β-CD (1:1) plus a molecule of H_2O.

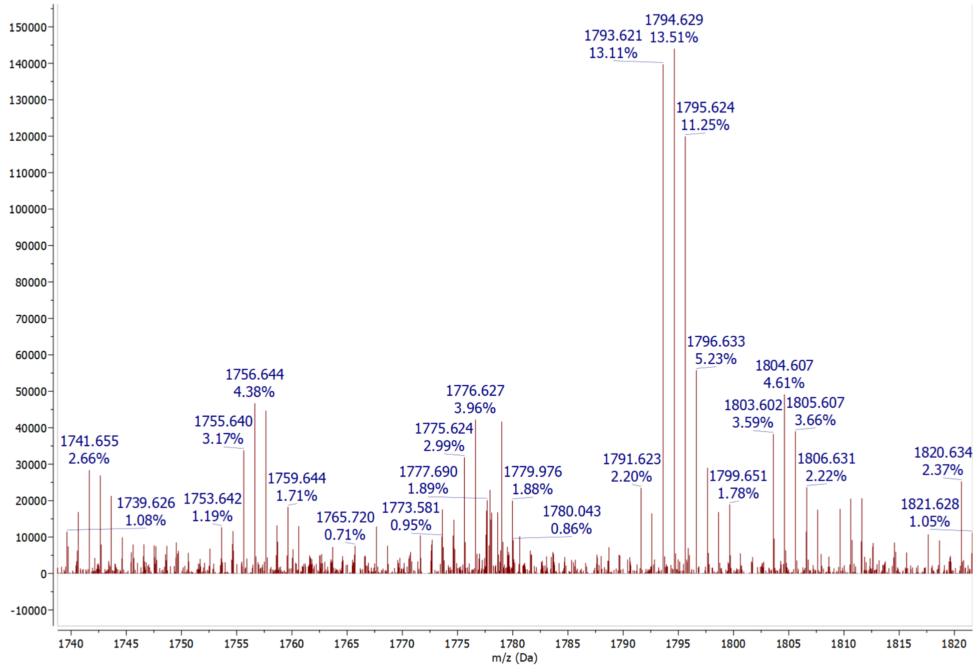

Figure A.55: MALDI-TOF MS result for **2**/γ-CD. The peak at 1741.655 represents 1:1 ratio of **2**/γ-CD. No 2:1 ratio was observed in the mass spectroscopy analysis of this complex.

A.19 TD-DFT results for π- and T-dimers

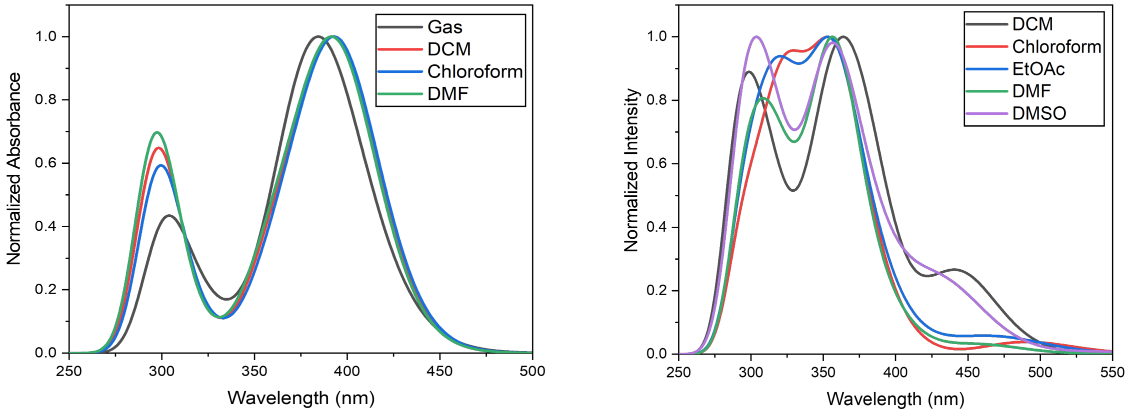

Figure A.56: Simulated normalized absorbance (left) and emission (right) spectra of $\mathbf{2}_2$ (π-dimer arrangement) calculated via M06-2X/def2-SVP method.

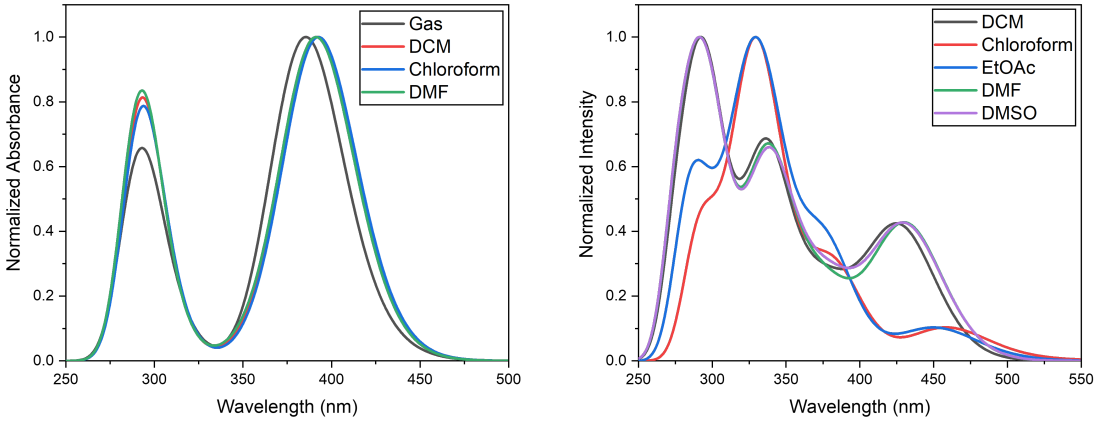

Figure A.57: Simulated normalized absorbance (left) and emission (right) spectra of $\mathbf{2}_2$ (T-dimer arrangement) calculated via M06-2X/def2-SVP method.

A.20 Photographic images

The following Figures show the photographic images of the fluorescence emission of **2** in different organic solvents and that of its complexation with β-CD and γ-CD under different conditions (excitation source is a UV lamp with $\lambda_{exc} = 365$ nm).

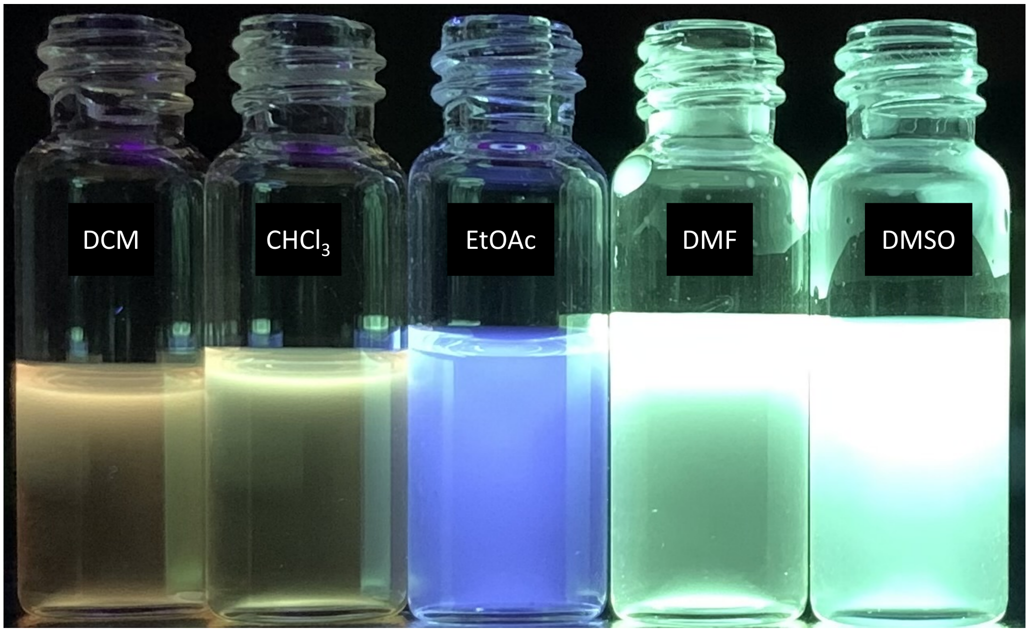

Figure A.58: Photographic images of **2** (1.0×10^{-3} M) dissolved in different organic solvents.

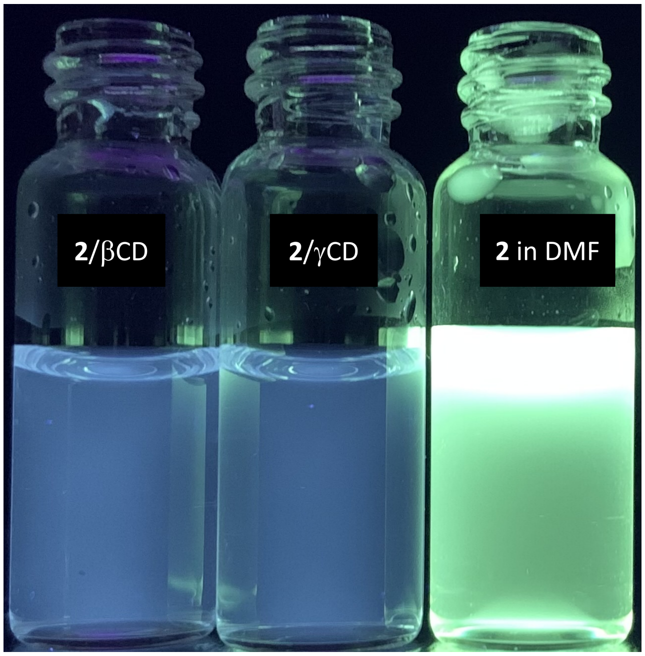

Figure A.59: Photographic images of left: **2**/β-CD (1.0 $\times 10^{-3}$ M and 5.0 $\times 10^{-3}$ M, respectively) dissolved in DMF/H_2O (1:1), middle: **2**/γ-CD (1.0 $\times 10^{-3}$ M and 5.0 $\times 10^{-3}$ M, respectively) dissolved in DMF/H_2O (1:1), and right: **2** (1.0 $\times 10^{-3}$ M) in DMF.

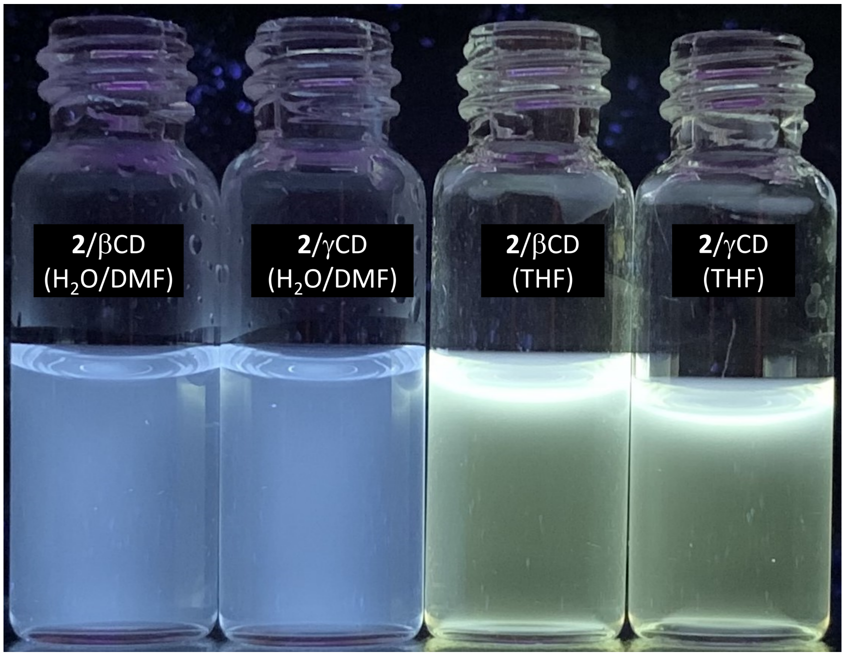

Figure A.60: Photographic images of the two left vials: **2** (1.0 $\times 10^{-3}$ M) in β-CD (5.0 $\times 10^{-3}$ M), and **2** (1.0 $\times 10^{-3}$ M) in γ-CD (5.0 $\times 10^{-3}$ M) dissolved in DMF/H_2O (1:1), and the two right vials: **2** (1.0 $\times 10^{-3}$ M) in β-CD (5.0 $\times 10^{-3}$ M), and **2** (1.0 $\times 10^{-3}$ M) in γ-CD (5.0 $\times 10^{-3}$ M) dissolved in THF.